KoG

SCIENTIFIC - PROFESSIONAL JOURNAL
OF CROATIAN SOCIETY FOR GEOMETRY AND GRAPHICS

No. 25. (2021)
ISSN 1331-1611

KoG

Official publication of the Croatian Society for Geometry and Graphics publishes scientific and professional papers from the fields of geometry, applied geometry and computer graphics.

Founder and Publisher

Croatian Society for Geometry and Graphics

Design

Miroslav Ambruš-Kiš

Layout

Sonja Gorjanc, Ema Jurkin

Cover Illustration

Georg Glaeser, photography

Print

SAND d.o.o., Zagreb

URL address

http://www.hdgg.hr/kog
http://hrcak.srce.hr

Edition

150

Published annually

Guide for authors
Please, see the page 96.

KoG is reviewed by zbMATH.

This issue has been financially supported by the Foundation of the Croatian Academy of Sciences and Arts.

ISSN 1331–1611

KoG

No. 25

Zagreb, 2021

SCIENTIFIC AND PROFESSIONAL JOURNAL OF
CROATIAN SOCIETY FOR GEOMETRY AND GRAPHICS

CONTENTS

ORIGINAL SCIENTIFIC PAPERS

REVIEWS

ISSN 1331–1611

BROJ 25

Zagreb, 2021

ZNANSTVENO-STRUČNI ČASOPIS
HRVATSKOG DRUŠTVA ZA GEOMETRIJU I GRAFIKU

SADRŽAJ

ORIGINALNI ZNANSTVENI RADOVI

PREGLEDNI RADOVI

https://doi.org/10.31896/k.25.1
Original scientific paper
Accepted 5. 5. 2021.

RONALDO GARCIA
DAN REZNIK

Family Ties: Relating Poncelet 3-Periodics by their Properties

Family Ties: Relating Poncelet3-Periodics by their Properties

ABSTRACT

We compare loci types and invariants across Poncelet families interscribed in three distinct concentric Ellipse pairs: (i) ellipse-incircle, (ii) circumcircle-inellipse, and (iii) homothetic. Their metric properties are mostly identical to those of 3 well-studied families: elliptic billiard (confocal pair), Chapple's poristic triangles, and the Brocard porism. We therefore organized them in three related groups.

Key words: invariant, elliptic billiard, locus

MSC2010: 51M04 51N20 51N35 68T20

Familije: Povezivanje Ponceletovih 3-periodika po njihovim svojstvima

SAŽETAK

Uspoređujemo tipove geometrijskih mjesta točaka i invarijanti u Ponceletovim familijama upisanim u tri različita para koncentričnih elipsi: (i) elipsa - upisana kružnica, (ii) opisana kružnica - upisana elipsa i (iii) homotetične elipse. Njihova metrička svojstva su uglavnom identična svojstvima triju dobro proučavanih familija: eliptični bilijar (par sa zajedničkim fokusima), Chappleovi poristični trokuti i Brocardov porizam. Zbog toga ih organiziramo u tri povezane grupe.

Ključne riječi: invarijanta, eliptični bilijar, geometrijsko mjesto točaka

1 Introduction

We have been studying loci and invariants of Poncelet 3-periodics in the confocal ellipse pair (elliptic billiard). Classic invariants include Joachmisthal's constant J (all trajectory segments are tangent to a confocal caustic) and perimeter L [26].

A few properties detected experimentally [21] and later proved can be divided into two groups: (i) loci of triangle centers (we use the X_k notation in [17]), and (ii) invariants. In terms of loci, the following results have been proved: (i) the locus of the incenter [9, 23], barycenter [25], circumcenter [7, 9], orthocenter [11] and many others are ellipses; (ii) a special triangle center known as the Mittenpunkt X_9 is stationary [24].

For invariants we chiefly have (i) the sum of cosines [1, 2], (ii) the product of outer polygon cosines, and (iii) outer-to-3-periodic area ratio [4].

We continue our inquiry into loci and invariants by now considering 3-periodic families three other non-confocal though concentric ellipse pairs. Referring to Figure 1:

- Family I: outer ellipse and incircle, incenter X_1 is stationary.
- Family II: outer circumcircle and inellipse, circumcenter X_3 is stationary
- Family III: an axis aligned pair of homothetic ellipses, the barycenter X_2 is stationary.

One goal is to identify properties of the above common with previously-studied 3-periodic families, namely, (i) the confocal pair (elliptic billiard), (ii) Chapple's porism [8] and (iii) the so-called Brocard porism [3, 15]. A quick review of their geometry appears in Section 2.

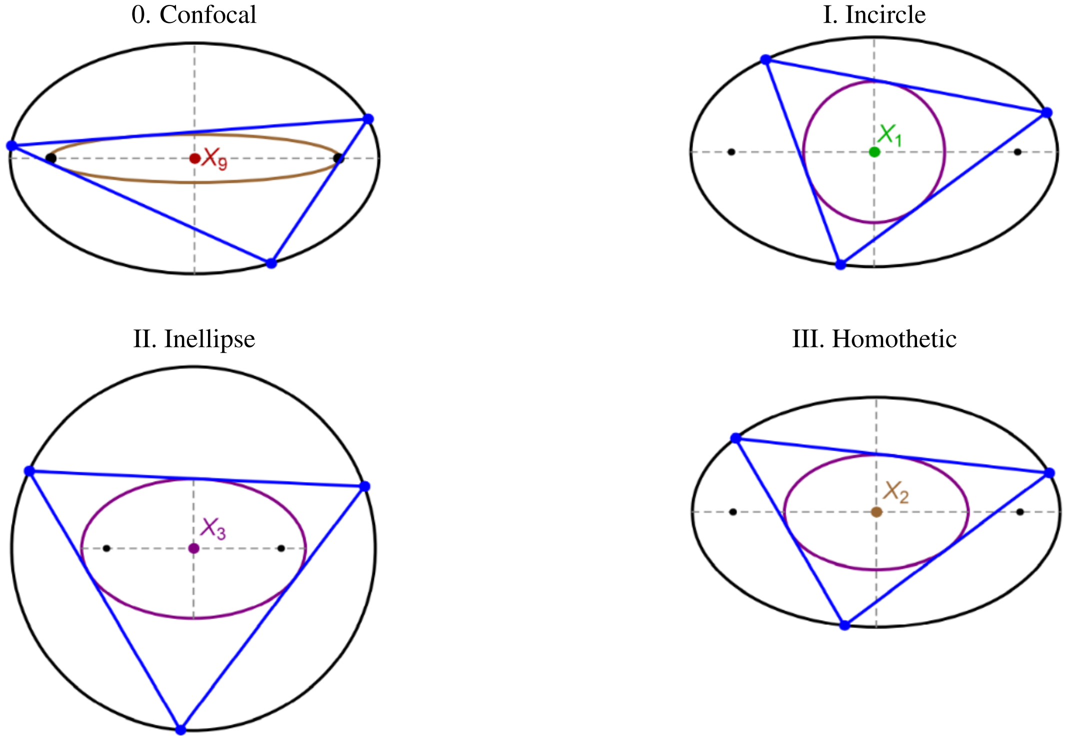

Figure 1: *Poncelet 3-periodic families in the various concentric ellipse pairs studied in the article. Properties and loci of the confocal pair (elliptic billiard) were studied in [21, 12, 11]. For each family the particular triangle center which is stationary is indicated.*

Main Results. Here are our main results:

- Family I
  - It conserves the circumradius, the sum of cosines, and the sum of sidelengths divided by their product.
  - Its sum of cosines is identical to that of the confocal pair which is its affine image.
  - The family is the image of Chapple's poristic family [19] under a variable rigid rotation.
  - The poristic family is the image of the confocal family under a variable similarity transform [10]. Therefore family I retains several all scale-free invariants identified for the elliptic billiard, including the sum of cosines.
- Family II
  - It conserves the cosine product and the sum of squared sidelengths.
  - Its product of cosines is identical to that of the excentral triangles in the confocal pair which is its affine image.
  - In the elliptic billiard, the locus of the incenter (resp. symmedian point) is an ellipse (resp. quartic) [11]. Here the roles swap: the incenter describes a quartic, and the symmedian is an ellipse.
  - The orthic triangles of this family are the image of the poristic family under a variable rigid rotation.
- Family III
  - It conserves area, sum of sidelengths squared, sum of cotangents (the latter implies that the Brocard angle is invariant).
  - Again in contradistinction with the elliptic billiard, the locus of the incenter X_1 is non-elliptic while that of X_6 is an ellipse.
  - The locus of irrational triangle centers X_k, k =13,14,15,16, i.e., the isodynamic and isogonic points, are circles! In the billiard, they are non-conic.
  - As shown in [20], this family is the image of Brocard porism triangles [3] under a variable similarity transform.

Thus, the following group Poncelet families is proposed with mostly identical properties: (i) family I: confocal, poristics; (ii) family II: confocal excentrals, poristic excentrals; (iii) family III: Brocard porism. Table 1 shows how loci types are shared and/or differ across families, and Figure 10 gives a bird's eye view of the kinship across these families via various transformations.

Related Work. Romaskevich proved the locus of the incenter X_1 over the confocal family is an ellipse [23]. Schwartz and Tabachnikov showed that the locus of barycenter and area centers of Poncelet trajectories are ellipses though the locus of the perimeter centroid in general isn't a conic [25]. For $N = 3$, the former correspond to X_2 and the latter to the Spieker center X_{10}. Garcia [9] and Fierobe [7] showed that the locus of the circumcenter of 3-periodics in the elliptic billiard are ellipses. Indeed, the loci of 29 out of the first 100 triangle centers listed in [17] are ellipses [11]. Tabachnikov and Tsukerman [27] and Chavez-Caliz [4] studied properties and loci of the "circumcenters of mass" of Poncelet N-periodics. This is a generalizations of the classical concept of circumcenter to generic polygons, based on triangulations, etc.

The following invariants for N-periodics in the elliptic billiard have been proved: (i) sum of cosines [1, 2], (ii) product of cosines of the outer polygons [1, 2], and (iii) area ratios and products of N-periodics and their polar polygons (excentral triangle for N=3); interestingly, these depend on the parity of N [2, 4]. Result (i) also holds for the Poncelet family interscribed between an ellipse and a concentric circle [1, Corollary 6.4].

Article structure. We start by reviewing the confocal, Chapple's, and Brocard porisms in Section 2. We then describe properties, invariants, and transformations of families I, II, and III in Sections 3, 4, and 5, respectively. We summarize all results in Section 6. Highlights include (i) a graph representing affine and/or similarity relations between the various families (Figure 10), (ii) a table of conserved quantities which we have found to continue to hold for $N > 3$ (proof pending), and (iii) a table with links to videos illustrating some phenomena herein.

2 Review of Classic Porisms and Proof Method

Grave's Theorem affirms that given a confocal pair $(\mathcal{E}, \mathcal{E}'')$, the two tangents to $\mathcal{E}''$ from a point P on $\mathcal{E}$ will be bisected by the normal of $\mathcal{E}$ at P [18]. A consequence is that any closed Poncelet polygon interscribed in such a pair, if regarded as the path of a moving particle bouncing elastically against the boundary, will be *N-periodic*. For this reason, this pair is termed the *elliptic billiard*; [26] is the seminal work. It is conjectured as the only integrable planar billiard [16]. One consequence, mentioned above, is that it conserves perimeter L. An explicit parametrization for 3-periodic vertices appears in Appendix A.1.

Referring to Figure 2, poristic triangles are a one-parameter Poncelet family with fixed incircle and circumcircle discovered in 1746 by William Chapple. Recently, Odehnal [19] has studied loci of its triangle centers. showing many of them are either stationary, ellipses, or circles. Surprisingly, the poristic family is the image of billiard 3-periodics under a variable similarity transform [10], and these two families share many properties and invariants.

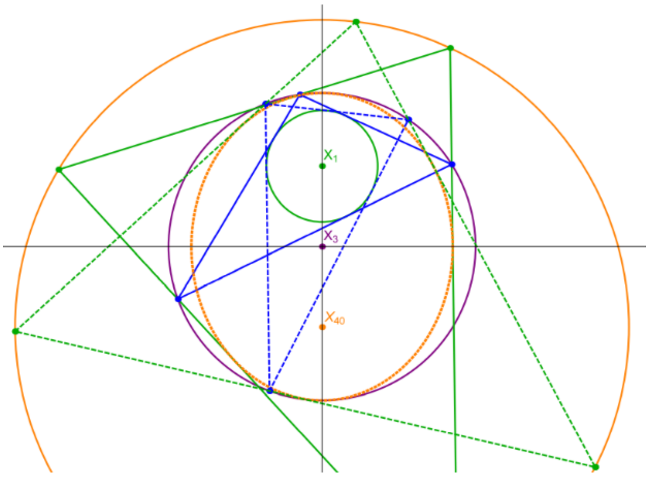

Figure 2: *The poristic triangle family (blue) [8] has a fixed incircle (green) and circumcircle (purple). Let r, R denote their radii. Its excentral triangles (green) are inscribed in a circle of radius $2R$ centered on the Bevan point X_{40} and circumscribe the MacBeath inconic (dashed orange) [28], centered on X_3 with foci at X_1 and X_{40}. A second configuration is also shown (dashed blue and dashed green).* Video

Referring to Figure 3, the Brocard porism [3] is a family of triangles inscribed in a circle and circumscribed to a special inellipse known as the "Brocard inellipse" [28, Brocard Inellipse]. Notably, the family's Brocard points are stationary and coincide with the foci of the inellipse. Also remarkable is the fact that the Brocard angle ω is invariant [15]. In [20] we showed this family is the image of family III triangles under a variable similarity transform.

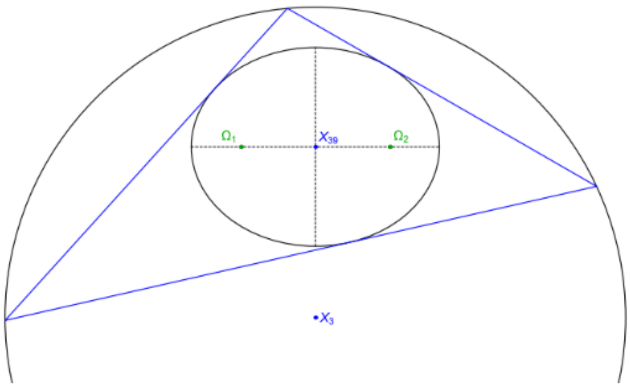

Figure 3: *The Brocard porism [3] is a 1d Poncelet family of triangles (blue) inscribed in a circle (black, upper half shown) and circumscribed about the Brocard inellipse [28] centered on X_{39} and with foci at the stationary Brocard points Ω_1 and Ω_2 of the family. The Brocard angle is invariant [15].* Video

A word about our proof method. We omit some proofs below as they are obtained from a consistent method used previously in [11]: (i) depart from symbolic expressions for the vertices of an isosceles 3-periodic (see Appendix A); (ii) obtain a symbolic expression for the invariant of interest; (iii) simplify it assisted by a CAS, arriving at a "candidate" symbolic expression for the invariant; (iv) verify the latter holds for any (non-isosceles) N-periodic and/or Poncelet pair aspect ratios and if it does, declare it as provably invariant.

3 Family I: Outer Ellipse, Inner Circle

Here we study a Poncelet family inscribed in an ellipse centered on O with semi-axes (a,b) and circumscribes a concentric circle of radius r, Figure 4 (left). An explicit parametrization is provided in Appendix A.2.

Cayley's closure condition [6] assumes a simple form for 3-periodics in a concentric, axis-aligned pair of ellipses [14]:

Proposition 1 *For 3-periodics in an axis-aligned, concentric ellipse pair:*

$$\frac{a'}{a}+\frac{b'}{b}=1, \tag{1}$$

where $a>b>0$, $a'>0$, and $b'>0$.

Corollary 1 *For family I 3-periodics, the radius r of the fixed incircle is given by:*

$$r=\frac{ab}{a+b}.$$

Proposition 2 *In the family I 3-periodics the locus of the barycenter X_2 is an ellipse with axes $a_2=a(a-b)/(3a+3b)$ and $b_2=b(a-b)/(3a+3b)$ centered on $O=X_1$.*

Theorem 1 *Family I 3-periodics have invariant circumradius $R=(a+b)/2$. Furthermore, the locus of the circumcenter X_3 is a circle of radius $d=R-b=a-R$ centered on $O=X_1$.*

Proof. Consider the explicit expressions derived for 3-periodic vertices in Appendix A.2. Let a first vertex $P_1=(x_1,y_1)$. From this, we obtain the center X_3 of the orbit's circumcircle:

$$X_3=\Bigg[-\frac{x_1\,(a-b)\left(-x_1^2\,(a+b)^2+a^2b\,(2\,a+b)\right)}{2a\left(\left(a^2-b^2\right)x_1^2+a^2b^2\right)},\;\frac{(a-b)\left(x_1^2\,(a+b)^2-a^2b^2\right)y_1}{2b\left(a^2x_1^2+b^2\left(a^2-x_1^2\right)\right)}\Bigg],$$

and radius $(a+b)/2$. We also obtain that the locus of X_3 is a circle with center $(0,0)$ and radius $(a-b)/2$. □

Proposition 3 *Over family I 3-periodics the locus of the orthocenter X_4 is an ellipse of axes $a_4=(a-b)b/(a+b)$ and $b_4=(a-b)a/(a+b)$ centered on $O=X_1$.*

Proposition 4 *Over family I 3-periodics the locus of the X_5 triangle center is a circle of radius $d=\frac{(a-b)^2}{4(a+b)}$ centered on $O=X_1$.*

Proposition 5 *The power of O with respect to the circumcircle is invariant and equal to $-ab$.*

Proof. Direct, analogous to [12, Thm.3]. □

Proposition 6 *Over family I 3-periodics, the locus of X_6 is a quartic given by the following implicit equation:*

$$\left(b\,(b+2a)\left(a^2+2ab+3b^2\right)x^2+a\,(a+2b)\left(3a^2+2ab+b^2\right)y^2\right)^2 - a^2b^2\,(a-b)^2\left(b^2\,(b+2a)^2x^2+a^2\,(a+2b)^2y^2\right)=0$$

3.1 Connection with the poristic family

Below we show that family I 3-periodics is the image of the poristic family [19] under a variable rigid rotation about X_1.

Recall the poristic family of triangles with fixed, non-concentric incircle and circumcircle with centers separated by $d=\sqrt{R(R-2r)}$ [8, 19]. Let I be a (moving) reference frame centered on X_1 with one axis oriented toward X_3. Referring to Figure 4 (right):

Theorem 2 *With respect to I, family I 3-periodics are the poristic triangle family (modulo a rigid rotation about X_1).*

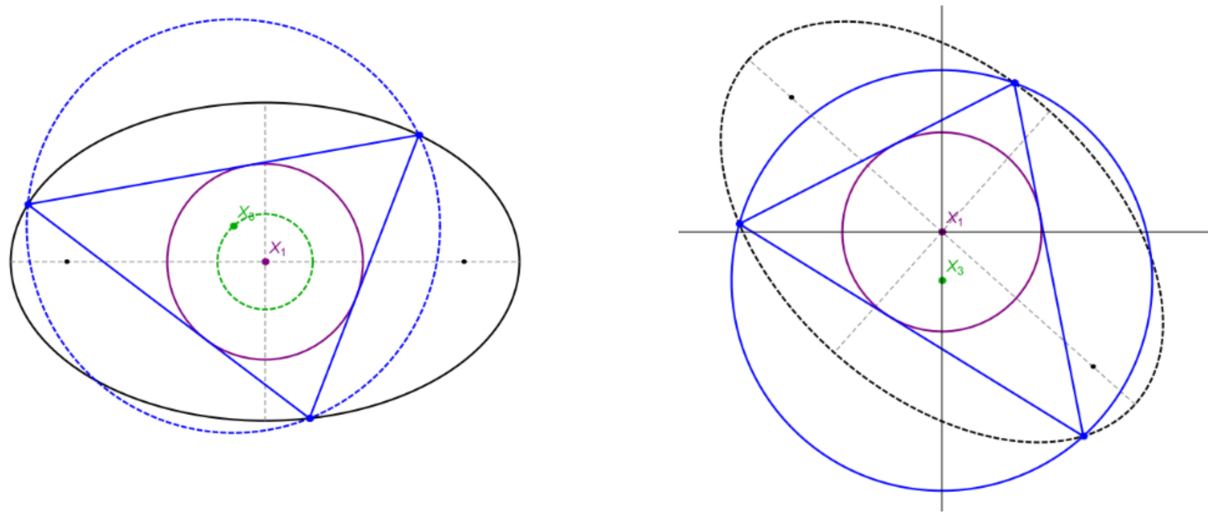

Figure 4: *Family I 3-periodics (left) are identical (up to rotation) to the family of poristic triangles (right) [8], if the former is observed with respect to a reference system where X_1 and X_3 are fixed. The fixed incircle (resp. circumcircle) are shown purple (resp. blue). The original outer ellipse (black on both drawings) becomes the X_1-centered circumellipse in the poristic case. Over the family, this ellipse is known to rigidly rotate about X_1 with axes $R+d, R-d$, where $d = |X_3 - X_1|$ [10].* Video

Proof. This stems from the fact that R, r, and d are constant. □

As proved in [10, Thm.3]:

Observation 1 *The X_1-centered circumconic to the poristic family is a rigidly-rotating ellipse with axes $R+d$ and $R-d$.*

Since this circumellipse is identical (up to rotation) to the outer ellipse of family I, then $R+d = a$ which is coherent with Proposition 1.
Furthermore, because poristic triangles are the image of billiard 3-periodics under a (varying) affine transform [10, Thm 4], it displays the same scale-free invariants.

Corollary 2 *Family I 3-periodics conserve the sum of cosines, product of half-sines, and all scale-free invariants.*

$$\sum_{i=1}^{3} \cos\theta_i = \frac{a^2+4ab+b^2}{(a+b)^2}, \quad \prod_{i=1}^{3} \sin\frac{\theta_i}{2} = \frac{ab}{2(a+b)^2}. \tag{2}$$

Note that invariant sum of cosines for family I N-periodics was proved for all N in [1, Corollary 6.4]. In fact:

Theorem 3 *Let $(\mathcal{E}_I, \mathcal{E}_I'')$ be a confocal pair of ellipses which is an affine image of a family I pair. Both families have invariant and identical sums of cosines.*

Proof. Let α, β and α'', β'' denote the semi-axes of $\mathcal{E}_I$ and $\mathcal{E}_I''$, respectively. For the pair to admit a 3-periodic family, the latter are given by [9]:

$$\alpha'' = \frac{\alpha(\delta-\beta^2)}{\alpha^2-\beta^2}, \quad \beta'' = \frac{\beta(\alpha^2-\delta)}{\alpha^2-\beta^2}.$$

Consider the following affine transformation:

$$T(x,y) = \left(\frac{\beta''}{\alpha''}x, y\right).$$

This takes $\mathcal{E}_I$ to an ellipse with semi-axes (a,b), $a = \alpha\frac{\beta''}{\alpha''}$ and $b = \beta$ and the caustic $\mathcal{E}_I''$ to a concentric circle of radius β''.
In [12, Thm.1] the following expression was given for invariant r/R in the confocal pair:

$$\frac{r}{R} = \frac{2(\delta-\beta^2)(\alpha^2-\delta)}{(\alpha^2-\beta^2)^2}, \quad \delta = \sqrt{\alpha^4-\alpha^2\beta^2+\beta^4}. \tag{3}$$

Recall that for any triangle, $\sum_{i=1}^{3}\cos\theta_i = 1 + r/R$ [28, Circumradius, Eqn. 4]. Plugging $a = \alpha\frac{\beta''}{\alpha''}$ and $b = \beta$ into to (2) yields (3) plus one. □

It turns out that the proof of [1, Corollary 6.4] implies that for all N, the cosine sum for family I N-periodics is invariant and identical to the one obtained with its confocal affine image [1].
A known relation for triangles is that $Rr = (s_1s_2s_3)/(4s)$, where s_1, s_2, s_3 are sidelengths and $s = (s_1+s_2+s_3)/2$ is the semiperimeter. Since both R and r are conserved:

Corollary 3 *The quantity $(s_1s_2s_3)/(4s)$ is conserved and is equal to $ab/2$.*

4 Family II: Outer Circle, Inner Ellipse

This family is inscribed in a circle of radius R centered on O and circumscribes a concentric ellipse with semi-axes a,b; see Figure 5. An explicit parametrization appears in Appendix A.3.
For the $N=3$ case, (1) implies $R=a+b$. By definition X_3 is stationary at O and R is the (invariant) circumradius. As shown in Figure 5:

Proposition 7 *Over family II 3-periodics, the loci of the orthocenter X_4 and nine-point center X_5 are concentric circles centered on $X_3=O$, with radii $2d'$ and d' respectively, where $d'=(a-b)/2$.*

Proof. CAS-assisted algebraic simplification. □

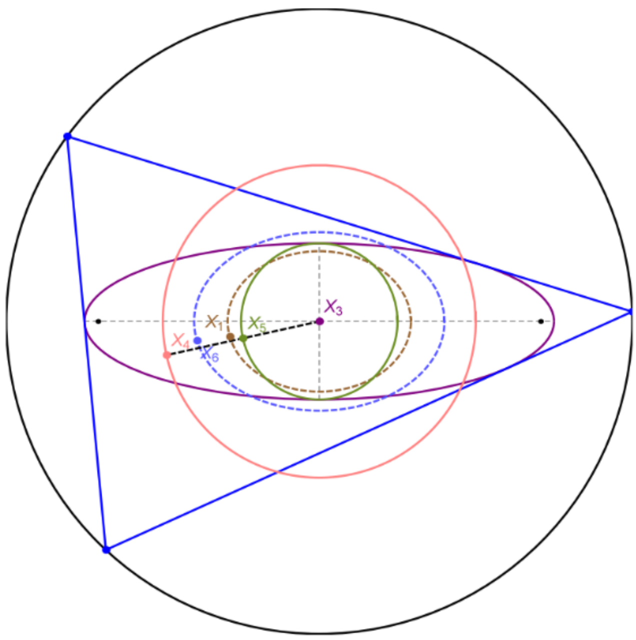

Figure 5: *Family II, the $N=3$ case: The loci of both orthocenter X_4 (pink) and nine-point center X_5 (olive green) are concentric with the external circle (black), with radii $2d'$ and d', respectively. I.e., $|X_4-X_5|=d'$. In contradistinction to the elliptic billiard, the locus of the incenter X_1 (dashed brown) is non-elliptic while that of the symmedian point X_6 (dashed blue) is an ellipse.* Video

Recall that in the confocal pair the locus of X_1 (resp. X_6) is an ellipse (resp. a quartic) [11]; see Appendix C. Interestingly:

Proposition 8 *Over family II 3-periodics, the locus of the symmedian point X_6 (resp. the incenter X_1) is an ellipse (resp. the convex component of a quartic – note the other component corresponds to the locus of the 3 excenters which can be concave). These are given by:*

locus of X_6 :

$$\frac{x^2}{a_6^2}+\frac{y^2}{b_6^2}=1,\ a_6=\frac{a^2-b^2}{a+2b},\ \ b_6=\frac{a^2-b^2}{2a+b},$$

locus of X_1 :

$$\left(x^2+y^2\right)^2-2\,(a+3\,b)\,(a+b)\,x^2-2\,(a+b)\,(3\,a+b)\,y^2$$
$$+\left(a^2-b^2\right)^2=0.$$

Proof. CAS-assisted simplification. □

Let s_i denote the sidelengths of an N-periodic.

Theorem 4 *Family II 3-periodics conserve $L_2=\sum_{i=1}^3 s_i^2=4(a+2b)(2a+b)$.*

Proof. Direct, using the parametrization for vertices in Appendix A.3. □

Note: the above is true for all N [1, Thm.8, corollary].

4.1 Family II and the poristic family

Below we show that the orthic triangles of Family II 3-periodics are the image of the poristic family [19] under a variable rigid rotation about X_3.

Lemma 1 *Family II 3-periodics conserve the product of cosines, given by:*

$$\prod_{i=1}^{3}\cos\theta_i=\frac{ab}{2(a+b)^2}.$$

Proof. CAS-assisted simplification. □

The orthic triangle has vertices at the feet of a triangle's altitudes [28]. Let R_h denote its circumradius. A known property is that $R_h=R/2$ [28, Orthic Triangle, Eqn. 7]. Therefore, it is invariant over family II 3-periodics. Referring to Figure 6 (left):

Proposition 9 *The inradius r_h of family II orthic triangles is invariant and given by $r_h=ab/(a+b)$.*

Proof. $r_h=2R\prod_{i=1}^3\cos\theta_i$ [28, Orthic Triangle, Eqn. 5]. Referring to Lemma 1 completes the proof. □

Let $(\mathcal{E}_{II},\mathcal{E}''_{II})$ denote the confocal pair which is an affine image of a circle-inellipse concentric pair. Let α,β and α'',β'' denote the semi-axes of $\mathcal{E}_{II}$, and $\mathcal{E}''_{II}$, respectively.

Theorem 5 *The invariant product of cosines for family II triangles is identical to the one obtained from excentral triangles of 3-periodics in $(\mathcal{E}_{II},\mathcal{E}''{}_{II})$.*

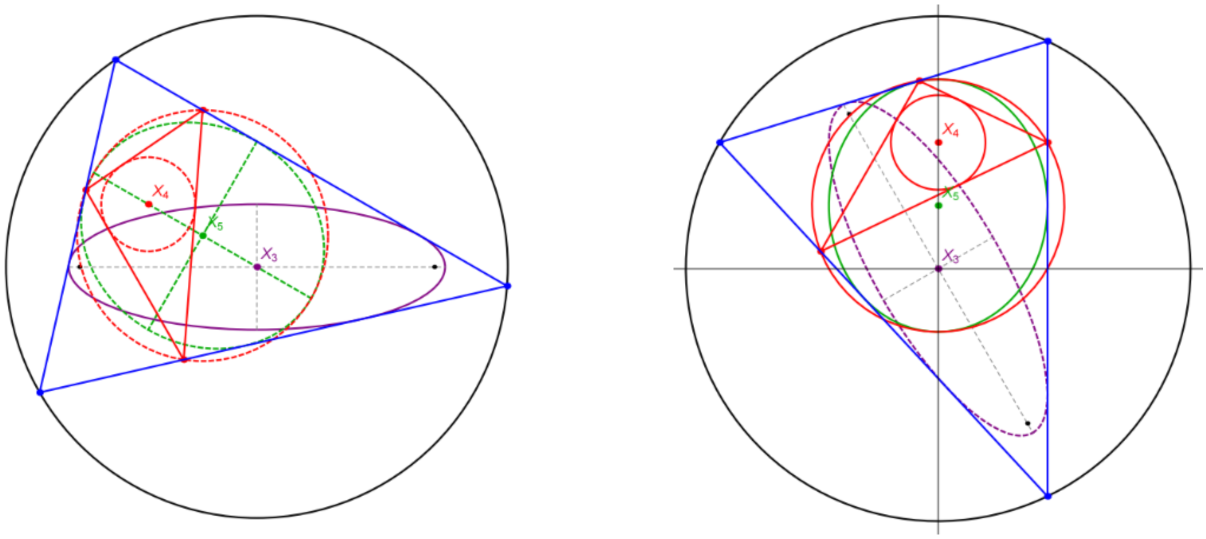

Figure 6: ***Left:*** *Family II 3-periodics (blue), and their orthic triangle (red). The latter's inradius and circumradius are invariant. The orthic triangle's incircle and circumcircle (both dashed red) are centered on the 3-periodic's orthocenter X_4 and the nine-point center X_5, respectively. Also shown is the rigidly-rotating MacBeath inellipse (dashed green), centered on X_5 with foci at X_3 and X_4.* ***Right:*** *Family II orthic triangles are identical (up to a variable rotation), to the poristic triangles (red) [19]. Equivalently, the original family is that of poristic excentral triangles (blue), for which both incircle and circumcircle (solid red) are stationary. Also stationary is the excentral MacBeath inellipse (green), i.e., it is the caustic [10], with center X_5 and foci X_3, and X_4, respectively. The original outer circle (black on both images) is also stationary on the poristic case, however the inner ellipse in the Poncelet pair (purple) becomes a rigidly-rotating X_3-centered excentral inellipse (dashed purple), whose axes are $R+d'$ and $R-d'$.* Video 1, Video 2

Proof. Excentrals in the confocal pair conserve the product of cosines [12, Corollary 2]. Recall that for any triangle:

$$\prod_{i=1}^{3}|\cos\theta_i'| = \frac{r}{4R},$$

where θ_i' are the angles of the excentral triangle. Plugging $a=\alpha''$ and $b=\frac{\alpha}{\beta}\beta''$ into (1) yields four times the above identity when r/R is computed as in (3), completing the proof. □

Lemma 2 *Family II 3-periodics are always acute.*

Proof. Since X_3 is the common center and is internal to the caustic, it will be interior to Family II 3-periodics, i.e., the latter are acute. □

Let I' be a (moving) reference frame centered on X_3 with one axis oriented toward X_5 (or X_4 as these 3 are collinear). Referring to Figure 4 (right):

Theorem 6 *With respect to I', family II 3-periodics are the excentral triangles to the poristic family (modulo a rigid rotation about X_3). Equivalently, family II orthics are identical (up to said variable rotation) to the poristic triangles.*

Proof. X_5 of a reference triangle is X_3 of the orthic triangle [17]. Since the family is always acute (Lemma 2), X_4 of the reference is X_1 of the orthic triangle [5]. By Proposition 7, $d'=|X_5-X_3|$ is invariant, i.e., the distance between X_1 and X_3 of the orthic triangle is invariant. The claim follows from noting X_3,X_5,X_4 are collinear [28] and that the orthic inradius and circumradius are invariant, Proposition 9. □

Recall from [10, Thm.2]:

Observation 2 *The X_3-centered inconic to the poristic excentral triangles is a rigidly-rotating ellipse with axes $R+d'$ and $R-d'$.*

Which makes sense when one considers the rotating reference frame. Also recall from [10, Thm.1] that:

Observation 3 *The MacBeath Inconic to the excentrals is stationary with axes R and $\sqrt{R^2-d'^2}$.*

Therefore its focal length is simply $2d'=|X_4-X_3|$. Furthermore, because poristic triangles are the image of billiard 3-periodics under a (varying) affine transform [10, Thm.4], Family II 3-periodics will share all scale-free invariants with billiard excentrals, such as product of cosines, ratio of area to its orthic triangle, etc., see [22].

5 Family III: Homothetic

This family is inscribed in an ellipse centered on O with semi-axes (a,b) and circumscribes an homothetic, axis-aligned, concentric ellipse with semi-axes (a'',b''); see Figure 7. An explicit parametrization is provided in Appendix A.4.

Proposition 10 *For family III 3-periodics, $a''=a/2$ and $b''=b/2$, the barycenter X_2 is stationary at O and the area A is invariant and given by:*

$$A=\frac{3\sqrt{3}}{4}ab\cdot$$

Proof. Family III is the affine image of a family of equilateral triangles interscribed within two concentric circles. The inradius of such a family is half its circumradius. Amongst triangle centers, the barycenter X_2 is uniquely invariant under affine transformations; it lies at the origin for an equilateral. Affine transformations preserve area ratios. A is the area of an equilateral triangle inscribed in a unit circle scaled by the Jacobian ab. This completes the proof. □

A known result is that the cotangent of the Brocard angle $\cot\omega$ of a triangle is equal to the sum of the cotangents of its three internal angles [28, Brocard Angle, Eqn. 1]. Surprisingly, we have:

Proposition 11 *Family III 3-periodics have invariant ω given by:*

$$\cot\omega=\sum_{i=1}^{3}\cot\theta_i=\frac{\sqrt{3}}{2}\frac{a^2+b^2}{ab}\cdot$$

Proof. Direct calculations using the explicit parametrization of vertices in Appendix A.4. □

A known relation is $\cot\omega=(\sum_{i=1}^{3}s_i^2)/(4A)$ [28, Brocard Angle, Eqn. 2]. Therefore, we have:

Corollary 4 *The sum of squared sidelengths s_i^2 is invariant and given by:*

$$\sum_{i=1}^{3}s_i^2=\frac{9}{2}\left(a^2+b^2\right)\cdot$$

As mentioned above, in the confocal pair the loci of X_1 (resp. X_6) is an ellipse (resp. a quartic) [11]; see Appendix C. Interestingly, we have:

Proposition 12 *For family III, the locus of the incenter X_1 (resp. symmedian point X_6) is a quartic (resp. an ellipse). These are given by:*

locus of X_1 :

$$16\left(a^2y^2+b^2x^2\right)\left(a^2x^2+b^2y^2\right)-8b^2\left(a^4+5a^2b^2+2b^4\right)x^2$$
$$-8a^2\left(2a^4+5a^2b^2+b^4\right)y^2+a^2b^2\left(a^2-b^2\right)^2=0,$$

locus of X_6 :

$$\frac{x^2}{a_6^2}+\frac{y^2}{b_6^2}=1,\; a_6=\frac{a(a^2-b^2)}{2(a^2+b^2)},\quad b_6=\frac{b(a^2-b^2)}{2(a^2+b^2)}.$$

Proof. CAS-assisted simplification. □

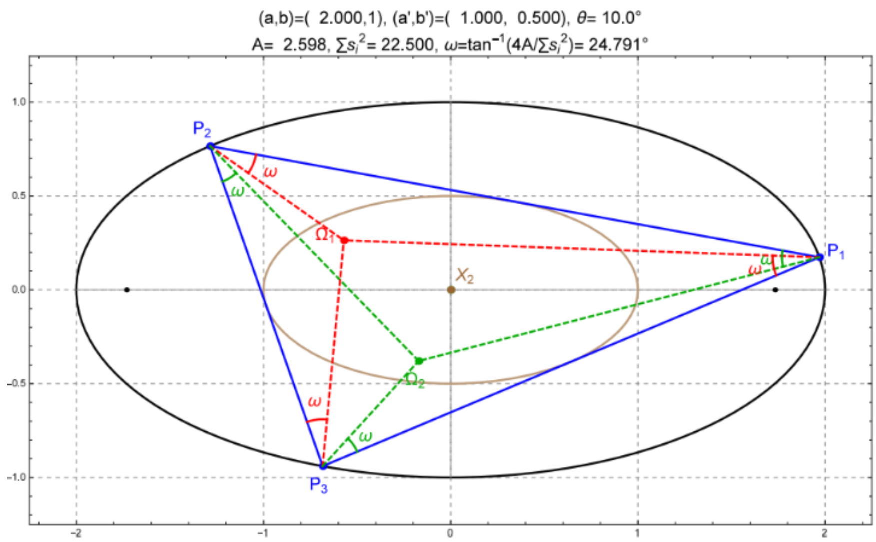

Figure 7: *Family III (homothetic pair) 3-periodics (blue). Also shown are the Brocard points Ω_1 and Ω_2. Since both area and sum of squared sidelengths are constant, so is the Brocard angle ω. Video*

5.1 Surprising Circular Loci

The two isodynamic points X_{13} and X_{14} as well as the two isogonic points X_{15} and X_{16} have trilinear coordinates which are irrational on the sidelengths of a triangle [17]. In the elliptic billiard their loci are non-elliptic. Indeed, in the elliptic billiard we haven't yet found any triangle centers with a conic locus whose trilinears are irrational. Referring to Figure 8, for family III, this is a surprising fact:

Proposition 13 *The loci of of X_k, k =13,14,15,16 are circles. Their radii are $(a-b)/2$, $(a+b)/2$, $(a-b)^2/z$, and $(a+b)^2/z$, respectively, where $z = 2(a+b)$.*

Observation 4 *Over all a/b, the radius of X_{16} is minimum when $a/b = 3$.*

5.2 Family III and the Brocard Porism

The Brocard porism [3] is a family of triangles inscribed in a circle and circumscribed about a special inellipse known as the "Brocard inellipse" [28, Brocard Inellipse]. Its foci coincide with the stationary Brocard points of the family. Furthermore, this family conserves the Brocard angle ω. Referring to Figure 7, we showed that over the homothetic family, the aspect ratio of the Brocard inellipse is invariant [20]. This leads to the following result, reproduced from [20, Theorem 3]:

Theorem 7 *The 3-periodic family in a homothetic pair and that of the Brocard porisms are images of one another under a variable similarity transform.*

As shown in [13], the locus of the center X_{39} of the Brocard inellipse is an ellipse (it is stationary in the Brocard porism).

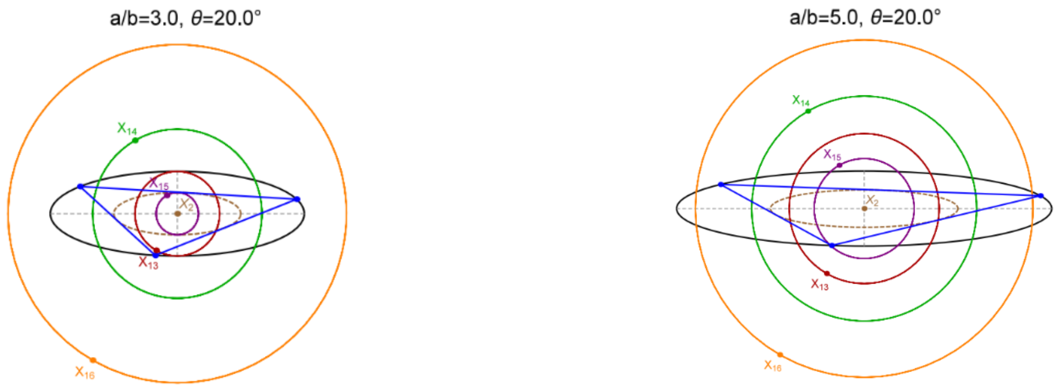

Figure 8: *Circular loci of the first and second Fermat points X_{13} and X_{14} (red and green) as well as the first and second isodynamic points X_{15} and X_{16} (purple and orange) for two aspect ratios of the homothetic pair: $a/b = 3$ (left) and $a/b = 5$ (right). The radius of the X_{16} locus is minimal at the first case.* Video

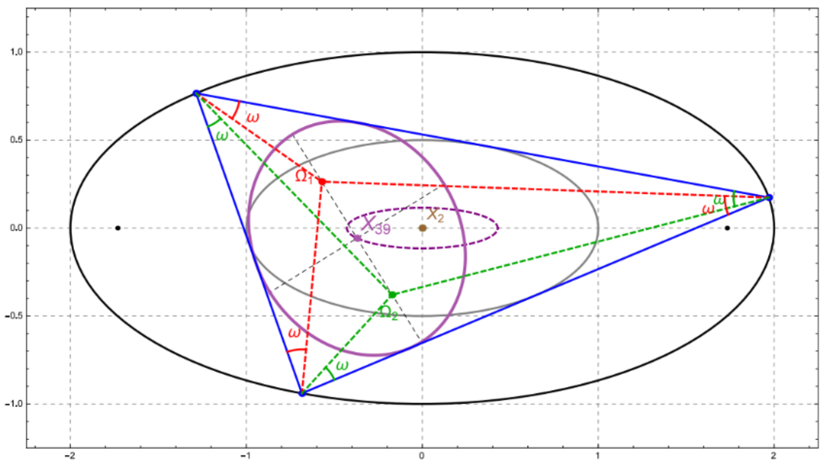

Figure 9: *Family III triangles (blue) are the image of Brocard porism triangles under a variable similarity transform [20]. This stems from the fact that the family's Brocard inellipse (purple), centered on X_{39} and with foci on the Brocard points Ω_1, Ω_2, has a fixed aspect ratio. Also shown is the elliptic locus of X_{39}.* Video

6 Summary

Table 1 summarizes the types of loci (point, circle, ellipse, etc.) for several triangle centers for all families mentioned above. These are organized within three groups A, B, and C with closely-related loci types. Exceptions are also indicated though we still lack a theory for it.

The first row reveals that out of the 8 families considered only in the confocal case is the locus of the incenter X_1 an ellipse. Additionaly experimentation has suggested an intriguing conjecture:

Conjecture 1 *Given a pair of conics which admits a Poncelet 3-periodic family, only when such conics are confocal will the locus of either the incenter X_1 or the excenters be a non-degenerate conic.*

The plethora of circles in the poristic family had already been shown in [19]. An above-than-expected frequency of ellipses for the confocal pair was signalled in [11]. As mentioned above, irrational centers X_k, $k \in [13,16]$ sweep out circles for the homothetic pair. X_{15} and X_{16} are known to be stationary over the Brocard family [3], however the locus of X_{13} and X_{14} are circles! Also noticeable is the fact that (i) though in the confocal pair the locus of X_1 and X_6 is an ellipse and a quartic, respectively, in both family II and family III said locus types are swapped. The reasons remain mysterious.

It is well-known that there is a projective transformation that takes any Poncelet family to the confocal pair, [6]. In this case only projective properties are preserved. If one restricts the set of possible transformations to either affine ones or similarities (which include rigid transformations), one can construct the two-clique graph of interrelations shown in Figure 10.

As mentioned above, the confocal family is the affine image of either family I or family II. In the first (resp. second) case the caustic (resp. outer ellipse) is sent to a circle. Though the affine group is non-conformal, we showed above that both families conserve their sum of cosines (Theorem 3). One way to see this is that there is an alternate, conformal path which takes family I triangles to the confocal ones, namely a rigid rotation (yielding poristic triangles), followed by a variable similarity (yielding the confocal family).

	Group A			Group B			Group C	
	Conf.	F.I	Por.	Conf. Exc	F.II	Por. Exc.	F.III	Broc.
X_1	E	P	P	X	X	X	4	X
X_2	E	E	C	E	C	P	P	C
X_3	E	C	P	E	P	P	E	P
X_4	E	E	C	E	C	P	E	C
X_5	E	C	C	E	C	P	E	C
X_6	4	4	**E**	P	E	C	E	P
X_7	E	E	C	X	X	X	X	X
X_8	E	E	C	X	X	X	X	X
X_9	P	E	C	X	X	X	X	X
X_{10}	E	E	C	X	X	X	X	X
X_{11}	E″	C″	C″	X	X	**C_5**	X	X
X_{12}	E	C	C	X	X	X	X	X
X_{13}	X	X	X	X	X	X	C	C
X_{14}	X	X	X	X	X	X	C	C
X_{15}	X	X	X	X	X	X	C	P
X_{16}	X	X	X	X	X	X	C	P
X_{99}	X	X	C′	**X**	C′	C′	E′	C′
X_{100}	E′	E′	C′	**X**	C′	C′	**X**	C′
X_{110}	X	X	C′	E′	C′	C′	**X**	C′

Table 1: *Types of loci for several triangle centers over several Poncelet triangle families, divided in 3 groups A,B,C with closely-related metric phenomena: (i) confocal, fam. I, poristics; (ii) confocal excentral, fam. II, poristic excentral triangles; (iii) fam. III and Brocard porism. Symbols P, C, E, and X indicate point, circle, ellipse, and non-elliptic (degree not yet derived) loci, respectively. A number refers to the degree of the non-elliptic implicit, e.g., '4' for quartic. A singly (resp. doubly) primed letter indicates a perfect match with the outer (resp. inner) conic in the pair. The symbol C_5 refers to the nine-point circle. The boldface entries indicate a discrepancy in the group (see text). Note: X_n for the confocal and poristic excentral triangles refer to triangle centers of the family itself (not of their reference triangles).*

A similar argument is valid for family II triangles: there is an affine path (non-conformal) to the confocal family though both conserve the product of cosines (Theorem 5). Notice an alternate conformal composition of rotation (yielding poristic excentral triangles) and a variable similarity (yielding confocal excentral triangles). All in this path conserve the product of cosines.

Finally, family III and Brocard porism triangles form an isolated clique. As mentioned in [20], these are variable similarity images of one another but cannot be mappable to the other families via similarities nor affinely.

Table 2 summarizes some properties of 3-periodics mentioned herein. The last column reveals that many of the invariants continue to hold for N>3. Animations illustrating some focus-inversive phenomena are listed in Table 3.

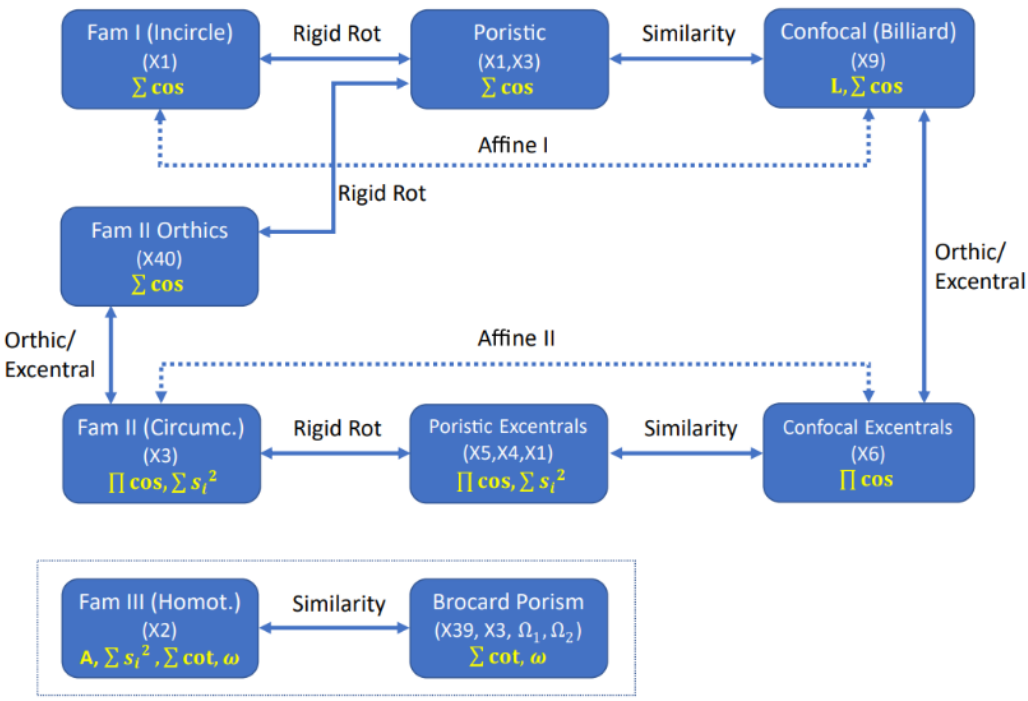

Figure 10: *Diagram of transformations that take one 3-periodic family into another. The families are specified in each box while the transformations label the arrows. The second (resp. third) line in each box lists the stationary point(s) (resp. main invariants) in the family.*

fam.	pair	N=3 outer conic	N=3 inner conic	N=3 invariants	N>3
	billiard	ellipse (a,b)	confocal caustic	$L,J,r/R,\sum\cos$	$L,J,\sum\cos$
I	inner circle	ellipse (a,b)	circle $r=\frac{ab}{a+b}$	$R,r/R,\sum\cos$	$\sum\cos$
II	outer circle	$R=(a+b)$	ellipse (a,b)	$\sum s_i^2,\prod\cos$	$\sum s_i^2,\prod\cos$
III	homothetic	ellipse (a,b)	ellipse $(a/2,b/2)$	$A,\sum s_i^2,\omega,\sum\cot$	$A,\sum s_i^2,\sum\cot$

Table 2: *Summary of properties across different concentric Poncelet families. The last column shows some invariants which continue to hold for N>3.*

id	family	N	Title	**youtu.be/...**
01	all	3	Concentric Poncelet families	8hkeksAsx0E
02	por.	3	Chapple's poristic family & excentral triangles	DS4ryndDK6Qo
03	por.	3	Poristics are image of billiard 3-periodics	NvjrX6XKSFw
04	I	3	Side-by-side w/ the poristic family	ML_AZoX736w
05	I	3,5	Circular loci of X3 & Steiner's curvature centroid	6010fxuSDGc
06	I	3,5	Invariant ratio of sidelength product to sum	7Jg2nRkkUhQ
07	II	3	Family is image of poristic excentrals	wUu2iMesv3U
08	II	3	Side-by-side w/the poristic family	xM1SAZO9bDc
09	II	3,5	Circular locus of generalized orthocenter	3f6YBohQCFg
10	III	3	Stationary X_2 and invariant Brocard angle	2fvGd8wioZY
11	III	3	Loci of X_k, k =13,14,15,16 are all circles!	ZwTfwaJJitE
12	III	3	Family is image of Brocard porism	h3GZz7pcJp0
13	I,II	5,6	Locus of generalized circum- and orthocenter	ZfQEDujbirQ
14	I,II	5	Locus of generalized circumcenter	RP18B82715I
15	I,II	5	Generalized circumcenter (Steiner's curv. centroid)	RP18B82715I
16	dual	3	The dual pair: stationary orthocenter	fpd_Zot5cKk
17	dual	3–8	Generalized stationary orthocenter	ttKjzWeG5B8
18	dual	5,7	Generalized stationary orthocenter	gNHiZvBhKF8

Table 3: *Videos illustrating some phenomena mentioned herein. The last column is clickable and provides the YouTube code.*

Acknowledgements

We would like to thank Mark Helman, Dominique Laurain, Arseniy Akopyan, Peter Moses, and Boris Odehnal for valuable insights. We are also indebted to the meticulous review by the referee. The first author is fellow of CNPq and coordinator of Project PRONEX/ CNPq/ FAPEG 2017 10 26 7000 508.

Appendix A. Explicit 3-Periodic Vertices

A.1. Pair 0: Confocal

Let (a,b) be the semi-axes of the external ellipse. Let $P_i = (x_i, y_i)/q_i$, $i = 1,2,3$, denote the 3-periodic vertices, given by [9]:

$$
\begin{aligned}
&q_1 = 1,\\
&x_2 = -b^4\left(\left(a^2+b^2\right)k_1 - a^2\right)x_1^3 - 2\,a^4 b^2 k_2 x_1^2 y_1\\
&\quad + a^4\left((a^2-3\,b^2)k_1 + b^2\right)x_1\,y_1^2 - 2a^6 k_2 y_1^3,\\
&y_2 = 2b^6 k_2 x_1^3 + b^4\left((b^2-3\,a^2)k_1 + a^2\right)x_1^2 y_1\\
&\quad + 2\,a^2 b^4 k_2 x_1 y_1^2 - a^4\left(\left(a^2+b^2\right)k_1 - b^2\right)y_1^3,\\
&q_2 = b^4\left(a^2 - c^2 k_1\right)x_1^2 + a^4\left(b^2 + c^2 k_1\right)y_1^2 - 2\,a^2 b^2 c^2 k_2 x_1\,y_1,\\
&x_3 = b^4\left(a^2 - \left(b^2+a^2\right)\right)k_1 x_1^3 + 2\,a^4 b^2 k_2 x_1^2 y_1\\
&\quad + a^4\left(k_1\left(a^2-3\,b^2\right) + b^2\right)x_1\,y_1^2 + 2\,a^6 k_2 y_1^3,\\
&y_3 = -2\,b^6 k_2 x_1^3 + b^4\left(a^2 + \left(b^2-3\,a^2\right)k_1\right){x_1}^2 y_1\\
&\quad - 2\,a^2 b^4 k_2 x_1 y_1^2 + a^4\left(b^2 - \left(b^2+a^2\right)k_1\right)\,y_1^3,\\
&q_3 = b^4\left(a^2 - c^2 k_1\right)x_1^2 + a^4\left(b^2 + c^2 k_1\right)y_1^2 + 2\,a^2 b^2 c^2 k_2\,x_1\,y_1,
\end{aligned}
$$

where:

$$
\begin{aligned}
&k_1 = \frac{d_1^2\delta_1^2}{d_2} = \cos^2\alpha,\ \ k_2 = \frac{\delta_1 d_1^2}{d_2}\sqrt{d_2 - d_1^4\delta_1^2} = \sin\alpha\cos\alpha,\\
&c^2 = a^2 - b^2,\ \ d_1 = (a\,b/c)^2,\ \ d_2 = b^4 x_1^2 + a^4 y_1^2,\\
&\ \delta = \sqrt{a^4+b^4-a^2b^2},\ \ \delta_1 = \sqrt{2\delta - a^2 - b^2},
\end{aligned}
$$

where α, though not used here, is the angle of segment P_1P_2 (and P_1P_3) with respect to the normal at P_1.

A.2. Pair I: Incircle

3-periodics are given by $P_1(t) = (x_1, y_1) = (a\cos t, b\sin t)$. Then, the $P_i = (x_i, y_i), i = 2,3$ are:

$$
\begin{aligned}
x_2 =& 2\,a^2 b^2\left(-a^2 b x_1 + k\,y_1\right)/q_2,\ \ y_2 = -2\,ab^3\left(a^2 b y_1 + k\,x_1\right)/q_2,\\
x_3 =& -2\,a^2 b^2\left(a^2 b x_1 + k\,y_1\right)/q_3,\ \ y_3 = 2\,b^3 a\left(-a^2 b y_1 + k\,x_1\right)/q_3,\\
k =& \sqrt{a^3\,(a+2\,b)\,x_1^2 + a^2 b\,(2\,a+b)\,y_1^2},\\
q_2 =& 2b^2(a+b)((a^2-b^2)x_1^2 + a^2b^2),\\
q_3 =& \left(b^2a^4 - y_1^2a^4 + 2\,a^2b^4 + a^2b^2x_1^2 - 2\,x_1^2b^4\right)(a+b)\cdot
\end{aligned}
$$

A.3. Pair II: Inellipse

3-periodics are given by $P_1(t) = (x_1, y_1) = R(\cos t, \sin t)$ with $R = a+b$. Then the $P_i = (x_i, y_i), i = 2,3$ are given by:

$$
\begin{aligned}
x_2 =& \left(-b^2 x_1 + y_1\,s_x\right)k_x,\ \ y_2 = -\left(y_1\,a^2 + x_1\,s_y\right)k_y,\\
x_3 =& -\left(b^2 x_1 + y_1\,s_x\right)k_x,\ \ y_3 = \left(-y_1\,a^2 + x_1\,s_y\right)k_y,\\
s_x =& \sqrt{a^3(a+2b) - (a^2-b^2)x_1^2},\ \ s_y = \sqrt{(a^2-b^2)y_1^2 + b^3(2a+b)},\\
k_x =& \frac{a}{(-a+b)\,x_1^2 + a^2\,(a+b)},\ \ k_y = \frac{b}{(a-b)\,y_1^2 + b^2\,(a+b)}.
\end{aligned}
$$

A.4. Pair III: Homothetic

3-periodics are given by $P_1(t) = (x_1, y_1) = (a\cos t, b\sin t)$. Then $P_i = (x_i, y_i), i = 2, 3$ are:

$$(x_2, y_2) = \left(\frac{\sqrt{3}\,ay_1 - bx_1}{2b}, \frac{-\sqrt{3}\,bx_1 - ay_1}{2a}\right),$$
$$(x_3, y_3) = \left(\frac{-\sqrt{3}\,ay_1 - bx_1}{2b}, \frac{\sqrt{3}\,bx_1 - ay_1}{2a}\right).$$

Appendix B. Elliptic Loci

Below we list triangle centers amongst X_k, $k = 1, \ldots, 200$ for each of the Poncelet pairs mentioned in this article, whose loci are either ellipses or circles.

- 0. Confocal pair (stationary X_9)
  - Ellipses: 1, 2, 3, 4, 5, 7, 8, 10, 11, 12, 20, 21, 35, 36, 40, 46, 55, 56, 57, 63, 65, 72, 78, 79, 80, 84, 88, 90, 100, 104, 119, 140, 142, 144, 145, 149, 153, 162, 165, 190, 191, 200. Note: the first 29 in the list were proved in [11].
  - Circles: n/a
- I. Incircle: (stationary X_1)
  - Ellipses: 2, 4, 7, 8, 9, 10, 20, 21, 63, 72, 78, 79, 84, 90, 100, 104, 140, 142, 144, 145, 149, 153, 191, 200.
  - Circles: 3, 5, 11, 12, 35, 36, 40, 46, 55, 56, 57, 65, 80, 119, 165.
- II. Inellipse (w/ circumcircle): (stationary X_3)
  - Ellipses: 6, 49, 51, 52, 54, 64, 66, 67, 68, 69, 70, 113, 125, 141, 143, 146, 154, 155, 159, 161, 182, 184, 185, 193, 195.
  - Circles: 2, 4, 5, 20, 22, 23, 24, 25, 26, 74, 98, 99, 100, 101, 102, 103, 104, 105, 106, 107, 108, 109, 110, 111, 112, 140, 156, 186.
- III. Homothetic: (stationary X_2)
  - Ellipses: 3, 4, 5, 6, 17, 20, 32, 39, 62, 69, 76, 83, 98, 99, 114, 115, 140, 141, 147, 148, 182, 187, 190, 193, 194.
  - Circles: 13, 14, 15, 16.

Semi-axes lengths for the elliptic loci of many triangle centers are available in [13].

Appendix C. Loci of Incenter and Symmedian in the Elliptic Billiard

Over 3-periodics in the elliptic billiard, the locus of the incenter X_1 is an origin centered ellipse with axes a_1, b_1 given by [9]:

$$a_1 = \frac{\delta - b^2}{a}, \quad b_1 = \frac{a^2 - \delta}{b}.$$

Over the same family, the locus of X_6 is a convex quartic given by [11, Theorem 2]:

$$\text{locus } X_6 : \; c_1x^4 + c_2y^4 + c_3x^2y^2 + c_4x^2 + c_5y^2 = 0,$$

where:

$$\begin{aligned} c_1 &= b^4(5\delta^2 - 4(a^2 - b^2)\delta - a^2b^2), & c_2 &= a^4(5\delta^2 + 4(a^2 - b^2)\delta - a^2b^2),\\ c_3 &= 2a^2b^2(a^2b^2 + 3\delta^2), & c_4 &= a^2b^4(3b^4 + 2(2a^2 - b^2)\delta - 5\delta^2),\\ c_5 &= a^4b^2(3a^4 + 2(2b^2 - a^2)\delta - 5\delta^2), & \delta &= \sqrt{a^4 - a^2b^2 + b^4}. \end{aligned}$$

Note: this curve has an isolated point at the origin whose geometric meaning is not yet understood.

Appendix D. Table of Symbols

symbol	meaning	note
O	center of concentric pair	
a,b	ellipse semi-axes	
s_i, s	sidelength and semiperimeter	$i = 1, \ldots N$
θ_i	internal angle	
L	perimeter	$\sum_i s_i$
L_2	sum of squared sidelengths	$\sum_i s_i^2$
K	Steiner's Curvature Centroid	$\sum_i w_i P_i / \sum_i w_i$
		$w_i = \sin(2\theta_i)$
r, R	inradius, circumradius	
d'	$\lvert X_4 - X_5 \rvert$	
r_h, R_h	inradius, circumradius of ortic	
ω	Brocard angle	$\tan(\omega) = 4A/L_2$
X_1	incenter	
X_2	barycenter	
X_3	circumcenter	
X_4	orthocenter	
X_5	center of 9-point circle	

Table 4: *Symbols used.*

References

[1] A. Akopyan, R. Schwartz, S. Tabachnikov, Billiards in ellipses revisited, *Eur. J. Math.* (2020), doi:10.1007/s40879-020-00426-9

[2] M. Bialy, S. Tabachnikov, Dan Reznik's identities and more, *Eur. J. Math.* (2020), doi:10.1007/s40879-020-00428-7

[3] C. Bradley, G. Smith, On a construction of Hagge, *Forum Geom.* **7** (2007), 231–247.

[4] A. Chavez-Caliz, More about areas and centers of Poncelet polygons, *Arnold Math J.* **7** (2021), 91–106, doi:10.1007/s40598-020-00154-8

[5] H.S.M. Coxeter, S.L. Greitze,, *Geometry Revisited*, vol. 19 of *New Mathematical Library*, New York: Random House, Inc., 1967.

[6] V. Dragović, M. Radnović, *Poncelet Porisms and Beyond: Integrable Billiards, Hyperelliptic Jacobians and Pencils of Quadrics*, Frontiers in Mathematics, Basel: Springer, 2011.

[7] C. Fierobe, On the circumcenters of triangular orbits in elliptic billiard, *J. Dyn. Control Syst.* (2021), doi:10.1007/s10883-021-09537-2

[8] W. Gallatly, *The modern geometry of the triangle*, Francis Hodgson, London, 1914.

[9] R. Garcia, Elliptic billiards and ellipses associated to the 3-periodic orbits, *Amer. Math. Monthly*, **126**(6) (2019), 491–504.

[10] R. Garcia, D. Reznik, Related by similarity I: Poristic triangles and 3-periodics in the elliptic billiard, *Intl. J. of Geom.* **10**(3) (2021), 52–70.

[11] R. Garcia, D. Reznik, J. Koiller, Loci of 3-periodics in an elliptic billiard: why so many ellipses?, arXiv:2001.08041, 2020.

[12] R. Garcia, D. Reznik, J. Koiller, New properties of triangular orbits in elliptic billiards, *Amer. Math. Monthly* (2020), to appear.

[13] R. Garcia, D. Reznik, J. Koiller, Semi-Axes of Elliptic Loci, GitHub., 2021. `http://dan-reznik.github.io/why-so-many-ellipses/`.

[14] V. Georgiev, V. Nedyalkova, Poncelet's porism and periodic triangles in ellipse, *Dynamat*, 2012, `www.dynamat.oriw.eu/upload_pdf/20121022_153833__0.pdf`.

[15] R.A. Johnson, *Modern Geometry: An Elementary Treatise on the Geometry of the Triangle and the Circle*, Boston, MA: Houghton Mifflin, 1929.

[16] V. KALOSHIN, A. SORRENTINO, On the integrability of Birkhoff billiards, *Phil. Trans. R. Soc. A.*, **376** (2018).

[17] C. KIMBERLING, Encyclopedia of triangle centers, 2020, `faculty.evansville.edu/ck6/encyclopedia/ETC.html`

[18] N. MILLER, A Generalization of a Property of Confocal Conics, *Amer. Math. Monthly*, **32**(4) (1925), 178–180.

[19] B. ODEHNAL, Poristic loci of triangle centers, *J. Geom. Graph.* **15**(1) (2011), 45–67.

[20] D. REZNIK, R. GARCIA, Related by similarity II: Poncelet 3-periodics in the homothetic pair and the brocard porism, *Intl. J. of Geom.* **10**(4) (2021), 18–31.

[21] D. REZNIK, R. GARCIA, J. KOILLER, Can the Elliptic Billiard still surprise us?, *Math Intelligencer*, **42** (2020), 6–17.

[22] D. REZNIK, R. GARCIA, J. KOILLER, Fifty new invariants of n-periodics in the elliptic billiard, *Arnold Math. J.* (2021), doi:10.1007/s40598-021-00174-y

[23] O. ROMASKEVICH, On the incenters of triangular orbits on elliptic billiards, *Enseign. Math.* **60**(3-4) (2014), 247–255.

[24] O. ROMASKEVICH, Proof the mittenpunkt is stationary, Private Communication, 2019.

[25] R. SCHWARTZ, S. TABACHNIKOV, Centers of mass of Poncelet polygons, 200 years after, *Math. Intelligencer* **38**(2) (2016), 29–34.

[26] S. TABACHNIKOV, Geometry and Billiards, vol.30 of *Student Mathematical Library*, Providence, RI: Mathematics Advanced Study Semesters, University Park, PA, 2005.

[27] S. TABACHNIKOV, E. TSUKERMAN, Remarks on the circumcenter of mass, *Arnold Math. J.* **1** (2015) 101–112.

[28] E. WEISSTEIN, Mathworld, *MathWorld–A Wolfram Web Resource*, 2019, `mathworld.wolfram.com`.

Ronaldo Garcia
orcid.org/0000-0001-8876-6956
e-mail: ragarcia@ufg.br

Universidade Federal de Goiás
Instituto de Matemática e Estatística
BR-74001970 Goiânia, GO, Brazil

Dan Reznik
orcid.org/0000-0002-0542-6014
e-mail: dreznik@gmail.com

Data Science Consulting, Rio De Janeiro, Brazil

https://doi.org/10.31896/k.25.2
Original scientific paper
Accepted 22. 2. 2021.

HIROSHI OKUMURA

Semicircles in the Arbelos with Overhang and Division by Zero

Semicircles in the Arbelos with Overhang and Division by Zero

ABSTRACT

We consider special semicircles, whose endpoints lie on a circle, for a generalized arbelos called the arbelos with overhang considered in [4] with division by zero.

Key words: arbelos, arbelos with overhang, Aida arbelos, semicircle touching at the endpoints, insemicircle, Archimedean semicircle, division by zero

MSC2010: 01A27 51M04

Polukružnice u arbelosima s produžecima i dijeljenje s nulom

SAŽETAK

U radu proučavamo posebne polukružnice, one čije krajnje točke leže na jednoj kružnici, u poopćenim arbelosima s produžecima kao u [4] uz korištenje dijeljenja s nulom.

Ključne riječi: arbelosi, arbelosi s produžecima, Aida arbelosi, polukružnice s diranjem u krajnjim točkama, unutarnje polukružnice, Arhimedove polukružnice, dijeljenje s nulom

1 Introduction

For a point O on the segment AB such that $|AO| = 2a$, $|BO| = 2b$, let A_h (resp. B_h) be a point on the half line OA (resp. OB) with initial point O such that $|OA_h| = 2(a+h)$ (resp. $|OB_h| = 2(b+h)$) for a real number h satisfying $-\min(a,b) < h$. In [4] we have considered a generalized arbelos consisting of the three semicircles α, β and γ of diameters A_hO, B_hO and AB, respectively, constructed on the same side of AB. The figure is denoted by $(\alpha,\beta,\gamma)_h$ and is called the arbelos with overhang h (see Figure 1). The ordinary arbelos is obtained from $(\alpha,\beta,\gamma)_h$ if $h = 0$, which is denoted by $(\alpha,\beta,\gamma)_0$.

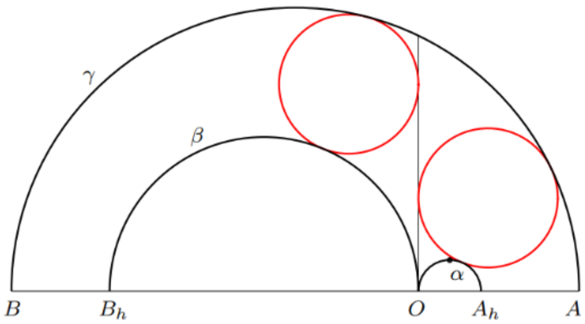

Figure 1: $(\alpha,\beta,\gamma)_h$, $-\min(a,b) < h < 0$.

Let $c = a+b$. The circle touching α (resp. β) externally, γ internally, and the axis from the side opposite to B (resp. A) has radius

$$r_{\mathrm{A}} = \frac{ab}{c+h}.$$

The two circles are called the twin circles of Archimedes of $(\alpha,\beta,\gamma)_h$. Circles of radius r_{A} are called Archimedean circles of $(\alpha,\beta,\gamma)_h$ or said to be Archimedean with respect to $(\alpha,\beta,\gamma)_h$.
In this article we consider special semicircles, which are counterpart to the incircle and Archimedean circles of $(\alpha,\beta,\gamma)_h$ using division by zero. At the last part of this paper we consider special case of $(\alpha,\beta,\gamma)_h$ considered by Aida [1]. We consider using a rectangular coordinate system with origin O such that the farthest point on α have coordinates $(a+h, a+h)$ (see Figure 1). The radical axis of α and β is called the axis.

2 Incircle and insemicircle

In this section we consider the incircle of $(\alpha,\beta,\gamma)_h$ and an inscribed semicircle in $(\alpha,\beta,\gamma)_h$. If a circle touches α and

β externally and γ internally, we call the circle the incircle of $(\alpha,\beta,\gamma)_h$ (see Figure 2). If the endpoints of a semicircles lie on a circle, we say that the semicircle touches the circle at the endpoints. If a semicircle touches α and β, and γ at the endpoints, we say that the semicircle is inscribed in $(\alpha,\beta,\gamma)_h$. We have considered such a semicircle in [2] for $(\alpha,\beta,\gamma)_0$. We use the next proposition.

Proposition 1 *A semicircle of radius s touches a circle of radius r at the endpoints if and only if $d^2+s^2=r^2$, where d is the distance between the centers of the semicircle and the circle.*

Let $v=\sqrt{(c+h)^2-2ab+h^2}$.

Theorem 1 *The following statements hold.*
(i) *The incircle of $(\alpha,\beta,\gamma)_h$ has radius*

$$i_c=\frac{ab(c+2h)}{(c+h)^2-ab}. \tag{1}$$

(ii) *If a semicircle is inscribed in $(\alpha,\beta,\gamma)_h$, then it has radius*

$$i_s=\frac{-v^2+\sqrt{8ab(c+2h)^2+v^4}}{2(c+2h)}. \tag{2}$$

Proof. We prove (ii). Let (x,y) and i_s be the coordinates of the center and the radius of the semicircle inscribed in $(\alpha,\beta,\gamma)_h$. Then we get $(x-(a+h))^2+y^2=((a+h)+i_s)^2$, $(x+(b+h))^2+y^2=((b+h)+i_s)^2$ and $(x-(a-b))^2+y^2+i_s^2=c^2$ by Proposition 1. Eliminating x and y from the three equations and solving the resulting equation for i_s, we get (2). The part (i) is proved similarly. □

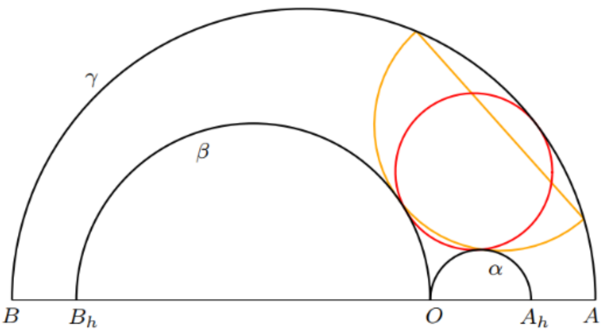

Figure 2

The theorem shows that an inscribed semicircle in $(\alpha,\beta,\gamma)_h$ is determined uniquely. Hence we can call it the insemicircle of $(\alpha,\beta,\gamma)_h$.
We consider a condition where a semicircle of radius i_s touches γ. If one of the endpoints of a semicircle S_1 lies on a semicircle S_2 and the other endpoints of S_1 lies on the reflection of S_2 in its diameter, we still say that S_1 touches S_2 at the endpoints. The circle of center of coordinates $((a+h)m,0)$ (resp. $(-(b+h)n,0)$ and passing through O is denoted by α_m (resp. β_n) for a real number m (resp. n) (see Figure 3). For points P and Q on a semicircle δ, we say that P, Q and the endpoints of δ lie counterclockwise if P, Q and one of the endpoints of δ lie counterclockwise. If a circle touches α_m, β_n and γ internally so that the points of tangency of this circle and each of β_m, α_n and γ lie counterclockwise, we say that the circle touches α_m, β_n and γ appropriately. Also if a semicircle touches α_m and β_n, and γ at the endpoints so that the points of tangency of the semicircle and each of β_n, α_m, and the endpoints lie counterclockwise, then we say that the semicircle touches α_m, β_n and γ appropriately.

Theorem 2 *If $m\neq 0$ and $n\neq 0$, the following three statements are equivalent.*
(i) *A circle of radius i_c touches α_m, β_n and γ appropriately.*
(ii) *A semicircle of radius i_s touches α_m, β_n and γ appropriately.*
(iii) $c+2h=\dfrac{a+h}{m}+\dfrac{b+h}{n}$.

Proof. Assume that (i) and (x,y) are the coordinates of the center of the circle in (i). Then we have $(x-m(a+h))^2+y^2=(m(a+h)+i_c)^2$, $(x+n(b+h))^2+y^2=(n(b+h)+i_c)^2$ and $(x-(a-b))^2+y^2=(c-i_c)^2$. Eliminating x and y from the three equations with (1), we get (iii). Conversely we assume (iii), and a circle of radius i_c touches α_m, $\beta_{n'}$ and γ appropriately for a real number n'. Then we have $a+b+2h=(a+h)/m+(b+h)/n'$ just as we have shown, i.e., $n=n'$. Hence $\beta_n=\beta_{n'}$, i.e., (iii) implies (i). Therefore (i) and (iii) are equivalent. The equivalence of (ii) and (iii) is proved similarly. □

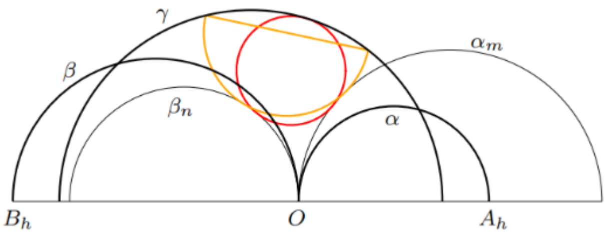

Figure 3: $1<m$ *and* $0<n<1$.

Theorem 2 does not consider the case in which α_m or β_n coincides with the axis. We consider the case in the next theorem (see Figure 4).

Theorem 3 *The following statements hold.*
(i) *A circle of radius i_c touches α_m $(m>0)$ externally, γ*

internally and the axis if and only if

$$m = m_0 = \frac{a+h}{c+2h}. \tag{3}$$

(ii) *A semicircle of radius i_s touches α_m $(m > 0)$ and the axis, and γ at the endpoints if and only if* (3) *holds.*
(iii) *A circle of radius i_c touches β_n $(n > 0)$ externally, γ internally and the axis if and only if*

$$n = n_0 = \frac{b+h}{c+2h}. \tag{4}$$

(iv) *A semicircle of radius i_s touches β_n $(n > 0)$ and the axis, and γ at the endpoints if and only if* (4) *holds.*

Proof. We prove (i). Let (x,y) be the coordinates of the center of the circle of radius i_c in (i). Then we have $x = i_c$, $(x-m(a+h))^2 + y^2 = (m(a+h)+i_c)^2$ and $(x-(a-b))^2 + y^2 = (a+b-i_c)^2$. Eliminating x and y from the three equations with (1), and solving the resulting equation for m, we get (3). Conversely, we assume that (3) and a circle of radius i_c touches $\alpha_{m'}$ $(m' > 0)$ externally, γ internally and the axis for a real number m'. Then we have $m' = m_0 = m$ as just we have proved. Therefore $\alpha_{m'} = \alpha_m$ and the converse is true. The rest of the theorem is proved similarly. □

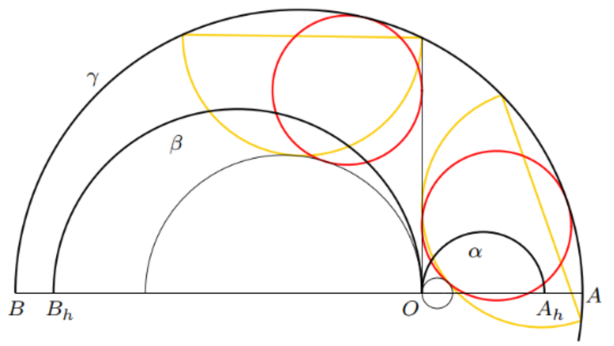

Figure 4

If $m = m_0$, then $(a+h)/m = c+2h$. Therefore if $(b+h)/n_x = 0$, and β_{n_x} coincides with the axis, then we can consider that Theorem 2 is true in the case $(m,n) = (m_0,n_x)$. Similarly if $n = n_0$ and $(a+h)/m_x = 0$ and α_{m_x} coincides with the axis, we can also consider that Theorem 2 holds in the case $(m,n) = (m_x,n_0)$. Therefore Theorems 2 and 3 can be unified in this case. We consider about this in section 4.

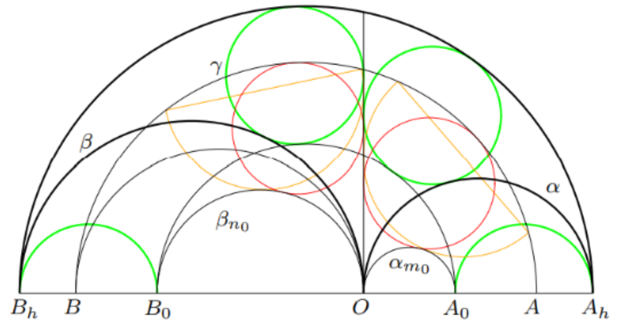

Figure 5

Theorem 4 *If A_0O and B_0O are the diameters of the circles α_{m_0} and β_{n_0}, respectively, then the circles of diameters A_0A_h and B_0B_h are Archimedean circles of the arbelos made by α, β and the semicircle of diameter A_hB_h constructed on the same side of AB as γ. Therefore the circle of diameter A_0B_0 is concentric to γ and touches the twin circles of Archimedes of the arbelos.*

Proof. Since the radius of the circle α_{m_0} equals $(a+h)m_0 = (a+h)^2/(c+2h)$ by (3), the circle of diameter A_0A_h has radius

$$(a+h) - \frac{(a+h)^2}{c+2h} = \frac{(a+h)(b+h)}{c+2h},$$

which equals the radius of Archimedean circles of the arbelos made by α, β and the semicircle of diameter A_hB_h (see Figure 5). Since the radius of the circle is symmetric in a and b, the other circle also has the same radius. □

3 Archimedean semicircles

In this section we consider another kind of semicircles touching γ at the endpoints.

Theorem 5 *The semicircle touching α and the axis and γ at the endpoints is congruent to the semicircle touching β and the axis and γ at the endpoints. The common radius equals*

$$s_A = \frac{1}{2}\left(\sqrt{(c+2h)^2 + 8ab} - c - 2h\right). \tag{5}$$

Proof. Let (s,y) be the coordinates of the center of the semicircle touching α and the axis, and γ at the endpoints. Then s equals the radius of the semicircle, and we have $(s-(a-b))^2 + y^2 + s^2 = c^2$ by Proposition 1 and $(s-(a+h))^2 + y^2 = ((a+h)+s)^2$. Eliminating y from the two equations and solving the resulting equation for s, we have $s = s_A$. Since s is symmetric in a and b, the other semicircle also has the same radius. □

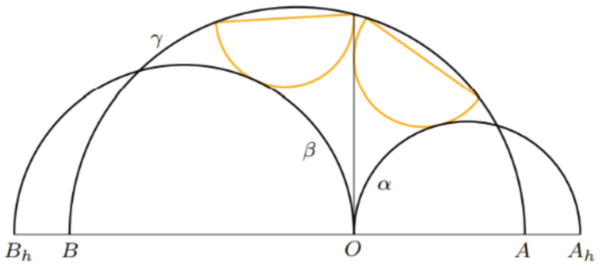

Figure 6

The two congruent semicircles in Theorem 5 may be called *the twin semicircles of Archimedes* (see Figure 6). A semicircle of radius s_A is called an *Archimedean semicircle* of $(\alpha,\beta,\gamma)_h$ or said to be *Archimedean* with respect to $(\alpha,\beta,\gamma)_h$. Let $w_k = \sqrt{a^2+kab+b^2}$. Theorem 5 shows that $(\alpha,\beta,\gamma)_0$ has Archimedean semicircles of radius $(w_{10}-c)/2$.

Theorem 6 *Assume that* $(m,n) \neq (1,0),(0,1)$ *and a semicircle touches* α_m, β_n *and* γ *appropriately. Then the semicircle is Archimedean with respect to* $(\alpha,\beta,\gamma)_h$ *if and only if*

$$\frac{1}{m}+\frac{1}{n}=1. \tag{6}$$

Proof. Assume that a semicircle of radius s_A touches α_m, β_n and γ appropriately and (x,y) are the coordinates of its center. Then we get $(x-m(a+h))^2+y^2=(m(a+h)+s_A)^2$, $(x+n(b+h))^2+y^2=(n(b+h)+s_A)^2$, and $(x-(a-b))^2+y^2+{s_A}^2=c^2$. Eliminating x and y from the three equations, we have (6). Conversely we assume (6) and assume that a semicircle of radius s_A touches α_m, $\beta_{n'}$ and γ appropriately. Then we have $1/m+1/n'=1$. Hence we get $n=n'$, i.e., $\beta_n=\beta_{n'}$. Hence the converse holds. □

While we have obtained the next theorem in [4].

Theorem 7 *If* $(m,n) \neq (1,0),(0,1)$ *and a circle touches* α_m, β_n *and* γ *appropriately, then the circle is Archimedean with respect to* $(\alpha,\beta,\gamma)_h$ *if and only if* (6) *holds.*

By Theorems 6 and 7 we have the next theorem.

Theorem 8 *If* $(m,n) \neq (1,0),(0,1)$*, the following statements are equivalent.*
(i) *The circle touching* α_m*,* β_n*, and* γ *appropriately is Archimedean with respect to* $(\alpha,\beta,\gamma)_h$.
(ii) *The semicircle touching* α_m*,* β_n*, and* γ *appropriately is Archimedean with respect to* $(\alpha,\beta,\gamma)_h$.
(iii) (6) *holds.*

It is commonly considered that the circles α_0 and β_0 are point circles and coincide with the origin O. This implies that Theorem 8 is not true in the cases $(m,n)=(1,0),(0,1)$. Therefore Theorems 8 does not consider the case of the twin circles of Archimedes and the case of the twin semicircles of Archimedes. We consider the case in the next section.

4 Division by zero

In this section we show that we can consider that the circles α_0 and β_0 coincide with the axis using recently made definition of division by zero [5].
For a field F we consider the following bijection $\psi : F \to F$:

$$\psi(a) = \begin{cases} a^{-1} & \text{if } a \neq 0 \\ 0 & \text{if } a = 0. \end{cases}$$

It is a custom to denote $z\psi(a)$ by z/a if $a \neq 0$, i.e., $z\psi(a) = a/z$ for $a \neq 0$. Following to this, we write

$$z \cdot \psi(0) = \frac{z}{0} \quad for\ \forall z \in F. \tag{7}$$

Then we have

$$z \cdot \psi(a) = \frac{z}{a} \quad for\ \forall a,z \in F. \tag{8}$$

Especially we have

$$\frac{z}{0} = z \cdot 0 = 0 \quad for\ \forall z \in F. \tag{9}$$

Notice that the concept of the reduction to common denominator can not be used for $z/0$, i.e., we have the following relation in general in the case $b=0$ or $d=0$:

$$\frac{a}{b}+\frac{c}{d} \neq \frac{ad+bc}{bd}.$$

We consider the circle α_m in the case $m=0$. The circle α_m has an equation $(x-m(a+h))^2+y^2=m^2(a+h)^2$, or

$$-2m(a+h)x+(x^2+y^2)=0. \tag{10}$$

This implies $x^2+y^2=0$ if $m=0$. Hence α_0 coincides with the origin in this case. On the other hand, (10) can be written as

$$-2(a+h)x+\frac{x^2+y^2}{m}=0. \tag{11}$$

Therefore we get $-2(a+h)x=0$, i.e., $x=0$ if $m=0$ by (9), i.e., α_0 coincides with the axis in this case. Now we can consider that α_0 is the origin or the axis, or the axis as the union of them. Similarly β_0 can be considered as the origin or the axis.
We can now consider that α_0 and β_0 coincide with the axis. Then Theorem 2 holds in the case $(m,n)=(m_0,0),(0,n_0)$ by (9). Also Theorem 8 holds in the case $(m,n)=$

$(1,0),(0,1)$. Our current mathematics avoids to consider (9). But our above observation shows that (9) is useful. Division by zero was founded by Saburou Saitoh in 2014. He has been making a list of successful example applying division by zero and its generalization called division by zero calculus, and there are more than 1200 evidences. It shows that a new world of mathematics can be opened if we admit them. For an extensive reference of division by zero and division by zero calculus including those evidences, see [5].

5 Aida arbelos

Aida (1747-1817) considered a figure consisting of two touching semicircles at their midpoints and the circle passing through the endpoints of the semicircles [1] (see Figure 7). He gave several notable properties of this figure, which are summarized in [3]. We conclude this paper by considering special circles and special semicircles for this figure.

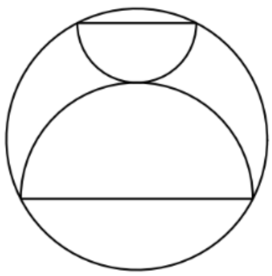

Figure 7: *Aida's figure.*

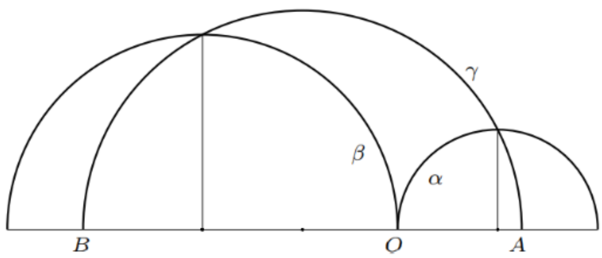

Figure 8: *Aida arbelos.*

Aida's figure is obtained from $(\alpha,\beta,\gamma)_h$, when $h = r_{\mathrm{A}}$ [3], or

$$h = \frac{ab}{c+h}. \tag{12}$$

Because (12) is equivalent to

$$r_{\mathrm{A}} = h = \frac{1}{2}(w_6 - c), \tag{13}$$

and (13) implies that the farthest points on α and β from AB lie on γ, where recall $w_k = \sqrt{a^2+kab+b^2}$. In this case we call $(\alpha,\beta,\gamma)_h$ an Aida arbelos (see Figure 8). Replacing h in the denominator of the right side of (12) by the right side of (12) repeatedly, we get a continued fraction expansion of r_{A} for the Aida arbelos:

$$r_{\mathrm{A}} = \frac{ab}{c+h} = \frac{ab}{c+\cfrac{ab}{c+h}} = \frac{ab}{c+\cfrac{ab}{c+\cfrac{ab}{c+\ddots}}}.$$

We assume $h \geq 0$. Let $\overline{\alpha}$ and $\overline{\beta}$ be the semicircles of diameters AO and BO, respectively, constructed on the same side of AB as γ, i.e., $\overline{\alpha}$, $\overline{\beta}$ and γ form $(\alpha,\beta,\gamma)_0$. The incircle of the curvilinear triangle made by α, $\overline{\alpha}$ (resp. β, $\overline{\beta}$) and the radical axis of α (resp. β) and γ has radius $(1/r_{\mathrm{A}}+1/h)^{-1}$ for $(\alpha,\beta,\gamma)_h$ [4]. Therefore the radius equals $r_{\mathrm{A}}/2$ for the Aida arbelos. The circles are denoted by green in Figure 9. The circle touching α or β externally, γ externally and the axis has radius ab/h for $(\alpha,\beta,\gamma)_h$ [4]. Hence the radius equals $ab/r_{\mathrm{A}} = c + r_{\mathrm{A}}$ for the Aida arbelos by (12). The circles are denoted by magenta in Figure 9.

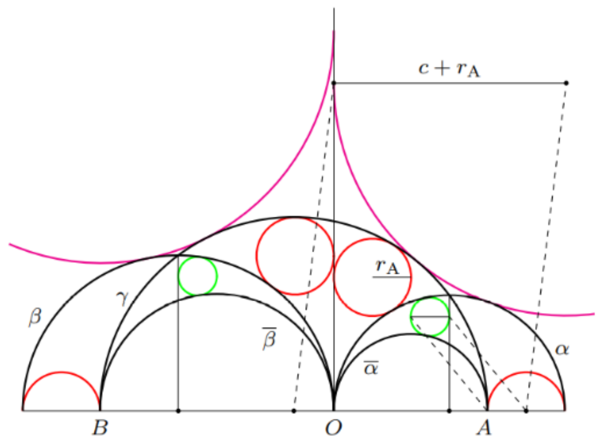

Figure 9: *The green circles have radius $r_{\mathrm{A}}/2$.*

Substituting (13) in (5), we get that the radius of Archimedean semicircles of the Aida arbelos equals

$$s_{\mathrm{A}} = \frac{1}{2}(w_{14} - w_6).$$

Since $i_c = w_6 h/c$ for the Aida arbelos [3], we get that the inradius of the Aida arbelos equals

$$i_c = \frac{w_6(w_6-c)}{2c}$$

by (13). Therefore we have

$$i_c + r_{\mathrm{A}} = \frac{2ab}{c}.$$

Hence the sum of i_c and r_A for the Aida arbelos equals the diameter of the Archimedean circle of $(\alpha,\beta,\gamma)_0$. Let $u = (w_6^4 + 16a^2b^2)^{1/4}$.

Theorem 9 *If the insemicircle of the Aida arbelos has center of coordinates (x_s, y_s), we have*

$$i_s = \frac{u^2 - c^2}{2w_6}, \tag{14}$$

$$(x_s, y_s) = \left(\frac{(b-a)i_s}{w_6}, \frac{4ab\sqrt{4ab+u^2}}{w_6^2} \right). \tag{15}$$

Proof. By (2) and (13), we get (14). Solving the equations $(x_s - (a+h))^2 + y_s^2 = ((a+h)+i_s)^2$ and $(x_s + (b+h))^2 + y_s^2 = ((b+h)+i_s)^2$ with (14), we get (15). □

The next theorem shows that the result for the insemicircle of $(\alpha,\beta,\gamma)_0$ obtained in [2] also holds for the Aida arbelos (see Figure 10).

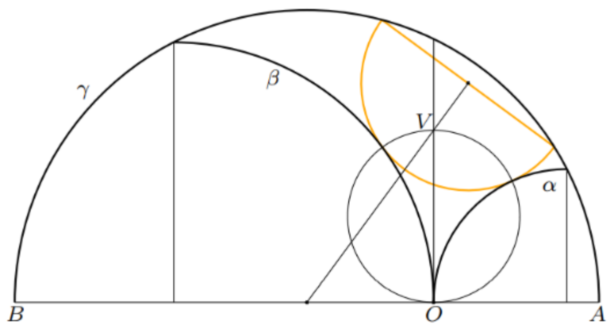

Figure 10

Theorem 10 *If the line joining the centers of γ and the insemicircle of the Aida arbelos meets the axis in a point V, then the circle of diameter OV is orthogonal to the insemicircle. Hence the circle passes through the points of tangency of two of α, β and the insemicircle.*

Proof. From (13) and (15), the circle of diameter OV has radius

$$r_v = \frac{4ab\sqrt{4ab+u^2}}{w_{10}^2 + u^2}$$

and the center of coordinates $(0, y_v) = (0, r_v)$. Then we have $(x_s - 0)^2 + (y_s - y_v)^2 = r_v^2 + i_s^2$. □

References

[1] Aida ed., Sampō Chikusaku Jutsu, Volume 2, Tohoku University Digital Collection.

[2] H. Okumura, The arbelos in Wasan geometry, the inscribed semicircle in the arbelos, *Sangaku J. Math.* **5** (2021), 1–8.

[3] H. Okumura, Wasan geometry. In: B. Sriraman ed., *Handbook of the Mathematics of the Arts and Sciences*, Springer, 2020, 1–52, doi: 10.1007/978-3-319-70658-0_122-1

[4] H. Okumura, The arbelos with overhang, *KoG* **18** (2014), 19–27.

[5] S. Saitoh, Introduction to the division by zero calculus, *Scientific Research Publishing*, 2021.

Hiroshi Okumura
orcid.org/0000-0003-4332-0189
e-mail: hokmr@yandex.com
Takahanadai Maebashi Gunma 371-0123, Japan

https://doi.org/10.31896/k.25.3
Original scientific paper
Accepted 18. 10. 2021.

Boris Odehnal

A Rarity in Geometry: a Septic Curve

A Rarity in Geometry: a Septic Curve

ABSTRACT

We study the locus $\mathcal{C}$ of all points in the plane whose pedal points on the six sides of a complete quadrangle lie on a conic. In the Euclidean plane, it turns out that $\mathcal{C}$ is an algebraic curve of degree 7 and genus 5 and not of degree 12 as it could be expected. Septic curves occur rather seldom in geometry which motivates a detailed study of this particular curve. We look at its singularities, focal points, and those points on $\mathcal{C}$ whose pedal conics degenerate. Then, we show that the septic curve occurs as the locus curve for a more general question. Further, we describe those cases where $\mathcal{C}$ degenerates or is of degree less than 7 depending on the shape of the initial quadrilateral.

Key words: quadrilateral, complete quadrangle, pedal point, conic, six conconic points, septic curve, Simson line, Miquel point

MSC2010: 14H45 14P99 51F99 51N15

Rijetkost u geometriji: septika

SAŽETAK

U radu se proučava geometrijsko mjesto $\mathcal{C}$ točaka ravnine čija nožišta na šest strana potpunog četverovrha leže na jednoj konici. Pokazuje se da je u euklidskoj ravnini $\mathcal{C}$ algebarska krivulja 7. reda i roda 5, a ne 12. reda kao što bi se očekivalo. Septike se u geometriji rijetko pojavljuju pa je ta činjenica potaknula detaljnije proučavanje ove krivulje. Promatraju se njezini singulariteti, žarišta i one točke krivulje $\mathcal{C}$ čije su nožišne konike raspadnute. Zatim se pokazuje da se septika pojavljuje kao geometrijsko mjesto točaka u jednom općenitijem slučaju. Nadalje, opisuju se oni slučajevi kad se $\mathcal{C}$ raspada ili kad je reda manjeg od 7 u ovisnosti o obliku polaznog četverostrana.

Ključne riječi: četverostran, potpuni četverovrh, nožište, konika, šest konkoničnih točaka, septika, Simsonov pravac, Miquelova točka

1 Introduction

1.1 Septic curves and curves related to a quadrilateral

Algebraic curves of degree two, three, and four (conics, cubics, and quartics) appear frequently in many geometrical problems (see, *e.g.*, [9, 11, 14, 15, 17, 18, 23]). This is caused by the fact that many problems in geometry involve distances between points or angles between lines and a quadratic form is responsible for measuring distances and angles in the Euclidean plane. Curves of odd degrees proved useful in Computer Aided Geometric Design: Cubic, quintic, and even septic curves (in plane and in space) are well suited for solving interpolation tasks with tangent or curvature continuity [6, 7, 13, 19, 21] and are also helpful in spaces of geometric objects, such as lines and spheres [20].

Planar curves of odd degree may be the images of algebraic curves under certain Cremona transformations: Linear components of the image curve will split off if the initial curve passes through base points of the transformation [4, 5, 8] as is the case with many but not all cubic curves and most of the algebraic curves which are related to the geometry of a triangle, see the list on B. Gibert's page [10].

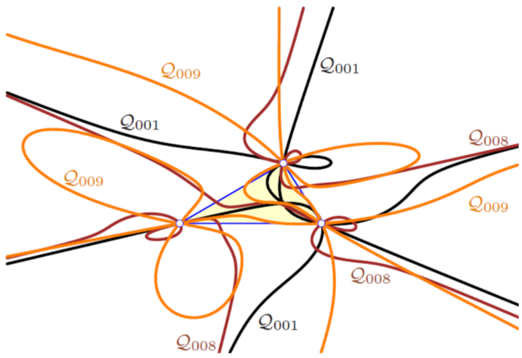

Figure 1: *Triangle related septics: The curves $\mathcal{Q}_{001}$, $\mathcal{Q}_{008}$, $\mathcal{Q}_{009}$ are labeled according to Gibert's list [10].*

On GIBERT's page [10], we find, among many other curves, 12 septic curves related to the geometry of the triangle. Three of these septics are shown in Figure 1. For example, the Darboux septic $\mathcal{Q}_{001}$ is the locus of all 4$^{\text{th}}$ pedal points of a point P on the circumconics of a triangle $\Delta = ABC$ such that the circumconic's normals at A, B, C concur in P. This curve was derived and described in [12]. The septic $\mathcal{Q}_{008}$ is the isogonal image of a circular octic which collects the perspectors of pedal and projection triangles of a triangle Δ, while $\mathcal{Q}_{009}$ is related to orthologic triangles.

However, the rational septic also related to a geometric question about triangles found by É. LEMOINE (cf. [16]) does not show up in [10]. Compared to the huge amount of special conics, cubics, and quartics related to many geometric questions, these 13 septics are a rather poor aggregation. It seems that K. FLADT [8] may be right when he stated that *"there could hardly be some curves of degree 7 that could be of interest and of geometrical relevance"*, although the space of septic plane curves is 35-dimensional (including even degenerate ones) since the implicit equation of a septic involves 36 coefficients where only the ratio matters.

Cubic curves related to triangles can be characterized by geometric properties [9]. While no vertex of a triangle is distinguished and the ordering of the vertices does not matter, this is not the case with a quadruple of points, say A, B, C, D. There are three different orderings of four points (up to cyclic and reverse rearrangements), and so, they define three different quadrilaterals. Asking for the locus of all points P in the plane of the quadruple with *concyclic* pedal points on four side lines of one particular quadrilateral defined on the point quadruple results in a certain cubic. Since there are three different orderings, the *four points actually define three cubics* one of which passes through the quadrilateral's respective Miquel point (see [3] and cf. Figure 2).

It seems that asking for the locus $\mathcal{C}$ for only one ordering of points may not deliver the complete picture.

In the following, we assume that we are given a planar quadrilateral $\mathcal{Q} = ABCD$ with vertices A, B, C, D, no two of which may coincide and no three shall be collinear. (Later, we shall discuss the case where three of these points are collinear as the only acceptable degenerate case.) Clearly, these four points define six lines $[A,B]$, $[A,C]$, $[A,D]$, $[B,C]$, $[B,D]$, $[C,D]$, *i.e.*, the joins of all six pairs out of the four points. The union of the four points and the six lines is called a *complete quadrangle*.

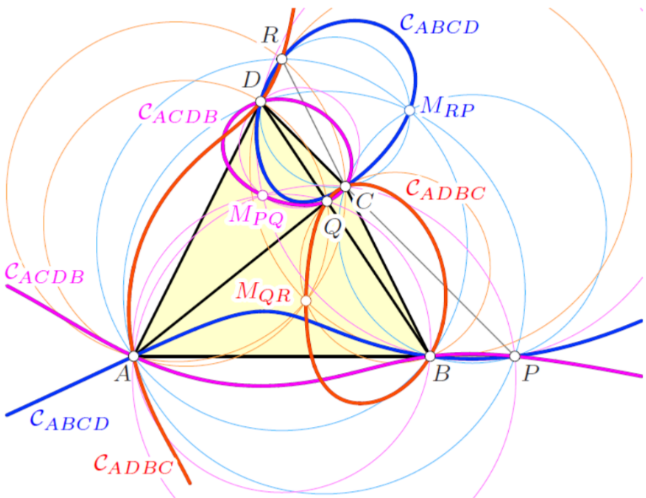

Figure 2: *The loci $\mathcal{C}_{ABCD}$, $\mathcal{C}_{ACDB}$, $\mathcal{C}_{ADBC}$ of points with four concyclic pedal points on the sides of the three quadrilaterals on four points A, B, C, D.*

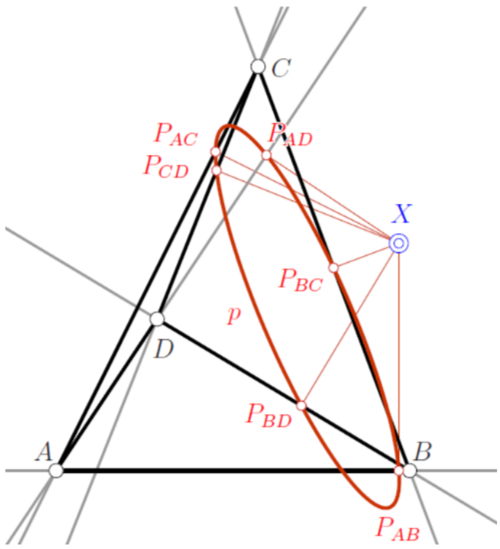

Figure 3: *The characteristic property of the points on $\mathcal{C}$: The six pedal points $P_{..}$ of the point X lie on a single conic p.*

Now, we raise the following question (cf. Figure 3): *What is the locus $\mathcal{C}$ of points X in the quadrilateral's plane such that the pedal points of X on the six lines of the complete quadrilateral are conconic,* i.e., *they are located on a single conic?*
In order to answer this question, the remainder of this section collects necessary notations and provides some basic results. In Section 2, we shall derive the equation of $\mathcal{C}$ for a generic quadrilateral and study $\mathcal{C}$'s algebraic properties. However, the equation of $\mathcal{C}$ is given in the Appendix A in full length because of its complexity (2318 terms).

A rather intricate computation will show that beside the diagonal points and three Miquel points there are only 4 further real points on $\mathcal{C}$ that deliver singular pedal conics. Subsequently, Section 3 will show that the curve $\mathcal{C}$ is the locus curve for a more general formulation of the initial problem. Then, Section 4 deals with those quadrilaterals and complete quadrangles where the degree of the curve $\mathcal{C}$ drops. In all these cases, $\mathcal{C}$ becomes a sextic either of genus 1 or 3 and carries no real point off the real (isolated) singularities. We also show that the degree of $\mathcal{C}$ is always larger than 5.

1.2 Prerequisites, notations, and basic results

Although we are mostly dealing with Euclidean geometry, we shall describe points by homogeneous coordinates whenever this is favorable. The Cartesian coordinates (x,y) of a point X can easily made homogeneous by writing $X = 1:x:y$. On the contrary, from the homogeneous coordinates $x_0:x_1:x_2$ of a point, we can change to its Cartesian coordinates by setting $x = x_1x_0^{-1}$ and $y = x_2x_0^{-1}$, provided that $x_0 \neq 0$. In this way, we have performed the projective closure of the Euclidean plane and $x_0 = 0$ is the equation of the ideal line (line at infinity). On this line, we find the absolute points of Euclidean geometry $0:1:\pm\mathrm{i}$ which are henceforth denoted by I and $J = \overline{I}$.
The condition on six points to lie on a single conic can be written in form of a vanishing determinant of a 6×6 matrix whose rows (or columns likewise) are the quadratic Veronese images of the six points in question see [11]. For a point X with homogeneous coordinates $x_0:x_1:x_2$, the quadratic Veronese image has the homogeneous coordinates

$$v(x_0,x_1,x_2) = x_0^2 : x_0x_1 : x_0x_2 : x_1^2 : x_1x_2 : x_2^2. \tag{1}$$

Each conic c in the plane has a homogeneous equation of the form

$$\sum_{i,j=0}^{2} a_{ij}x_ix_j = 0$$

(with $a_{ik} \in \mathbb{R}$ not simultaneously vanishing). The conic c is regular/singular if, and only if, the symmetric matrix $(a_{ij}) \in \mathbb{R}^{2\times 2}$ is regular/singular. Each point incident with the conic corresponds to a hyperplane in the space $\mathbb{P}^5$ of all Veronese images. Six linearly dependent hyperplanes in $\mathbb{P}^5$ correspond to six conconic points, and hence, the 6×6 matrix of the respective Veronese images is of rank less than 6. A less algebraic and more geometric condition on six points to lie on a conic is given by PAPPUS's theorem [11]. However, the algebraic formulation of PAPPUS's theorem is equivalent to (1).
Now, it is natural to conjecture that the locus $\mathcal{C}$ is a curve of degree twelve: The computation/construction of the pedal points of the normals from X to the sides of the complete quadrangle is linear. Algebraically speaking, the coordinates of the six pedal points can be expressed linearly in terms of the coordinates of X.
Therefore, the entries of the 6×6 matrix are quadratic in the coordinates of the pedal points, and thus, quadratic in the coordinates of X. Finally, the determinant of the 6×6 matrix is a polynomial of degree twelve which, set equal to zero, is the equation of an algebraic curve of degree twelve. Whatever the locus $\mathcal{C}$ may be, the following can be shown without any computation:

Theorem 1 *The vertices A, B, C, D and the diagonal points $P = [A,B]\cap[C,D]$, $Q = [A,C]\cap[B,D]$, $R = [A,D]\cap[B,C]$ are located on $\mathcal{C}$.*

Proof. If X coincides with one diagonal point, say P, then the pedal points on $[A,B]$ and $[C,D]$ coincide and equal P. So, there are only five different pedal points naturally having a unique circumconic. The same holds true for the other diagonal points.
If X equals a vertex of $\mathcal{Q}$, say A, then even three pedal points fall in one point, *i.e.*, the pedal points of A on $[A,B]$, $[A,C]$, and $[A,D]$ (the three side lines through A). Therefore, the four vertices of $\mathcal{Q}$ are located on $\mathcal{C}$ and are singular points on $\mathcal{C}$. □

We shall also verify that A, B, C, and D are double points on $\mathcal{C}$ by computation in Thm. 3.

Remark 1 *The pedal conic of a vertex of $\mathcal{Q}$, say A, is not uniquely determined. It passes through the three pedal points on $[B,C]$, $[C,D]$, $[D,B]$, and A. These four points will, in general, serve as the base points of a pencil of pedal conics (cf. [11]).*

2 The equation of $\mathcal{C}$

2.1 The generic quadrilateral

In order to give an equation of $\mathcal{C}$, we attach a Cartesian coordinate system to the given quadrilateral. It means no loss of generality, if we assume that the vertices of the quadrilateral are given by the homogenized Cartesian coordinates

$$A = 1:0:0,\ \ B = 1:a:0,$$
$$C = 1:b:c,\ \ D = 1:d:e.$$

We could simplify the coordinates of these four points a little bit more by setting $a = 1$. Regarding the question we are trying to answer, this is admissible, since it would only scale the quadrilateral and the problem of conconic pedal points is invariant under equiform transformations in general. However, we do not set $a = 1$ in order to keep the coefficients of $\mathcal{C}$ homogeneous (polynomials in a,b,c,d,e).

Later, some quadratic functions in terms of a,b,c,d,e shall occur frequently and in order to simplify many expressions, we label the *squares* of the six Euclidean lengths between the given points by

$$\begin{aligned} l_1 &:= \overline{AB} = a^2,\\ l_2 &:= \overline{AC} = b^2+c^2,\\ l_3 &:= \overline{AD} = d^2+e^2,\\ l_4 &:= \overline{BC} = (b-a)^2+c^2,\\ l_5 &:= \overline{BD} = (d-a)^2+e^2,\\ l_6 &:= \overline{CD} = (d-b)^2+(e-c)^2. \end{aligned} \tag{2}$$

For the same reason, we denote the areas of the four subtriangles of $\mathcal{Q}$ by

$$\begin{aligned} F_D &:= \operatorname{area}(ABC) = \tfrac{1}{2}ac,\\ F_C &:= \operatorname{area}(ABD) = \tfrac{1}{2}ae,\\ F_B &:= \operatorname{area}(ACD) = \tfrac{1}{2}(be-cd),\\ F_A &:= \operatorname{area}(BCD) = \tfrac{1}{2}(ac-ae+be-cd), \end{aligned} \tag{3}$$

where, for example, F_A is the area of the triangle BCD (*i.e.*, the area is labeled by the point that does not contribute).

Now, let $X=(x,y)$ (or likewise $1:x:y$) be a point in the plane of $\mathcal{Q}$. It is elementary to compute the six pedal points from X to the sides of the complete quadrilateral. Then, we replace the Cartesian coordinates of X by homogeneous coordinates according to $x \to x_1x_0^{-1}$ and $y \to x_2x_0^{-1}$. For example, the pedal point P_{AC} on the side line $[A,C]$ has the homogeneous coordinates

$$P_{AC} = l_2x_0 : b(bx_1+cx_2) : c(bx_1+cx_2).$$

Subsequently, we apply the Veronese mapping (1) and compute the determinant of the 6×6 matrix

$$\begin{aligned} V := (&v(P_{AB}), v(P_{AC}), v(P_{AD}),\\ &v(P_{BC}), v(P_{BD}), v(P_{CD})). \end{aligned} \tag{4}$$

This results in a homogeneous polynomial of degree 12 in the variable homogeneous coordinates $x_0:x_1:x_2$ of X. Surprisingly, $\det V$ factors and we have

$$\det V = -2^8 l_1^{-1} F_A^2F_B^2F_C^2F_D^2 \cdot x_0^5 \cdot P_7, \tag{5}$$

where $P_7 = \sum_{k=0}^{7} q_k x_0^k$ is a degree 7 form in $x_0:x_1:x_2$ with

$$\begin{aligned} &q_7 = q_6 = 0,\\ &q_5 = 2^4 l_1 l_2 F_AF_BF_CF_D(x_1^2+x_2^2),\\ &q_4 = \ldots,\ q_3 = \ldots,\\ &q_2 = (\ldots)(x_1^2+x_2^2),\ q_1 = (\ldots)(x_1^2+x_2^2)^2,\\ &q_0 = 4(al_1)^{-1}(4(F_C-F_D)(l_1F_B(F_B-F_C)\cdot\\ &\cdot(F_B+F_D)+l_2F_C^2(F_C-F_B)-l_3F_D^2\cdot\\ &\cdot(F_B+F_D))x_1+(l_1^2F_B^2(F_B-F_C-F_D)-\\ &-l_2^2F_C^2F_D-2l_3^2F_D^3+l_1l_2F_C((4F_B-5F_C)\cdot\\ &\cdot(F_B-F_C)+(F_B-F_C)F_D)+\\ &+l_1l_3F_D(4F_B^2-4F_BF_C-F_C^2+\\ &+3F_D(F_B-F_C+F_D))+l_3l_4F_C^2F_D+\\ &+l_2l_3F_CF_D(F_C+2F_D)-l_2l_4F_C^2(2F_C-F_D)-\\ &-16F_BF_CF_D((F_B-F_C)\cdot\\ &\cdot(F_C+F_D)+F_D^2))x_2)(x_1^2+x_2^2)^3. \end{aligned} \tag{6}$$

The polynomial P_7 is given in full length in the Appendix A in term of inhomogeneous (Cartesian) coordinates.
Now, we have:

Theorem 2 *The locus $\mathcal{C}$ of points X in the Euclidean plane with conconic pedal points on the six lines of a complete quadrangle is, in general, a tricyclic algebraic curve of degree 7 with the equation $P_7=0$ having one real point at infinity.*

We have added the phrase *in general* since we shall soon see that for some special configurations of the four points A, B, C, D the degree will drop.

Proof. By virtue of (5), we can see that the (in general) non-degenerate factor of $\det V$ is a polynomial P_7 of degree 7. Obviously, the factor x_0^5 splits off from $\det V$, and thus, the line at infinity is a component with multiplicity 5. However, this component does not matter, since one cannot draw normals from ideal points to proper lines. Therefore, the affine part of $\mathcal{C}$ is only of degree 7. (An example is shown in Figure 4.)
In the projective closure and the complex extension of the Euclidean plane, the term q_0 of degree 7 (given in (6)) consists of a linear factor corresponding to the one and only real point at infinity and the term $(x_1^2+x_2^2)^3=(x_1+\mathrm{i}x_2)^3(x_1-\mathrm{i}x_2)^3$ whose solutions are the absolute points (circle points) of Euclidean geometry each with multiplicity 3. □

Later, we shall have a look at all types of quadrilaterals including those with symmetry. In some cases the degree of the curve $\mathcal{C}$ will drop. For some special quadrilaterals, the curve $\mathcal{C}$ will consist of a finite number of isolated real points and complex branches without any real point.

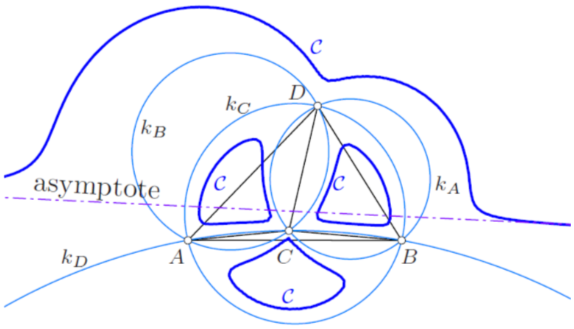

Figure 4: *The septic locus $\mathcal{C}$ of points whose six pedal points on the sides of a complete quadrilateral $\mathcal{Q} = ABCD$ lie on a conic.*

Remark 2 *The equations of the cubics showing up in [3] as the loci of points with four concyclic pedal points on the four sides of a quadrilateral are also the irreducible parts of polynomials of degree 8. The concyclicity of the four pedal points is equivalent to the vanishing of the determinant of the 4×4 matrix whose rows (columns) are Veronese images*

$$(p_1^2 + p_2^2, p_0p_1, p_0p_2, p_0^2)$$

(cf. [11, p. 241]) of the four homogenized pedal points. Surprisingly, from this degree 8 polynomial the factor x_0^5 (the ideal line) also splits off with multiplicity 5.

We can state and prove:

Theorem 3 *The vertices of the quadrilateral $\mathcal{Q} = ABCD$ are isolated double points on the septic $\mathcal{C}$. The four vertices are focal points of $\mathcal{C}$. The curve $\mathcal{C}$ is of class 22 and genus 5.*

Proof. From (6), we see that q_7 and q_6 are equal to zero, and therefore, A is a double point on $\mathcal{C}$. The coefficient $q_5 \neq 0$ (cf. (6)) tells us that the point A is a double point on $\mathcal{C}$. The linear factors of q_5 are the equations of $\mathcal{C}$'s tangents at the double point. Since

$$x_1^2 + x_2^2 = (x_1 + \mathrm{i}x_2)(x_1 - \mathrm{i}x_2) = 0,$$

we see that the tangents at A are isotropic lines and A is an isolated double point.
We recall VON STAUDT's definition of focal points on algebraic curves: *A point F is a* focal point *of an algebraic curve if the curve's tangents at F are isotropic lines* (cf. [1, 5]). According to this, A is a focal point since the tangents of the curve at A are isotropic lines.
The other vertices B, C, D are of the like kind. This can be shown by applying translations to $\mathcal{Q}$ and to the septic curve $\mathcal{C}$ such that each vertex of $\mathcal{Q}$ coincides with the origin of the coordinate system (three different translations). This does not change the algebraic and geometric properties of $\mathcal{C}$ and the linear factors of q_0 are the equations of the tangents at the origin. In all three cases, q_0 will turn out to be a scalar multiple of $x_1^2 + x_2^2$ (since this quadratic form is invariant under Euclidean transformations). Consequently, all four vertices of $\mathcal{C}$ are isolated double points and focal points of $\mathcal{C}$.
There are no further singularities on $\mathcal{C}$ (different from A, B, C, D, I, J). This can be shown either with a CAS (like Maple) or by considering the following: At a singular point of $\mathcal{C}$ at least three pedal points have to coincide which is not possible for any other point (different from the already known singularities).
With the Plücker formulae for planar algebraic curves (cf. [2, 4, 5, 8, 14]), we find the genus g and the class m of $\mathcal{C}$:

$$g = \tfrac{1}{2}(7-1)\cdot(6-1) - 1\cdot 4 - 3\cdot 2 = 5,$$
$$m = 7\cdot(7-1) - 2\cdot 4 - 6\cdot 2 = 22$$

since there are 4 ordinary double points and 2 ordinary triple points on $\mathcal{C}$. □

Figure 5 shows that the curve $\mathcal{C}$ can have up to six real separated components as is to be expected for a curve of genus 5. These six components occur if one vertex lies close to one side.

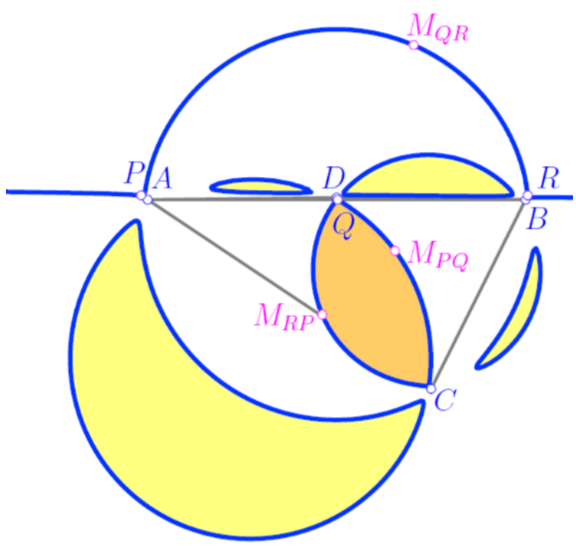

Figure 5: *If one vertex (here D) comes close to one side line (here $[A,B]$), then the curve $\mathcal{C}$ consists of 6 separated real components.*

Remark 3 *The well-known Plücker formulae (cf. [2, 4, 5, 8, 14, 23]) for the genus and class of a planar algebraic curve have to be adapted if the degree d is larger than or equal to 4 since curves of sufficiently high degree may have singularities of multiplicity larger than 2. In the present case with $d = 7$ and ordinary triple points, the formulae* *for the class m, the number w of inflection points, and the genus g read*

$$\begin{aligned} m &= d(d-1) - 2d - 3s - 6t, \\ w &= 3d(d-2) - 6d - 8s - 18t, \\ g &= \tfrac{1}{2}(d-1)(d-2) - \sum \delta_i. \end{aligned}$$

Herein, d, s, t, δ_i are the numbers of (ordinary) double points, cusps (of the first kind), (ordinary) triple points, and the δ-invariants of all singularities. The δ-invariant can be computed with Maple's function `singularities` *provided by the* `algcurves` *package.*

It is rather technical to show that each (ordinary) triple point has to be weighted with the factors 6 and 18 in the class and inflection point formula.

This allows us to conjecture that

$$w = 3 \cdot 7 \cdot (7-2) - 6 \cdot 4 - 18 \cdot 2 = 45.$$

is an upper bound *for the number of* real *inflection points on $\mathcal{C}$.*

2.2 Miquel points determine singular pedal conics

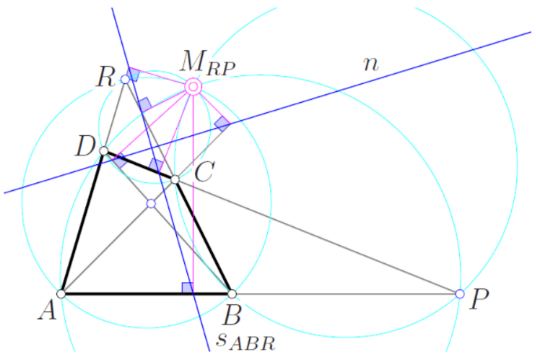

Figure 6: *The Miquel point M_{RP} lies on the septic $\mathcal{C}$, for its six pedals with respect to the lines of a complete quadrilateral form a degenerate conic $m = s_{ABR} \cup n$.*

Each quadrilateral $\mathcal{Q} = ABCD$ defines three Miquel points each of which is common to four circles on two pairs of opposite vertices and the respective diagonal points of $\mathcal{Q}$ (cf. [22]). We shall denote the Miquel points by M_{PQ}, M_{QR}, M_{RP} pointing to the diagonal points involved. It is well-known that the Miquel points are located on the following circles (cf. [22]):

$$\begin{aligned} M_{PQ} &\in \quad k_{ACP},\ k_{BDP},\ k_{ABQ},\ k_{CDQ}, \\ M_{QR} &\in \quad k_{ADQ},\ k_{BCQ},\ k_{ACR},\ k_{BDR}, \\ M_{RP} &\in \quad k_{ABR},\ k_{CDR},\ k_{ADP},\ k_{BCP}, \end{aligned}$$

where k_{XYZ} denotes the circle on the three (pairwise different) points X, Y, and Z. We are able to show that these points play an outstanding role:

Theorem 4 *The three Miquel points M_{PQ}, M_{QR}, M_{RP} are located on the septic $\mathcal{C}$. The three pedal conics defined by the six pedal points of each Miquel point are degenerate and split into pairs of lines.*

Proof. It is sufficient to show the validity of the above theorem for one particular Miquel point, say M_{RP}. For the remaining two the proof uses the same arguments for different subtriangles.

The Miquel point M_{RP} is the common point of the circumcircles k_{ABR}, k_{CDR}, k_{ADP}, k_{BCP} of the respective subtriangles.

Since $M_{RP} \in k_{ABR}$, the three pedal points of M_{RP}'s normals to $[A,B]$, $[B,R]$, $[R,A]$ are collinear: They lie on the Simson line of the triangle ABR. The triangles ABR and CDR share two side lines: $[A,R] = [D,R]$ and $[B,R] = [C,R]$. Thus, two by two pedal points coincide: $P_{M_{RP},[A,R]} = P_{M_{RP},[D,R]}$ and $P_{M_{RP},[B,R]} = P_{M_{RP},[C,R]}$. So, the two triangles ABR and CDR share the Simson line $s_{ABR} = s_{CDR}$ on which also the pedal points $P_{M_{RP},[A,B]}$ and $P_{M_{RP},[C,D]}$ have to lie. This makes in total four collinear pedal points.

The remaining two pedal points $P_{M_{RP},[A,C]}$ and $P_{M_{RP},[B,D]}$ span a second line n. The union of s_{ABR} and n is the singular conic m. Since m is a (singular) conic, M_{RP} has to lie on $\mathcal{C}$ by the very definition. □

Figure 7 shows the three Miquel points of the complete quadrangle $\mathcal{Q}$ together with the three singular pedal conics. Each point and line displayed in Figure 7 can be constructed only with a ruler (linearly): Each Miquel point is a common point of two circles sharing an already known point. The singular pedal conics of the Miquel points are Simson lines which require only linear constructions.

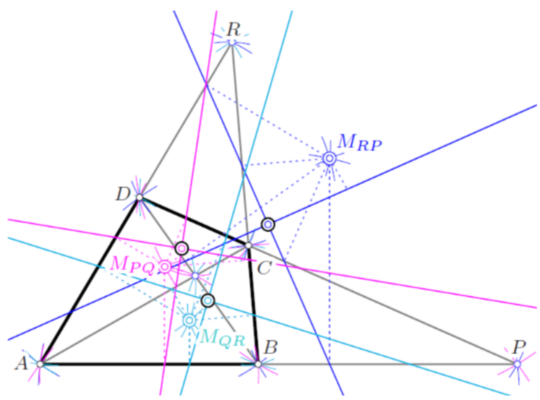

Figure 7: *The three Miquel points and their singular pedal conics.*

It is noteworthy that the triangle built by the centers of the singular conics is perspective to the diagonal triangle PQR of $\mathcal{Q}$:

$$PQR \barwedge C_{QR}C_{RP}C_{PQ}$$

(with C_{QR} denoting the center of the singular pedal conic of M_{QR}. Further, the triangle formed by the three Miquel points is also perspective to the diagonal triangle, *i.e.*,

$$PQR \barwedge M_{QR}M_{RP}M_{PQ}.$$

Remark 4 *Theorem 4 can also be verified by means of computation. For that purpose, only the coordinates*

$$\begin{aligned} M_{RP} = {} & 2(l_1-l_2+l_3+l_4-l_5+l_6): \\ & : a(l_1-l_2+2l_3-l_5+l_6): \\ & : 4a(F_C-F_B), \end{aligned}$$

$$\begin{aligned} M_{PQ} = {} & 2(l_1+l_2-l_3-l_4+l_5+l_6): \\ & : a(l_1+2l_2-l_3-l_4+l_6): \\ & : 4a(F_B+F_D), \end{aligned}$$

$$\begin{aligned} M_{QR} = {} & 4a(l_1-l_2-l_3-l_4-l_5+l_6): \\ & : l_1(l_1-l_2-l_3-l_4-l_5)+ \\ & \quad +(l_4-3l_2)l_3+ \\ & \quad +(l_2+l_4)l_5-16F_CF_D: \\ & : 8(l_1(F_C-F_B)-F_Dl_3-l_4F_C), \end{aligned}$$

of the three Miquel points (with the abbreviations given in (2) *and* (3)*) have to be inserted into* (5)*.*

We are able to show that the Miquel points are not the only points whose six pedal points lie on a singular conic:

Theorem 5 *In the Euclidean plane of a generic quadrilateral $\mathcal{Q}$ there exist, in general, 4 real points (different from the Miquel point, the diagonal points, and the vertices of $\mathcal{Q}$) whose pedal conics are singular.*

Proof. Unfortunately, this proof requires some computation. We assume that $W = 1:\xi:\eta$ is a point on $\mathcal{C}$, and thus, its coordinates annihilate P_7 from (5) and (6). By the very definition of $\mathcal{C}$, the six pedal points of W lie on a conic. We can use (4) to determine the equation of the conic c_{CD} on the pedals P_{AB}, P_{AC}, P_{AD}, P_{BC}, P_{BD} of W (note that P_{CD} is missing). The determinant of the coefficient matrix M_{CD} has to vanish in order to make c_{CD} singular. Surprisingly, $\det M_{CD}$ splits into quadratic factors:

$$\begin{aligned} \det M_{CD} = {} & \iota_A\cdot\iota_B\cdot k_C\cdot k_D\cdot \\ & \cdot k_{ABR}\cdot k_{ABQ}\cdot k_{BCQ}\cdot k_{ADQ}\cdot k_{ACR}\cdot k_{BDR}. \end{aligned}$$

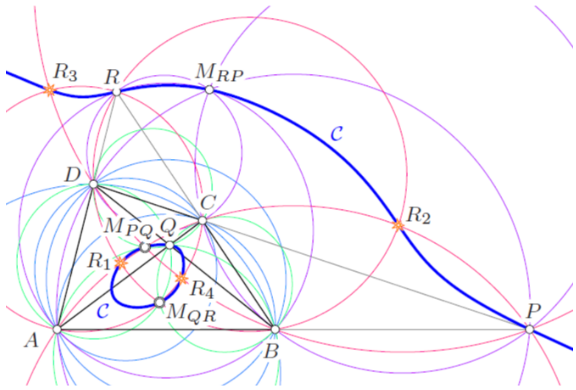

Figure 8: *The cycle $\mathcal{L}$ consists of 16 circles and 8 isotropic lines. It intersects $\mathcal{C}$ in possible candidates of points with degenerate pedal conics.*

The factors in the latter product are the equations of some circles and pairs of isotropic lines. For example, $\iota_A = \xi^2+\eta^2$ is the equation of the pair of isotropic lines through A, k_A is the (equation of the) circumcircle k_A of BCD, and k_{ABR} is the (equation of the) circumcircle of ABR (with P, Q, and R still being $\mathcal{Q}$'s diagonal points as defined in Thm. 1).

So far, it seems that the pedal point P_{CD} does not play a role. In order not to miss a single pedal point, we compute the least common multiple L of all determinants $\det M_{kl}$ (with $k \neq l$ and $(k,l) \in \{A,B,C,D\}$) and find

$$\begin{aligned} L = {} & \underbrace{\iota_A\cdot\iota_B\cdot\iota_C\cdot\iota_D}_{\substack{\text{isotropic lines}\\ \text{through vertices}}}\cdot\underbrace{k_A\cdot k_B\cdot k_C\cdot k_D}_{\substack{\text{circumcircles}\\ \text{of subtriangles}}}\cdot \\ & \underbrace{\cdot k_{ABR}\cdot k_{CDR}\cdot k_{ADP}\cdot k_{BCP}\cdot}_{\substack{\text{circles through}\\ \text{the Miquel point } M_{RP}}} \\ & \underbrace{\cdot k_{ACP}\cdot k_{BDP}\cdot k_{ABQ}\cdot k_{CDQ}\cdot}_{\substack{\text{circles through}\\ \text{the Miquel point } M_{PQ}}} \\ & \underbrace{\cdot k_{ADQ}\cdot k_{BCQ}\cdot k_{ACR}\cdot k_{BDR}\cdot}_{\substack{\text{circles through}\\ \text{the Miquel point } M_{QR}}} \end{aligned}$$

The points on $\mathcal{C}$ with degenerate conics through their pedal points are found as the intersection of the curve $\mathcal{C}: P_7 = 0$ and the cycle $\mathcal{L}: L = 0$ of degree 40. The cycle $\mathcal{L}$ consists of 16 circles and the 8 isotropic lines passing through the four vertices of $\mathcal{Q}$, cf. Figure 8. According to BÉZOUT's theorem, we have to expect up to 280 common points of $\mathcal{C}$ and $\mathcal{L}$. As we shall see, many of them are not real and a huge amount of them coincides with already known points.

In order to get rid of solutions that we already now and, further, in order to simplify the computation we have to discuss the intersection of the components of $\mathcal{L}$ with $\mathcal{C}$.

The four pairs of isotropic lines can be cut out immediately: The pair described by $\iota_A = 0$ intersects $\mathcal{C}$ in 14 points 6 of which coincide with A (since A is an ordinary double point on ι_A and $\mathcal{C}$ and both (isotropic) components of ι_A are tangents to $\mathcal{C}$ at A). Three intersection points each are located at I and J (since they are ordinary triple points on $\mathcal{C}$ (cf. Thm. 2) and regular points on ι_A). The two remaining points cannot be real since ι_A does not contain any real point different from A. The same arguments hold for the other pairs. Therefore, we can cut out the cycle of degree 8 given by the equation $\iota_A \cdot \iota_B \cdot \iota_C \cdot \iota_D = 0$.

The circumcircles can also be canceled: For example, the circle k_A (passing through B, C, D) intersects $\mathcal{C}$ at B, C, D with multiplicity 2 at each point (since they are double points on $\mathcal{C}$, cf. Thm. 1 and Thm. 3). At both absolute points I and J, the intersection multiplicity of k_A and $\mathcal{C}$ equals 3. Further, k_A and $\mathcal{C}$ have a pair of complex conjugate proper points in common. These two points are never real since the discriminant Δ_A of the respective quadratic equations is a full square with a minus ahead:

$$\Delta_A = -4l_1^{-1}(l_1F_B + l_3F_D - l_2F_C)^2 \cdot \\ \cdot (l_1(l_3 - l_2 - l_4 + l_5) + ad(l_2 - l_3 + l_6) - 4F_BFC)^2.$$

Hence, k_A does not lead to new real points on $\mathcal{C}$ with singular pedal conics, as is the case with k_B, k_C, k_D for the same reasons. Therefore, the cycle $k_A \cdot k_B \cdot k_C \cdot k_D = 0$ of degree eight being the union of the circumcircles of the four subtriangles can also be cut out.

Finally, we have to study the last three quadruples of circles passing through their respective Miquel point: At first, we shall have a look at the four circles passing through one particular Miquel point. For example the circles k_{ABR}, k_{CDR}, k_{ADP}, k_{BCP} share only the points A, B, C, D, R, P, M_{RP}, I, and J with $\mathcal{C}$ (with multiplicities 4, 4, 4, 4, 2, 2, 4, 16, 16). Which is similarly true for the other quadruples of circles passing through the Miquel points M_{PQ} and M_{QR} and does not deliver new points.

Surprisingly, the following combinations of circles yield real points on $\mathcal{C}$

$$k_{ACP} \cap k_{BDR} = \{R_1, R_2\}, \\ k_{ACR} \cap k_{BDP} = \{R_3, R_4\}$$

while all other combinations of circles lead to intersections which are either already known or not on $\mathcal{C}$, or, if on $\mathcal{C}$, two points which can never be real. □

Table 1 lists the intersection points of $\mathcal{L}$ and $\mathcal{C}$ with their respective multiplicities, and thus, it summarizes the proof of Thm. 5.

A	B	C	D	P	Q	R	M_{PQ}	M_{QR}	M_{RP}	I	J
24	24	24	24	4	4	4	4	4	4	60	60

R_1	R_2	R_3	R_4	compl. pts.	Σ
2	2	2	2	32	280

Table 1: *The common points of $\mathcal{L}$ and $\mathcal{C}$ algebraically counted.*

Remark 5 *The cycle $\mathcal{L}$ is of degree 40 and it is the union of 16 circles and 8 isotropic lines. It has four 11-fold points at A, B, C, D; six 4-fold points at P, Q, R, M_{PQ}, M_{QR}, M_{RP}; and the absolute points I, J are 20-fold points. Further it has 128 ordinary double points (among them $R_1, \ldots, R_4$).*

2.3 Degenerate quadrilaterals

Quadrilaterals may degenerate in many ways. Until now, we have assumed that none of the four vertices falls into a line spanned by two others, *i.e.*, $\mathcal{Q} = ABCD$ is a proper quadrilateral. If we exclude cases where two or more vertices coincide, the only possible degenerate quadrilaterals are those where one vertex, say C, lies on the side line $[A,B]$. In any other case, we can relabel the points. In this rather special case, we can state:

Theorem 6 *Assume that all vertices of $\mathcal{Q}$ are pairwise different, but, for example, $C \in [A,B]$. Then, the septic curve $\mathcal{C}$ becomes the septic cycle consisting of the line $[A,B]$ and the circumcircles of the three non-degenerate subtriangles ABD, ACD, and BCD.*

The line $[A,B]$ serves as the degenerate circumcircle of the improper triangle ABC.

Proof. If C lies on $[A,B]$, then $C = 1 : b : 0$, *i.e.*, $c = 0$. Inserting this into P_7, yields

$$P_7 = (a-b)^2b^2 \cdot x_2 \cdot (e(x_1^2+x_2^2) - bex_0x_1 + \\ +(bd-d^2-e^2)x_0x_2) \cdot \\ \cdot (e(x_1^2+x_2^2) - aex_0x_1 + (ad-d^2-e^2)x_0x_2) \cdot \\ \cdot (e(x_1^2+x_2^2) - (a+b)ex_0x_1 + \\ +((a+d)(d-b)-e^2)x_0x_2 + abex_0^2).$$

The linear factor is the equation of $[A,B]$, the quadratic factors are the equations of the circumcircles k_C, k_B, k_A of ABD, ACD, BCD. □

The points on the septic cycle described in Theorem 6 define only degenerate conics: Let X be some point on the circumcircle of $\Delta_C = ABD$. The pedal points P_{AB}, P_{AD}, P_{BD} of X on the sides of Δ_C are collinear and lie on the Simson line s_{ABD}. Since $C \in [A,B]$, $[A,B] = [A,C] = [B,C]$, and thus, $P_{AB} = P_{AC} = P_{BC}$. Therefore, the conic on the six pedals is the union of two lines, the Simson line s_{ABD} and the line $[P_{CD}, P_{AB}]$.

Here, we have only four different pedal points, and four points always lie on at least one conic, indeed, they form the basis of a pencil of conics.

3 A more general point of view

We have drawn the normals from some point X to the lines of a complete quadrilateral and determined the pedal points. However, these six pedal points are very special points on the six normals through P.

Let again P_{kl} denote the pedal point of X on the line $[k,l]$ (with $k \neq l$ and $(k,l) \in \{A,B,C,D\}$) and let further denote P_{kl}^{ω} the ideal point of the normal of $[k,l]$ through X. Then, we shall determine the points P_{kl}^{δ} on the normal such that the crossratio of P_{kl}, P_{kl}^{ω}, X, and P_{kl}^{δ} equals $\delta \in \mathbb{R} \setminus \{0\}$.

Now, we can ask for the set $\mathcal{C}^{\delta}$ of all points X such that the six points P_{kl}^{δ} lie on a single conic. We can show the astonishing result:

Theorem 7 *Let $\mathcal{Q} = ABCD$ be a quadrilateral in the projectively extended Euclidean plane. Then, define six perspective collineations κ_{kl}^{δ} whose axes are the six lines $[k,l]$ ($k \neq l$, $k,l \in \{A,B,C,D\}$) of the complete quadrangle determined by $\mathcal{Q}$, their centers P_{kl}^{δ} being the ideal points of the normals of $[k,l]$, and $\delta \in \mathbb{R} \setminus \{0\}$ be their (common) characteristic crossratio.*

Then, the set $\mathcal{C}^{\delta}$ of all points X whose images P_{kl}^{δ} under the six perspective collineations κ_{kl}^{δ} lie on a single conic form the septic curve $\mathcal{C}$ described in Theorem 2 independent of the choice of $\delta \neq 0$.

Proof. With the Cartesian coordinates of X and P_{kl} and the characteristic cross ratio $\delta \in \mathbb{R}$, the points P_{kl}^{δ} can be written as a linear combination of X and and the respective pedal point P_{kl}

$$P_{kl}^{\delta} = (1-\delta)X + \delta P_{kl}$$

(where $\delta \neq 0$, $(k,l) \in \{A,B,C,D\}$, and $k \neq l$) since P_{kl}^{ω} is a point at infinity. Again, the determinant of the matrix (4) factors and equals

$$\det V = -2^8 l_1^{-1} F_A^2 F_B^2 F_C^2 F_D^2 \cdot \delta^8 \cdot x_0^5 \cdot P_7$$

with the same polynomial P_7 of degree 7 as we know from (5) and (6) which is independent of δ. Hence $P_7 = 0$ is the equation of $\mathcal{C}^{\delta} = \mathcal{C}$. □

Theorem 7 contains a very special case: If $\delta = -1$, then the collinear images of X are the reflections of X in the six side lines of the complete quadrilateral. Obviously, these points are conconic if X lies on the septic $\mathcal{C}$. Figure 9 shows the septic together with some point $X \in \mathcal{C}$ and the conics on the six pedal points P_{kl} and the six reflections R_{kl}.

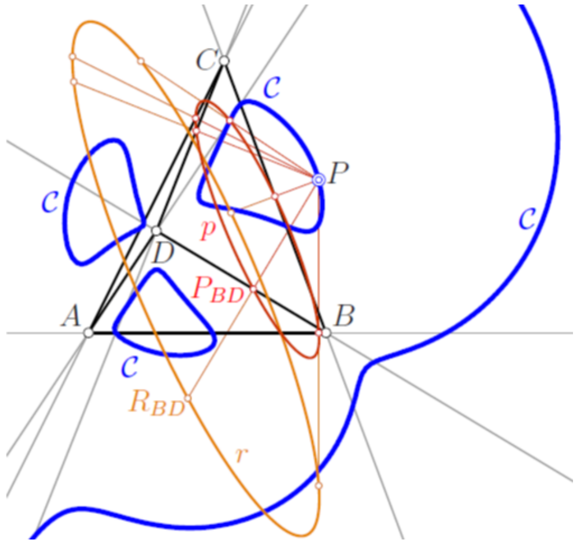

Figure 9: *The conics p and r collect the pedal points and reflections of $P \in \mathcal{C}$. Here, the conic r is the image of p under the central similarity with center P and similarity factor 2.*

It is clear that the conics corresponding to two different characteristic cross ratios $\delta_1, \delta_2 \neq 0$ are related by a central similarity with center X and similarity factor $\delta_1 \delta_2^{-1}$ (or its reciprocal).

4 Exceptional quadrilaterals, degree reduction

4.1 Special configurations

In the case of the locus curve described in [3], the cubic may degenerate, *i.e.*, it splits into lower degree parts, depending on the shape of the quadrilateral. From Thm. 6, we know that $\mathcal{C}$ becomes the union of three circles and a straight line if three points out of $\{A,B,C,D\}$ are collinear (while still being pairwise different). This seems to be the only case (as is indicated by a detailed study of the curve $\mathcal{C}$ for all possible types of quadrilaterals – up to Euclidean transformations).

Now, we shall ask under what circumstances the degree of $\mathcal{C}$ is less than 7. We have the following:

Theorem 8 *Let $\mathcal{Q} = ABCD$ be a proper quadrilateral such that, for example, the point D is the orthocenter of*

ABC. The curve $\mathcal{C}$ associated with the complete quadrangle on $\mathcal{Q}$ is of degree 6 and genus 1, has 9 (isolated) double points and no further singularities. It is of class 12 and has no real branch.

Proof. The contents of this theorem can be verified by setting

$$A = 1:0:0,\ B = 1:a:0,\ C = 1:b:c,$$

and since D has to be the orthocenter of ABC, we have

$$D = c : bc : b(a-b).$$

With (4), we find the (homogeneous) equation of $\mathcal{C}$ as

$$\begin{gathered}\mathcal{C}: c^2(x_1^2+x_2^2)^3-\\ -2c((a+b)cx_1^3+3bcx_1x_2^2+(ab-b^2+c^2)x_2^3)\cdot\\ \cdot(x_1^2+x_2^2+abx_0^2)x_0+(c^2(a^2+4ab+b^2)x_1^4+\\ +6(a+b)bc^2x_1^2x_2^2++4bc(ab-b^2+c^2)x_1x_2^3+\\ +(a^2b^2-2ab^3+4abc^2+b^4-b^2c^2+c^4)x_2^4)x_0^2+\\ +a^2b^2c^2(x_1^2+x_2^2)x_0^4=0\end{gathered} \tag{7}$$

which is obviously of degree 6 and allows us to locate the singularities (isolated double points) at the three diagonal points of $\mathcal{Q}$. (According to Thm. 3, the vertices of $\mathcal{Q}$ are singular points on $\mathcal{C}$ in any case.) Although the leading term in (7) is $(x_1^2+y_2^2)^3$, the absolute points I and J are only double points. (This can be shown at hand or the ranks of the tensors of the partial derivatives of order 3 of (7) with respect to the three variables x_i or using the `singularities` command in Maple's `algcurves` package.) Besides A, B, C, D, P, Q, R, I, J there are no further singularities.

With the Plücker formulae (cf. [2, 4, 5, 8, 14]), we find

$$\begin{aligned} g &= \tfrac{1}{2}(6-1)\cdot(6-2)-9\cdot 1 = 1,\\ m &= 6\cdot(6-1)-2\cdot 9 = 12\end{aligned}$$

for the genus and the class of $\mathcal{C}$. □

Symmetries of the initial quadrilateral may not necessarily cause a reduction of the degree of $\mathcal{C}$. However, if two diagonal points of $\mathcal{Q}$ move to the line at infinity, then their join splits off from $\mathcal{C}$. This yields to the following result:

Theorem 9 *Let $\mathcal{Q} = ABCD$ be a parallelogram. The curve $\mathcal{C}$ associated with the complete quadrangle on $\mathcal{Q}$ is of degree 6 and genus 3, has 7 (isolated) double points, is of class 16 and has no real branch.*

Proof. We proceed in a similar way as in the proof of Thm. 8 with

$$\begin{aligned} &A = 1:0:0,\ \ B = 1:a:0,\\ &C = 1:a+u:c,\ \ D = 1:u:c.\end{aligned}$$

It is not necessary to write down the rather lengthy equation of $\mathcal{C}$. (The reader may convince her-/himself by using a CAS that it is of degree 6.)

Now, the singularities are still the vertices of $\mathcal{Q}$ (according to Thm. 3), the absolute points I, J are double points, and the diagonal point $Q = [A,B]\cap[C,D]$ is the seventh (isolated) double point. Since there are no further singularities, the genus equals 3 and the class equals 16. □

We shall make explicit the fact that Thm. 9 contains the cases of *rhombi*, *rectangles*, and *squares*.

For *trapezoids*, in general, (no matter if they are symmetric, cyclic, tangential, or bicentric, equipped with right angles, or three equally long sides (as long as they are none of the above) the degree of $\mathcal{C}$ equals 7.

Kites (different from rhombi), *cyclic*, *tangential*, and *bicentric* quadrilaterals (as long as they do not fall into one of the above mentioned classes of quadrilaterals) always defined a *septic* $\mathcal{C}$ as the locus of points with six conconic pedal points on the complete quadrangle's sides.

4.2 Degree less than 6?

Finally, we want to show that the degree of $\mathcal{C}$ cannot be less than 6: Prior to Thm. 9, we have pointed out that a parallelogram has two diagonal points on the line ω at infinity, and thus, ω splits off from $\mathcal{C}$ once and $\deg\mathcal{C} = 6$. In a *classical projective plane*, the diagonal points of a quadrilateral are never collinear. Therefore, the ideal line will never splits off with multiplicity 3.

However, by virtue of (6), we see that the greatest common divisor of coefficients q_i of P_7 for $i\in\{0,1,2,5,6,7\}$ equals $x_1^2+x_2^2=\Omega$. The degree of P_7 would reduce about 2 if $\gcd(q_3,q_4)=\Omega$. In this case the resultant

$$r_3 := \operatorname{res}(q_3,\Omega,x_i),\quad r_4 := \operatorname{res}(q_4,\Omega,x_i)$$

for any variable x_i ($i\in\{0,1,2\}$) have to be equal to zero. We build the resultants with respect to x_1 (and would find the same results if we would eliminate x_2):

$$\begin{aligned} r_3 &= x_2^8\cdot l_2^2 l_3^2 l_4 l_5 l_6\cdot(l_1^2l_4-l_1l_2l_5-2l_1l_3l_4+\\ &\quad +l_1l_3l_5+l_2^2l_5-l_2l_3l_5+l_3^2l_4),\\ r_4 &= x_2^6\cdot l_1 l_2^2 l_3^2 l_4 l_5 l_6\cdot(2aF_B-el_2+cl_3)^2.\end{aligned}$$

By assumption, $l_i\neq 0$ for all $i\in\{1,\dots,6\}$, hence $r_4=0$ yields

$$a=\frac{e\,l_2-c\,l_3}{2F_B},$$

and after inserting into r_3, we find

$$r_4 = x_2^8\cdot l_2^4 l_3^4 l_6^6 F_C^4 F_D^4 F_B^{-8}.$$

None of the (squares of the) lengths l_i and none of the areas of the subtriangles are allowed to vanish, otherwise Q would degenerate. Therefore, neither r_3 nor r_4 can vanish, and thus, Ω is a common divisor of q_3 and q_4. Since there are no other (non-constant) factors of q_5, Ω cannot split off from P_7 and deg C cannot be equal to 5.

References

[1] M. BERGER, *Geometry.* 1–2, Springer, Berlin, 1987.

[2] E. BRIESKORN, H. KNÖRRER: *Planar Algebraic Curves,* Birkhäuser, Basel, 1986.

[3] J. BLAŽEK, P. PECH, On one locus in the plane, *ICCG 2018 - Proceedings of the 18th International Conference on Geometry and Graphics.*

[4] W. BURAU, *Algebraische Kurven und Flächen. I – Algebraische Kurven der Ebene,* De Gruyter, Berlin, 1962.

[5] J.L. COOLIDGE, *A Treatise on Algebraic Plane Curves,* Dover Publications, New York, 1959.

[6] G. FARIN, *Curves and Surfaces for CAGD,* 5th edn., Morgan Kaufmann, San Francisco, 2001.

[7] R.T. FAROUKI, *Pythagorean-Hodograph Curves: Algebra and Geometry Inseparable,* Springer-Verlag, Berlin Heidelberg, 2008.

[8] K. FLADT, *Analytische Geometrie spezieller ebener Kurven,* Akademische Verlagsgesellschaft, Frankfurt am Main, 1962.

[9] B. GIBERT, *Catalogue of Triangle Cubics,* `https://bernard-gibert.pagesperso-orange.fr/ctc.html`

[10] B. GIBERT, *Curves related to a triangle.,* `https://bernard-gibert.pagesperso-orange.fr/relatedcurves.html`

[11] G. GLAESER, H. STACHEL, B. ODEHNAL, *The Universe of Concis - From the ancient Greeks to 21st century developments*, Springer-Spektrum, Springer-Verlag, Heidelberg, 2016.

[12] A. HAARBLEICHER, *De l'emploi des droites isotropes comme axes de coordonnées. Nouvelle géométrie du triangle*, Paris, Gauthier-Villars, 1931, 61–70.

[13] B. JÜTTLER, Hermite interpolation by Pythagorean hodograph curves of degree seven, *Math. Comp.* **70** (2000), 1089–1111.

[14] E. KUNZ, *Introduction to plane algebraic curves,* Birkhäuser, Boston, 2000.

[15] J.D. LAWRENCE, *A catalog of special plane curves.* Dover Publications, New York, 1972.

[16] É. LEMOINE, Propriétés diverses du cercle et de la droite de Brocard, *Mathesis V* (1885), 103–108.

[17] G. LORIA, *Spezielle algebraische und transzendente ebene Kurven,* B.G. Teubner, Leipzig, 1908.

[18] G. LORIA, *Ebene algebraische und transzendente Kurven,* B.G. Teubner, Leipzig-Berlin, 1910.

[19] D.S. MEEK, D.J. WALTON, Geometric Hermite interpolation with Tschirnhausen cubics, *J. Comput. Appl. Math.* **81** (1997), 299–309.

[20] B. ODEHNAL, Hermite interpolation with ruled and channel surfaces, *G - slovenský Časopis pre Geometriu a Grafiku* **14**(28) (2017), 35–58.

[21] N. PAPAMICHAEL, M.J. SOARES, Cubic and quintic spline-on-spline interpolation, *J. Comp. Applied Math.* **20** (1987), 359–366.

[22] M. ROLÍNEK, L.A. DUNG, The Miquel points, Pseudocircumcenter, and Euler-Poncelet-Point of a Complete Quadrilateral, *Forum Geom.* **14** (2014), 145–153.

[23] H. WIELEITNER, *Spezielle ebene Kurven.* G.J. Göschen'sche Verlagshandlung, Leipzig, 1908.

Boris Odehnal
orcid.org/0000-0002-7265-5132
e-mail: boris.odehnal@uni-ak.ac.at

University of Applied Arts Vienna
Oskar-Kokoschka-Platz 2, A-1010 Vienna, Austria

Appendix A. Equation of $\mathcal{C}$

For the sake of completeness, we add the equation of $\mathcal{C}$ in terms of inhomogeneous coordinates.

$$
\begin{gathered}
\mathcal{C}:\ (\mathbf{x^2}+\mathbf{y^2})^{\mathbf{3}}\cdot \\
\cdot(4c(c^2F_Bl_3-2c^2F_Cl_3+c^2F_Dl_3-ceF_Bl_3+ceF_Bl_5+ceF_Cl_3-e^2F_Bl_5+ \\
+e^2F_Bl_6-4F_B^3+4F_B^2F_C-4F_B^2F_D)\mathbf{x}+(c^3l_2l_3+c^3l_3l_4-2c^3l_3l_5-2c^3l_3l_6+ \\
+16c^2eF_B^2-16c^2eF_BF_C-2c^2el_2l_3+c^2el_3^2+c^2el_3l_5-2c^2el_3l_6-16ce^2F_B^2+ \\
+16ce^2F_BF_C-32aF_B^3+16aF_B^2F_C-24aF_B^2F_D+24aF_BF_CF_D-4cF_B^2l_2+ \\
+4cF_B^2l_3-4cF_B^2l_4+12cF_B^2l_5+8cF_B^2l_6+8cF_BF_Cl_2-12cF_BF_Cl_3-12cF_BF_Cl_5+ \\
+24cF_BF_Dl_3-12cF_C^2l_2-4cF_CF_Dl_3+16cF_D^2l_3+8eF_B^2l_2)\mathbf{y})+ \\
+2(\mathbf{x^2}+\mathbf{y^2})^{\mathbf{2}}\cdot \\
\cdot((c^4l_2l_3-c^4l_3^2-c^4l_3l_6+16c^3eF_B^2-16c^3eF_BF_C-c^3el_2l_3+c^3el_3^2-2c^3el_3l_6- \\
-16c^2e^2F_B^2+16c^2e^2F_BF_C-4c^2F_B^2l_2-4c^2F_B^2l_3+8c^2F_B^2l_5+4c^2F_B^2l_6+ \\
+4c^2F_BF_Cl_2+20c^2F_BF_Cl_3-12c^2F_BF_Cl_5-8c^2F_BF_Dl_3-4c^2F_C^2l_2-12c^2F_C^2l_3+ \\
+24c^2F_CF_Dl_3-8c^2F_D^2l_3+8ceF_B^2l_2+12ceF_B^2l_3-8ceF_B^2l_6-12ceF_BF_Cl_3+ \\
+8ceF_BF_Cl_5-32F_B^3F_D+16F_BF_CF_D^2)\mathbf{x^2}+(2c^3dl_3l_6-8c^3eF_Bl_5+8c^2e^2F_Bl_5+ \\
-8c^2e^2F_Bl_6-96c^2F_B^2F_C+64c^2F_BF_C^2-32c^2F_BF_CF_D+10c^2F_Bl_2l_3+ \\
+4c^2F_Bl_2l_5-2c^2F_Bl_3^2-10c^2F_Bl_3l_4+6c^2F_Bl_3l_5+4c^2F_Bl_3l_6-8c^2F_Cl_2l_3+2c^2F_Cl_3^2+ \\
+12c^2F_Cl_3l_4-6c^2F_Cl_3l_5+2c^2F_Dl_2l_3+4c^2F_Dl_3^2-6c^2F_Dl_3l_4+32ceF_B^3 \\
-32ceF_BF_C^2-2ceF_Bl_2^2-6ceF_Bl_2l_3+2ceF_Bl_2l_6-16F_B^3l_1-56F_B^3l_2+ \\
+40F_B^3l_4+8F_B^2F_Cl_1+96F_B^2F_Cl_2-16F_B^2F_Dl_1-40F_B^2F_Dl_2-48F_B^2F_Dl_3+ \\
+24F_B^2F_Dl_4-8F_BF_C^2l_2+32F_BF_CF_Dl_2+64F_BF_CF_Dl_3-16F_BF_D^2l_2- \\
-24F_BF_D^2l_3-24F_C^3l_2+24F_C^2F_Dl_2)\mathbf{xy}+(-c^4l_2l_3+c^4l_3^2+c^4l_3l_6-16c^3eF_B^2+ \\
+16c^3eF_BF_C+c^3el_2l_3-c^3el_3^2+2c^3el_3l_6+16c^2e^2F_B^2-16c^2e^2F_BF_C+4c^2F_B^2l_2+ \\
+12c^2F_B^2l_3-16c^2F_B^2l_5-4c^2F_B^2l_6-12c^2F_BF_Cl_2-12c^2F_BF_Cl_3+12c^2F_BF_Cl_5+ \\
+16c^2F_BF_Dl_3+12c^2F_C^2l_2+12c^2F_C^2l_3-24c^2F_CF_Dl_3-2c^2l_2l_3^2-c^2l_2l_3l_4+2c^2l_3^3+ \\
+c^2l_2l_3l_5+c^2l_2l_3l_6+c^2l_3^2l_4-c^2l_3^2l_5-c^2l_3^2l_6-8ceF_B^2l_2+4ceF_B^2l_3-4ceF_BF_Cl_3+ \\
+2cel_2^2l_3-2cel_2l_3^2-cel_2l_3l_6+64F_B^3F_D-32F_B^2F_CF_D+64F_B^2F_D^2-4F_B^2l_1l_2+ \\
+4F_B^2l_1l_3-12F_B^2l_2l_3+4F_B^2l_2l_4+4F_B^2l_2l_5-4F_B^2l_2l_6-48F_BF_CF_D^2+4F_BF_Cl_2^2+ \\
+20F_BF_Cl_2l_3+4F_BF_Cl_2l_5+8F_BF_Dl_1l_3-36F_BF_Dl_2l_3+12F_BF_Dl_3^2-4F_BF_Dl_3l_4- \\
-12F_C^2l_2l_3+4F_C^2l_2l_4-4F_C^2l_2l_5-4F_CF_Dl_1l_3+20F_CF_Dl_2l_3+4F_CF_Dl_3l_4+4F_D^2l_1l_3- \\
-12F_D^2l_2l_3+4F_D^2l_3^2-4F_D^2l_3l_4)\mathbf{y^2})+ \\
+(\mathbf{x^2}+\mathbf{y^2})\cdot \\
\cdot((128c^3F_BF_C^2-128c^3F_B^2F_C+12c^3F_Bl_2l_3-12c^3F_Bl_3^2-8c^3F_Bl_3l_4+12c^3F_Cl_3^2+ \\
+24c^3F_Bl_3l_5-4c^3F_Bl_3l_6+12c^3F_Cl_2l_3-24c^3F_Dl_3^2+64c^2eF_B^3+64c^2eF_B^2F_C- \\
-128c^2eF_BF_C^2-12c^2eF_Bl_2l_3-4c^2eF_Bl_3l_5+4c^2eF_Bl_3l_6-64aF_B^3F_D-32aF_B^2F_D^2+ \\
+96aF_B^2F_CF_D+32aF_BF_CF_D^2-48cF_B^3l_2-96cF_B^3l_3+32cF_B^3l_4+48cF_B^3l_5+16cF_B^3l_6+ \\
+80cF_B^2F_Cl_2+48cF_B^2F_Cl_3-48cF_B^2F_Cl_5-192cF_B^2F_Dl_3+48cF_BF_C^2l_3-16cF_BF_C^2l_5- \\
-32cF_BF_CF_Dl_2+64cF_BF_CF_Dl_3-112cF_BF_D^2l_3-48cF_C^3l_2+32cF_C^2F_Dl_2+16cF_D^3l_3+ \\
+48cF_C^2F_Dl_3-48cF_CF_D^2l_3)\mathbf{x^3}+(112c^3F_B^2l_3-96c^3F_B^2l_5-288c^3F_BF_Cl_3-2c^3l_2^2l_3+ \\
+64c^3F_BF_Cl_5+96c^3F_BF_Dl_3+7c^3l_2l_3^2+7c^3l_2l_3l_5+2c^3l_2l_3l_6-5c^3l_3^3-14c^3l_3^2l_4+ \\
+7c^3l_3^2l_5-48c^2eF_B^2l_2-80c^2eF_B^2l_3+48c^2eF_B^2l_5+16c^2eF_B^2l_6+80c^2eF_BF_Cl_3- \\
-64c^2eF_BF_Cl_5+4c^2el_2^2l_3-4c^2el_2l_3^2+2c^2el_2l_3l_6+16aF_B^3l_1+120aF_B^3l_2- \\
-88aF_B^3l_4-8aF_B^2F_Cl_1-272aF_B^2F_Cl_2-8aF_B^2F_Dl_1-24aF_B^2F_Dl_2-120aF_B^2F_Dl_3+ \\
+104aF_BF_C^2l_2+112aF_BF_CF_Dl_2+32aF_BF_CF_Dl_3-48aF_BF_D^2l_3+24aF_C^3l_2- \\
-96aF_C^2F_Dl_2-72aF_C^2F_Dl_3+120aF_CF_D^2l_3+24aF_D^3l_3-64cF_B^4-192cF_B^3F_C+ \\
+384cF_B^3F_D+192cF_B^2F_C^2+192cF_B^2F_CF_D+384cF_B^2F_D^2+8cF_B^2l_2^2-68cF_B^2l_2l_3+ \\
+12cF_B^2l_2l_5-8cF_B^2l_2l_6+56cF_B^2l_3l_4+64cF_BF_C^3-320cF_BF_C^2F_D-320cF_BF_CF_D^2+ \\
-24cF_C^2l_2l_3-140cF_BF_Dl_2l_3-72cF_BF_Dl_3^2+44cF_BF_Dl_3l_4-4cF_C^2l_2^2+36cF_C^2l_3l_4- \\
+168cF_BF_Cl_2l_3+36cF_C^2l_2l_4+40cF_CF_Dl_2l_3+32cF_CF_Dl_3^2-72cF_CF_Dl_3l_4- \\
28cF_D^2l_2l_3-16cF_D^2l_3^2+8eF_B^2l_2^2)\mathbf{x^2y}+(384c^3F_B^2F_C-128c^3F_BF_C^2-36c^3F_Bl_2l_3+ \\
+52c^3F_Bl_3^2+24c^3F_Bl_3l_4-40c^3F_Bl_3l_5-4c^3F_Bl_3l_6-20c^3F_Cl_2l_3+4c^2dl_2l_3^2-
\end{gathered}
$$

$$\begin{gathered}
-20c^3F_Cl_3^2+40c^3F_Dl_3^2-2c^2dl_2^2l_3-2c^2dl_3^3-2c^2dl_2l_3l_6+2c^2dl_3^2l_6+64c^2eF_B^3-\\
-192c^2eF_B^2F_C+128c^2eF_BF_C^2-8c^2eF_Bl_3^2+16c^2eF_Bl_2^2-4c^2eF_Bl_2l_3+32aF_B^2l_2^2-\\
-16c^2eF_Bl_2l_6-4c^2eF_Bl_3l_5+4c^2eF_Bl_3l_6+192aF_B^3F_D-32aF_B^2F_CF_D+8aF_B^2l_2l_6-\\
-32aF_B^2F_D^2+40aF_B^2l_1l_2-24aF_B^2l_1l_3-8aF_B^2l_2l_3-32aF_B^2l_2l_4+8aF_BF_Dl_2^2-\\
-32aF_B^2l_2l_5+32aF_BF_CF_D^2-16aF_BF_Cl_1l_2-72aF_BF_Cl_2^2-40aF_BF_Cl_2l_3+\\
+8aF_BF_Cl_2l_5+32aF_BF_Dl_2l_3+16aF_BF_Dl_3^2+24aF_C^2l_2^2-8aF_C^2l_2l_4+8aF_C^2l_2l_5-\\
-8aF_BF_Dl_3l_4+48aF_C^2l_2l_3+8aF_CF_Dl_1l_3-104aF_CF_Dl_2l_3-32aF_CF_Dl_3^2-\\
-8aF_CF_Dl_3l_4-8aF_D^2l_1l_3+16aF_D^2l_2l_3+48aF_D^2l_3^2-16cF_B^3l_5+16cF_B^3l_6+8aF_D^2l_3l_4+\\
+144cF_B^3l_2-32cF_B^3l_3-96cF_B^3l_4-240cF_B^2F_Cl_2-16cF_B^2F_Cl_3+16cF_B^2F_Cl_5+\\
+192cF_B^2F_Dl_3-192cF_BF_C^2l_2+48cF_BF_C^2l_3-16cF_BF_C^2l_5-4cF_Bl_2^2l_3-4cF_Bl_2^2l_5+\\
+224cF_BF_CF_Dl_2-64cF_BF_CF_Dl_3+80cF_BF_D^2l_3-32cF_Bl_2l_3^2-4cF_Bl_2l_3l_6-4cF_Bl_3^2l_4+\\
+4cF_Bl_2l_3l_4+32cF_Bl_2l_3l_5+144cF_C^3l_2-160cF_C^2F_Dl_2-144cF_C^2F_Dl_3+144cF_CF_D^2l_3+\\
+44cF_Cl_2^2l_3+12cF_Cl_2l_3^2-16cF_Cl_2l_3l_4+16cF_Cl_3^2l_4+4cF_Dl_3^3-16cF_Dl_3^2l_4-4eF_Bl_2^3+\\
+16cF_D^3l_3-12cF_Dl_2^2l_3-48cF_Dl_2l_3^2+16cF_Dl_2l_3l_4+12eF_Bl_2^2l_3+4eF_Bl_2^2l_6)\mathbf{xy^2}+\\
(32c^3F_B^2l_5-16c^3F_B^2l_3+32c^3F_BF_Cl_3-32c^3F_BF_Dl_3+2c^3l_2^2l_3-c^3l_2l_3^2-c^3l_2l_3l_5+\\
+16c^2eF_B^2l_2-2c^3l_2l_3l_6-c^3l_3^3+2c^3l_3^2l_4-c^3l_3^2l_5-16c^2eF_B^2l_3-16c^2eF_B^2l_5-16aF_B^3l_1-\\
+16c^2eF_B^2l_6+16c^2eF_BF_Cl_3-4c^2el_2^2l_3+4c^2el_2l_3^2-2c^2el_2l_3l_6-40aF_B^3l_2+\\
+40aF_B^3l_4-8aF_B^2F_Cl_1+112aF_B^2F_Cl_2-8aF_B^2F_Dl_1+8aF_B^2F_Dl_2+8aF_B^2F_Dl_3+\\
-24aF_BF_C^2l_2+16aF_BF_CF_Dl_2-64aF_BF_CF_Dl_3+16aF_BF_D^2l_3-2aF_Bl_1^2l_2+\\
+2aF_Bl_1^2l_3+2aF_Bl_1l_2^2-12aF_Bl_1l_2l_3+2aF_Bl_1l_2l_5-2aF_Bl_1l_3^2-2aF_Bl_1l_3l_4-\\
-2aF_Bl_2^3+12aF_Bl_2^2l_3-2aF_Bl_2^2l_5+2aF_Bl_2^2l_6-10aF_Bl_2l_3^2-88cF_BF_Cl_2l_3+\\
+8aF_Bl_2l_3l_4-8aF_Bl_2l_3l_5-8aF_Bl_2l_3l_6+2aF_Bl_3^2l_4-8aF_C^3l_2+32aF_C^2F_Dl_2+\\
+24aF_C^2F_Dl_3-40aF_CF_D^2l_3+2aF_Cl_1l_2^2+4aF_Cl_1l_2l_3-2aF_Cl_2^2l_3-2aF_Cl_2^2l_5+\\
+8aF_Cl_2l_3^2-12aF_Cl_2l_3l_4+8aF_Cl_2l_3l_5-8aF_D^3l_3-8aF_Dl_1l_2l_3+2aF_Dl_1l_3^2-\\
-4aF_Dl_2l_3^2+8aF_Dl_2l_3l_4-2aF_Dl_3^3-2aF_Dl_3^2l_4-64cF_B^4+64cF_B^3F_C-128cF_B^3F_D-\\
-64cF_B^2F_C^2-320cF_B^2F_CF_D-128cF_B^2F_D^2-8cF_B^2l_2^2+12cF_B^2l_2l_3-4cF_B^2l_2l_5+\\
+8cF_B^2l_2l_6-8cF_B^2l_3l_4+64cF_BF_C^3+192cF_BF_C^2F_D-64cF_BF_CF_D^2+16cF_BF_Cl_2^2-\\
+36cF_BF_Dl_2l_3+8cF_BF_Dl_3^2-20cF_BF_Dl_3l_4-20cF_C^2l_2^2+24cF_C^2l_2l_3-12cF_C^2l_2l_4-\\
-12cF_C^2l_3l_4+8cF_CF_Dl_2l_3-32cF_CF_Dl_3^2+24cF_CF_Dl_3l_4+4cF_D^2l_2l_3-cl_2^3l_3+\\
+16cF_D^2l_3^2+7cl_2^2l_3^2+cl_2^2l_3l_4+3cl_2^2l_3l_5-6cl_2l_3^3-8cl_2l_3^2l_4+3cl_2l_3^2l_5+4cl_2l_3^2l_6+\\
+cl_3^3l_4-8eF_B^2l_2^2-2el_2^3l_3+2el_2^2l_3^2+4el_2^2l_3l_6)\mathbf{y^3})+
\end{gathered}$$

$$\begin{gathered}
+(128c^2F_B^2F_C^2-256c^2F_B^3F_C+128c^2F_B^2F_CF_D+16c^2F_B^2l_2l_3+8c^2F_B^2l_3^2-\\
-16c^2F_B^2l_3l_4-8c^2F_B^2l_3l_5+128c^2F_BF_C^3-128c^2F_BF_C^2F_D+8c^2F_BF_Cl_2l_3-\\
-16c^2F_BF_Cl_3^2+16c^2F_BF_Cl_3l_5-8c^2F_BF_Dl_2l_3-8c^2F_BF_Dl_3^2+8c^2F_BF_Dl_3l_4+\\
+48c^2F_C^2l_2l_3-24c^2F_CF_Dl_2l_3-24c^2F_CF_Dl_3^2+8ceF_B^2l_2l_3-64F_B^4l_1-64F_B^4l_2-\\
+64F_B^4l_4+64F_B^3F_Cl_1+128F_B^3F_Cl_2-32F_B^3F_Dl_1+32F_B^3F_Dl_2+96F_B^3F_Dl_3+\\
-32F_B^3F_Dl_4+32F_B^2F_CF_Dl_1-128F_B^2F_CF_Dl_2-96F_B^2F_CF_Dl_3+96F_B^2F_D^2l_3+\\
-64F_BF_C^3l_2+64F_BF_C^2F_Dl_2-32F_BF_C^2F_Dl_3+32F_BF_CF_D^2l_2-128F_BF_CF_D^2l_3-\\
+32F_BF_D^3l_3+32F_C^3F_Dl_2-32F_C^2F_D^2l_2-32F_C^2F_D^2l_3+32F_CF_D^3l_3)\mathbf{x^4}+
\end{gathered}$$

$$\begin{gathered}
+(64c^2F_B^3l_3-64c^2F_B^3l_5+128c^2F_B^2F_Cl_2+64c^2F_B^2F_Cl_3+64c^2F_B^2F_Dl_3-8c^2F_Dl_3^3-\\
-192c^2F_BF_C^2l_2-128c^2F_BF_C^2l_3+64c^2F_BF_C^2l_5+512c^2F_BF_CF_Dl_3+8c^2F_Bl_2l_3l_4-\\
-8c^2F_Bl_2^2l_3+8c^2F_Bl_2l_3^2-8c^2F_Bl_2l_3l_5+64c^2F_C^3l_2-64c^2F_CF_D^2l_3+8c^2F_Cl_2^2l_3+\\
+24c^2F_Cl_2l_3^2-16c^2F_Cl_2l_3l_4-16c^2F_Cl_3^2l_4-24c^2F_Dl_2l_3^2+32c^2F_Dl_3^2l_4-32F_B^3l_1l_2+\\
+256F_B^4F_D+256F_B^3F_D^2-32F_B^3l_1^2+32F_B^3l_2^2-32F_B^3l_2l_4-256F_B^2F_C^2F_D+32F_B^2F_Cl_1l_2+\\
-96F_B^2F_Cl_2^2+160F_B^2F_Dl_1l_3+160F_B^2F_Dl_2l_3-128F_B^2F_Dl_3l_4-768F_BF_C^2F_D^2+\\
+128F_BF_C^2l_1l_2+96F_BF_C^2l_2^2-32F_BF_CF_Dl_1l_2-32F_BF_CF_Dl_1l_3-64F_C^3l_1l_2-\\
-384F_BF_CF_Dl_2l_3+64F_BF_D^2l_1l_3+64F_BF_D^2l_2l_3-32F_BF_D^2l_3^2+32F_C^2F_Dl_1l_2+\\
+32F_C^2F_Dl_1l_3-64F_C^3l_2^2+64F_C^3l_2l_4+64F_C^2F_Dl_2l_3-32F_C^2F_Dl_2l_4-32F_C^2F_Dl_3l_4-\\
+96F_CF_D^2l_2l_3+32F_CF_D^2l_3^2-128F_D^3l_3^2)\mathbf{x^3y}+
\end{gathered}$$

$$\begin{gathered}
+(256c^2F_B^2F_C^2-256c^2F_B^3F_C-1024c^2F_B^2F_CF_D-48c^2F_B^2l_2l_3+64c^2F_B^2l_2l_5-\\
-16c^2F_B^2l_3l_4+80c^2F_BF_Cl_2l_3-16c^2F_BF_Cl_3^2+16c^2F_BF_Cl_3l_5-16c^2F_BF_Dl_3^2-\\
-64c^2F_BF_Dl_3l_4-96c^2F_C^2l_2l_3+48c^2F_CF_Dl_2l_3+48c^2F_CF_Dl_3^2+2c^2l_2^2l_3^2-2c^2l_2l_3^3-
\end{gathered}$$

$$\begin{gathered}
-4c^2l_2^2l_3l_5+4c^2l_2l_3^2l_4+4c^2l_2l_3^2l_5-4c^2l_3^3l_4+16ceF_B^2l_2l_3-2cel_2^3l_3+2cel_2^2l_3^2+\\
+2cel_2^2l_3l_6-64F_B^4l_1-64F_B^4l_2+64F_B^4l_4+64F_B^3F_Cl_1+128F_B^3F_Cl_2+16F_B^2l_1^2l_2-\\
-320F_B^3F_Dl_1-512F_B^3F_Dl_2+64F_B^3F_Dl_3+256F_B^3F_Dl_4+64F_B^2F_CF_Dl_1-24F_D^2l_1l_2l_3+\\
+768F_B^2F_CF_Dl_2-64F_B^2F_CF_Dl_3-256F_B^2F_D^2l_2+64F_B^2F_D^2l_3-16F_C^2l_1l_2^2-32F_C^2l_1l_2l_3+\\
+16F_B^2l_1^2l_3+16F_B^2l_1l_2^2+24F_B^2l_2^2l_3-16F_B^2l_2^2l_5-16F_B^2l_2l_3l_4+32F_D^2l_2l_3^2+8F_D^2l_3^3-\\
-64F_BF_C^3l_2-64F_BF_C^2F_Dl_2-64F_BF_C^2F_Dl_3+64F_BF_CF_D^2l_2+16F_BF_Cl_1^2l_2-\\
-48F_BF_Cl_1l_2^2+8F_BF_Cl_1l_2l_3-16F_BF_Cl_1l_2l_5-72F_BF_Cl_2^2l_3+16F_BF_Cl_2^2l_5+\\
+320F_BF_D^3l_3-16F_BF_Dl_1^2l_3+8F_BF_Dl_1l_2l_3+16F_BF_Dl_1l_3l_4+64F_BF_Dl_2^2l_3+\\
+8F_BF_Dl_2l_3^2-16F_BF_Dl_3^2l_4-192F_C^3F_Dl_2+192F_C^2F_D^2l_2+192F_C^2F_D^2l_3+\\
+16F_C^2l_2^3+56F_C^2l_2^2l_3-24F_C^2l_2^2l_4+16F_C^2l_2^2l_5+8F_C^2l_2l_3l_4-192F_CF_D^3l_3+\\
+88F_CF_Dl_1l_2l_3+24F_CF_Dl_1l_3^2-80F_CF_Dl_2^2l_3-48F_CF_Dl_2l_3^2-24F_CF_Dl_3^2l_4\\
+8F_CF_Dl_2l_3l_4-40F_D^2l_1l_3^2+16F_D^2l_2^2l_3+16F_D^2l_3^2l_4)\mathbf{x^2y^2}+
\end{gathered}$$

$$\begin{gathered}
(64c^2F_B^3l_3-64c^2F_B^3l_5-128c^2F_B^2F_Cl_2+64c^2F_B^2F_Cl_3+64c^2F_B^2F_Dl_3+64c^2F_BF_C^2l_2\\
-128c^2F_BF_C^2l_3+64c^2F_BF_C^2l_5+8c^2F_Bl_2^2l_3-8c^2F_Bl_2l_3^2-8c^2F_Bl_2l_3l_4+8c^2F_Bl_2l_3l_5+\\
+64c^2F_C^3l_2-64c^2F_CF_D^2l_3+8c^2F_Cl_2^2l_3-8c^2F_Cl_2l_3^2-8c^2F_Dl_2l_3^2+8c^2F_Dl_3^3+2cdl_2^3l_3-\\
-4cdl_2^2l_3^2-2cdl_2^2l_3l_6+2cdl_2l_3^3-2cdl_2l_3^2l_6-8ceF_Bl_2^2l_3+8ceF_Bl_2l_3^2+256F_B^4F_D-64F_D^3l_3^2+\\
+256F_B^3F_D^2+32F_B^3l_1^2-32F_B^3l_1l_2-32F_B^3l_2^2+32F_B^3l_2l_4-256F_B^2F_C^2F_D-128F_BF_C^2l_1l_2+\\
+32F_B^2F_Cl_1l_2+96F_B^2F_Cl_2^2+32F_B^2F_Dl_1l_3-32F_B^2F_Dl_2l_3+256F_BF_C^2F_D^2-32F_BF_C^2l_2^2+\\
+32F_BF_CF_Dl_1l_2+32F_BF_CF_Dl_1l_3-64F_BF_D^2l_1l_3+32F_BF_D^2l_3^2-8F_Bl_1^2l_2^2+16F_Bl_1^2l_2l_3+\\
+8F_Bl_1^2l_3^2-16F_Bl_1l_2^2l_3+8F_Bl_1l_2^2l_5-8F_Bl_1l_2l_3^2+4F_Bl_1l_2l_3l_4-4F_Bl_1l_2l_3l_5-4F_Dl_1l_3^2l_4-\\
-8F_Bl_1l_3^2l_4+4F_Bl_2^3l_3-4F_Bl_2^2l_3^2-4F_Bl_2^2l_3l_5-4F_Bl_2^2l_3l_6+4F_Bl_2l_3^2l_4-12F_Dl_2l_3^3+\\
+64F_C^3l_1l_2-64F_C^3l_2l_4-32F_C^2F_Dl_1l_2-32F_C^2F_Dl_1l_3+64F_C^2F_Dl_2^2-64F_C^2F_Dl_2l_3+\\
+32F_C^2F_Dl_2l_4+32F_C^2F_Dl_3l_4-32F_CF_D^2l_2l_3+96F_CF_D^2l_3^2+4F_Cl_1^2l_2^2-12F_Cl_1^2l_2l_3+\\
+4F_Cl_1l_2^3+8F_Cl_1l_2^2l_3-4F_Cl_1l_2^2l_5-8F_Cl_1l_2l_3^2+16F_Cl_1l_2l_3l_4-4F_Cl_1l_2l_3l_5-\\
-4F_Cl_2^3l_5+16F_Dl_2l_3^2l_4+12F_Cl_2^2l_3^2-12F_Cl_2^2l_3l_4-4F_Dl_3^3l_4+16F_Cl_2^2l_3l_5-12F_Cl_2l_3^2l_4+\\
+4F_Dl_1^2l_2l_3+4F_Dl_1^2l_3^2-20F_Dl_1l_2^2l_3+12F_Dl_1l_2l_3^2-4F_Dl_1l_2l_3l_4+4F_Dl_1l_3^3)\mathbf{xy^3}+
\end{gathered}$$

$$\begin{gathered}
+(128c^2F_B^2F_C^2-128c^2F_B^2F_CF_D-8c^2F_B^2l_3^2+8c^2F_B^2l_3l_5-128c^2F_BF_C^3+128c^2F_BF_C^2F_D+\\
+8c^2F_BF_Cl_2l_3+8c^2F_BF_Dl_2l_3-8c^2F_BF_Dl_3^2-8c^2F_BF_Dl_3l_4-16c^2F_C^2l_2l_3+8c^2F_CF_Dl_2l_3+\\
+3l_1l_2^2l_3^2+8c^2F_CF_Dl_3^2-2c^2l_2^2l_3^2+2c^2l_2l_3^3+8ceF_B^2l_2l_3+2cel_2^3l_3-2cel_2^2l_3^2-2cel_2^2l_3l_6-\\
-32F_B^3F_Dl_1-32F_B^3F_Dl_2-32F_B^3F_Dl_3+32F_B^3F_Dl_4+32F_B^2F_CF_Dl_1+128F_B^2F_CF_Dl_2+\\
+32F_B^2F_CF_Dl_3-32F_B^2F_D^2l_3+16F_B^2l_1l_2l_3+8F_B^2l_2^2l_3-128F_BF_C^2F_Dl_2-32F_BF_C^2F_Dl_3+\\
+32F_BF_CF_D^2l_2+128F_BF_CF_D^2l_3-24F_BF_Cl_1l_2l_3-8F_BF_Cl_2^2l_3+32F_BF_D^3l_3+8F_BF_Dl_1l_2l_3+\\
+16F_BF_Dl_1l_3^2+8F_BF_Dl_2l_3^2+32F_C^3F_Dl_2-32F_C^2F_D^2l_2-32F_C^2F_D^2l_3+16F_C^2l_1l_2l_3-l_2^2l_3^3-\\
-8F_C^2l_2^2l_3+3l_2^2l_3^2l_4+8F_C^2l_2^2l_4-8F_C^2l_2l_3l_4+32F_CF_D^3l_3-8F_CF_Dl_1l_2l_3-8F_CF_Dl_1l_3^2-\\
-16F_CF_Dl_2l_3^2+3l_2^2l_3^2l_5-8F_CF_Dl_2l_3l_4+8F_CF_Dl_3^2l_4+8F_D^2l_1l_2l_3+8F_D^2l_1l_3^2-16F_D^2l_2l_3^2+\\
+8F_D^2l_3^3+l_1^3l_2l_3-2l_1^2l_2^2l_3-2l_1^2l_2l_3^2-l_1^2l_2l_3l_4-l_1^2l_2l_3l_5+l_1l_2^3l_3-l_1l_2^2l_3l_4-l_2l_3^3l_4-l_2l_3^2l_4l_5+\\
+2l_1l_2^2l_3l_5+l_1l_2l_3^3+2l_1l_2l_3^2l_4-l_1l_2l_3^2l_5+l_1l_2l_3l_4l_5-l_2^3l_3^2-l_2^3l_3l_5-l_2^2l_3l_4l_5-2l_2^2l_3^2l_6)\mathbf{y^4}+
\end{gathered}$$

$$\begin{gathered}
+(32aF_B^4l_2-32aF_B^4l_4-64aF_B^3F_Cl_2-32aF_B^3F_Dl_3+32aF_B^2F_C^2l_2+32aF_B^2F_CF_Dl_2+\\
+32aF_B^2F_CF_Dl_3-32aF_BF_C^2F_Dl_2+32aF_BF_CF_D^2l_3+256cF_B^3F_CF_D-256cF_B^2F_C^2F_D-\\
-32cF_B^2F_Cl_2l_3-16cF_B^2F_Dl_2l_3+16cF_B^2F_Dl_3l_4+16cF_BF_C^2l_2l_3-32cF_BF_CF_Dl_2l_3+\\
+16cF_BF_D^2l_3^2+16cF_C^3l_2l_3-32cF_C^2F_Dl_2l_3+16cF_CF_D^2l_2l_3)\mathbf{x^3}+
\end{gathered}$$

$$\begin{gathered}
+(8aF_B^3l_1l_2-16aF_B^3l_2^2+16aF_B^3l_2l_4-8aF_B^2F_Cl_1l_2+48aF_B^2F_Cl_2^2-8aF_B^2F_Dl_1l_3-\\
-56aF_BF_C^2l_2^2+24aF_C^3l_2^2-48aF_BF_CF_Dl_2l_3-8aF_BF_D^2l_2l_3+32aF_BF_D^2l_3^2+24aF_D^3l_3^2+\\
+24aF_C^2F_Dl_2l_3-48aF_CF_D^2l_2l_3-24aF_CF_D^2l_3^2-64cF_B^2F_C^2l_2-128cF_B^2F_CF_Dl_2-\\
-64cF_B^2F_CF_Dl_3+64cF_BF_C^3l_2+128cF_BF_C^2F_Dl_2+64cF_BF_C^2F_Dl_3-64cF_BF_CF_D^2l_3+\\
+8cF_D^2l_3^3+8cF_BF_Dl_2^2l_3-8cF_BF_Dl_2l_3l_4+16cF_C^2l_2^2l_3-24cF_C^2l_2l_3l_4-4cF_CF_Dl_2^2l_3-\\
-20cF_CF_Dl_2l_3^2+12cF_CF_Dl_2l_3l_4+12cF_CF_Dl_3^2l_4)\mathbf{x^2y}+
\end{gathered}$$

$$\begin{gathered}
+(32aF_B^4l_2-32aF_B^4l_4-64aF_B^3F_Cl_2-32aF_B^3F_Dl_3+32aF_B^2F_C^2l_2+32aF_B^2F_CF_Dl_2+\\
+32aF_B^2F_CF_Dl_3-8aF_B^2l_1l_2^2+8aF_B^2l_1l_2l_3-8aF_B^2l_2^2l_3+8aF_B^2l_2^2l_5+8aF_B^2l_2l_3l_4-\\
-32aF_BF_C^2F_Dl_2+32aF_BF_CF_D^2l_3+16aF_BF_Cl_1l_2^2-8aF_BF_Cl_1l_2l_3+24aF_BF_Cl_2^2l_3-\\
-16aF_BF_Cl_2^2l_5-8aF_BF_Dl_1l_2l_3-16aF_BF_Dl_1l_3^2-8aF_BF_Dl_2^2l_3-8aF_BF_Dl_2l_3^2+
\end{gathered}$$

$$
\begin{gathered}
+16aF_BF_Dl_3^2l_4-8aF_C^2l_1l_2^2+8aF_C^2l_1l_2l_3-24aF_C^2l_2^2l_3+8aF_C^2l_2^2l_5-8aF_C^2l_2l_3l_4+\\
+8aF_CF_Dl_1l_2l_3+24aF_CF_Dl_2^2l_3+32aF_CF_Dl_2l_3^2-8aF_CF_Dl_2l_3l_4-8aF_D^2l_1l_3^2-\\
-24aF_D^2l_2l_3^2-8aF_D^2l_3^3+8aF_D^2l_3^2l_4+256cF_B^3F_CF_D-256cF_B^2F_C^2F_D-32cF_B^2F_Cl_2l_3-\\
-16cF_B^2F_Dl_2l_3+16cF_B^2F_Dl_3l_4+64cF_BF_C^2l_2^2+16cF_BF_C^2l_2l_3-96cF_BF_CF_Dl_2l_3+\\
+16cF_BF_D^2l_3^2+4cF_Bl_2^2l_3^2-4cF_Bl_2^2l_3l_5-64cF_C^3l_2^2+16cF_C^3l_2l_3+96cF_C^2F_Dl_2l_3+\\
+16cF_CF_D^2l_2l_3-64cF_CF_D^2l_3^2-4cF_Cl_2^3l_3-4cF_Cl_2^2l_3^2+4cF_Cl_2^2l_3l_4-4cF_Cl_2l_3^2l_4+\\
+8cF_Dl_2^2l_3^2-4cF_Dl_2l_3^2l_4+4cF_Dl_3^3l_4)\mathbf{xy^2}+
\end{gathered}
$$

$$
\begin{gathered}
+(8aF_B^3l_1l_2+16aF_B^3l_2^2-16aF_B^3l_2l_4-8aF_B^2F_Cl_1l_2-48aF_B^2F_Cl_2^2-8aF_B^2F_Dl_1l_3+\\
+16aF_BF_CF_Dl_2l_3-8aF_BF_D^2l_2l_3-32aF_BF_D^2l_3^2+4aF_Bl_1l_2l_3^2-2aF_Bl_1l_2l_3l_4+\\
+2aF_Bl_1l_2l_3l_5-2aF_Bl_2^3l_3+2aF_Bl_2^2l_3^2-2aF_Bl_2^2l_3l_5+2aF_Bl_2^2l_3l_6+2aF_Bl_2l_3^2l_4-\\
-8aF_C^3l_2^2-8aF_C^2F_Dl_2l_3+16aF_CF_D^2l_2l_3+8aF_CF_D^2l_3^2-2aF_Cl_1l_2l_3^2+2aF_Cl_2^3l_3-\\
-4aF_Cl_2^2l_3^2+2aF_Cl_2^2l_3l_4-2aF_Cl_2^2l_3l_5+2aF_Cl_2l_3^2l_4-8aF_D^3l_3^2+2aF_Dl_1l_2l_3^2+\\
+2aF_Dl_2l_3^3-2aF_Dl_2l_3^2l_4-64cF_B^2F_C^2l_2+128cF_B^2F_CF_Dl_2-64cF_B^2F_CF_Dl_3-\\
+64cF_BF_C^2F_Dl_3-64cF_BF_CF_D^2l_3+16cF_BF_Cl_2^2l_3-8cF_BF_Dl_2^2l_3-8cF_D^2l_3^3+\\
+8cF_C^2l_2l_3l_4-4cF_CF_Dl_2^2l_3+12cF_CF_Dl_2l_3^2-4cF_CF_Dl_2l_3l_4-4cF_CF_Dl_3^2l_4+\\
-128cF_BF_C^2F_Dl_2+8cF_BF_Dl_2l_3l_4+64cF_BF_C^3l_2+40aF_BF_C^2l_2^2+\\
+cl_2^3l_3^2+cl_2^2l_3^3+cl_2^2l_3^2l_4-2cl_2^2l_3^2l_5+cl_2l_3^3l_4)\mathbf{y^3}+
\end{gathered}
$$

$$
+32l_2l_3F_BF_CF_D(F_B-F_C+F_D)(\mathbf{x^2}+\mathbf{y^2})=0
$$

https://doi.org/10.31896/k.25.4
Original scientific paper
Accepted 3. 11. 2021.

Marija Šimić Horvath
Vladimir Volenec

On Diagonal Triangle of Non Cyclic Quadrangle in Isotropic Plane

On Diagonal Triangle of Non Cyclic Quadrangle in Isotropic Plane

ABSTRACT

Geometry of the non cyclic quadrangle in the isotropic plane was introduced in [2] and [6]. Herein, its diagonal triangle is studied and some nice properties of it are given.

Key words: isotropic plane, non cyclic quadrangle, diagonal triangle

MSC2010: 51N25

Dijagonalni trokut netetivnog četvreovrha u izotropnoj ravnini

SAŽETAK

Geometrija netetivnog četverovrha u izotropnoj ravnini uvedena je u člancima [2] and [6]. Ovdje se proučava dijagonalni trokut i daju se neka njegova lijepa svojstva.

Ključne riječi: izotropna ravnina, netetivni četverovrh, dijagonalni trokut

1 Introduction

The isotropic plane is a real projective metric plane where metric is induced by figure consisting of an *absolute point* Ω and an *absolute line* ω incident to it. If $T = (x_0 : x_1 : x_2)$ denotes any point in the plane presented in homogeneous coordinates then usually a projective coordinate system where $\Omega = (0:1:0)$ and the line ω with the equation $x_2 = 0$ is chosen.

Isotropic points are the points incident with the absolute line ω and the *isotropic lines* are the lines passing through the absolute point Ω.

Metric quantities and all the notions related to the geometry of the isotropic plane can be found in [5] and [4]. Now, we recall few facts that will be used further on wherein we assume that $x = \dfrac{x_0}{x_2}$ and $y = \dfrac{x_1}{x_2}$.

Two lines are *parallel* if they have the same isotropic point, and two points are *parallel* if they are incident with the same isotropic line.

For two non parallel points $T_1 = (x_1, y_1)$ and $T_2 = (x_2, y_2)$, a *distance* between them is defined as $d(T_1, T_2) := x_2 - x_1$. In the case of parallel points $T_1 = (x, y_1)$ and $T_2 = (x, y_2)$, a *span* is defined by $s(T_1, T_2) := y_2 - y_1$. Both quantities are directed.

Two non isotropic lines p_1 and p_2 in the isotropic plane can be given by $y = k_i x + l_i, \quad k_i, l_i \in \mathbb{R}, i = 1,2$, labelled by $p_i = (k_i, l_i), \quad i = 1,2$ in line coordinates. Therefore, the angle formed by p_1 and p_2 is defined by $\varphi = \angle(p_1, p_2) := k_2 - k_1$, being directed as well. Any two points $T_1 = (x_1, y_1)$ and $T_2 = (x_2, y_2)$ have the midpoint $M = \left(\dfrac{1}{2}(x_1 + x_2), \dfrac{1}{2}(y_1 + y_2)\right)$ and any two lines with the equations $y = k_i x + l_i \quad (i = 1,2)$ have the bisector with the equation $y = \dfrac{1}{2}(k_1 + k_2)x + \dfrac{1}{2}(l_1 + l_2)$.

A triangle in the isotropic plane is called *allowable* if none of its sides is isotropic (see [3]).

The classification of conics in the isotropic plane can be found in [1] and [4]. To recall, the *circle* in the isotropic plane is the conic touching the absolute line ω at the absolute point Ω. The equation of such a circle is given by $y = ux^2 + vx + w, \quad u \neq 0, \quad u, v, w \in \mathbb{R}$.

As the principle of duality is valid in the projective plane, it is preserved in the isotropic plane as well.

2 Non cyclic quadrangle in isotropic plane

We consider a complete quadrangle $ABCD$ in the isotropic plane. The points A,B,C,D are the *vertices* of the quadrangle, and lines AB,AC,AD,BC,BD,CD stand for the *sides* of the quadrangle $ABCD$. The pairs of sides AB,CD; AC,BD and AD,BC are called the *opposite sides*. There is exactly one conic incident to five points A,B,C,D and Ω. If that conic touches the absolute line ω at the point Ω, the conic is a circle and the considered quadrangle $ABCD$ is the *cyclic quadrangle*. In the case, when the conic intersects the line ω at the point Ω and residually at the point Γ (different from Ω), then the conic is a special hyperbola circumscribed to the quadrangle $ABCD$. In this case, the quadrangle $ABCD$ is called a *non cyclic quadrangle*. More on the geometry of such quadrangle is given in [2] and [6]. Let us denote the circumscribed special hyperbola by $\mathcal{H}$. Tangents to $\mathcal{H}$ at points Ω and Γ are the asymptotes of this special hyperbola, δ is the isotropic one and γ is a non-isotropic line. The intersection point S of lines δ and γ is the center of hyperbola $\mathcal{H}$. Without loss of generality affine coordinate system can be chosen in a way: S is the origin, and γ and δ stand for the coordinate axes. Although the right angle does not have any geometric sense in the isotropic plane, in the Euclidean model of the isotropic plane the coordinate system is presented as the rectangular one. Hence, due to [2] the following is valid:

Theorem 1 *Any non cyclic quadrangle ABCD, by the appropriate choice of an affine coordinate system, has the vertices given with*

$$A=\left(a,\frac{1}{a}\right),B=\left(b,\frac{1}{b}\right),C=\left(c,\frac{1}{c}\right),D=\left(d,\frac{1}{d}\right), \quad (1)$$

sides of the form

$$\begin{aligned}
AB\ldots y&=-\frac{1}{ab}x+\frac{a+b}{ab},\\
AC\ldots y&=-\frac{1}{ac}x+\frac{a+c}{ac},\\
AD\ldots y&=-\frac{1}{ad}x+\frac{a+d}{ad},\\
BC\ldots y&=-\frac{1}{bc}x+\frac{b+c}{bc},\\
BD\ldots y&=-\frac{1}{bd}x+\frac{b+d}{bd},\\
CD\ldots y&=-\frac{1}{cd}x+\frac{c+d}{cd},
\end{aligned} \quad (2)$$

and the circumscribed special hyperbola with the equation

$$xy=1. \quad (3)$$

For such quadrangle $ABCD$ from Theorem 1 it is said to be in *standard position* or it is a *standard quadrangle*. Due to Theorem 1 every non cyclic quadrangle can be represented in the standard position. So, it is sufficient to prove the properties for the standard quadrangle.
The following symmetric functions of numbers a,b,c,d will be of great benefit:

$$\begin{aligned}
s&=a+b+c+d,\\
q&=ab+ac+ad+bc+bd+cd,\\
r&=abc+abd+acd+bcd,\\
p&=abcd.
\end{aligned} \quad (4)$$

The study so far ([2]) has shown several facts:
Euler circle of the triangle ABC (see [3]) is given by

$$\mathcal{E}_D\ldots abcy=-2x^2+(a+b+c)x. \quad (5)$$

Because of symmetry on a,b,c,d circles $\mathcal{E}_A$, $\mathcal{E}_B$, $\mathcal{E}_C$ are easy to obtain.
Due to Theorem 2 in [2] Euler circles are intersected in one point $O=(0,0)$, *Euler center* of the non cyclic quadrangle $ABCD$.
In [2], the forms of circumscribed circles and inscribed circles of triangles BCD,ACD,ABD,ABC are obtained as well. On the example of the triangle ABC, its circumscribed circle is

$$\mathcal{O}_d\ldots abcy=x^2-(a+b+c)x+bc+ca+ab, \quad (6)$$

and its inscribed circle is given by

$$\mathcal{U}_d\ldots 4abcy=x^2-2(a+b+c)x+(a+b+c)^2. \quad (7)$$

For the triangle ABC, the radical axis of $\mathcal{O}_D$ and $\mathcal{E}_D$ is an *orthic* of that triangle,

$$\mathcal{H}_d\ldots 3abcy=-(a+b+c)x+2(bc+ca+ab). \quad (8)$$

Theorem 2 *The median of the quadrilateral formed by the orthics of triangles BCD,CDA,DAB,ABC of the standard quadrangle has the equation*

$$\mathcal{H}\ldots y=-\frac{s}{3r}x+\frac{r}{3p}. \quad (9)$$

The principle of duality is preserved in the isotropic plane and due to [2] the *medial point* and the *focal line* of the non cyclic quadrangle are obtained as well:

Theorem 3 *Bisectors of the pairs of opposite sides of the non cyclic quadrangle are passing through the one point*

$$N=\left(0,\frac{r}{2p}\right). \quad (10)$$

The point N from Theorem 3 is called a *medial point* of the standard quadrangle.
The common tangent of the inscribed circles $\mathcal{U}_d,\mathcal{U}_c,\mathcal{U}_d$ and $\mathcal{U}_a$ of the triangles ABC,ABD,ACD,BCD is a *focal line* of the quadrangle $ABCD$ with equation

$$\mathcal{M}\ldots y=0. \quad (11)$$

3 On diagonal triangle of standard non cyclic quadrangle

In this chapter we study diagonal triangle of the standard non cyclic quadrangle in the isotropic plane. The vertices of such diagonal triangle are intersection points of the opposite sides of quadrangle $T_{AB,CD} = AB \cap CD$, $T_{AC,BD} = AC \cap BD$ te $T_{AD,BC} = AD \cap BC$. The joint lines of these points are sides of diagonal triangle: $\mathcal{T}_{AB,CD} = T_{AC,BD}T_{AD,BC}$, $\mathcal{T}_{AC,BD} = T_{AB,CD}T_{AD,BC}$ and $\mathcal{T}_{AD,BC} = T_{AB,CD}T_{AC,BD}$.
The following theorems give the forms of vertices and sides of the diagonal triangle.

Theorem 4 *The vertices of the diagonal triangle of the standard quadrangle ABCD are given by*

$$T_{AB,CD} = \left(\frac{ab(c+d)-cd(a+b)}{ab-cd}, \frac{a+b-c-d}{ab-cd}\right),$$
$$T_{AC,BD} = \left(\frac{ac(b+d)-bd(a+c)}{ac-bd}, \frac{a+c-b-d}{ac-bd}\right),$$
$$T_{AD,BC} = \left(\frac{ad(b+c)-bc(a+d)}{ad-bc}, \frac{a+d-b-c}{ad-bc}\right). \tag{12}$$

Proof. Following equalities

$$ab(a+b-c-d) = (a+b)(ab-cd)+cd(a+b)-ab(c+d),$$

$$cd(a+b-c-d) = (c+d)(ab-cd)+cd(a+b)-ab(c+d)$$

prove that $T_{AB,CD}$ is the intersection point of the sides AB and CD. □

Theorem 5 *The diagonal triangle of the standard quadrangle ABCD has the sides*

$$\mathcal{T}_{AB,CD} \ldots [cd(a+b)-ab(c+d)]y = (a+b-c-d)x- \\ -2(ab-cd),$$
$$\mathcal{T}_{AC,BD} \ldots [bd(a+c)-ac(b+d)]y = (a+c-b-d)x- \\ -2(ac-bd),$$
$$\mathcal{T}_{AD,BC} \ldots [bc(a+d)-ad(b+c)]y = (a+d-b-c)x- \\ -2(ad-bc). \tag{13}$$

Proof. According to

$$(a-b+c-d)[cd(a+b)-ab(c+d)] = \\ -2(ab-cd)(ac-bd) \\ +(a+b-c-d)[ac(b+d)-bd(a+c)],$$

and

$$(a-b-c+d)[cd(a+b)-ab(c+d)] = \\ -2(ab-cd)(ad-bc) \\ +(a+b-c-d)[ad(b+c)-bc(a+d)]$$

points $T_{AC,BD}$ and $T_{AD,BC}$ are incident to the side $\mathcal{T}_{AB,CD}$. □

Theorem 6 *The circle $\mathcal{K}_D$ circumscribed to the diagonal triangle has the equation*

$$\mathcal{K}_D \ldots [ab(c+d)-cd(a+b)][ac(b+d)-bd(a+c)]\cdot \\ \cdot[bc(a+d)-ad(b+c)]y = 2(ab-cd)(ac-bd)(ad-bc)x^2 \\ +\{a^2b^2c^2(a+b+c)+a^2b^2d^2(a+b+d) \\ +a^2c^2d^2(a+c+d)+b^2c^2d^2(b+c+d)-2p[ab(a+b) \\ +ac(a+c)+ad(a+d)+bc(b+c)+bd(b+d) \\ +cd(c+d)]+3pr]\}x \tag{14}$$

The proof of the Theorem 6 is very similar to one in Theorem 5.

Corollary 1 *The circumscribed circle $\mathcal{K}_D$ is incident to Euler's center of the standard quadrangle.*

Figure 1 presents the non cyclic quadrangle with its diagonal triangle and illustrates Corollary 1 as well.

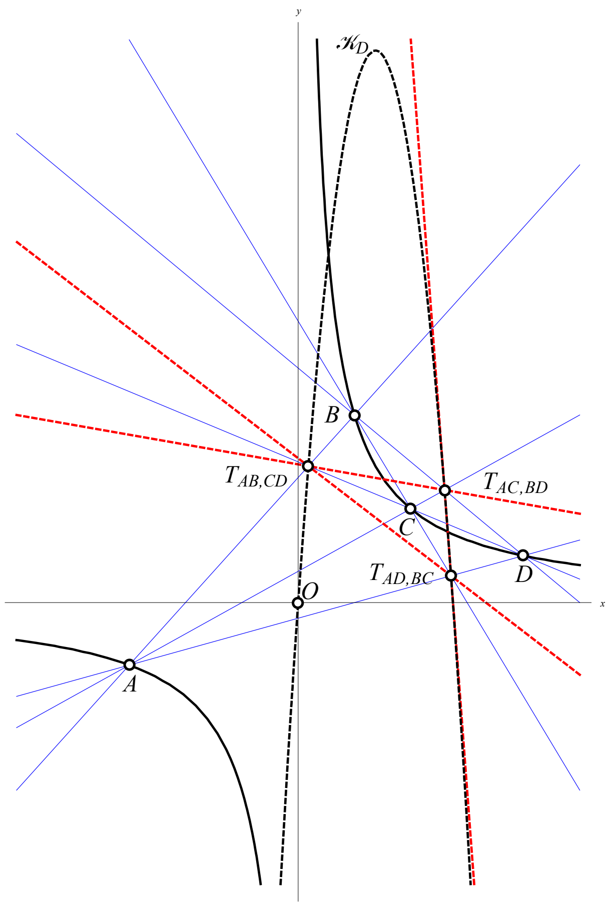

Figure 1: *Non cyclic quadrangle with its diagonal triangle*

Theorem 7 *If we join the points parallel to the vertices A,B,C,D and incident to the sides of the diagonal triangle $\mathcal{T}_{AB,CD}$, $\mathcal{T}_{AC,BD}$, $\mathcal{T}_{AB,CD}$ to the diagonal points $T_{AB,CD}$, $T_{AC,BD}$, $T_{AD,BC}$ of the standard quadrangle ABCD, then they form four lines in a group $\mathcal{A}_B,\mathcal{B}_A$, $\mathcal{C}_D,\mathcal{D}_C$; $\mathcal{A}_C,\mathcal{B}_D,\mathcal{C}_A,\mathcal{D}_B$; $\mathcal{A}_D,\mathcal{B}_C,\mathcal{C}_B,\mathcal{D}_A$. If $\mathcal{A},\mathcal{B},\mathcal{C},\mathcal{D}$ are tangents to the special hyperbola circumscribed to the standard quadrangle at points A,B,C,D then the quadraples of lines $\mathcal{A},\mathcal{B}_A$, $\mathcal{C}_A,\mathcal{D}_A$; $\mathcal{B},\mathcal{A}_B,\mathcal{C}_B,\mathcal{D}_B$; $\mathcal{C},\mathcal{A}_C,\mathcal{B}_C,\mathcal{D}_C$; $\mathcal{D},\mathcal{A}_D,\mathcal{B}_D,\mathcal{C}_D$ are incident to four points parallel to the medial point.*

Proof. The point

$$A_B=\left(a,\frac{a(a+b-c-d)-2(ab-cd)}{cd(a+b)-ab(c+d)}\right).$$

is obviously parallel to A and incident to $\mathcal{T}_{AB,CD}$ from (13). The line $\mathcal{A}_B$ is of the form

$$y=-\frac{ab-b^2+bc+bd-2cd}{b(abc+abd-acd-bcd)}x+\frac{2}{b}$$

and it is joint line of the points A_B and $T_{AB,CD}$ because of

$$\frac{a(a+b-c-d)-2(ab-cd)}{cd(a+b)-ab(c+d)}= -a\frac{ab-b^2+bc+bd-2cd}{b(abc+abd-acd-bcd)}+\frac{2}{b},$$

$$\frac{a+b-c-d}{ab-cd}=-\frac{ab-b^2+bc+bd-2cd}{b(ab-cd)}+\frac{2}{b}.$$

Analogously, lines $\mathcal{C}_B$ i $\mathcal{D}_B$

$$\mathcal{C}_B\ldots y=-\frac{bc-b^2+ab+bd-2ad}{b(abc+bcd-acd-abd)}x+\frac{2}{b},$$

$$\mathcal{D}_B\ldots y=-\frac{bd-b^2+bc+ab-2ac}{b(bcd+abd-acd-abc)}x+\frac{2}{b}.$$

obviously pass through the point $K_B=\left(0,\frac{2}{b}\right)$ parallel to the medial point $N=\left(0,\frac{r}{2p}\right)$. The line $\mathcal{B}$ given by $y=-\frac{1}{b^2}x+\frac{2}{b}$ is incident to the point K_B as well. □

Theorem 8 *The circle that touches the focal line and the side AB at the point A has the common tangents to the circle $\mathcal{U}_a$ consisting of the focal line and the line that passes through the diagonal point $T_{AB,CD}$. There are twelwe such lines where each four of them pass through each diagonal points $T_{AB,CD},T_{AC,BD},T_{AD,BC}$.*

Proof. The circle $\mathcal{U}_a$ similar to (7)

$$4bcdy=x^2-2(b+c+d)x+(b+c+d)^2,$$

and a circle

$$4ab^2y=x^2-2(a+2b)x+a^2+4ab+b^2 \tag{15}$$

have the common tangents, the focal line and the line with equation

$$y=\frac{c+d-a-b}{b(ab-cd)}x+ +\frac{(a+b-c-d)(ab^2+abc+abd-acd-2bcd)}{b(ab-cd)^2}. \tag{16}$$

Indeed, the equalities

$$4bcd\frac{(a+b-c-d)(ab^2+abc+abd-acd-2bcd)}{b(ab-cd)^2}+ +4bcd\frac{(-a-b+c+d)x}{b(ab-cd)}=x^2-2(b+c+d)x+(b+c+d)^2,$$

i.e.

$$\left(x-\frac{ab^2+abc+abd-2acd-3bcd+c^2d+cd^2}{ab-cd}\right)^2=0$$

and

$$x^2-2(a+2b)x+a^2+4ab+4b^2= =4ab^2\left(\frac{(-a-b+c+d)x}{b(ab-cd)} +\frac{(a+b-c-d)(ab^2+abc+abd-acd-2bcd)}{b(ab-cd)^2}\right),$$

respectively,

$$\left(x-\frac{-a^2b+2bc+2abd-acd-2bcd}{ab-cd}\right)^2=0$$

show that the line (16) touches the circle $\mathcal{U}_a$ and the circle (15) as well.
Furthermore, out of

$$\frac{a+b-c-d}{ab-cd}= =\frac{(a+b-c-d)(ab^2+abc+abd-acd-2bcd)}{b(ab-cd)^2} +\frac{(-a-b+c+d)[ab(c+d)-cd(a+b)]}{b(ab-cd)^2}$$

it follows that the diagonal point $T_{AB,CD}$ is incident to the line (16).
It is easy to prove that the line AB touches the circle (15) exactly at the point A. □

Theorem 9 *The intersection points of the bisectors of the angles of the diagonal triangle of the standard quadrangle ABCD are incident to its circumscribed special hyperbola.*

Proof. It is easy to show that the bisector at the vertex $T_{AB,CD}$ from (12) of the lines $\mathcal{T}_{AC,BD}$ and $\mathcal{T}_{AD,BC}$ given in (13) is of the form

$$\mathcal{S}_{AB,CD}\dots y=\left\{\frac{a+c-b-d}{2[bd(a+c)-ac(b+d)]}+\frac{a+d-b-c}{2[bc(a+d)-ad(b+c)]}\right\}x+\frac{ab(a+b)(c-d)^2-cd(c+d)(a-b)^2}{a^2b^2(c-d)^2-c^2d^2(a-b)^2}.$$

Analogously, there are two more bisectors

$$\mathcal{S}_{AC,BD}\dots y=\left\{\frac{a+b-c-d}{2[cd(a+b)-ab(c+d)]}+\frac{a+d-b-c}{2[bc(a+d)-ad(b+c)]}\right\}x+\frac{ac(a+c)(b-d)^2-bd(b+d)(a-c)^2}{a^2c^2(b-d)^2-b^2d^2(a-c)^2},$$

$$\mathcal{S}_{AD,BC}\dots y=\left\{\frac{a+c-b-d}{2[bd(a+c)-ab(c+d)]}+\frac{a+b-c-d}{2[cd(a+b)-ab(c+d)]}\right\}x+\frac{ad(a+d)(b-c)^2-bc(b+c)(a-d)^2}{a^2d^2(b-c)^2-b^2c^2(a-d)^2}.$$

The point of intersection $S_{AD,BC}=\mathcal{S}_{AB,CD}\cap\mathcal{S}_{AC,BD}$ is

$$S_{AD,BC}=\left(\frac{ad(b+c)-bc(a+d)}{ad-bc},\frac{ad-bc}{ad(b+c)-bc(a+d)}\right).$$

For example, the equality

$$\frac{ad-bc}{ad(b+c)-bc(a+d)}=\left\{\frac{a+b-c-d}{2[cd(a+b)-ab(c+d)]}+\frac{a+d-b-c}{2[bc(a+d)-ad(b+c)]}\right\}\frac{ad(b+c)-bc(a+d)}{ad-bc}+\frac{ac(a+c)(b-d)^2-bd(b+d)(a-c)^2}{a^2c^2(b-d)^2-b^2d^2(a-c)^2}$$

proves that $S_{AD,BC}$ is incident to the bisector $\mathcal{S}_{AC,BD}$. Because of symmetry a,b,c,d there are two more similar intersections

$$S_{AC,BD}=\left(\frac{ac(b+d)-bd(a+c)}{ac-bd},\frac{ac-bd}{ac(b+d)-bd(a+c)}\right),$$
$$S_{AB,CD}=\left(\frac{ab(c+d)-cd(a+b)}{ab-cd},\frac{ab-cd}{ab(c+d)-cd(a+b)}\right).$$

Obviously, they all lie on the special hyperbola $xy=1$. □

All Theorems 7-9 have no analogous in Euclidean plane.

References

[1] J. BEBAN-BRKIĆ, M. ŠIMIĆ, V. VOLENEC, On Foci and Asymptotes of Conics in Isotropic Plane, *Sarajevo J. Math.* **3**(16) (2007), 257–266.

[2] J. BEBAN-BRKIĆ, M. ŠIMIĆ , V. VOLENEC, On some properties of non-cyclic quadrangle in isotropic plane, *Proceedings of 13th International Conference on Geometry and Graphics*, Dresden, 2008.

[3] R. KOLAR-ŠUPER, Z. KOLAR-BEGOVIĆ, V. VOLENEC, J. BEBAN-BRKIĆ, Metrical relationships in standard triangle in an isotropic plane, *Math. Commun.* **10** (2005), 159–167.

[4] H. SACHS, *Ebene isotrope Geometrie*, Vieweg-Verlag, Braunschweig-Wiesbaden, 1987.

[5] K. STRUBECKER, Geometrie in einer isotropen Ebene, *Math. Naturwiss. Unterr.* **15** (1962-63), 297–306, 343–351, 385–394.

[6] M. ŠIMIĆ, V. VOLENEC, J. BEBAN-BRKIĆ, On umbilic axes of circles of the non-cyclic quadrangle in the isotropic plane, *Math. Pannon.* **21**(2) (2010), 1–12.

Marija Šimić Horvath
orcid.org/0000-0001-9190-5371
e-mail: msimic@arhitekt.hr

Faculty of Architecture, University of Zagreb
Kačićeva 26, HR-10000 Zagreb, Croatia

Vladimir Volenec
orcid.org/0000-0001-7418-8972
e-mail: volenec@math.hr

Faculty of Science, University of Zagreb
Bijenička cesta 30, HR-10000 Zagreb, Croatia

https://doi.org/10.31896/k.25.5
Original scientific paper
Accepted 18. 11. 2021.

MILENA STAVRIĆ
ALBERT WHILSCHE
GUNTER WEISS

Polyhedrons the Faces of which are Special Quadric Patches

Polyhedrons the Faces of which are Special Quadric Patches

ABSTRACT

We seize an idea of Oswald Giering (see [1] and [2]), who replaced pairs of faces of a polyhedron by patches of hyperbolic paraboloids and link up edge-quadrilaterals of a polyhedron with the pencil of quadrics determined by that quadrilateral. Obviously only ruled quadrics can occur. There is a simple criterion for the existence of a ruled hyperboloid of revolution through an arbitrarily given quadrilateral. Especially, if a (not planar) quadrilateral allows one symmetry, there exist two such hyperboloids of revolution through it, and if the quadrilateral happens to be equilateral, the pencil of quadrics through it contains even three hyperboloids of revolution with pairwise orthogonal axes. To mention an example, for right double pyramids, as for example the octahedron, the axes of the hyperboloids of revolution are, on one hand, located in the plane of the regular guiding polygon, and on the other, they are parallel to the symmetry axis of the double pyramid.

Not only for platonic solids, but for all polyhedrons, where one can define edge-quadrilaterals, their pairs of face-triangles can be replaced by quadric patches, and by this one could generate roofing of architectural relevance. Especially patches of hyperbolic paraboloids or, as we present here, patches of hyperboloids of revolution deliver versions of such roofing, which are also practically simple to realize.

Key words: polyhedron, quadric, hyperboloid of revolution, Bézier patch

MSC2010: 51Mxx, (51M20, 51M30), 51N05, 51N20, 15Axx

Poliedri čije su strane dijelovi posebnih kvadrika

SAŽETAK

Preuzimamo ideju Oswalda Gieringa (vidi [1] i [2]), koji je par strana poliedra zamijenio dijelom hiperboličnog paraboloida i povezao bridni četverostran poliedra s pramenom kvadrika određenim tim četverostranom. Očito se samo pravčaste kvadrike mogu pojaviti. Postoji jednostavan nužan uvjet postojanja pravčastog rotacijskog hiperboloida kroz dani četverostran. Posebno, ako (prostorni) četverostran ima jednu ravninu simetrije, onda postoje dva rotacijska hiperboloida kroz njega, a ako je četverostran jednakostraničan, onda pramen kvadrika kroz njega sadrži čak tri rotacijska hiperboloida s međusobno okomitim osima. Na primjer, kod pravilne dvostruke piramide, kao što je oktaedar, osi rotacijskih hiperboloida su, s jedne strane, u ravnini pravilnog mnogokuta (osnovke), a s druge strane, su usporedne s osi simetrije dvostruke piramide.

Parove strana (trokute) ne samo Platonovih tijela, već svih poliedara kod kojih se mogu definirati bridni četverostrani, moguće je zamijeniti dijelovima kvadrika, i na taj način proizvesti krovišta od arhitektonskog značaja. Posebno zanimljiva krovišta mogu nastati primjenom dijelova hiperboličnih paraboloida, ili kao što je ovdje prikazano, rotacijskih hiperboloida koje je jednostavno i realizirati u praksi.

Ključne riječi: poliedar, kvadrika, rotacijski hiperboloid, Bézierova zakrpa

Excerpt of what we aim to present in the following chapters

Chapter 1 deals with the regular octahedron $\mathfrak{p}$ as a standard example and replace pairs of triangles by quadric patches. Here we can already show the principle of how to proceed. Among the pencil of quadrics through an edge quadrilateral of $\mathfrak{p}$ we look for the hyperbolic paraboloid ("HP-surface") and for hyperboloids of revolution ("R-hyperboloids"). It turns out that descriptive geometric methods highly support an analytic treatment of the problem.

In Chapter 2 we deal with a criterion for quadrilaterals, which are generators of an R-hyperboloid. For a quadrilateral fulfilling the criterion we give a construction of the axis and the skirt circle of an R-hyperboloid through it as well as analytic descriptions of the R-hyperboloid by its equation and as a tensor-product patch ("TP-patch"). Additionally, we also ask for the set of R-hyperboloids through two skew given lines. This set is, to some extent, a 3D-generalisation of a (planar) elliptic pencil of circles.

The third chapter concerns polyhedrons $\mathfrak{p}$, the faces of which are n-gons ($n > 3$). By adding pyramids of a certain height h to these faces one can interpret the original polyhedron $\mathfrak{p}$ as the limit of the set of polyhedrons $\mathfrak{p}(h)$ for $h \to 0$. This gives a more "natural" set of edge-quadrilaterals than that proposed by Giering [1] and [2] for the cube. We apply this way of splitting an n-gon-face into triangles for e.g. a box shaped polyhedron. Finally we show images of some Johnson polyhedrons with R-hyperboloid patches as faces.

Concluding we note that Giering's idea to replace pairs of planar faces by HP-surfaces works for any polyhedron, while R-hyperboloids exist only for edge-quadrilaterals fulfilling the criterion mentioned in Chapter 2. Anyway, by choosing a certain quadric out of the pencil of quadrics through an edge-quadrilateral and describe it as a TP-patch one wins an additional design parameter, what works for all polyhedrons independent from the criterion. This could be of relevance for architectural design, too.

1 The regular octahedron and its R-hyperboloid faces

We connect a Cartesian frame with the regular octahedron $\mathfrak{p} = \{A,B,C,D,E,F\}$ such that its midpoint becomes the origin O and one of its diagonals becomes the z-axis. The x- and y-axes are parallel to edges BC and AB (Figure 1). We consider the (equilateral) edge-quadrilateral $\mathcal{H} = \{A,B,E,F\}$ and the pencil $\mathfrak{Q}$ of quadrics $\Phi(t)$ through it. Setting the edge length $\overline{AB} = \sqrt{2}$ we obtain the vertex coordinates $A = (\frac{\sqrt{2}}{2}, \frac{\sqrt{2}}{2}, 0)$, $B = (\frac{\sqrt{2}}{2}, -\frac{\sqrt{2}}{2}, 0)$, $E = (0,0,1)$, $F = (0,0,-1)$.

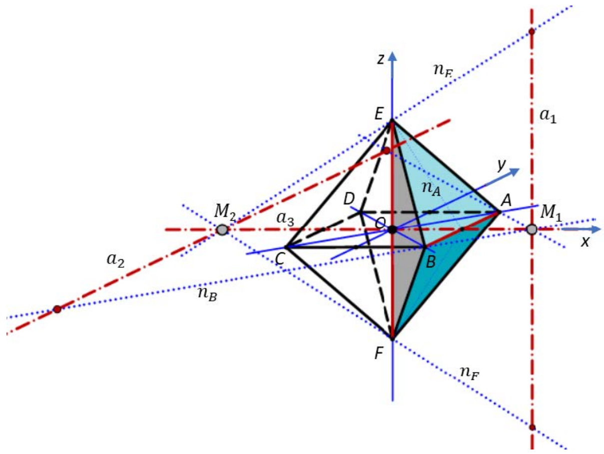

Figure 1: *The octahedron $\mathfrak{p}$, its edge-quadrilateral $\mathcal{H} = \{A,B,E,F\}$, and the normals $n\ldots$, which are common for all quadrics of the pencil $\mathfrak{Q}$ through $\mathcal{H}$. The lines a_1, a_2, a_3 (dashed red) represent the axes of three* R-*hyperboloids through $\mathcal{H}$.*

The pencil $\mathfrak{Q}$ is spanned by the pairs of face planes $\Phi_1 = (AEF) \cup (BEF)$ and $\Phi_2 = (ABE) \cup (ABF)$, such that a general ruled quadric $\Phi(t)$ can be written as

$$\Phi(t) = (1-t)\Phi_1 + t\Phi_2. \tag{1}$$

By the equations of Φ_1, Φ_2

$$\Phi_1 \ldots (x+y)(x-y) = 0,$$
$$\Phi_2 \ldots (z + (\sqrt{2}.x - 1))(z - (\sqrt{2}.x - 1)) = 0, \tag{2}$$

follows

$$\Phi(t) \ldots (1-t)(x^2 - y^2) + t(z^2 - 2x^2 - 2\sqrt{2}.x - 1) = 0. \tag{3}$$

We see immediately that for $t = \frac{1}{2}$ one gets the R-hyperboloid Φ_{R1}

$$\Phi_{R1} \ldots (x - \sqrt{2})^2 + y^2 - z^2 = 1, \tag{4}$$

and for $t = \frac{1}{4}$ the R-hyperboloid Φ_{R2}

$$\Phi_{R2} \ldots (x + \sqrt{2})^2 + z^2 - 3y^2 = 3. \tag{5}$$

For $t = \frac{1}{3}$ we obtain the hyperbolic paraboloid Φ_P

$$\Phi_P \ldots 2y^2 - z^2 - 2\sqrt{2}.x + 1 = 0. \tag{6}$$

These results (4), (5), and (6) verify what one already knows because of geometric properties of the pencil $\mathfrak{Q}$:

(a) The quadrics $\Phi(t)$ have the same symmetries as the quadrilateral $\mathcal{H}$. In our special case of $\mathcal{H}$ being equilateral, the planes xy and xz are symmetry planes. Therefore, the x-axis is a common axis of $\Phi(t)$. If $\Phi(t)$ is a hyperboloid with three axes, a second axis is parallel to EF, while the third one is parallel to AB.

(b) The diagonals of an arbitrarily given quadrilateral $\mathcal{H}$ are reciprocal polar lines for all quadrics $\Phi(t)$.

(c) The quadrics $\Phi(t)$ through $\mathcal{H}$ have the surface normals n_A, n_B, n_E, n_F at the vertices A, B, E, F in common. For an R-hyperboloid Φ_{Ri} all surface normals meet the rotation axis a_i. Therefore, a_i must of course intersect these special normals n_A, n_B, n_E, n_F. In the general case, when $\mathcal{H}$ has no symmetries, the normals n_A, n_B, n_E, n_F are pairwise skew, and we expect (in algebraic sense) two lines l_i, which meet these four lines. Such a line l_i is an axis of an R-hyperboloid, if and only if it includes the same angle with each of the four edges of $\mathcal{H}$.

Finally, we visualise the octahedron $\mathfrak{p}$ with its edge-quadrilateral $\mathcal{H}$ and the three R-hyperboloids Φ_{R1}, Φ_{R2}, Φ_{R3} though $\mathcal{H}$ in Figure 2, 3 and 4:

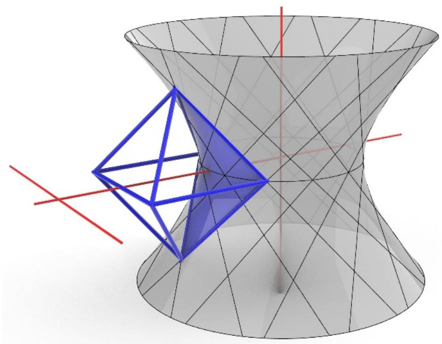

Figure 2: *R-hyperboloid Φ_{R1} through an edge-quadrilateral of an octahedron*

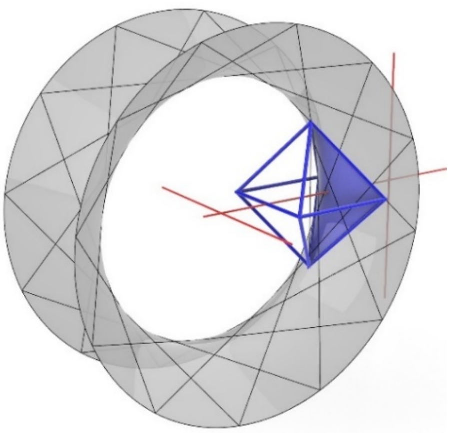

Figure 3: *R-hyperboloid Φ_{R2} through an edge-quadrilateral of an octahedron*

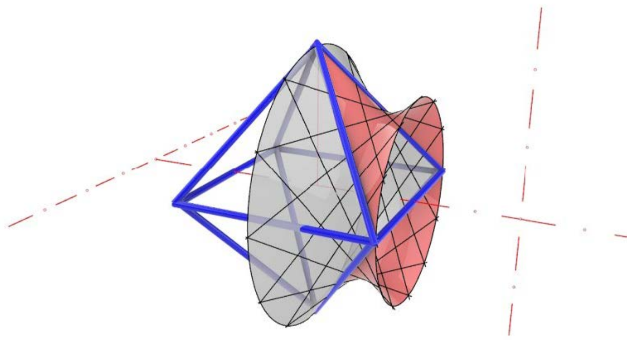

Figure 4: *R-hyperboloid Φ_{R3} through an edge-quadrilateral of an octahedron*

2 A criterion for quadrilaterals, which are generators of an R-hyperboloid

An arbitrarily given quadrilateral $\mathcal{H}$ consists of two pairs of skew generators (e_1,e_2), (f_1,f_2) of different reguli of the quadrics through $\mathcal{H}$. We look for properties of $\mathcal{H}$, such that there exists an R-hyperboloid Φ_R among the pencil of quadrics through $\mathcal{H}$, (we continue the numbering of properties of Chapter 1):

(d) Generators of an R-hyperboloid Φ_R include a fixed angle with its axis a and they are equidistant from a.

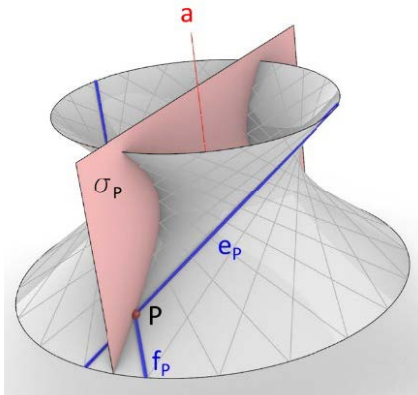

Figure 5: *One symmetry plane of two intersecting generators of an R-hyperboloid Φ_R contains the axis a of Φ_R.*

If we had a quadrilateral of generators on an R-hyperboloid Φ_R, then its normal projection in direction of the axis a of Φ_R yields a planar quadrilateral subscribed to the image of the circle of the gorge g. Because of property (d) yields, the lengths of the quadrilateral's edges are distorted by the same factor such that relations deduced for the lengths of edge images also hold for the situation in space.

There can occur different cases of such a normal projection, see Figures 6 and 7.

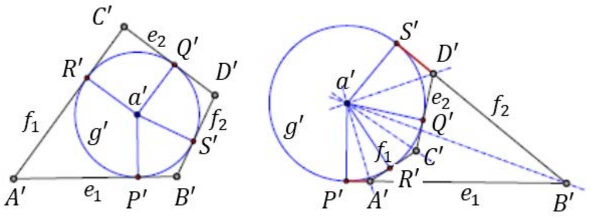

Figure 6: *Normal projection of a quadrilateral $\mathcal{H} = (ABCD)$ contained on an R-hyperboloid Φ_R; direction of projection parallel to the axis a of Φ_R*

For example, for the case shown in Figure 6, left, by adding segment lengths we obtain (see also [4])

$$\overline{A'B'}+\overline{C'D'}=\overline{A'C'}+\overline{B'D'} \iff |e_1|+|e_2|=|f_1|+|f_2|. \tag{7.1}$$

For the case shown in Figure 6, right, because of
$\overline{P'A'}=\overline{R'A'}$, $\overline{S'D'}=\overline{Q'D'}$ and
$\overline{A'B'}+\overline{P'A'}-\overline{S'D'}-\overline{D'B'}=0$ and
$\overline{C'D'}-\overline{Q'D'}-\overline{C'A'}+\overline{R'A'}=0$,
one derives

$$|e_1|-|e_2|=|f_1|-|f_2|. \tag{7.2}$$

In the left case in Figure 6 the R-hyperboloid does fill the interior of the quadrilateral, and therefore it is not suited for a TP-representation, because a TP-patch is contained in the interior of the convex hull of $\mathcal{H}$. (An f-generator passing to an inner point of segment e_1 cannot meet segment e_2 in an inner point, see Figure 6, left.)
A similar calculation shows that the cases shown in Figure 7 both lead to

$$|e_1|-|e_2|=|f_2|-|f_1|. \tag{7.3}$$

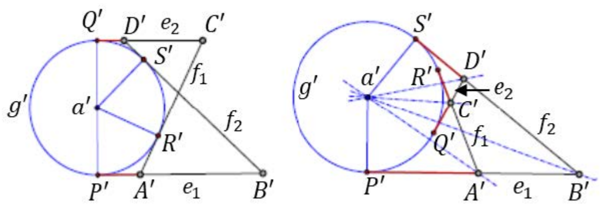

Figure 7: *Additional cases of images of $\mathcal{H}$*

Therewith we can formulate a criterion for the existence of an R-hyperboloid Φ_R through a given quadrilateral $(ABCD)$, (c.f. [4]):

Criterion 1 *The pencil of quadrics through a quadrilateral $\mathcal{H} = (ABCD)$ contains an R-hyperboloid Φ_R, if and only if at least one of the three conditions (7.1), (7.2), (7.3) holds.*

We complete this section by the following

Theorem 1 *If $\mathcal{H}$ is symmetric with respect to a symmetry plane through CB, then (7.1) and (7.2) are automatically fulfilled and there are two R-hyperboloids Φ_{R1}, Φ_{R2} through $\mathcal{H}$. If $\mathcal{H}$ is equilateral, all three conditions (7.1), (7.2), (7.3) are fulfilled and there are three R-hyperboloids Φ_{R1}, Φ_{R2}, Φ_{R3} through $\mathcal{H}$, and the R-hyperboloids have pairwise orthogonal axes.*

The case with three R-hyperboloids occurs as shown with the example in Chapter 1.
In the following we identify the points of the quadrilateral $\mathcal{H} = (A,B,C,D)$ with their coordinate vectors, such that $\vec{e}_1 = B-A$, $\vec{e}_2 = D-C$, $\vec{f}_1 = A-C$, $\vec{f}_2 = D-B$. Therewith the edge vectors are oriented such that the following closure condition (8) is fulfilled

$$\vec{e}_1+\vec{f}_2-\vec{e}_2-\vec{f}_1=0. \tag{8}$$

We will also omit vector arrows, but keep in mind the orientation of the edges of $\mathcal{H}$. As (7.1) does not suit for a TP-patch representation of the R-hyperboloid, we can focus on the conditions (7.2) and (7.3), where we assume that at least one of them is fulfilled.

3 Further conditions for R-hyperboloids through a given quadrilateral

Two generators e and f of an R-hyperboloid Φ intersecting in $P \in \Phi$ are symmetric with respect to the plane spanned by the axis a of Φ and by P (see Figure 5). This property can be used for finding a condition, that the pencil $\mathfrak{Q}$ of hyperboloids through a given quadrilateral $\mathcal{H} = (e_1,e_2,f_1,f_2)$ contains an R-hyperboloid: Four of the symmetry planes of (e_i,f_j) must belong to a pencil of planes. If so, then they will intersect in the axis a of an R-hyperboloid. In each vertex of $\mathcal{H}$ there exist two symmetry planes σ_X^i spanned by the normal $e_i \times f_j$ and the symmetry lines s_X^i in the planes $e_i \vee f_j$, see Figure 8.
From Figure 8 we read off that of all possible combinations of symmetry planes there are only $\frac{1}{2}\binom{4}{2}=3$, which make sense: *a*) $\{\sigma_A^1,\sigma_B^1,\sigma_C^1,\sigma_D^1\}$, *b*) $\{\sigma_A^2,\sigma_B^2,\sigma_C^2,\sigma_D^2\}$, and *c*) $\{\sigma_A^2,\sigma_B^1,\sigma_C^1,\sigma_D^2\}$. This suits again to the maximally three R-hyperboloids in the pencil $\mathfrak{Q}$. (Here and in the following we use the labelling in Figure 8.)
The normal vector of σ_A^1 resp. σ_A^2 is

$$s_A^2 = \frac{e_1}{\|e_1\|}+\frac{f_1}{\|f_1\|} \quad \text{resp.} \quad s_A^1 = \frac{e_1}{\|e_1\|}-\frac{f_1}{\|f_1\|}, \tag{9}$$

and, similarly, also for the other symmetry planes, σ_X^1 has normal vector s_X^2, while s_X^1 is normal to σ_X^2.

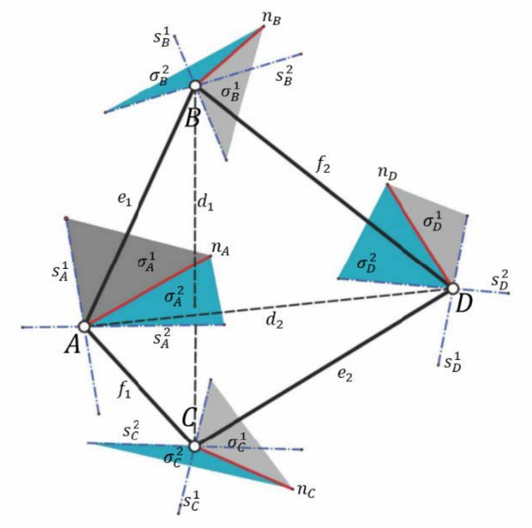

Figure 8: *A quadrilateral $\mathcal{H}$ and the symmetry planes of its pairs of consecutive edges.*

In case of *a*) we demand that $\{s_A^2, s_B^2, s_C^2, s_D^2\}$ necessarily are parallel to a plane. This means that

$$det(s_A^2, s_B^2, s_C^2) = 0 \quad \wedge \quad det(s_A^2, s_B^2, s_D^2) = 0. \tag{10}$$

By replacing s_X^2 by $\frac{e_i}{\|e_i\|} \pm \frac{f_j}{\|f_j\|}$ in (10) we obtain the same condition (11) for both equations:

$$\|e_1\|.det(e_2, f_1, f_2) - \|e_2\|.det(e_1, f_1, f_2) = \\ = \|f_1\|.det(e_1, e_2, f_2) - \|f_2\|.det(e_1, e_2, f_1). \tag{11}$$

This means that, if one of the necessary conditions (10) is fulfilled, then the other is fulfilled, too. When we substitute the closure condition (8) $e_2 = e_1 + f_2 - f_1$ into (11) we get $det(e_1, f_1, f_2)(\|e_1\| - \|f_2\| - \|e_2\| + \|f_1\|) = 0$, which is equivalent to (7.3).
In case of *b*), if we proceed in the same manner for the two conditions $(s_A^1, s_B^1, s_C^1) = 0$, $(s_A^1, s_B^1, s_D^1) = 0$, and we obtain the equation

$$\|e_1\|.det(e_2, f_1, f_2) + \|e_2\|.det(e_1, f_1, f_2) = \\ = \|f_1\|.det(e_1, e_2, f_2) - \|f_2\|.det(e_1, e_2, f_1), \tag{12}$$

which turns out to be equivalent to (7.1).
For case *c*) the conditions read as $(s_A^1, s_B^2, s_C^2) = 0$ and $(s_A^1, s_B^2, s_D^1) = 0$. The resulting single condition now becomes

$$\|e_1\|.det(e_2, f_1, f_2) + \|e_2\|.det(e_1, f_1, f_2) = \\ = -\|f_1\|.det(e_1, e_2, f_2) - \|f_2\|.det(e_1, e_2, f_1), \tag{13}$$

which is equivalent to (7.2). We collect these statements as

Theorem 2 *Four symmetry planes of consecutive edges of a quadrilateral $\mathcal{H}$ intersect in a common line a, if and only if at least one of the conditions (11), (12), (13) is fulfilled. These conditions are equivalent to the conditions (7.3), (7.1) and (7.2) respectively. Therefore, such a common line a is the axis of an R-hyperboloid Φ through $\mathcal{H}$.*

4 Bézier representation of quadrics through a given quadrilateral

We consider the quadrangle $\mathcal{H}$ again and want to calculate the generators of a hyperboloid $\Phi(p)$ through it aiming at a Bézier-patch representation of $\Phi(p)$, see Figure 9. We use the fact that the f-generators intersect two e-generators of a ruled quadric "with equal cross-ratios". This means that

$$CR(U, E, A, B) = CR(U', E', C, D). \tag{14}$$

The generator $e_1 = AB$ is parameterised by $A \widehat{=} 0$, $B \widehat{=} 1$ and the midpoint $E \widehat{=} \frac{1}{2}$ of segment $[AB]$ and similarly for generator $e_2 = CD$. A third "f-generator" passing through $E \in e_1$ intersects e_2 in a point $E' \widehat{=} (\frac{1}{2})' =: p + \frac{1}{2}$. Obviously, for $p = 0$ one gets the paraboloid $\Phi(0) \in \mathfrak{Q}$.

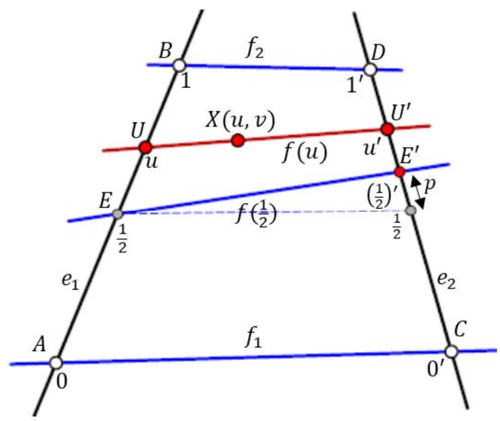

Figure 9: *The fixed f-generators f_1, f_2 of $\mathcal{H}$ together with a third f-generator define a hyperboloid $\Phi(p) \in \mathfrak{Q}$.*

Putting $u' = \frac{u+s}{qu+r}$ according to (14), then with $u = 0 \mapsto u' = 0$, $u = 1 \mapsto u' = 1$, $u = \frac{1}{2} \mapsto u' = \frac{1}{2} + p$ we obtain $s = 0$, $r = 1 - q$ and finally

$$u' = \frac{u}{qu + r} \quad \text{with} \quad q(p) = \frac{4p}{1+2p},\ r(p) = \frac{1-2p}{1+2p}. \tag{15}$$

Another convenient representation of condition (14) then is

$$t' := \frac{u'}{1-u'} = \frac{u(1-2p)}{(1-u)(1+2p)} =: t\frac{1}{r}. \tag{16}$$

Therewith follows for a Bézier-patch representation for $\Phi(p)$

$$X(u,v) = (1-v)((1-u)A+uB)+v((1-u')C+u'D),$$
$$(u,u',v \in [0,1]), \tag{17}$$

with v the parameter on generator $f(u) = vU + (1-v)U'$. (As before, we use the same symbols for points and their coordinate vectors.)

The form parameter $p = 0$ in (15) describes the unique paraboloid $\Phi(0) \in \mathfrak{Q}$. The parameter values $p = \pm\frac{1}{2}$ describe the singular quadrics, namely the pairs of planes in the pencil $\mathfrak{Q}$. We are now interested in the parameter value p for an R-hyperboloid in the quadric pencil $\mathfrak{Q}$ through $\mathcal{H}$, which is assumed to fulfil one of the conditions (7.2), (7.3). Because of the cross-ratio condition (14) it is enough to demand that one further generator, say $f(\frac{1}{2})$, together with $\frac{1}{2}e_1$, $(\frac{1}{2}+p)e_2$ and f_1 fulfils (7.2) or (7.3). For the vector $f(\frac{1}{2})$ follows

$$f(\tfrac{1}{2}) = f_1 + (\tfrac{1}{2}+p)e_2 - \tfrac{1}{2}e_1, \tag{18}$$

its squared norm is therefore

$$f^2(\tfrac{1}{2}) = f_1^2 + (\tfrac{1}{2}+p)^2 e_2^2 + \tfrac{1}{4}e_1^2 + 2(\tfrac{1}{2}+p)(e_2 f_1)$$
$$-(\tfrac{1}{2}+p)(e_1 e_2) - (e_1 f_1). \tag{19}$$

The R-hyperboloid conditions (7.2), (7.3) for $f(\frac{1}{2})$ are

$$\mp\|f(\tfrac{1}{2})\| = \tfrac{1}{2}\|e_1\| - (\tfrac{1}{2}+p)\|e_2\| \mp \|e_1\|\|f_1\|. \tag{20}$$

and we square (20) receiving

$$f^2(\tfrac{1}{2}) = \tfrac{1}{4}e_1^2 + (\tfrac{1}{2}+p)^2 e_2^2 + f_1^2 \pm 2(\tfrac{1}{2}+p)\|e_2\|\|f_1\|$$
$$-(\tfrac{1}{2}+p)\|e_1\|\|e_2\| \mp \|e_1\|\|f_1\|. \tag{21}$$

Now we compare (19) and (21) and get a linear equation in p. (In fact, there occur two such equations because of the different signs.)

$$(e_1 f_1) \pm \|e_1\|\|f_1\| = (\tfrac{1}{2}+p)[(-\|e_1\|\|e_2\| + (e_1 e_2))$$
$$+2(\pm\|e_2\|\|f_1\| - (e_2 f_1))]. \tag{22}$$

Here we see that (22) involves the angles between consecutive edges of $\mathcal{H}$, too:

$$(\frac{1}{2}+p) =$$
$$\frac{\|e_1\|\|f_1\|(\cos\sphericalangle e_1 f_1 \pm 1)}{\|e_1\|\|e_2\|(\cos\sphericalangle e_1 e_2 - 1) + 2\|e_2\|\|f_1\|(\pm 1 - \cos\sphericalangle e_2 f_1)}. \tag{23}$$

We put $\sphericalangle e_1 f_1 =: \alpha$, $\sphericalangle f_1 e_2 =: \gamma$, $\sphericalangle e_1 e_2 =: \varepsilon$; then, because of $1-\cos\xi = 2\sin^2\xi/2$ and $1+\cos\xi = 2\cos^2\xi/2$ equation (23) can be written as

$$p_1 = \frac{\|e_1\|\|f_1\|\cos^2\alpha/2}{2\|e_2\|\|f_1\|\sin^2\gamma/2 - \|e_1\|\|e_2\|\sin^2\varepsilon/2} - \frac{1}{2} \tag{24.1}$$

$$p_2 = \frac{\|e_1\|\|f_1\|\sin^2\alpha/2}{2\|e_2\|\|f_1\|\cos^2\gamma/2 + \|e_1\|\|e_2\|\sin^2\varepsilon/2} - \frac{1}{2} \tag{24.2}$$

Now we can state

Theorem 3 *An R-hyperboloid $\Phi(p)$ through a quadrilateral $\mathcal{H}$, which fulfils the conditions (7.2) resp. (7.3) allows the tensor-product representation (17), whereby the form parameter p takes the value p_1 (24.1) resp. p_2 (24.2).*

In the following chapter we will apply these results to some polyhedrons. As the chosen starting polyhedrons have regular faces, edge quadrilaterals are symmetric. This facilitates the calculation of the parameters p_1 and p_2.

5 Examples of polyhedrons with patches of R-hyperboloids as faces

If the start polyhedron has n-gons as faces ($n > 3$), see Figure 10 and 11, we split such a face into triangles. It is also possible to add pyramids to such a face to obtain an additional form parameter by the pyramid's height.

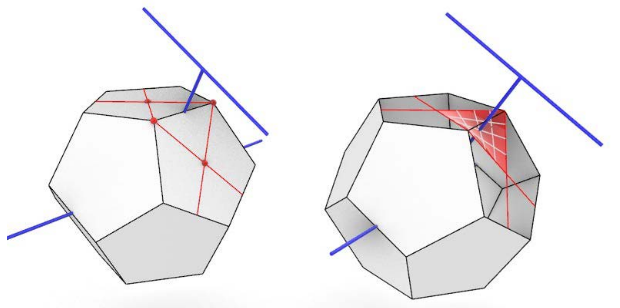

Figure 10: *The principle, how one can proceed in case of non-triangular faces of a polyhedron, shown at a regular dodecahedron*

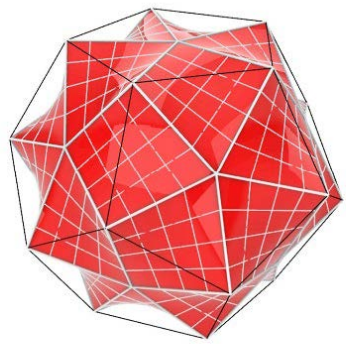

Figure 11: *The dodecahedron's faces are completely replaced by paraboloid patches.*

Because the pentagonal faces are tangential to the five patches connected at the midpoint of the face, the 12 midpoints must be interpreted as additional vertices, such that the object has got 32 vertices and 30 quadric patches. Almost the same object emerges by adding pyramids to the pentagonal faces of a dodecahedron, such that it gets 60 isosceles triangles as faces, see Figure 12. This object is a Catalan polyhedron and is called pentakis-dodecahedron or kisdodecahedron. Again pairs of triangles are replaced by quadric patches.

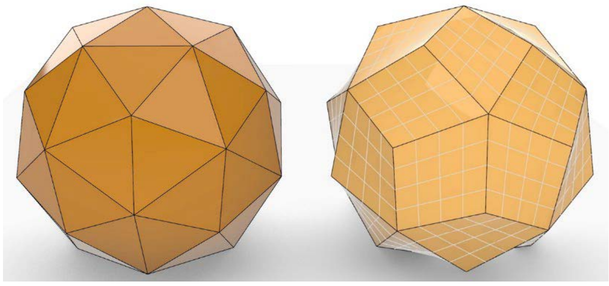

Figure 12: *The dodecahedron's faces are completely replaced by paraboloid patches.*

Choosing the height of the pyramids added to the faces of a dodecahedron suitably one can get a Kepler star. We show the principle of replacing two adjacent triangles by R-hyperboloid patches through equilateral edge quadrilateral in Figure 13.

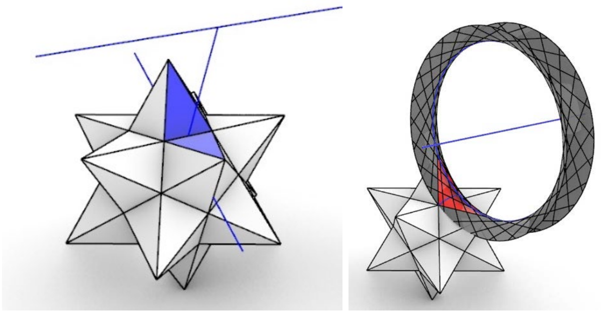

Figure 13: *A Kepler star with an R-hyperboloid patch through an equilateral edge quadrilateral*

The next object, an elongated pentagonal cupola, might have at least some architectural relevance by its "windows" formed by R-hyperboloids, Figure 15. The used edge quadrilaterals are equilateral. In this case we refrained from the patch representation according Theorem 3 and applied condition (7.1) as well as geometric properties derived from the octahedron in Chapter 1.

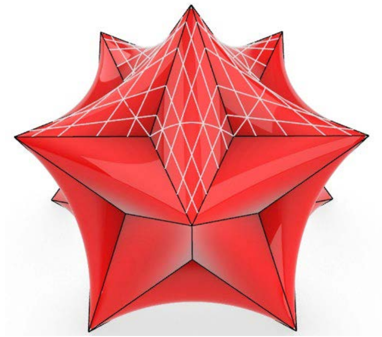

Figure 14: *A Kepler star completely covered with R-hyperboloid patches*

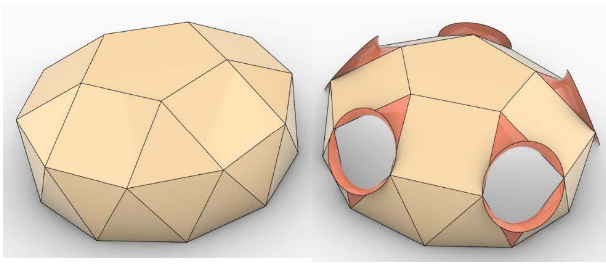

Figure 15: *R-hyperboloids through equilateral edge quadrangles forming "windows" into an elongated pentagonal cupola*

6 Pencils of R-hyperboloids and final remarks

The previous chapters were concerned with R-hyperboloids through a given quadrilateral of generators $\mathcal{H} = (e_1 e_2 f_1 f_2)$ and we derived conditions for the existence of an R-hyperboloid through $\mathcal{H}$. Another approach could be to consider the pencil of R-hyperboloids through the skew generators e_1, e_2 and the second pencil through f_1 and f_2. The axes of such a pencil of R-hyperboloids are generators of the symmetry paraboloid $\Psi(e)$ of e_1 and e_2 resp. $\Psi(f)$ of f_1 and f_2, c.f. [3]. The two pencils have an R-hyperboloid in common, if and only if $\Psi(e)$ and $\Psi(f)$ have a common generator a, which acts as axis of the common R-hyperboloid. Obviously the conditions for that must be again (7.1), (7.2) and (7.3).

In [3] the symmetry paraboloid of two skew lines e_1 and e_2 is considered as the set of points, which are equidistant from these lines. When interpreting it as set of axes of R-hyperboloids through these lines one takes a line geometric viewpoint. (For line geometry c.f. e.g. [5]). The place of action is the projectively enclosed Euclidean 3-space. Indeed, it seems worthwhile to look at pencils of R-hyperboloids that way. They can be seen as 3D-generalisations of pencils of circles. The skew (and real) proper lines e_1 and e_2 span a hyperbolic linear congruence of lines meeting both, e_1 and e_2. If e_1 and e_2 coincide in the way that the line congruence becomes parabolic, we might ask again for the then parabolic pencil of R-hyperboloids in this congruence of lines. If e_1 and e_2 are skew and imaginary, they are axes of an elliptic linear congruence. Here pops up a case, where all R-hyperboloids are coaxial, such that the symmetry paraboloid $\Psi(e)$ degenerates into a single line.

There are many other ways to replace the planar faces of a polyhedron by patches of curved surfaces. One could e.g. blow up a balloon in the materialised edge frame of a closed polyhedron. Such structures are almost omnipresent in our environment. Pairs of faces replaced by minimal surfaces, a topic of differential geometry, will, in the most cases differ not essentially from quadric patches. This might justify the use of patches of paraboloids or R-hyperboloids instead for architectural purposes.

References

[1] O. GIERING, Mit HP-Flächen variierte Platonische Polyeder, *IBDG* **39**(2) (2015), 28–31.

[2] O. GIERING, Mit HP-Flächen variierte Platonische Polyeder II, *IBDG* **40**(1) (2021), 37–38.

[3] M. L. HUSTY, H. SACHS, Abstandsprobleme zu windschiefen Geraden I, *Sb. d österr. Ak. d. Wiss.* **203** (1990), 31–55.

[4] B. ODEHNAL, H. STACHEL, G. GLAESER, *The Universe of Quadrics*, Springer-Verlag, Berlin Heidelberg, 2020, doi.org/10.1007/978-3-662-61053-4

[5] H. POTTMANN, J. WALLNER, *Computational Line Geometry*, Springer-Verlag, Berlin Heidelberg, 2001.

Milena Stavrić
orcid.org/0000-0002-8682-2026
e-mail: mstavric@tugraz.at

University of Technology Graz
8010 Graz, Kronesgasse 5/DG

Albert Wiltsche
e-mail: wiltsche@tugraz.at

University of Technology Graz
8010 Graz, Kronesgasse 5/DG

Gunter Weiss
e-mail: weissgunter@gmx.at

University of Technology Vienna,
Karlsplatz 13, 1040 Vienna, Austria

University of Technology Dresden,
Helmholtzstrße 10, 01069 Dresden, Germany

https://doi.org/10.31896/k.25.6
Original scientific paper
Accepted 2. 12. 2021.

Anastasios N. Zachos

Generalized Regularity and the Symmetry of Branches of "Botanological" Networks

To the weighted regularity of Euclid.

Generalized Regularity and the Symmetry of Branches of "Botanological" Networks

ABSTRACT

We derive the generalized regularity of convex quadrilaterals in $\mathbb{R}^2$, which gives a new evolutionary class of convex quadrilaterals that we call generalized regular quadrilaterals in $\mathbb{R}^2$. The property of generalized regularity states that the Simpson line defined by the two Steiner points passes through the corresponding Fermat-Torricelli point of the same convex quadrilateral. We prove that a class of generalized regular convex quadrilaterals consists of convex quadrilaterals, such that their two opposite sides are parallel. We solve the problem of vertical evolution of a "botanological" thumb (a two way communication weighted network) w.r to a boundary rectangle in $\mathbb{R}^2$ having two roots,two branches and without having a main branch, by applying the property of generalized regularity of weighted rectangles. We show that the two branches have equal weights and the two roots have equal weights, if the thumb inherits a symmetry w.r to the midperpendicular line of the two opposite sides of the rectangle, which is perpendicular to the ground (equal branches and equal roots). The geometric, rotational and dynamic plasticity of weighted networks for boundary generalized regular tetrahedra and weighted regular tetrahedra lead to the creation of "botanological" thumbs and "botanological" networks (with a main branch) having symmetrical branches.

Key words: Fermat-Torricelli problem, Fermat-Torricelli point, Steiner tree, Steiner points, generalized regular quadrilaterals, generalized regularity, "thumb"

MSC2010: 51N20, 51M20, 51E10, 52A15

Generalizirana regularnost i simetrija "botanologičnih" mreža

SAŽETAK

Izvodimo generaliziranu regularnost konveksnih četverokuta u $\mathbb{R}^2$ koja daje novu evolucijsku klasu konveksnih četverokuta koju mi nazivamo generalizirani regularni četverokuti u $\mathbb{R}^2$. Svojstvo generalizirane regularnosti kaže da Simpsonov pravac definiran s dvije Steinerove točke prolazi odgovarajućom Fermat-Torricellijevom točkom tog istog četverokuta. Dokazujemo da se klasa generaliziranih regularnih konveksnih četverokuta sastoji od konveksnih četverokuta takvih da su njihove dvije nasuprotne stranice paralelne. Rješavamo problem vertikalne evolucije "botanologičnog palca" (težinska mreža, u oba smjera) s obzirom na granični pravokutnik u $\mathbb{R}^2$ koji ima dva korijena, dvije grane, bez da ima glavnu granu, primjenjujući svojstvo generalizirane regularnosti težinskih pravokutnika. Pokazujemo da dvije grane imaju jednake težine kao i dva korijena ako "palac" nasljeđuje simetriju s obzirom na poluokomit pravac dvaju nasuprotnih stranica pravokutnika koji je okomit na tlo (jednake grane i jednaki korijeni). Geometrijski, rotacijski i dinamični plasticitet težinskih mreža za granični generalizirani regularni tetraedar i težinski regularni tetraedar vodi ka stvaranju "botanologičnih palčeva" i "botanologičnih" mreža (s glavnom granom) koja ima simetrične grane.

Ključne riječi: Fermat-Torricellijev problem, Fermat-Torricellijeva točka, Steinerovo stablo, Steinerove točke, generalizirani regularni četverokuti, generalizirana regularnost, "palac"

1 Introduction

Let $A_1, A_2, \ldots, A_n$ be the vertices of a polygon $A_1A_2A_3\ldots A_n$ in a cyclic order.

An affinely regular polygon in $\mathbb{R}^2$ is derived by applying an affine transformation to a regular polygon ([1]). Coxeter introduced the affine regularity of polygons and proved the following result ([2], [3]):

$A_1A_2A_3...A_n$ is affinely regular if and only if there is $m \geq 0$, such that
$\overrightarrow{A_{i-1}A_{i+2}} = m\overrightarrow{A_iA_{i+1}}$, for $i = 1,2,...,n$.
Triangles are affine regular and parallelograms are affine regular quadrilaterals in $\mathbb{R}^2$.
Gerber connected the affine regularity with the Euclidean regularity of $n-gons$ in [4], (see also [2] and [3])) and proved the result: If you construct regular $n-gons$ outwardly (or inwardly) on the sides of any affine regular $n-gon$, then their centers form the vertices of a regular $n-gon$. The case $n = 4$ was proved by Thebault, who gave the first generalization of Napoleon's regularity for the case $n = 3$ (Napoleon's theorem) ([2, p. 185]).
We start by giving the definitions of a weighted Fermat-Torricelli tree and weighted Steiner tree for a boundary quadrilateral, in order to derive a new regularity of quadrilaterals which is different from Coxeter's, Gerber's and Thebault's approach. The new regularity of quadrilaterals is achieved by the construction of isosceles triangles outwardly on the parallel sides of a rectangle or a trapezoid.
Let $A_1A_2A_3A_4$ be a convex quadrilateral in $\mathbb{R}^2$. We denote by $A_i(x_i,y_i)$ the vertices of $A_1A_2A_3A_4$, by B_i a positive real number (weight) which corresponds to A_i, by $O_{12}(x_{012},y_{012})$, by $O_{34}(x_{034},y_{034})$ two points in $\mathbb{R}^2$ with given weights B_{12} in O_{12} and B_{34} in O_{34}, by $d(X,Y)$ the Euclidean distance $\|XY\|$, for $X,Y \in \mathbb{R}^2$.
The weighted Steiner problem for $A_1A_2A_3A_4$ in $\mathbb{R}^2$ states that:

Problem 1 *Find $O_i(x_{0i},y_{0i})$, for $i = \{12,34\}$, such that*

$$\begin{aligned} f(O_{12},O_{34}) &= B_1d(O_{12},A_1)+B_2d(O_{12},A_2)+ \\ &+B_3d(O_{34},A_3)+B_4d(O_{34},A_4)+ \\ &+\frac{B_{12}+B_{34}}{2}d(O_{12},O_{34}) \to min. \quad (1)\end{aligned}$$

For $B_1 = B_2 = B_3 = B_4$, the solution of the (unweighted) Steiner problem is called a Steiner tree. Gilbert and Pollack introduce the Steiner tree topologies for $A_1A_2A_3A_4$, in their classical study ([5]). They mention three topologies of solutions w.r to the boundary $A_1A_2A_3A_4$:
1. If we set one point (node) F (Fermat-Torricelli point) different from A_i, the solution is called a Fermat-Torricelli tree. The Fermat-Torricelli point F has four connections $\{FA_1,FA_2,FA_3,FA_4\}$. This is a special case of the unweighted Steiner problem, by setting $B_{12} = 0$ or $B_{34} = 0$.
2. If we set two points (nodes) O_{12} and O_{34} (Steiner points) and $B_{12}+B_{34} = 2$, such that the objective function (40) is minimized, then we derive a solution which is called a full Steiner tree. The Steiner points O_{12} and O_{34} have three connections $\{A_1O_{12},A_2O_{12},O_{12}O_{34}\}$ and $\{A_3O_{34},A_4O_{34},O_{12}O_{34}\}$, respectively.
3. If we set one point (node) Steiner point O_{12} and $O_{34} \equiv A_3 or A_4$, such that the objective function (40) is minimized, then we derive a degenerate Steiner tree.

It is well known that the Steiner point with three connections possesses the equiangular property $\frac{360^o}{3}$. The angle formed by the Steiner point as a vertex and two connections is 120^o, for the unweighted case and by assuming that $B_{12}+B_{34} = 2$ ([5]). The same property holds for the Fermat-Torricelli point for a boundary triangle, which coincides with the Steiner point. The Fermat-Torricelli tree of a convex quadrilateral consists of the two diagonals A_1A_3 and A_2A_4, which meet at the intersection point F (Fermat-Torricelli point) for the unweighted case.
Rubinstein, Thomas and Weng studied in [8] the unweighted Steiner problem for tetrahedra in $\mathbb{R}^3$. They succeeded in locating the Simpson line, which passes through the two Steiner points O_{12} and O_{34} in $\mathbb{R}^3$. The vertex A_{12} of the equilateral $\triangle A_{12}A_1A_2$, which lies on the opposite side of A_1A_2 to O_{12} is referred to as the e-point of A_1A_2. The vertex A_{34} of the equilateral $\triangle A_{34}A_4A_3$, which lies on the opposite side of A_3A_4 to O_{34} is referred to as the e-point of A_3A_4. The Simpson line passes through the e-points of A_1A_2 and A_3A_4, respectively, and

$$\begin{aligned} &d(A_{12},A_{34}) = \\ &d(O_{12},A_1)+d(O_{12},A_2)+d(O_{34},A_3)+d(O_{34},A_4) = L.\end{aligned}$$

The Melzak Circle is a circle $C(O_1,r_{12})$, which passes through A_1, A_2, A_{12} and intersects the Simpson line at O_{12}. Similarly, the Melzak Circle $C(O_2,r_{34})$ passes through A_3, A_4, A_{34} and intersects the Simpson line at O_{34}. The Melzak construction via the method of e-points is established in [7]. Furthermore, Rubinstein, Thomas and Weng gave explicit formulas for computing Steiner trees for four points in $\mathbb{R}^2$, for all possible cases, in which the lines defined by A_1A_2 and A_3A_4 either intersect or are parallel ([8, Chapter 3, Cases (1), (2)]). We set $\varphi \equiv \angle(\overrightarrow{A_1A_2},\overrightarrow{A_3A_4})$. For $\varphi = 0$, (A_1A_2 and A_3A_4 are parallel), we refer to this solution as the Steiner zero solution. The Steiner zero solution depends on the distance h between the two parallel lines, the midpoints of A_1A_2 and A_3A_4, respectively and the radius of Melzak circles r_{12} and r_{34} ([8, Chapter 3, Expicit formulas Case (2), page 65]).
Ivanov and Tuzhilin introduced the concept of the weighted Simpson line and they found the relation of the length of the weighted network with the length of a Simpson line ([6, Theorem 1]) which gives

$$\begin{aligned} &\frac{B_{12}+B_{34}}{2}L = \\ &B_1d(O_{12},A_1)+B_2d(O_{12},A_2)+B_3d(O_{34},A_3)+B_4d(O_{34},A_4).\end{aligned}$$

We note that A_{12} and A_{34} are not the e-points for the weighted case.
In this paper, we introduce the generalized (weighted) regularity of convex quadrilaterals and tetrahedra, which gives a new evolutionary class of convex quadrilaterals and tetrahedra in $\mathbb{R}^3$.

The property of generalized regularity states that the Simpson line defined by the two Steiner points O_{12} and O_{34} passes through the corresponding Fermat-Torricelli point of the same convex quadrilateral. The property of weighted regularity for weighted rectangles states that the weighted Simpson line defined by the two weighted Steiner points passes through the corresponding weighted Fermat-Torricelli point of the same rectangle.

The main results are:

1. The property of generalized regularity possess a class of convex quadrilaterals (generalized regular quadrilaterals), which corresponds to the Steiner zero solution and it consists of quadrilaterals having two of their opposite sides parallel (Theorem 1).

2. Let $A_1A_2A_3A_4$ be a rectangle in $\mathbb{R}^2$ and A_1F, A_2F be the two roots of the corresponding weighted Fermat-Torricelli tree (thumb), the weighted Fermat-Torricelli point F is located on the ground and A_3F, A_4F are two branches of the weighted Fermat-Torricelli tree (thumb).
If the weighted Simpson line $A_{12}A_{34}$ is perpendicular to the ground and $A_1A_2A_3A_4$ is a generalized regular quadrilateral, we prove that $B_1^2+B_3^2=B_2^2+B_4^2$ (Theorem 2).

3. Two branches have equal weights and the two roots have equal weights, if the thumb inherits a symmetry w.r to the midperpendicular line of the two opposite sides of the rectangle, which is perpendicular to the ground (equal branches and equal roots, Proposition 3).

4. The dynamic Plasticity of weighted network with two roots and two growing branches states that:
Given the weighted Fermat-Torricelli point A_{0i} that has got a subconscious $\bar{B}_{0i}$ to be an interior point of the tetrahedron $A_{1i}A_{2i}A_{3i}A_{4i}$ with the vertices lie on four prescribed rays that meet at A_{0i} the positive real weights $\bar{B}_{ji}$ depends on the five given values of α_{102i}, α_{103i}, α_{104i}, α_{203i}, α_{204i} and $\bar{B}_{0i}$ (Theorem 3).

5. We assume that the common perpendicular line of each tetrahedron $A_{1i}A_{2i}A_{3i}A_{4i}$ passes through the common midpoints m_{12} and m_{34} of $A_{1i}A_{2i}$ and $A_{4i}A_{3i}$, respectively and $m_{12}m_{34} >> A_{1i}A_{2i}$. We prove the following theorem for a botanological thumb (without a main branch) (Theorem 4):
If A_{0i} lies on the common perpendicular segment $m_{12}m_{34}$, then $\bar{B_{1i}}=\bar{B_{2i}}$ and $\bar{B_{3i}}=\bar{B_{4i}}$.

6. We prove the following theorem for a “botanological” network (with a main branch) (Theorem 4):
If A_{0i} lies on the common perpendicular segment $m_{12}m_{34}$, then $\bar{B_{1i}}=\bar{B_{2i}}$ and $\bar{B_{3i}}=\bar{B_{4i}}$.

The dynamic plasticity (Theorem 3), geometric plasticity (Lemma 2) and rotational plasticity (Proposition 4) of generalized regular tetrahedra (Definition 7) and generalized weighted regular tetrahedra (Definition 8) develops a symmetry for the weights for a “botanological” thumb (Theorem 4, Evolutionary scheme) or a botanological network in $\mathbb{R}^3$ (Theorem 10, Evolutionary scheme).

2 The property of generalized regularity of convex quadrilaterals in $\mathbb{R}^2$

Let $A_1A_2A_3A_4$ be a convex quadrilateral in $\mathbb{R}^2$, such that $B_1=B_2=B_3=B_4=1$ and $B_{12}+B_{34}=2$. We recall that a weight B_i corresponds to the vertex A_i, for $i=1,2,3,4$, a weight $B_{12}\equiv 1$ corresponds to the Steiner point O_{12} and $B_{34}\equiv 1$ corresponds to the Steiner point O_{34}. The Fermat-Torricelli point F is the intersection of the two diagonals of A_1A_3 and A_2A_4. We denote by L the Simpson line, which passes through the e-points A_{12}, A_{34} and O_{12}, O_{34} and by T_{12}, T_{34} the intersection points of the common angle bisector of the vertical angles A_1FA_2 and A_3FA_4 and the line segments A_1A_2 and A_3A_4, respectively.

Definition 1 (Generalized regularity) *A generalized regular quadrilateral is a convex quadrilateral in $\mathbb{R}^2$, such that the Simpson line L passes through the Fermat-Torricelli point F.*

Definition 2 (Weighted regularity) *A weighted regular quadrilateral is a convex quadrilateral in $\mathbb{R}^2$, such that the weighted Simpson line L passes through the weighted Fermat-Torricelli point F.*

Without loss of generality, we assume that:
$A_i=A_1(x_i,y_i)$, for $i=1,2,3,4$, $F=(x_F,y_F)$, $A_{34}=A_{34}(x_{34},y_{34})$ and $A_{12}=A_{12}(x_{12},y_{12})$, such that:
$y_4>y_3>y_2>y_1, x_1<x_4<x_3<x_2$.

Theorem 1 *The property of generalized regularity possess a class of convex quadrilaterals (generalized regular quadrilaterals), which corresponds to the Steiner zero solution and it consists of quadrilaterals having two of their opposite sides parallel.*

Proof. The intersection of the two diagonals A_1A_3, A_2A_4 is the unweighted Fermat-Torricelli point $F=(x_F,y_F)$, where

$$x_F=\frac{\frac{x_1(y_3-y_1)}{x_3-x_1}-\frac{x_2(y_4-y_2)}{x_4-x_2}-y_1+y_2}{\frac{y_3-y_1}{x_3-x_1}-\frac{y_4-y_2}{x_4-x_2}} \qquad (2)$$

and

$$y_F=\frac{(y_3-y_1)\left(\frac{\frac{x_1(y_3-y_1)}{x_3-x_1}-\frac{x_2(y_4-y_2)}{x_4-x_2}-y_1+y_2}{\frac{y_3-y_1}{x_3-x_1}-\frac{y_4-y_2}{x_4-x_2}}-x_1\right)}{x_3-x_1}+y_1. \qquad (3)$$

We shall express the coordinates of the e-point $A_{34}=A_{34}(x_{34},y_{34}$ x_{34} and y_{34} w.r. to x_3,y_3,x_4,y_4 (see Fig 1).

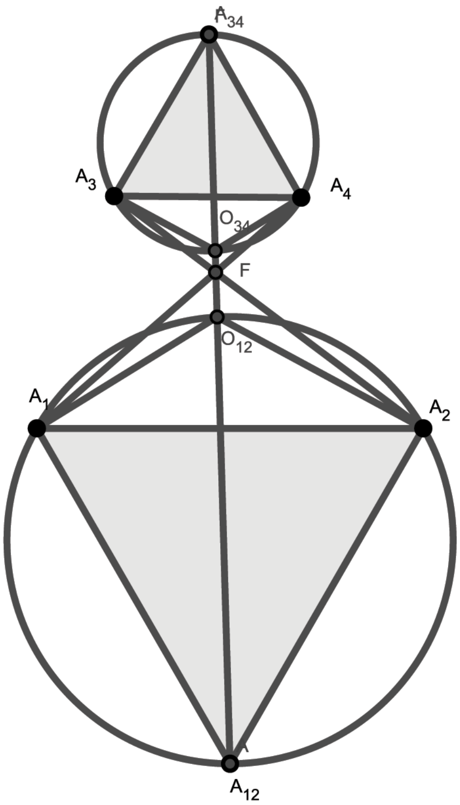

Figure 1: *Generalized regularity of quadrilaterals*

The relation $A_{34}A_3 = A_3A_4$ yields:

$$(x_{34}-x_3)^2+(y_{34}(x_3,y_3,x_4,y_4,x_{34})-y_3)^2 = (x_3-x_4)^2+(y_3-y_4)^2. \tag{4}$$

The midperpendicular line which is defined by $A_{34} = A_{34}(x_{34}, y_{34})$ and the midpoint $M_{34} = (\frac{x_3+x_4}{2}, \frac{y_3+y_4}{2})$ yields:

$$(y_{34}(x_3,y_3,x_4,y_4,x_{34}) = \frac{(x_4-x_3)\left(\left(x_{34}-\frac{x_3+x_4}{2}\right)\right)}{y_3-y_4}+\frac{1}{2}(y_3+y_4). \tag{5}$$

By replacing (5) in (4), we derive a second order degree polynomial w.r. to x_{34} and taking into account $x_{34} > \frac{x_3+x_4}{2}$, we obtain:

$$x_{34} = \frac{x_3y_3^2+x_3y_4^2-2x_3y_3y_4+\sqrt{3}M+x_4y_3^2}{2(x_3-x_4)^2+(y_3-y_4)^2} + \frac{x_4y_4^2-2x_4y_3y_4+x_3^3-x_4x_3^2-x_4^2x_3+x_4^3}{2(x_3-x_4)^2+(y_3-y_4)^2} \tag{6}$$

where

$M \equiv (x_3-x_4)^2+(y_3-y_4)^2|y_3-y_4|.$ □

By working similarly, we derive a second order degree polynomial w.r. to x_{12} and taking into account $x_{12} < \frac{x_1+x_2}{2}$, we obtain:

$$x_{12} = \frac{x_1y_1^2+x_1y_2^2-2x_1y_1y_2-\sqrt{3}N+x_2y_1^2}{2(x_1-x_2)^2+(y_1-y_2)^2} + \frac{x_2y_2^2-2x_2y_1y_2+x_1^3-x_2x_1^2-x_2^2x_1+x_2^3}{2(x_1-x_2)^2+(y_1-y_2)^2} \tag{7}$$

where

$N \equiv (x_1-x_2)^2+(y_1-y_2)^2|y_1-y_2|.$

The area of $\triangle A_{12}A_{34}F$ is given by:

$$A(\triangle A_{12}A_{34}F) = \left|\det\begin{pmatrix} x_F & y_F & 1 \\ x_{12} & y_{12} & 1 \\ x_{34} & y_{34} & 1\end{pmatrix}\right|. \tag{8}$$

By substituting $y_4 = y_3 + \frac{y_2-y_1}{x_2-x_1}(x_4-x_3)$ in (8) and by getting as a common factor $\frac{d(A_1,A_2)}{|y_1-y_2|}$, we derive that
$A(\triangle A_{12}A_{34}F) =$
$f(x_1,y_1,x_2,y_2,x_3,y_3,x_4,y_4)g(x_1,y_1,x_2,y_2,x_3,y_3,x_4,y_4)$
where

$$g(x_1,y_1,x_2,y_2,x_3,y_3,x_4,y_4) = x_3-x_4+(x_1-x_2)\frac{|x_3-x_4|}{|x_1-x_2|}. \tag{9}$$

Without loss of generality, we assume that $x_2 > x_1$ and $x_3 > x_4$.
Hence, by calculating (9), we deduce that $A(\triangle A_{12}A_{34}F) = 0$ and A_{12}, A_{34} and F are collinear only when A_1A_2 is parallel to A_4A_3.
We denote by H the distance between A_1A_2 and A_3A_4. Suppose that $H > d(A_1,A_2)+d(A_3,A_4)$ and $\varphi \geq \angle A_2A_1A_3 \leq 120^\circ$, $\varphi \geq \angle A_1A_2A_4 \leq 120^\circ$, where $\varphi = \arctan\left(\frac{H}{d(A_1,A_2)+H\frac{\sqrt{3}}{3}+d(A_3,A_4)}\right)$.

Proposition 1 *If $A_1A_2 \parallel A_4A_3$, the intersection point of the common angle bisector of $\angle A_1FA_2$ and $\angle A_3FA_4$ and the Simpson line defined by $A_{12}A_{34}$ is the Fermat-Torricelli point F.*

Proof. By applying Theorem 1, F lies on the Simpson line. Therefore, the common angle bisector of $\angle A_1FA_2$ and $\angle A_3FA_4$ and the Simpson line defined by $A_{12}A_{34}$ passes through the Fermat-Torricelli point F. □

Remark 1 *If $x_{34} < \frac{x_3+x_4}{2}$ and $x_{12} < \frac{x_1+x_2}{2}$, we derive:*

$$x_{34} = \frac{x_3y_3^2+x_3y_4^2-2x_3y_3y_4-\sqrt{3}M+x_4y_3^2}{2(x_3-x_4)^2+(y_3-y_4)^2} + \frac{x_4y_4^2-2x_4y_3y_4+x_3^3-x_4x_3^2-x_4^2x_3+x_4^3}{2(x_3-x_4)^2+(y_3-y_4)^2} \tag{10}$$

and taking into account

$$x_{12} = \frac{x_1 y_1^2 + x_1 y_2^2 - 2x_1 y_1 y_2 - \sqrt{3}N + x_2 y_1^2}{2(x_1-x_2)^2 + (y_1-y_2)^2} + \\ + \frac{x_2 y_2^2 - 2x_2 y_1 y_2 + x_1^3 - x_2 x_1^2 - x_2^2 x_1 + x_2^3}{2(x_1-x_2)^2 + (y_1-y_2)^2},$$

the corresponding determinant of the area $A(\triangle A_{12}A_{34}F)$ *is non-zero.*

Examples of generalized regular quadrilaterals are the square, rectangle and the isosceles trapezoid.
The following results are a direct consequence of Theorem 1:

Proposition 2 *A square is a generalized regular quadrilateral, which corresponds to two Steiner zero solutions, having their Simpson lines perpendicular and meet at the Fermat-Torricelli point F.*

Corollary 1 *A square is a generalized regular quadrilateral, such that the two Simpson lines and the two corresponding angle bisectors w.r to the vertical angles coincide (two minimum Steiner trees).*

Corollary 2 *A rectangle is a generalized regular quadrilateral, such that the two Simpson lines and the two corresponding angle bisectors w.r to the vertical angles coincide and the Simpson line which is midperpendicular w.r. to the parallel sides with greater length does not given a minimum Steiner tree (a unique minimum Steiner tree).*

Corollary 3 *An isosceles trapezoid is a generalized regular quadrilateral, such that the Simpson line (midperpendicular) which passes through the Fermat-Torricelli point F and the corresponding angle bisector w.r to the vertical angles coincide.*

3 Creation of a "botanological" thumb for a boundary rectangle in $\mathbb{R}^2$

A "botanological" network for four non-collinear points in $\mathbb{R}^2$ is introduced and studied in [13] for open systems (Botany).

Definition 3 ("Botanological" network, [13]) *A "botanological" network for four non-collinear points is a two-way communication network, which has the topology of a weighted minimal Steiner tree in* $\mathbb{R}^2$*, having two weighted Fermat-Torricelli nodes (Steiner nodes), two weighted roots, two weighted branches and one main branch.*

Let $A_1A_2A_3A_4$ be a weighted rectangle in $\mathbb{R}^2$, B_i be a weight which corresponds to each vertex A_i, for $i = 1,2,3,4$, A_1F, A_2F are the two roots of the corresponding weighted Fermat-Torricelli tree (thumb). We assume that the weighted Fermat-Torricelli point F is located on the ground and A_3F, A_4F are two branches of the weighted Fermat-Torricelli tree (thumb) and $A_1A_4 >> A_1A_2$.
The weighted Simpson line is a line defined by $A_{12}A_{34}$, where A_{12} is a vertex of $\triangle A_{12}A_1A_2$, which lies on the opposite side of A_1A_2 to O_{12} and A_{34} is a vertex of $\triangle A_{34}A_4A_3$, which lies on the opposite side of A_3A_4 to O_{34}. The weighted Steiner points O_{12} and O_{34} are the two nodes of the weighted Steiner tree and they both lie on $A_{12}A_{34}$, with equal weights $\frac{B_{12}+B_{34}}{2}$.

Definition 4 *A "botanological" thumb for a boundary rectangle is a two-way communication network, which has the topology of a weighted Fermat-Torricelli tree in* $\mathbb{R}^2$*, having one weighted Fermat-Torricelli node, two weighted roots and two weighted branches, which is enriched by the property of generalized regularity of quadrilaterals, such that* $A_{12}A_{34}$ *is perpendicular to* A_1A_2.

We assume that the weighted Fermat-Torricelli point F of $A_1A_2A_3A_4$ ($B_{12} = B_{34} = 0$) lies on the ground and A_1A_2 is parallel to the ground.
Our main result is the following theorem, which gives a weighted condition for the four weights of a thumb whose weighted Simpson line is perpendicular to the ground and A_1A_2 and passes through the corresponding weighted Fermat-Torricelli point F.

Theorem 2 *If* $A_{12}A_{34}$ *is perpendicular to* A_1A_2,

$$B_1^2 = B_2^2 + B_4^2 - B_3^2. \tag{11}$$

Proof. We consider the weighted Steiner tree for the boundary $A_1A_2A_3A_4$. We recall that the objective function is given by:

$$f(O_{12},O_{34}) = B_1 d(O_{12},A_1) + B_2 d(O_{12},A_2) + B_3 d(O_{34},A_3) \\ + B_4 d(O_{34},A_4) + \frac{B_{12}+B_{34}}{2} d(O_{12},O_{34}) \to min, \tag{12}$$

where O_{12} is the weighted Fermat-Torricelli point (Steiner node) of $\triangle A_1A_2O_{34}$ with corresponding weights B_1, B_2 and $\frac{B_{12}+B_{34}}{2}$, respectively, and O_{34} is the weighted Fermat-Torricelli point (Steiner node) of $\triangle A_3A_4O_{34}$ with corresponding weights B_3, B_4 and $\frac{B_{12}+B_{34}}{2}$, respectively.
Hence, the construction of the weighted Simpson line yields the following relations:

$$B_1 \sin\angle A_1A_2A_{12} = B_2 \sin\angle A_2A_1A_{12} \tag{13}$$

and

$$B_3 \sin\angle A_3A_4A_{34} = B_4 \sin\angle A_4A_3A_{34}. \tag{14}$$

The weighted balancing condition of the weighted Fermat-Torricelli point F for $A_1A_2A_3A_4$ taking into account that

$\vec{B_{14}} = -\vec{B_{23}}$, $\vec{B_{12}} = -\vec{B_{34}}$ and $\vec{B_{12}}$ is perpendicular to $\vec{B_{23}}$, we obtain that:

$$B_1 \cos\angle A_1A_2A_{12} = B_4 \cos\angle A_4A_3A_{34} \tag{15}$$

and

$$B_2 \cos\angle A_2A_1A_{12} = B_3 \cos\angle A_3A_4A_{34}. \tag{16}$$

By squaring both sides of (13),(14),(15) and (16) and by adding the first and third derived relation and the second and fourth derived relation, we deduce (11). ☐

We need the following lemma, in order to prove that the symmetry of a thumb is determined by a pair of equal weights w.r. to the two symmetrical roots and a pair of equal weights w.r. to the two symmetrical branches. Let $O = O(0,0)$, be the intersection of the diagonals of $A_1A_2A_3A_4$.

Lemma 1

$$d(A_1,F)^2 + d(A_3,F)^2 = d(A_2,F)^2 + d(A_4,F)^2. \tag{17}$$

Proposition 3 *If the thumb inherits a symmetry w.r to the midperpendicular line of the two opposite sides of the rectangle, which is perpendicular to the ground (equal branches and equal roots), then $B_1 = B_2$ and $B_3 = B_4$.*

Proof. By replacing $d(A_1,F) = d(A_2,F)$ in (17), we get

$d(A_3,F) = d(A_4,F)$.

The weighted Simpson line $A_{12}A_{34}$ is the midperpendicular line of A_1A_2 and A_3A_4 and passes through the weighted Fermat-Torricelli point F. Therefore, $A_1A_2A_3A_4$ is a generalized weighted regular rectangle. Thus, we get:

$$B_1 \sin\angle A_1A_2A_{12} = B_2 \sin\angle A_2A_1A_{12} \tag{18}$$

and

$$B_3 \sin\angle A_3A_4A_{34} = B_4 \sin\angle A_4A_3A_{34}. \tag{19}$$

By replacing $\angle A_1A_2A_{12} = \angle A_2A_1A_{12}$ in (18) and $\angle A_3A_4A_{34} = \angle A_4A_3A_{34}$ in (19), we get: $B_1 = B_2$ and $B_3 = B_4$. ☐

4 Creation of a "botanological" thumb with symmetrical branches in the three dimensional Euclidean Space

Let $A_{1i}A_{2i}A_{3i}A_{4i}$ be n tetrahedra in $\mathbb{R}^3$ and B_{ji} be the weight (positive real number) which corresponds to the vertex A_{ji}, for $i = 1,2,...,n$ and $j = 1,2,3,4$.

Weighted Fermat-Torricelli trees and weighted Steiner trees that have got a subconscious have been established in [10] and [11].

We denote by $\vec{u}(A_{ik},A_{jk})$ the unit vector from A_{ik} to A_{jk}. We assume that $\|\sum_{j=1}^{4} B_{jk}\vec{u}(A_{ik},A_{jk})\| > B_{ik}$ hold, in order to locate weighted Fermat-Torricelli trees with four branches $\{A_{0k}A_{1k}, A_{0k}A_{2k}, A_{0k}A_{3k}, A_{0k}A_{4k}\}$ that got a subconscious node.

Lemma 2 (Geometric plasticity of weighted Fermat-Torricelli trees that have got a subconscious node[10]) *If we select a point P_{ik} with a non-negative weight B_{ik} on the ray that is defined by the line segment $A_{0k}A_{ik}$, such that:*

$$\|\sum_{j=1}^{4} B_{jk}\vec{u}(P_{ik},P_{jk})\| > B_{ik},$$

Then the corresponding weighted Fermat-Torricelli node P_{0k} that has got a subconscious of $\{P_{0k}P_{1k}, P_{0k}P_{2k}, P_{0k}P_{3k}, P_{0k}P_{4k}\}$ remains the same with A_{0k}, for $k = 1,2,3,...,n$.

The modified weighted Fermat-Torricelli problem for tetrahedra states that:

Problem 2 (Modified weighted Fermat-Torricelli problem [10])
Let $A_{1k}A_{2k}A_{3k}A_{4k}$ be a tetrahedron in $\mathbb{R}^3$, $\mathcal{B}_{ik}$ be a non-negative number (weight) which corresponds to each line segment $A_{0k}A_{ik}$, respectively. Find a point A_{0k} which minimizes the sum of the lengths of the line segments a_{0ik} that connect every vertex A_{ik} with A_{0k} multiplied by the positive weight $\mathcal{B}_{ik}$:

$$\sum_{i=1}^{4} \mathcal{B}_i a_{0ik} = minimum. \tag{20}$$

By letting $\mathcal{B}_{ik} = B_{ik}$, for $i = 1,2,3,4$, $k = 1,2,...,n$, the weighted Fermat-Torricelli problem for tetrahedra and the corresponding modified weighted Fermat-Torricelli problem for tetrahedra are equivalent by collecting instantaneous images of the weighted Fermat-Torricelli network via the geometric plasticity of tetrahedra in $\mathbb{R}^3$.

The geometric plasticity of tetrahedra connects the weighted Fermat-Torricelli problem for tetrahedra with the modified weighted Fermat-Torricelli problem for boundary tetrahedra by allowing a mass flow continuity for the weights, such that the corresponding weighted Fermat-Torricelli point remains the same in $\mathbb{R}^3$.

The weighted Fermat-Torricelli nodes remain the same $P_{0k} \equiv A_{0k}$ but different values of the subconscious (remaining weight) may occur.

We denote by B_{ji} a mass flow which is transferred from A_{ji} to A_{0i} for $j = 1,2$ by B_{0i} a residual weight which remains at A_0 and by B_{ki} a mass flow which is transferred from A_{0i} to A_{ki} for $k = 3,4$.

We denote by $\tilde{B}_{ji}$ a mass flow which is transferred from A_{0i} to A_{ji} for $i = 1,2$, by $\tilde{B}_{0i}$ a residual weight which remains

at A_{0i} and by $\tilde{B}_{ki}$ a mass flow which is transferred from A_{ki} to A_{0i}, for $k = 3,4$.
Thus, we derive the weighted outward flow condition and weighted inward flow condition:

$$B_{1i} + B_{2i} = B_{3i} + B_{4i} + B_{0i} \tag{21}$$

and

$$\tilde{B}_{1i} + \tilde{B}_{2i} + \tilde{B}_{0i} = \tilde{B}_{3i} + \tilde{B}_{4i}. \tag{22}$$

By adding (21) and (22) and by setting $\bar{B}_{0i} = B_{0i} - \tilde{B}_{0i}$, we obtain:

$$\bar{B}_{1i} + \bar{B}_{2i} = \bar{B}_{3i} + \bar{B}_{4i} + \bar{B}_{0i} \tag{23}$$

such that:

$$\bar{B}_{1i} + \bar{B}_{2i} + \bar{B}_{3i} + \bar{B}_{4i} = c, \tag{24}$$

where c is a positive real number, for $i = 1,2,...,n$.

We denote by a_{0im} the length of the line segment $A_{0m}A_{im}$, $\alpha_{i0jm} \equiv \angle A_{im}A_0A_{jm}$ and $\alpha_{i,j0km}$ the angle which is formed by the line segment that connects A_{0m} with the trace of the orthogonal projection of A_{im} to the plane defined by $\triangle A_{jm}A_0A_{km}$ with a_{0im}, for $i,j,k,l = 1,2,3,4$, $i \neq j \neq k \neq i$ and $m = 1,2,3,...,n$

Lemma 3 (Determination of the position of A_{0i} on exactly five given angles [10, Proposition 2.9, p. 902], [12, Formulas (10), (11), p. 120])
Each angle $\alpha_{i,k0ml}$ depends on α_{102l}, α_{103l}, α_{104l}, α_{203l} and α_{204l}, for $i,k,m = 1,2,3,4$, $i \neq k \neq m$, and $l = 1,2,,...,n$

$$\cos^2(\alpha_{i,k0ml}) = \frac{\sin^2(\alpha_{k0ml}) - \cos^2(\alpha_{m0il}) - \cos^2(\alpha_{k0il})}{\sin^2(\alpha_{k0ml})} + \\ + \frac{2\cos(\alpha_{m0il})\cos(\alpha_{k0il})\cos(\alpha_{k0ml})}{\sin^2(\alpha_{k0ml})} \tag{25}$$

and

$$\cos\alpha_{304} = -\frac{1}{4}[2b+ \\ + 4\cos\alpha_{102}(\cos\alpha_{104}\cos\alpha_{203} + \cos\alpha_{103}\cos\alpha_{204}) - \\ - 4(\cos\alpha_{103}\cos\alpha_{104} + \cos\alpha_{203}\cos\alpha_{204})]\csc^2\alpha_{102} \tag{26}$$

or

$$\cos\alpha_{304} = \frac{1}{4}[4\cos\alpha_{103}(\cos\alpha_{104} - \cos\alpha_{102}\cos\alpha_{204}) + \\ + 2(b + 2\cos\alpha_{203}(-\cos\alpha_{102}\cos\alpha_{104} + \cos\alpha_{204}))]\csc^2\alpha_{102} \tag{27}$$

where

$$b \equiv \sqrt{\prod_{i=3}^{4}(1 + \cos(2\alpha_{102}) + \cos(2\alpha_{10i}) + \cos(2\alpha_{20i}) - 4\cos\alpha_{102}\cos\alpha_{10i}\cos\alpha_{20i})}.$$

We denote by α_l the dihedral angle which is formed by the planes defined by $\triangle A_{1l}A_{0l}A_{2l}$ and $\triangle A_{1l}A_{2l}A_{3l}$, and by $\alpha_{g_{4l}}$ the dihedral angle formed by the planes defined by $\triangle A_{1l}A_{4l}A_{2l}$ and $\triangle A_{1l}A_{2l}A_{3l}$, for $l = 1,2,...,n$.

Lemma 4 [[10, Formula (27), p. 997]]
The variable length a_{04l} is given by

$$a_{04l}^2 = a_{02}^2 + a_{24l}^2 - 2a_{24l}\Bigg[\sqrt{a_{02l}^2 - h_{0,12l}^2}\cos\alpha_{124l} + \\ + h_{0,12l}\sin\alpha_{124l}\left(\cos\alpha_{g_{4l}}\left(\frac{\left(\frac{a_{02}^2 + a_{23}^2 - a_{03}^2}{2a_{23}}\right) - \sqrt{a_{02l}^2 - h_{0,12l}^2}\cos\alpha_{123l}}{h_{0,12l}\sin\alpha_{123l}}\right) + \\ + \sin\alpha_{g_{4l}}\sin\arccos\left(\frac{\left(\frac{a_{02l}^2 + a_{23l}^2 - a_{03l}^2}{2a_{23l}}\right) - \sqrt{a_{02l}^2 - h_{0,12l}^2}\cos\alpha_{123l}}{h_{0,12l}\sin\alpha_{123l}}\right)\right)\Bigg] \tag{28}$$

and

$$h_{0,12l} = \frac{a_{01l}a_{02l}}{a_{12l}}\sqrt{1 - \left(\frac{a_{01l}^2 + a_{02l}^2 - a_{12l}^2}{2a_{01l}a_{02l}}\right)^2}. \tag{29}$$

Theorem 3 [Dynamic Plasticity of weighted network with two roots and two growing branches]
Given the weighted Fermat-Torricelli point A_{0i} that has got a subconscious $\bar{B}_{0i}$ to be an interior point of the tetrahedron $A_{1i}A_{2i}A_{3i}A_{4i}$ with the vertices lie on four prescribed rays that meet at A_{0i} and from the five given values of α_{102i}, α_{103i}, α_{104i}, α_{203i}, α_{204i}, the positive real weights $\bar{B}_{ji}$ are given by:

$$\bar{B}_{1i} = \left(\frac{\sin\alpha_{4,203i}}{\sin\alpha_{1,203i}}\right)\frac{c - \bar{B}_{0i}}{2}, \tag{30}$$

$$\bar{B}_{2i} = \left(\frac{\sin\alpha_{4,103i}}{\sin\alpha_{2,103i}}\right)\frac{c - \bar{B}_{0i}}{2}, \tag{31}$$

$$\bar{B}_{3i} = \left(\frac{\sin\alpha_{4,102i}}{\sin\alpha_{3,102i}}\right)\frac{c - \bar{B}_{0i}}{2}, \tag{32}$$

$$\bar{B_{4i}} = \frac{c - \bar{B}_{0i}}{2}, \tag{33}$$

under the weighted conditions

$$\bar{B}_{1i} + \bar{B}_{2i} + \bar{B}_{3i} + \bar{B}_{4i} = c, \tag{34}$$

and

$$\bar{B}_{1i} + \bar{B}_{2i} = \bar{B}_{3i} + \bar{B}_{4i} + \bar{B}_{0i}. \tag{35}$$

Proof. By considering a two-way communication network and by assuming mass flow continuity the weights $\bar{B}_{ki}$, for $i = 1,2,3,4$, are determined by the weighted outward and inward flow conditions (21), (22), which yield the weighted conditions (34) and (35).
Thus, we obtain that:

$$\sum_{k=1}^{4} B_{ki} a_{0ki} + \sum_{k=1}^{4} \tilde{B}_{ki} a_{0ki} \to min, \tag{36}$$

which gives

$$\sum_{k=1}^{4} \bar{B}_{ki} a_{0ki} \to min. \tag{37}$$

By differentiating (37) w.r. to a_{01l}, a_{02l} a_{03l}, respectively, taking into account the derivative of a_{04l} w.r. to a_{01l}, a_{02l} a_{03l}, by lemma 4, we obtain (30), (31), (32) and (33). □

Remark 2 *We note that the dynamic plasticity equations of Theorem 3 have been derived in [10] for weighted Fermat-Torricelli trees, which consist of two roots one branch and one growing branch that have inherited a subconscious (weighted Fermat-Torricelli node) under different weighted (inflow - outflow conditions):*
$\bar{B_{1i}} + \bar{B_{2i}} + \bar{B_{3i}} = \bar{B_{0i}} + \bar{B_{4i}}$ *for* $i = 1,2,...,n.$

We assume that the common perpendicular line of $A_{1i}A_{2i}A_{3i}A_{4i}$ passes through the common midpoints m_{12} and m_{34} of $A_{1i}A_{2i}$ and $A_{4i}A_{3i}$, respectively and $m_{12}m_{34} >> A_{1i}A_{2i}$. We denote by φ_i the angle formed by $\overrightarrow{A_{1i}A_{2i}}$ and $\overrightarrow{A}_{4i}A_{3i}$ and by B_{ji} the weight (positive real number) which corresponds to the vertex A_{ji}, for $j = 1,2,3,4$, $i = 1,2,...,n$. Hence, by rotating $A_{1i}A_{2i}A_{3i}A_{4i}$ by φ_i with respect to $m_{12}m_{34}$, we obtain n weighted isosceles trapezoid $A'_{1i}A'_{2i}A'_{3i}A'_{4i}$ and $B'_{ji} = B_{ji}$. We denote by O_i the intersection point of the equal diagonals $A'_{1i}A'_{3i}$ and $A'_{2i}A'_{4i}$, by A_{0i} the corresponding weighted Fermat-Torricelli node with remaining weight B_{0i} (one node that has got a subconscious) and by O_{12i} and O_{34i} the two corresponding weighted Steiner nodes with remaining weights B_{12i} and B_{34i} (two nodes that got a subconscious) for $A'_{1i}A'_{2i}A'_{3i}A'_{4i}$.

Theorem 4 *If* A_{0i} *lies on the common perpendicular segment* $m_{12}m_{34}$, *then*

$$\bar{B_{1i}} = \bar{B_{2i}} \tag{38}$$

and

$$\bar{B_{3i}} = \bar{B_{4i}} \tag{39}$$

Proof. By substituting $\alpha_{4,102i} = \alpha_{3,102i}$ in (32) and (33), we obtain (39). By working cyclically with the indices and by exchanging the indices $3 \to 2$, $4 \to 1$ and $1 \to 4$, $2 \to 3$, we derive (38). □

We may consider that $\{A_{1i}, A_{2i}\}$ lie on a circular cone C_{012i}, having $m_{12}m_{34}$ as axis of rotation with vertex the weighted Fermat-Torricelli point A_{0i} and $\{A_{3i}, A_{4i}\}$ lie on a circular cone C_{034i}, having $m_{12}m_{34}$ as axis of rotation with vertex the weighted Fermat-Torricelli point A_{0i}. We note that C_{012i} and C_{034i} intersect only at A_{0i}.

Proposition 4 (Rotational plasticity of tetrahedra) *If we select* $\{R_{1i}, R_{2i}\}$ *two points with weights* B_{1i}, B_{2i}, *respectively, on* C_{012i}, *such that their midpoint* m_{12i} *lies on the line defined by* $m_{12}m_{34}$ *and* $\{R_{3i}, R_{4i}\}$ *two points with weights* B_{3i} *and* B_{4i}, *respectively, on* C_{034i}, *such that their midpoint* m_{34i} *lies on the line defined by* $m_{12}m_{34}$, *then the corresponding weighted Fermat-Torricelli point* R_{0i} *of* $R_{1i}R_{2i}R_{3i}R_{4i}$ *remains the same with* A_{0i} *for* $B_{1i} = B_{2i}$ *and* $B_{3i} = B_{4i}$, *for* $i = 1,2,...,n.$

Proof. It is a direct consequence of Theorem 4 and taking into account that
$R_{1i}R_{2i}R_{3i}R_{4i}$ are derived by rotating the two isosceles triangles $\triangle R_{1i}A_{0i}R_{2i}$ and $\triangle R_{3i}A_{0i}R_{4i}$ along $m_{12}m_{34}$. By rotating properly $R_{1i}R_{2i}R_{3i}R_{4i}$, we may derive a weighted isosceles trapezoid or a weighted rectangle ($R_{1i}R_{2i} = R_{3i}R_{4i}$) for $B_{1i} = B_{2i}$ and $B_{3i} = B_{4i}$. Thus, the weighted balancing condition $\sum_{j=1}^{4} B_{ji}\overrightarrow{u(A_{0i}, A_{ji})} = \vec{0}$, yields $R_{0i} \equiv A_{0i}$. □

Definition 5 *A "botanological" thumb for a boundary symmetric tetrahedron* $A_{1i}A_{2i}A_{3i}A_{4i}$ *whose common perpendicular passes through the common midpoints* m_{12} *and* m_{34} *of* $A_{1i}A_{2i}$ *and* $A_{4i}A_{3i}$, *respectively and* $m_{12}m_{34} >> A_{1i}A_{2i}$ *is a "botanological" network, which is transformed to a botanological "thumb" for a boundary rectangle or a boundary isosceles trapezoid, by rotating properly* $A_{1i}A_{2i}$ *w.r.* $m_{12}m_{34}$.

Definition 6 *A "botanological" thumb is a collection of "botanological" thumbs for a finite number of boundary symmetric tetrahedra in* $\mathbb{R}^3$.

We will describe an evolutionary scheme for the creation of a "botanological" thumb in $\mathbb{R}^3$.

1. Evolutionary Phase 1
At time $t = 0$, we consider a point "seed" A_{0i} on the ground.

2. Evolutionary Phase 2
After time t, by assuming mass flow continuity two equal roots start to grow underground and two equal branches start to grow overground, such that their endpoints form a boundary rectangle $A'_{1i}A'_{2i}A'_{3i}A'_{4i}$. Taking into account Proposition 3, we derive that $B_{1i} = B_{2i}$ and $B_{3i} = B_{4i}$.

3. Evolutionary Phase 3
We consider two cases: (i) If A_{0i} is the intersection of the diagonals $A'_{1i}A'_{3i}$ and $A'_{2i}A'_{4i}$ the weighted Fermat-Torricelli node A_{0i} has acquired a subconscious $\bar{B}_{0i}$. (ii) If A_{0i} lies

on the midperpendicular line segment $m_{12}m_{34}$ the weighted Fermat-Torricelli node A_{0i} has acquired a subconscious $\bar{B}_{0i}$.

4. Evolutionary Phase 4
The subconscious $\bar{B}_{0i}$ may cause a geometric plasticity and/or a rotational plasticity of the weighted Fermat-Torricelli tree $\{A'_{1i}A_{0i}, A'_{2i}A_{0i}, A'_{3i}A_{0i}, A'_{4i}A_{0i}\}$.

(i) The geometric plasticity (Theorem 2) yields a weighted Fermat-Torricelli tree $\{R_{1i}A_{0i}, R_{2i}A_{0i}, R_{3i}A_{0i}, R_{4i}A_{0i}\}$, such that their endpoints form an isosceles trapezoid $R_{1i}R_{2i}R_{3i}R_{4i}$, $A''_{0i} \equiv A_{0i}$ and $\bar{B}_{ji}$ corresponds to R_{ji}, for $j = 1,2,3,4$ and $i = 1,2,...,n$.

(ii) The rotational plasticity (Proposition 4), the dynamic plasticity (Theorem 3) and the symmetry of boundary tetrahedra taken from Theorem 4, creates a "botanological" thumb for $i = 1,2,...,n$, having the corresponding weighted Fermat-Torricelli node A_{0i} constant on the ground (point "seed"), but with different subconscious quantities $\bar{B}_{0i}$, for $i = 1,2,...,n$.

5 Generalized regularity for tetrahedra in the three dimensional Euclidean Space

The weighted Steiner problem for a boundary weighted tetrahedron $A_1A_2A_3A_4$ in $\mathbb{R}^3$ having two subconscious nodes (weighted Fermat-Torricelli or weighted Steiner points) has been studied recently in [11].

We denote by $A_1A_2A_3A_4$ a tetrahedron in $\mathbb{R}^3$, with $A_i(x_i,y_i,z_i)$ $(i = 1,2,3,4)$, by b_i a positive real number(weight) which corresponds to the vertex A_i, O_{12}, O_{34} two interior points (nodes) of $A_1A_2A_3A_4$ in $\mathbb{R}^3$, by b_{12} the weight which corresponds to O_{12}, b_{34} the weight which corresponds to O_{34}, by H the length of the common perpendicular (Euclidean distance) between the two lines defined by A_1A_2, A_4A_3, by A_iA_j the Euclidean distance from A_i to A_j, by $O_{12}O_{34}$ the Euclidean distance from O_{12} to O_{34}, by A_iO_{12} the Euclidean distance from A_i to O_{12} and by A_jO_{34} the Euclidean distance from A_j to O_{34}, by T_{12} the intersection point of the line defined by $O_{12}O_{34}$ and the line defined by A_1A_2 and by T_{34} the intersection point of the line defined by $O_{12}O_{34}$ and the line defined by A_4A_3, M_{12} the midpoint of A_1A_2 and M_{34} the midpoint of A_4A_3, for $i,j = 1,2,3,4$.

We denote by A''_4 the intersection point of the line defined by the A_4A_3 and the line defined by the common perpendicular of A_1A_2 and A_4A_3 and by A''_1 the intersection point of the line defined by A_1A_2 and the line defined by the common perpendicular of A_1A_2

We set
$\vec{a}_{ij} \equiv \overrightarrow{A_iA_j}$, for $i,j = 1,2,3,4$, $i \neq j \neq k$, $\alpha_{12} \equiv \angle A_1O_{12}A_2$, $\alpha_{34} \equiv \angle A_3O_{34}A_4$, $\alpha_1 \equiv \angle A_2O_{12}O_{34}$, $\alpha_2 \equiv \angle A_1O_{12}O_{34}$, $\alpha_3 \equiv \angle A_4O_{34}O_{12}$, $\alpha_4 \equiv \angle A_3O_{34}O_{12}$, $\varphi \equiv \arccos(\frac{\vec{a}_{12}\cdot\vec{a}_{43}}{a_{12}a_{43}})$ and $b_{ST} = \frac{b_{12}+b_{34}}{2}$.

Furthermore, we denote by A_{12} the vertex of $\triangle A_1A_{12}A_2$, such that: $\angle A_1A_{12}A_2 = \pi - \alpha_{12}$, $\angle A_{12}A_1A_2 = \pi - \alpha_1$ and $\angle A_1A_2A_{12} = \pi - \alpha_2$, by A_{34} the vertex of $\triangle A_4A_{34}A_3$, such that: $\angle A_4A_{34}A_3 = \pi - \alpha_{34}$, $\angle A_{34}A_4A_3 = \pi - \alpha_4$ and $\angle A_4A_3A_{34} = \pi - \alpha_3$, by H_{12} the trace of the height of $\triangle A_1A_{12}A_2$ w.r to the base A_1A_2 and by A_{34} the vertex of $\triangle A_4A_{34}A_3$, such that: $\angle A_4A_{34}A_3 = \pi - \alpha_{34}$, $\angle A_{34}A_4A_3 = \pi - \alpha_4$ and $\angle A_4A_3A_{34} = \pi - \alpha_3$ and by H_{34} the trace of the height of $\triangle A_4A_{34}A_3$ w.r to the base A_4A_3.

We set $H \equiv A''_4A''_1$, $t_{34} \equiv A''_4T_{34}$ $t_{12} \equiv A''_1T_{12}$ $k_1 \equiv A''_1A_1$ and $k_2 \equiv A''_4A_4$, $m_{12} \equiv A''_1M_{12}$ and $m_{34} \equiv A''_4M_{34}$, $h'_{12} \equiv A''_1H_{12}$ and $h'_{34} \equiv A''_4H_{34}$.

We assume that: $A_1A_4 + A_2A_3 > A_1A_2 + A_3A_4$.

The weighted Steiner problem for $A_1A_2A_3A_4$ in $\mathbb{R}^3$ states that:

Problem 3 ([11, Problem 5]) *Find $O_{12}(x_0,y_0,z_0)$ and $O_{34}(x_{0'},y_{0'},z_{0'})$ with given weights b_{12} in O_{12} and b_{34} in O_{34}, such that*

$$f(O_{12},O_{34}) = b_1A_1O_{12} + b_2A_2O_{12} + b_3A_3O_{34} + b_4A_4O_{34} + \\ + \frac{b_{12}+b_{34}}{2}O_{12}O_{34} \to min. \tag{40}$$

Theorem 5 ([11, Theorem 3]) *The solution of the weighted Steiner problem is a weighted Steiner tree in $\mathbb{R}^3$ whose nodes O_{12} and O_{34} (weighted Fermat-Torricelli points) are seen by the angles:*

$$\begin{aligned} \cos\alpha_{12} &= \frac{b_{ST}^2 - b_1^2 - b_2^2}{2b_1b_2}, \\ \cos\alpha_1 &= \frac{b_1^2 - b_2^2 - b_{ST}^2}{2b_2b_{ST}}, \\ \cos\alpha_{34} &= \frac{b_{ST}^2 - b_3^2 - b_4^2}{2b_3b_4}, \\ \cos\alpha_4 &= \frac{b_4^2 - b_3^2 - b_{ST}^2}{2b_3b_{ST}}. \end{aligned} \tag{41}$$

The inradius r_{12} is the radius of the inscribed circle of triangle $\triangle A_1A_{12}A_2$ with sides $A_1A_2 = \lambda\frac{b_{12}+b_{34}}{2}$, $A_1A_{12} = \lambda b_2$ and $A_2A_{12} = \lambda b_1$, where $\lambda = \frac{A_1A_2}{\frac{b_{12}+b_{34}}{2}}$.

The inradius r_{34} is the radius of the inscribed circle of triangle $\triangle A_3A_{34}A_4$ with sides $A_3A_4 = \lambda\frac{b_{12}+b_{34}}{2}$, $A_3A_{34} = \lambda b_4$ and $A_4A_{34} = \lambda b_3$, where $\lambda = \frac{A_3A_4}{\frac{b_{12}+b_{34}}{2}}$.

We use the substitutions for r_{12} and r_{34}, ([11, Section 2, p. 6]):

$$r_{12} \equiv \frac{A_1A_2}{(b_1+b_2+\frac{b_{12}+b_{34}}{2})(b_1+b_2-\frac{b_{12}+b_{34}}{2})(b_2+\frac{b_{12}+b_{34}}{2}-b_1)(b_1+\frac{b_{12}+b_{34}}{2}-b_2)},$$

$$r_{34} \equiv \frac{A_4A_3}{(b_3+b_4+\frac{b_{12}+b_{34}}{2})(b_3+b_4-\frac{b_{12}+b_{34}}{2})(b_3+\frac{b_{12}+b_{34}}{2}-b_4)(b_4+\frac{b_{12}+b_{34}}{2}-b_3)},$$

$$\beta_{12} = \arccos(\frac{A_1A_2}{2r_{12}}),$$

$$\beta_{34} = \arccos(\frac{A_4A_3}{2r_{34}}).$$

Theorem 6 ([11, Theorem 4]) *The following system of equations w.r. to t_{34} and t_{12} allows the computation of the position of the weighted Simpson line $O_{12}O_{34}$ of the weighted full Steiner tree for $A_1A_2A_3A_4$:*

$$\frac{t_{34}-t_{12}\cos\phi}{\sqrt{H^2+t_{12}^2\sin^2\phi}}=\frac{h'_{34}-t_{34}}{r_{34}} \tag{42}$$

and

$$\frac{t_{12}-t_{34}\cos\phi}{\sqrt{H^2+t_{34}^2\sin^2\phi}}=\frac{h'_{12}-t_{12}}{r_{12}} \tag{43}$$

Proposition 5 ([11, Proposition 1])

$$\frac{t_{34}-t_{12}\cos\phi}{\sqrt{H^2+t_{12}^2\sin^2\phi}}=\frac{m_{34}-t_{34}}{a_{34}\frac{\sqrt{3}}{2}} \tag{44}$$

and

$$\frac{t_{12}-t_{34}\cos\phi}{\sqrt{H^2+t_{34}^2\sin^2\phi}}=\frac{m_{12}-t_{12}}{a_{12}\frac{\sqrt{3}}{2}} \tag{45}$$

Theorem 7 ([11, Theorem 5]) *The following system of equations w.r. to t_{34}, t_{12} and $\angle A_4FA_3$ allows the computation of the position of the line defined by $T_{12}T_{34}$ of the (unweighted) Fermat-Torricelli tree of $A_1A_2A_3A_4$:*

$$\frac{t_{34}-t_{12}\cos\phi}{\sqrt{H^2+t_{12}^2\sin^2\phi}}=\frac{m_{34}-t_{34}}{\frac{a_{34}}{2}\tan\frac{\angle A_4FA_3}{2}}, \tag{46}$$

$$\frac{t_{12}-t_{34}\cos\phi}{\sqrt{H^2+t_{34}^2\sin^2\phi}}=\frac{m_{12}-t_{12}}{\frac{a_{12}}{2}\tan\frac{\angle A_4FA_3}{2}}, \tag{47}$$

$$\cot\frac{\angle A_4FA_3}{2}= \frac{2(H^2+k_1(t_{12}-t_{34}^2\cos\varphi))+k_2(t_{34}-t_{12}\cos\varphi)}{(t_{12}-k_1)\sqrt{H^2+t_{34}^2\sin^2\varphi}+(t_{34}-k_2)\sqrt{H^2+t_{12}^2\sin^2\varphi}}. \tag{48}$$

We denote by ω the dihedral angle (twist angle) formed by the planes $A_1A_2T_{12}T_{34}$ and $A_4A_3T_{34}T_{12}$, by $\varphi_{12}=\angle A_1T_{12}T_{34}$ and $\varphi_{34}=\angle A_4T_{34}T_{12}$.

Theorem 8 ([11, Theorem 6]) *The twist angle ω is given by*

$$\cos\omega=\frac{\cos\varphi-\cos\varphi_{12}\cos\varphi_{34}}{\sin\varphi_{12}\sin\varphi_{34}}. \tag{49}$$

Remark 3 *We correct two typographical errors that occur in [11] by replacing $\sqrt{H^2+t_{34}\sin^2\phi}$ by $\sqrt{H^2+t_{34}^2\sin^2\phi}$ and the angle φ_{34} by $\sin\varphi_{34}$ in [11, Formula (3.1)].*

Definition 7 *A generalized regular tetrahedron is a tetrahedron, which determines a generalized (weighted) regular quadrilateral, formed by rotating A_1A_2 or A_3A_4 by the twist angle ω, w.r. to the (weighted) Simpson line $A_{12}A_{34}$.*

We denote by ω_F the twist angle formed by the planes defined by $\triangle A_1FA_2$ and $\triangle A_3FA_4$ and by ω_S the twist angle formed by the planes $\triangle A_1O_{12}A_2$ and $\triangle A_3O_{34}A_4$.

Theorem 9 (Generalized regularity of tetrahedra) *If $A_1A_2A_3A_4$ is a generalized regular quadrilateral, then generalized regular tetrahedra are derived by:*
(i) rotating the twist angle ω_F w.r. to the line defined by $M_{12}M_{34}$

$$\cos\omega_F=\frac{\cos\varphi-\cos^2\angle A_1M_{12}F}{\sin^2\angle A_1M_{12}F}. \tag{50}$$

or (ii)rotating the twist angle ω_F w.r. to the Simpson line defined by $T_{12}T_{34}$

$$\cos\omega_S=\frac{\cos\varphi-\cos^2\angle A_1T_{12}O_{12}}{\sin^2\angle A_1T_{12}O_{12}}. \tag{51}$$

Proof. A generalized regular convex quadrilateral is a trapezoid having the property: $A_1A_2 \parallel A_3A_4$. Thus, the Fermat-Torricelli point F is the intersection of diagonals A_1A_3 and A_2A_4 and lies on the line defined by $M_{12}M_{34}$, which yields $\angle A_1M_{12}F=\angle A_3M_{34}F$. By substituting $\angle A_1M_{12}F=\angle A_3M_{34}F$ in (49), we obtain (50). We recall that $A_1A_2A_{12}$ and $A_3A_4A_{34}$ are equilateral triangles outward from $A_1A_2A_3A_4$ and the Simpson line intersects A_1A_2 and A_3A_4 at T_{12} and T_{34}, respectively. By substituting $\angle A_1T_{12}O_{12}=\angle A_3T_{34}O_{34}$ in (49), we obtain (51). □

Remark 4 *The position of A''_1 and A''_4 may be calculated by Theorem 7.*

Definition 8 *A weighted regular tetrahedron is a tetrahedron in $\mathbb{R}^3$, such that the weighted Simpson line L passes through the weighted Fermat-Torricelli point F.*

We assume that $A_1A_2A_3A_4$ is a weighted regular tetrahedron $A_1A_2A_3A_3$, such that: $M_{12}M_{34} >> \max A_1A_2, A_3A_4$.

Theorem 10 (Weighted regularity of tetrahedra) *The common perpendicular line of A_1A_2 and A_3A_4 passes through the common midpoints M_{12} and M_{34}, respectively, if and only if $b_1=b_2$ and $b_3=b_4$.*

Proof. The weighted Simpson line passes through A_{12}, A_{34}, the weighted Steiner nodes O_{12}, O_{34}, the weighted Fermat-Torricelli point F and M_{12}, M_{34}. Therefore, $\triangle A_1A_2A_{12}$ and $A_3A_4A_{34}$ are isosceles triangles $A_1A_{12} = A_2A_{12}$ and $A_3A_{34} = A_4A_{34}$, which yield $b_1 = b_2$ and $b_3 = b_4$. Hence, it is shown one direction.
We assume that the common perpendicular line of A_1A_2 and A_3A_4 does not pass through the common midpoints M_{12} and M_{34}, $b_1 = b_2$ and $b_3 = b_4$. By substituting $b_1 = b_2$ and $b_3 = b_4$ and given a subconscious weight B_S in (41), we derive that $\angle A_1O_{12}O_{34} = \angle A_2O_{12}O_{34}$ and $\angle A_3O_{34}O_{12} = \angle A_4O_{34}O_{12}$. By substituting $b_1 = b_2$, $b_3 = b_4$ in (42) and (43) we obtain the values of t_{12} and t_{34}, in order to calculate the twist angle ω_S. By rotating A_1A_2 w.r. to $A_{12}A_{34}$ by ω_S, $A_1A_2 \parallel A_3A_4$, and $A_{12}A_{34}$ passes through M_{12}, M_{34}, otherwise O_{12}, O_{34} and F are not collinear. It proves another direction and the theorem as well. □

We may follow the same evolutionary scheme for a "botanological" thumb in $\mathbb{R}^3$. Taking into account that the point seed which has got a subconscious B_{ST} is located underground, an evolutionary two way communication network will start to grow having two roots one main branch and two branches. By assuming a constant mass flow continuity that corresponds to the two roots $b_1 = b_2$ (O_{12} is located underground) one main branch with remaining weight B_{ST} and two branches with weights $b_3 = b_4$ (O_{34} is located overground). Therefore, by applying Theorem 10 we obtain a boundary weighted regular tetrahedron formed by the endpoints of two symmetrical roots and two symmetrical branches, such that the main branch is perpendicular to the ground.

References

[1] H. S. M. Coxeter, Affinely regular polygons, *Abh. Math. Semin. Univ. Hamb.* **34** (1969), 38–58.

[2] H. S. M. Coxeter, Affine regularity, *C. R. Math. Acad. Sci., Soc. R. Can.* **13** (5) (1991), 181–186.

[3] H. S. M. Coxeter, Affine regularity, *Abh. Math. Semin. Univ. Hamb.* **62** (1992), 249–253.

[4] L. Gerber, Napoleon's theorem and the parallelogram inequality for affine regular polygons, *Am. Math. Mon.* **87** (1980), 644–648.

[5] E. N. Gilbert, H. O. Pollak, Steiner Minimal trees, *SIAM J. Appl. Math.* **16** (1968), 1–29.

[6] A. O. Ivanov, A. A. Tuzhilin, Weighted minimal binary trees, *Russ. Math. Surv.* **50**(3) (1995), 623–624.

[7] Z. A. Melzak, On the Steiner problem, *Canad. Math. Bull.* **4** (1961), 143–148.

[8] J. H. Rubinstein, D. A. Thomas, J. Weng, Minimum networks for four Points in Space, *Geom. Dedicata.* **93** (2002), 57–70.

[9] A. N. Zachos, Exact location of the weighted Fermat-Torricelli point on flat surfaces of revolution, *Result. Math.* **65**(1-2) (2014), 167–179.

[10] A. Zachos, The plasticity of some mass transportation networks in the three dimensional Euclidean space, *J. Convex Anal.* **27**(3) (2020), 989–1002.

[11] A. N. Zachos, An evolutionary design of weighted minimum networks for four points in the three-dimensional Euclidean space, *Analysis (Munchen)* **41**(2) (2021), 79–112.

[12] A. Zachos, G. Zouzoulas, The weighted Fermat-Torricelli problem for tetrahedra and an "inverse" problem, *J. Math. Anal. Appl.* **353** (2009), 114–120.

[13] A. Zachos, G. Zouzoulas, An evolutionary structure of convex quadrilaterals. III., *J. Convex Anal.* **25**(3) (2018), 759–765.

Anastasios N. Zachos
orcid.org/0000-0002-7137-3096
azachos@gmail.com

University of Patras, Department of Mathematics
GR-26500 Rion, Greece

https://doi.org/10.31896/k.25.7
Original scientific paper
Accepted 9. 12. 2021.

ARNASLI YAHYA
JENÖ SZIRMAI

Visualization of Sphere and Horosphere Packings Related to Coxeter Tilings by Simply Truncated Orthoschemes with Parallel Faces

Visualization of Sphere and Horosphere Packings Related to Coxeter Tilings by Simply Truncated Orthoschemes with Parallel Faces

ABSTRACT

In this paper we describe and visualize the densest ball and horoball packing configurations to the simply truncated 3-dimensional hyperbolic Coxeter orthoschemes with parallel faces, using the results of [24]. These beautiful packing arrangements describe and show the very interesting structure of the mentioned orthoschemes and the corresponding Coxeter reflection group. We use the Beltrami-Cayley-Klein ball model of 3-dimensional hyperbolic space $\mathbb{H}^3$, the images were made by the Python programming language.

Key words: Coxeter group, horosphere, hyperbolic geometry, packing, tilings

MSC2010: 52C17 52C22 52B15

Vizualizacija pakiranja sfera i horosfera povezanih s Coxeterovim popločavanjem krnjim ortoshemama paralelnih strana

SAŽETAK

U ovom radu opisujemo i vizualiziramo najgušće konfiguracije pakiranja sfera i horosfera na krnjim 3-dimenzionalnim hiperboličnim Coxeterovim ortoshemama s paralelnim stranama, koristeći rezultate [24]. Ovi lijepi rasporedi pakiranja opisuju i pokazuju vrlo zanimljivu strukturu spomenutih ortoshema i odgovarajuće Coxeterove zrcalne grupe. Koristimo sferni Beltrami-Cayley-Kleinov model 3-dimenzionalnog hiperboličnog prostora $\mathbb{H}^3$. Slike su izrađene programskim jezikom Python.

Ključne riječi: Coxeterova grupa, horosfera, hiperbolična geometrija, pakiranje, popločavanje

1 Introduction

Visualization of mathematical problems is not only a representation of specific objects or an approach in the teaching process, but also plays an important role in understanding the problem and developing solution steps. It can be shown the deeper context of the problem and the possibilities to move forward.

In hyperbolic spaces $\mathbb{H}^n$ for $2 \leq n \leq 9$, the known densest ball and horoball configurations are derived by Coxeter simplex tilings, generated by reflections in the simplex hyperplanes [5]. In the former papers, they do not have parallel faces.

In periodic ball or horoball packings, the local density described below can be extended to the entire hyperbolic space and it is related to the simplicial density function that we generalized in [19] and [20]. In this paper, we shall use such definition of packing density by [24].

A Coxeter simplex in $\overline{\mathbb{H}}^n$ has dihedral angles either integral submultiples of π or zero. Thus, the group generated by reflections in the simplex side hyperplanes is isometry group of $\mathbb{H}^n$ with the Coxeter simplex as fundamental domain. Hence the group gives regular tessellations. We note here that the Coxeter groups are finite for $\mathbb{S}^n$, and infinite for $\mathbb{E}^n$ or $\overline{\mathbb{H}}^n$ [1, 5, 7, 8, 9, 17, 23].

There are non-compact Coxeter simplices in $\overline{\mathbb{H}}^n$ with ideal vertices in $\partial\mathbb{H}^n$, however, only for dimensions $2 \leq n \leq 9$;

and only a finite number of them exists in dimensions $n \geq 3$, see Johnson *et al.* [9] and Kellerhals [10]. Such simplices are the most elementary building blocks of hyperbolic manifolds, the volume of which is an important topological invariant.

The simplicial packing density upper bound $d_3(\infty) = (1 + \frac{1}{2^2} - \frac{1}{4^2} - \frac{1}{5^2} + \frac{1}{7^2} + \frac{1}{8^2} - \frac{1}{10^2} - \frac{1}{11^2} + \dots)^{-1} = 0.85327\dots$ cannot be achieved by packing regular balls, instead it is realized by horoball packings of $\overline{\mathbb{H}}^3$, the regular ideal simplex tiles. More precisely, the centres of horoballs in $\partial\overline{\mathbb{H}}^3$ lie at the vertices of the ideal regular Coxeter simplex tiling with Schläfli symbol $(3,3,6)$, see [2, 3, 4, 6, 18].

In [11] we have proved that this optimal horoball packing configuration in $\mathbb{H}^3$ is not unique. We gave asymptotic Coxeter packings by horoballs of different types, that have different relative densities with respect to the fundamental domain, yielding the Böröczky–Florian-type simplicial upper bound [4].

Furthermore, in [19, 20] we have found that, by allowing horoballs of different types at each vertex of a totally asymptotic simplex and generalizing the simplicial density function to $\overline{\mathbb{H}}^n$ for $(n \geq 2)$, the Böröczky-type density upper bound is not valid for the fully asymptotic simplices for $n \geq 4$. For example, in $\overline{\mathbb{H}}^4$ the locally optimal simplicial packing density is $0.77038\dots$, higher than the Böröczky-type density upper bound of $d_4(\infty) = 0.73046\dots$ using horoballs of a single type. However, these ball packing configurations are only locally optimal and cannot be extended to the entirety of the ambient space $\overline{\mathbb{H}}^n$. In [12] we found seven horoball packings of Coxeter simplex tilings in $\overline{\mathbb{H}}^4$ that yield densities of 0.71645, counterexamples to L. Fejes Tóth's conjecture stated in his foundational book *Regular Figures* [6, p. 323].

In [24], we reported [13] and [14] and considered the Coxeter tilings in $\mathbb{H}^3$ where the generating orthoscheme was a simple truncated one with some parallel faces i.e. their dihedral angle is zero (symbol ∞). Here we studied the Coxeter tilings with Schläfli symbol (∞, q, r, ∞) (see Fig. 1. second graph). We determined their optimal ball and horoball packings, proved that the densest packing was realized at tilings $(\infty, 3, 6, \infty)$, and $(\infty; 6; 3; \infty)$ with density ≈ 0.8413392, see Fig.1, 12, 19 and [20, 21, 22] and [14, 15, 16] for further connections.

2 Basic Notions

For the computations and visualization, we use the projective model of the hyperbolic space $\mathbb{H}^3$ [1, 16, 23]. The model is defined in general in the pseudo-Euclidean or Lorentz space $\mathbb{E}^{1,n}$ with signature $(1,n)$, i.e. consider real vector space $\mathbf{V}^{n+1}$ equipped with the bilinear form:

$$\langle\, \mathbf{x},\ \mathbf{y} \rangle = -x^0y^0 + x^1y^1 + \dots + x^ny^n$$

and the following equivalence relation:

$$\mathbf{x}(x^0, ..., x^n) \sim \mathbf{y}(y^0, ..., y^n) \Leftrightarrow \exists\, c \in \mathbb{R}\backslash\{0\} : \mathbf{y} = c \cdot \mathbf{x}$$

to interpret the same point $[x] = [y]$ of $\mathbb{H}^n$. The following quadratic form (as a cone in V^{n+1}):

$$Q = \{[\mathbf{x}] \in \mathcal{P}^n | \langle\, \mathbf{x},\ \mathbf{x} \rangle = 0\} =: \partial\mathbb{H}^n$$

defines the boundary points (at infinity), the inner or proper points of $\mathbb{H}^n$ (for them $\langle\, \mathbf{x},\ \mathbf{x} \rangle < 0$), and the points lying outside of Q are outer points of $\mathbb{H}^n$ (for them $\langle\, \mathbf{x},\ \mathbf{x} \rangle > 0$). We can also define a linear polarity between the points and hyperplanes: the polar hyperplane (a) of a point $[\mathbf{x}] \in \mathcal{P}^n$ is $Pol(\mathbf{x}) := (a) = \{[\mathbf{y}] \in \mathcal{P}^n | \langle\, \mathbf{x},\ \mathbf{y} \rangle = 0\}$, and hence $\mathbf{x} \in \mathbf{V}^{n+1}$ is incident with $a \in V_{n+1}$ iff $\mathbf{x}\ a = 0$. In this projective model, we can define a metric structure related to the above bilinear form, where for the distance of two proper (inner) points:

$$\cosh\left(\frac{d(\mathbf{x},\mathbf{y})}{k}\right) = \frac{-\langle\, \mathbf{x},\ \mathbf{y} \rangle}{\sqrt{\langle\, \mathbf{x},\ \mathbf{x} \rangle \langle\, \mathbf{y},\ \mathbf{y} \rangle}}, \tag{1}$$

(at present we may choose $k = 1$).

This corresponds to the distance formula in the well-known Beltrami-Cayley-Klein model of $\mathbb{H}^n$ of constant curvature $K = -k^2 = -1$. We do not detail the analogous angle metric for the dual form space V_{n+1} that present hyperfaces and $-cos$ expresses their angles of normal vectors (through complex numbers), like in the spherical plane and space [1, 9, 16, 17, 24](see also sect 3).

For a general projective coordinate simplex $A_0A_1A_2A_3$ we use the vector basis $\mathbf{a}_0, \mathbf{a}_1, \mathbf{a}_2, \mathbf{a}_3 \in \mathbf{V}^4$; for its faces b^0, b^1, b^2, b^3 stand $b^0, b^1, b^2, b^3 \in V_4$ with $\mathbf{a}_i b^j = \delta_i^j$, the Kronecher symbol (Einstein convention). A symmetric linear polarity, i.e. plane $\longrightarrow$ point mapping: $V \ni u \longrightarrow \mathbf{u} \in \mathbf{V}^4$ will be defined by $b^i \longrightarrow B^i$, $b^i \longrightarrow b^{ij}\mathbf{a}_j$ with $b^{ij} = b^{ji} (i,j \in \{0,1,2,3\})$, equivalent with a scalar product $\langle u, v \rangle \longrightarrow \mathbb{R}$, $\langle b^i u_i, b^j v_j \rangle = b^{ir} u_i \mathbf{a}_r b^j v_j = u_i b^{ir} \delta_r^j v_j = u_i b^{ij} v_j$.

If the polarity is invertible, i.e $(b^{ij})^{-1} = a_{ij} = \langle \mathbf{a}_i, \mathbf{a}_j \rangle$, as for $\mathbb{H}^3$, then forms (normal vectors of planes) and vectors can be "identified", as later on a polar plane $\longleftrightarrow$ with its pole point in $\mathbb{H}^3$.

3 The structure of truncated asymptotic orthoscheme

Our aim is to visualize the truncated simply asymptotic orthoschemes that contain parallel faces in $\mathbb{H}^3$. This orthoschemes are represented by their Coxeter graphs (see Fig.1-2), where the angle parameters p,q,r satisfy the inequalities $\frac{\pi}{p}+\frac{\pi}{q}<\frac{\pi}{2}$ and $\frac{\pi}{q}+\frac{\pi}{r}\geq\frac{\pi}{2}$.

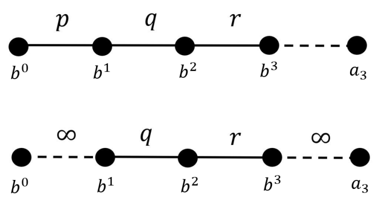

Figure 1: *Coxeter graphs of truncated asymptotic orthoscheme*

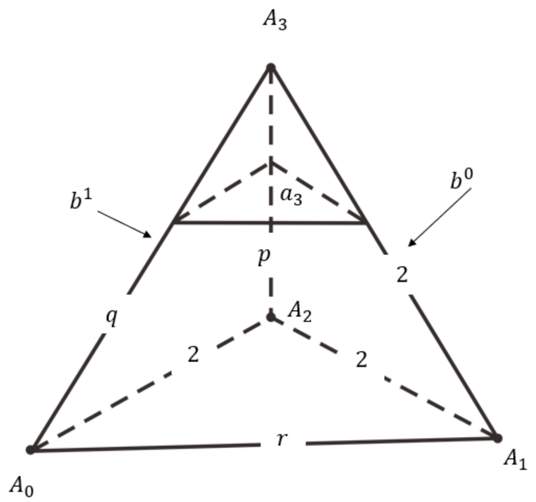

Figure 2: *A simply truncated orthoscheme with polar a_3 of A_3 $\frac{\pi}{p}+\frac{\pi}{q}<\frac{\pi}{2}$, $\frac{\pi}{q}+\frac{\pi}{r}\geq\frac{\pi}{2}$*

First, we will study the truncated orthoschemes that have the corresponding singular Coxeter-Schläfli matrix as follows (e.g from [7, 17]):

$$C=\begin{bmatrix} 1 & -\cos\left(\frac{\pi}{p}\right) & 0 & 0 & 0 \\ -\cos\left(\frac{\pi}{p}\right) & 1 & -\cos\left(\frac{\pi}{q}\right) & 0 & 0 \\ 0 & -\cos\left(\frac{\pi}{q}\right) & 1 & -\cos\left(\frac{\pi}{r}\right) & 0 \\ 0 & 0 & -\cos\left(\frac{\pi}{r}\right) & 1 & c_4 \\ 0 & 0 & 0 & c_4 & 1 \end{bmatrix}, \tag{2}$$

where the constant c_4 can be uniquely determined by the zero determinant condition.

$$c_4=-\sqrt{\frac{1+\cos^2(\frac{\pi}{p})\cos^2(\frac{\pi}{r})-\cos^2(\frac{\pi}{p})-\cos^2(\frac{\pi}{q})-\cos^2(\frac{\pi}{r})}{1-\cos^2(\frac{\pi}{p})-\cos^2(\frac{\pi}{q})}}.$$

In our case, there are two parallel faces that meet in an ideal point. That means the dihedral angle between these two hyperplanes is equal to 0. Therefore, we assume that these two hyperplanes are b^0 and b^1. Thus, their dihedral angle is $w^{01}=\frac{\pi}{p}\to 0$, if p tends to ∞, then Coxeter-Schläfli matrix (2) would change to the following form

$$C^{'}=\begin{bmatrix} 1 & -1 & 0 & 0 & 0 \\ -1 & 1 & -\cos\left(\frac{\pi}{q}\right) & 0 & 0 \\ 0 & -\cos\left(\frac{\pi}{q}\right) & 1 & -\cos\left(\frac{\pi}{r}\right) & 0 \\ 0 & 0 & -\cos\left(\frac{\pi}{r}\right) & 1 & -1 \\ 0 & 0 & 0 & -1 & 1 \end{bmatrix}. \tag{3}$$

As a consequence, plane b^3 and the polar plane a_3 of vertex A_3 will also be parallel, as the second graph in Fig. 1 shows.

The computer visualization of the truncated orthoschemes are given in Fig. 4.

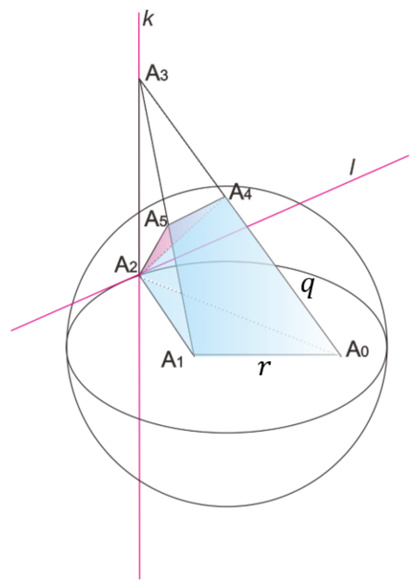

Figure 3: *Truncated orthoscheme with the two intersection pairs of its parallel faces. b^0 and b^1 intersect in ideal line k, b^3 and $a_3=A_2A_4A_5$ do that in l. The ideal vertex $A_2\in k,l$.*

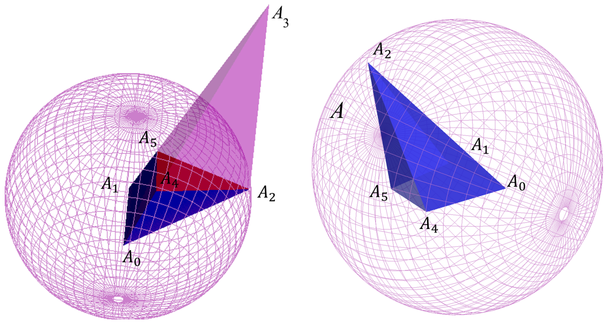

Figure 4: *Truncated orthoscheme, where the truncating face is* $A_2A_4A_5$

4 On sphere packings

In constructing the insphere, the largest inscribed classical sphere, in the truncated orthoscheme, we followed in [24] the procedure of [8] by bisector hyperplane.

The visualization of the optimum insphere in truncated orthoscheme $(\infty,3,3,\infty)$ is given in Fig. 5. The problem may occur if the insphere intersect the truncating hyperplanes a_3 (see Fig 6).

The complete packings densities of insphere packings (and their optimum density) can be found in [24], that gave the optimum packing density ≈ 0.2623649, attained by sphere packing in $(\infty,3,3,\infty)$, small enough, not relevant, related to [17].

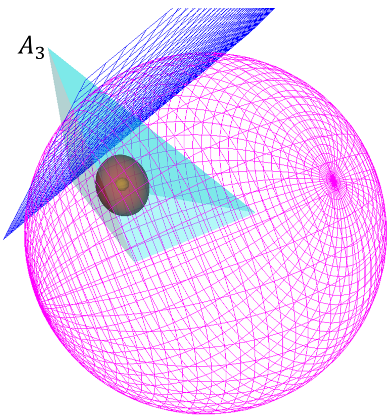

Figure 5: *Optimum insphere in the truncated orthoscheme* $(\infty,3,3,\infty)$

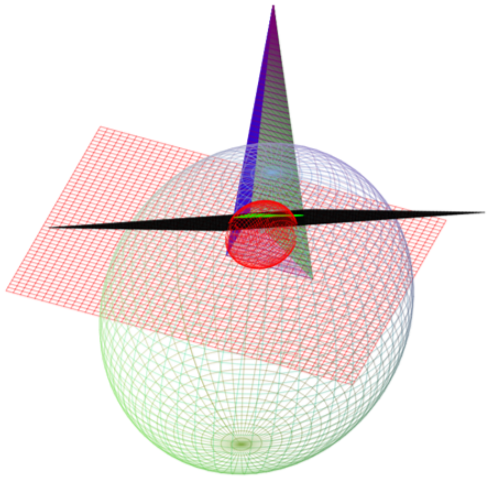

Figure 6: *The insphere intersects the truncating polar plane* a_3 *of vertex* A_3

5 On horosphere packings

A horosphere in hyperbolic geometry is the surface orthogonal to the set of parallel lines, passing through the same ideal point on the absolute quadratic surface (simply absolute) $\partial\mathbb{H}^n$ (at present $n=3$).

We introduce Cartesian homogeneous projective coordinate system using vector basis $\mathbf{e}_i$ $(i=0,1,2,3)$ for $\mathcal{P}^3$ where the coordinate centre of the model is $O=(1,0,0,0)=\mathbf{e}_0$. We pick an arbitrary point at infinity $A_2=(1,0,0,1)$.

As it is known, the equation of a horosphere with centre $A_2=(1,0,0,1)$ through point $S=(1,0,0,s)$ $(s\in(-1,1))$ is

$$\frac{(s-1)^2}{1-s^2}(-x^0x^0+x^1x^1+x^2x^2+x^3x^3)+(x^0-x^3)^2=0$$

This surface can be described in the usual Cartesian coordinate system by the formula

$$\frac{2(x^2+y^2)}{1-s}+\frac{4(z-(\frac{s+1}{2}))^2}{(1-s)^2}=1, \tag{4}$$

where $x=\frac{x^1}{x^0}$, $y=\frac{x^2}{x^0}$, $z=\frac{x^3}{x^0}$.

In computer visualization, it is very powerful to convert the horosphere equation into a polar coordinate system. We use the following conversion

$$x=\sqrt{\frac{1-s}{2}}\cos\theta\sin\phi, \quad y=\sqrt{\frac{1-s}{2}}\sin\theta\sin\phi,$$
$$z=\frac{1+s}{2}+\frac{1-s}{2}\cos\phi, \tag{5}$$

where parameters $\theta\in[0,2\pi)$, $\phi\in[0,\pi]$.

We will apply the previous truncated orthoscheme (based on the set of unit normal Napier cycles) in [7, 24] as before.

We separate our discussion into two cases depending on the number of vertices lying at infinity A_0, A_2 or both. We can also attach two horospheres altogether, where they are touching each other on edge A_0A_2.

5.1 Packings with one horosphere

We have some truncated orthoschemes given with Schläfli symbols such that it has only one point at the infinity: $(\infty,3,3,\infty)$, $(\infty,3,4,\infty)$, $(\infty,3,5,\infty)$, $(\infty,4,3,\infty)$, $(\infty,5,3,\infty)$. However, if the truncated orthoscheme has two ideal vertices of truncated orthoscheme we can also study the corresponding horosphere packing centred at one either of these vertices.

It is clear that the densest horoshpere packing configuration would be reached whenever this horosphere (horoball) with centre A_2 touch the opposite face (represented by hyperplane b^2). One could simply take the projection of A_2 into b^2 by the projection formula $\mathbf{a}_2 \longmapsto a_2^p = \mathbf{a}_2 - \langle \mathbf{a}_2, \mathbf{b}^2 \rangle \mathbf{b}^2$. The optimal horosphere should contain the point A_2^p therefore we can determine the parameter s and so the actual equation (4) of the horosphere.

We provide the computer visualization of optimum horospheres packing, attained by truncated orthoscheme tilings with Schläfli symbols $(\infty,3,3,\infty)$, in Fig. 7-9. The optimum packing density is ≈ 0.8188080, see [24].

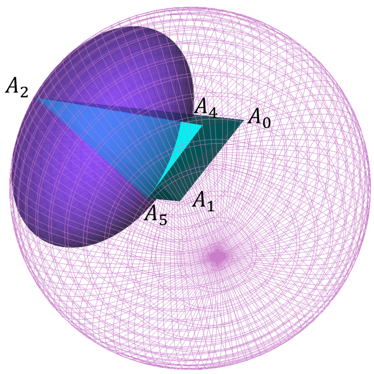

Figure 7: *The largest horoball related to truncated orthoscheme of tiling* $(\infty,3,3,\infty)$

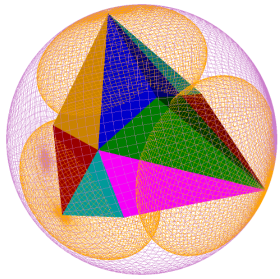

Figure 8: *The neighbouring turncated orthoschemes to horosphere configuration (first crown) to tiling* $(\infty,3,3,\infty)$

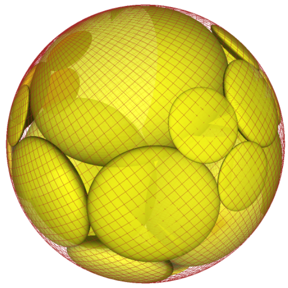

Figure 9: *The first to third crowns of neighbouring horosphere configurations to tiling* $(\infty,3,3,\infty)$

5.2 Packing with two horospheres

Now, we focus on the orthoscheme tiling with the Schläfli symbols $(\infty,3,6,\infty)$, $(\infty,4,4,\infty)$, and $(\infty,6,3,\infty)$.

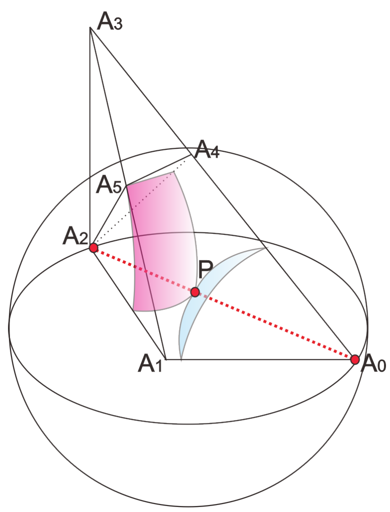

Figure 10: *Two horospheres,* $\mathcal{B}_0$ *and* $\mathcal{B}_2$*, that touch each other at a point lying on edge* A_0A_2

Remark 1 *: These two horospheres could not intersect the opposite faces b^0 and b^2, therefore there will be a restriction for the movement of the point of tangency along edge A_2A_0.*

We can parameterize the possible movement of the point of tangency P along edge A_2A_0, see Fig. 10, e.g. $P(\mathbf{r}(t)) = (1-t)\mathbf{a}_2 + t\cdot\mathbf{a}_0$. Then, for every possible t, we have parameters s_i $(i = 1,2)$ related to both horospheres.

Optimal horoball packing of tiling $(\infty,4,4,\infty)$

In this situation, we have quite interesting structure, we obtain that the possible parameter of t lies in $[\approx 0.2150 < t <\approx 0.3497]$. We can compute the volumes of horoball sectors as the functions of t. It is analogous to the previous case, the volume function of horoball sectors centred at A_2 is a monotonic increasing function of t if the point of tangency moving with direction to A_0 while the volume function of horoball sectors centred at A_0 is decreasing in this situation.

In this case, we proved (in [24]) that the density was increasing as a function of t, see Fig. 11. Furthermore, the maximum density $\delta_{opt} \approx 0.8188081$ is attained when t is largest, i.e when the horosphere centred at A_2 touches the opposite face b^2.

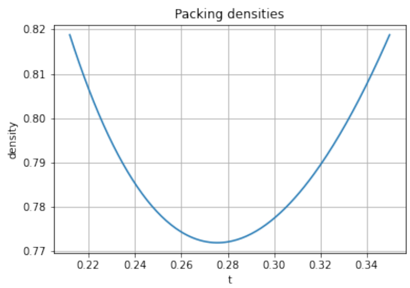

Figure 11: *The plot of density function for all possible t in case $(\infty,4,4,\infty)$*

Optimal horoball packing of tilings $(\infty,3,6,\infty)$ **and** $(\infty,6,3,\infty)$

We similarly visualize the densest horosphere (horoball) packings to the truncated orthoscheme tilings with Schläfli symbol $(\infty,3,6,\infty)$ and $(\infty,6,3,\infty)$.

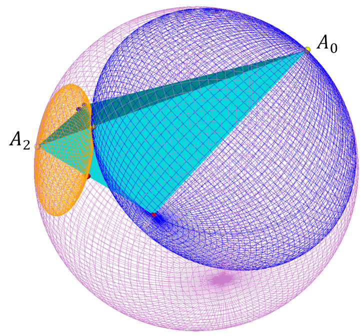

Figure 12: *Two horospheres, $\mathcal{B}_0$ and $\mathcal{B}_2$, that touch each other at the point lying on A_0A_2 related to tiling $(\infty,3,6,\infty)$.*

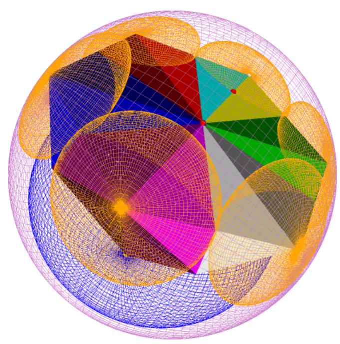

Figure 13: *Adjacent orthoschemes and the corresponding horosphere configuration (first crown) to truncated orthoscheme tiling$(\infty,3,6,\infty)$*

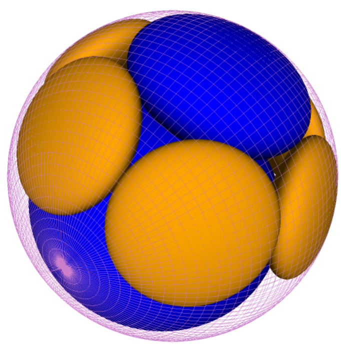

Figure 14: *The horosphere configuration (first crown) related to tiling $(\infty,3,6,\infty)$*

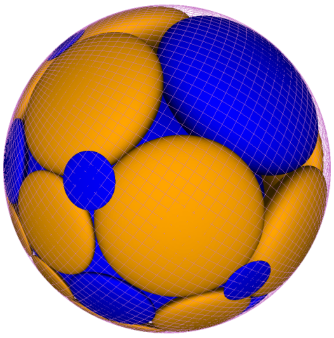

Figure 15: *The optimum packing density horospheres configuration (first-third crown) to the orthoscheme tiling* $(\infty, 3, 6, \infty)$ *with density 0.8413392.*

There are some basic facts for these (dual) orthoschemes.

1. In these symmetric dual situations, there is only one possible value of parameter t in each case, $t_{(3,6)} \approx 0.2119416$, $t_{(6,3)}, \approx 0.5745582$.
2. If $(q,r) = (3,6)$ then the optimal horosphere $\mathcal{B}_2$ touches the plane b^2 and $\mathcal{B}_0$ touches the face b^0 and if $(q,r) = (6,3)$ $\mathcal{B}_2$ touches the plane b^2 and $\mathcal{B}_0$ touches the polar face a_3.
3. The packing density of these two configurations are the same, ≈ 0.8413392, see [24].

Finally, we give the computer visualization in Fig. 12-15 related to Coxeter tiling $(\infty, 3, 6, \infty)$ and in Fig. 16-19 for Coxeter tiling $(\infty, 6, 3, \infty)$.

In our opinion, non-Euclidean tilings and packings and their investigations will play an important role in the research of material structure in the near future, thus visualization of them is also important to know them better.

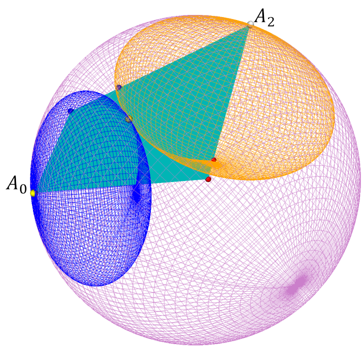

Figure 16: *Two horospheres,* $\mathcal{B}_0$ *and* $\mathcal{B}_2$*, that touch each other at a point on edge* A_0A_2 *related to tiling* $(\infty, 6, 3, \infty)$.

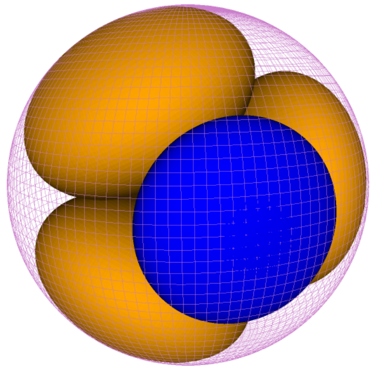

Figure 17: *The horosphere configuration (first crown) to truncated orthoscheme tiling* $(\infty, 6, 3, \infty)$

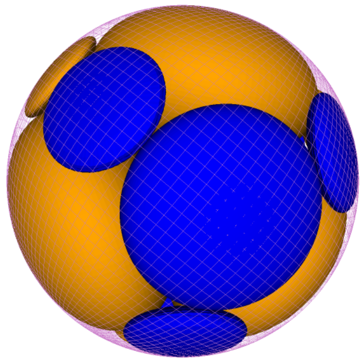

Figure 18: *The optimum packing density horosphere configuration (first-second crown) related to the orthoscheme tiling* $(\infty, 6, 3, \infty)$.

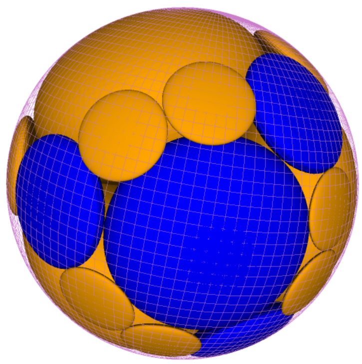

Figure 19: *The optimum packing density horosphere configuration (first-third crown) to the orthoscheme tiling* $(\infty, 6, 3, \infty)$.

References

[1] J. Böhm, E. Hertel, *Polyedergeometrie in n-dimensionalen Räumen konstanter Krümmung, Birkhäuser*, Basel, 1981.

[2] K. Böröczky, Gömbelhelyezések állandó görbületü terekben I-II., *Math. Lapok*, **25 26**, (1974, 1975).

[3] K. Böröczky, Packings of spheres in spaces of constant curvature, *Acta Math. Acad. Sci. Hungar.* **32** (1978), 243–261.

[4] K. Böröczky, A. Florian, Über die dichteste Kugelpackung im hyperbolischen Raum, *Acta Math. Acad. Sci. Hungar.* **15** (1964), 237–245.

[5] H. S. M. Coxeter, *Regular Polytopes*, Courier Corporation, 1973.

[6] L. Fejes Tóth, *Regular Figures*, Pergamon Press, 1964.

[7] H.-C. Im Hof, Napier cycles and hyperbolic Coxeter groups, *Bull. Soc. Math. Belgique* **42** (1990), 523–545.

[8] M. Jacquemet: The inradius of a hyperbolic truncated n-simplex, *Discrete Comput. Geom.* **51** (2014), 997–1016.

[9] N. W. Johnson, R. Kellerhals, J. G. Ratcliffe, S. T. Tschants, The Size of a Hyperbolic Coxeter Simplex, *Transformation Groups* **4**(4) (1999), 329–353.

[10] R. Kellerhals, On the volume of hyperbolic polyhedra, *Math. Ann.* **245** (1989), 541–569.

[11] R. T. Kozma, J. Szirmai, Optimally dense packings for fully assymptotic Coxeter tilings by horoballs of different types, *Monatsh. Math.* **168**(1) (2012), 27–47.

[12] R. T. Kozma, J. Szirmai, New lower bound for the optimal ball packing density of hyperbolic 4-space, *Discrete Comput. Geom.* (2014), doi: 10.1007/s00454-014-9634-1

[13] R. T. Kozma, J. Szirmai, New horoball packing density lower bound in hyperbolic 5-space, *Geom. Dedicata* **206** (2020), 1–25.

[14] R. T. Kozma, J. Szirmai, Horoball packing density lower bounds in higher dimensional hyperbolic n-space for $6 \leq n \leq 9$, *Submitted Manuscript*, (2019), arXiv:1907.00595

[15] R. T. Kozma, J. Szirmai, The structure and visualization of optimal horoball packings in 3-dimensional hyperbolic space, *Submitted Manuscript*, (2016), arXiv:1601.03620, (Appendix: `http://homepages.math.uic.edu/rkozma/SVOHP.html`))

[16] E. Molnár. The projective interpretation of the eight 3-dimensional homogeneous geometries, *Beitr. Algebra Geom.* **38** (1997), 261–288.

[17] E. Molnár, J. Szirmai, Top dense hyperbolic ball packings and coverings for complete Coxeter orthoscheme groups, *Publications de L'institut Mathématique* **103**(117) (2018), 129–146, doi: 10.2298/PIM1817129M

[18] C.A. Rogers, *Packing and Covering*, Cambridge Tracts in Mathematics and Mathematical Physics 54, Cambridge University Press, 1964.

[19] J. Szirmai, Horoball packings to the totally assymptotic regular simplex in the hyperbolic n-space, *Aequat. Math.* **85** (2013), 471–482, doi: 10.1007/s00010.012-0158-6

[20] J. Szirmai, Packings with horo- and hyperballs generated by simple frustum orthoschemes, *Acta Math. Hungar.* **152**(2) (2017), 365–382, doi: 10.1007/s10474-017-0728-0

[21] J. Szirmai, Decomposition method related to saturated hyperball packings, *Ars Math. Contemp.* **16** (2019), 349–358, doi: 10.26493/1855-3974.14850b1

[22] J. Szirmai, The least dense hyperball covering to the regular prism tilings in the hyperbolic n-space, *Ann. Mat. Pur. Appl.* **195**(1) (2016), 235–248, doi: 10.1007/s10231-014-0460-0

[23] E. B. Vinberg, *Geometry II: Spaces of constant curvature*, Springer-Verlag, Berlin, 1993.

[24] A. Yahya, J. Szirmai: Optimal ball and horoball packings generated by 3-dimensional simply truncated Coxeter orthoschemes with parallel faces, *Submitted manuscript*, (2021), arXiv:2107.08416.

Arnasli Yahya
orcid.org/0000-0001-9149-7144
e-mail: arnasli@math.bme.hu

Jenö Szirmai
orcid.org/0000-0001-9610-7993
e-mail: szirmai@math.bme.hu

Budapest University of Technology and Economics
Institute of Mathematics, Department of Geometry
Budapest, P. O. Box: 91, H-1521

https://doi.org/10.31896/k.25.8
Review
Accepted 25. 11. 2021.

Leonard Weydemann
Christian Clemenz
Clemens Preisinger

On the Structural Properties of Voronoi Diagrams

On the Structural Properties of Voronoi Diagrams

ABSTRACT

A Voronoi diagram is a tessellation technique, which subdivides space into regions in proximity to a given set of objects called seeds. Patterns emerging naturally in biological processes (for example, in cell tissue) can be modelled in a biomimicry process via Voronoi diagrams. As they originate in nature, we investigate the physical properties of such patterns to determine whether they are optimal given the constraints imposed by surrounding geometry and natural forces.

This paper describes under what circumstances the Voronoi tessellation has optimal (structural) properties by surveying recent studies that apply this tessellation technique across different scales. To investigate the properties of random and optimized Voronoi tessellations in comparison to a regular tessellation method, we additionally run and evaluate a simulation in Karamba3D, a parametric structural engineering tool for Rhinoceros3D.

The novelty of this research lies in presenting a simple and straightforward simulation of Voronoi diagrams and highlighting how and where their advantages over regular tessellations can be exploited by surveying more advanced approaches as found in literature.

Key words: Voronoi diagrams, 3D tessellations, 3D scaffolds

MSC2010: 51-02, 52C25, 05B45

O strukturalnim svojstvima Voronoi dijagrama

SAŽETAK

Voronoi dijagram je tehnika popločavanja koja čini particiju prostora s obzirom na udaljenosti od zadanog skupa objekata koje nazivamo lokacije (en. *seeds*). Uzorke koji nastaju tokom bioloških procesa (na primjer u staničnom tkivu) možemo modelirati biomimikrijskim procesima korištenjem Voronoi dijagrama. Kako je izvor takvih struktura prirodan, proučavamo fizička svojstva takvih uzoraka da bismo ispitali njihovu optimalnost s obzirom na ograničenja koja nameću vanjska geometrija i prirodne sile.

U ovom članku opisujemo slučajeve u kojima je Voronoi popločavanje (strukturalno) optimalno proučavanjem nedavnih ispitivanja koja ovo popločavanje koriste u različitim razmjerima. Da bismo usporedili svojstva slučajnog te optimiziranog Voronoi popločavanja i metode pravilnog popločavanja, razvili smo simulaciju korištenjem Karamba3D, alata za parametarsko strukturalno inženjersko modeliranje unutar programa Rhinoceros3D.

Novost ovog istraživanja je predstavljanje jednostavne i izravne simulacije Voronoi dijagrama, isticanje njenih prednosti nad pravilnim popločavanjima te pregled korištenja tih prednosti u naprednijim pristupima iz literature.

Ključne riječi: Voronoi dijagrami, 3D popločavanja, 3D konstrukcije

1 Introduction

Figure 1 shows some example patterns found in nature next to a two-dimensional Voronoi diagram, exemplifying the resemblance between some naturally arising patterns and Voronoi tessellation. Since these patterns arise naturally we ask ourselves if there is a reason for this occurrence. If this pattern developed through evolution, there might be some properties that are optimal under constraints imposed by geometry and natural forces. To this end we first created a three-dimensional Voronoi diagram in Grasshopper and investigated its structural properties using the Karamba3D

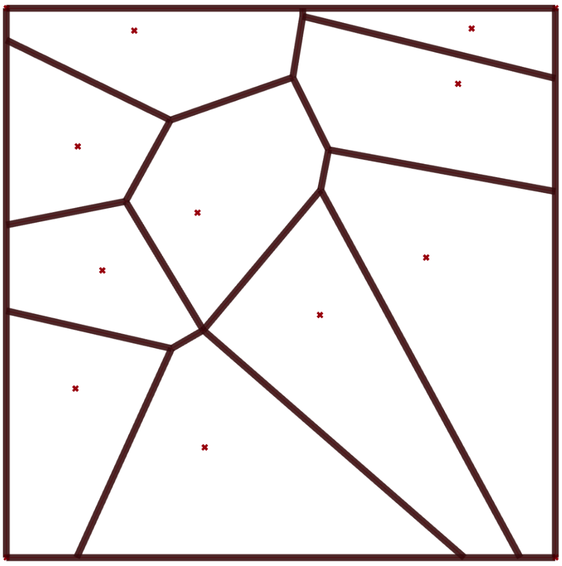

(a)

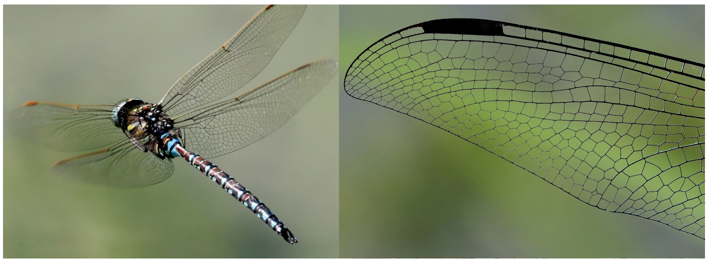

(b)

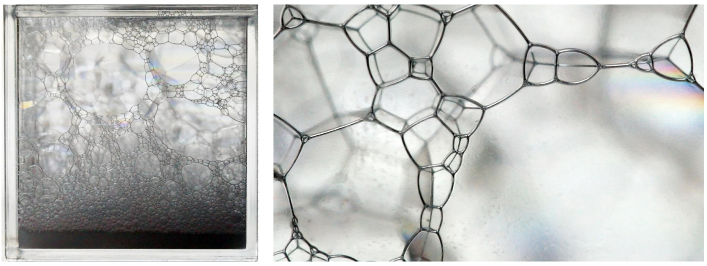

(c)

Figure 1: *(a) shows a two-dimensional Voronoi diagram within a square boundary. (b) shows a similar pattern found in dragonfly wings. (c) shows foam in a transparent cube, after it has settled, displaying a Voronoi-like pattern*[1].

[10] plugin, a structural engineering tool. We do this by creating random Voronoi tessellations of a cube. We compare this to a regular triangle mesh tessellation. Since evolution is an optimization process, we further test a model of a Voronoi tessellation which is optimized in terms of weight and elastic energy of the structure using Octopus [11], which employs a genetic algorithm. We then research relevant literature which employs Voronoi diagrams and exploit its properties in some way. The paper is structured as follows: In Section 2 we discuss the definition and creation of a Voronoi diagram. Section 3 compares random and optimized Voronoi tessellations of a cube with a regular triangle mesh under load. We survey relevant literature on methods where the properties of Voronoi diagrams can be exploited in Section 4. Finally, we give our closing remarks on how and when Voronoi diagrams can be utilized in Section 5.

2 Background

The Voronoi diagram describes a partition of space into regions surrounding a number of seed points. The definition below follows the one found in [1]. For the two-dimensional case, let S be the set of n seed-points. The dominance of a seed p over q, $p,q \in S$, is defined as

$$\mathrm{dom}(p,q) = \{x \in \mathbb{R} | \delta(x,p) \leq \delta(x,q)\}. \tag{1}$$

Here, δ describes the Euclidean distance. This can be adapted for higher dimensions and other metrics. A result of this is the partitioning of space into points lying closer to p or q, creating regions per seed p where portions of the plane lie in all of the dominances of p over remaining seeds in S. Formally, this means

$$\mathrm{reg}(p) = \bigcap_{q \in S-p} \mathrm{dom}(p,q). \tag{2}$$

For each region, the boundary consists of at most $n-1$ edges and vertices, the endpoints of the edges. The points lying on an edge are equidistant from exactly two seeds. The vertices are equidistant from at least three. Thus, the regions form a polygonal partition of the plane, which is called the Voronoi diagram. For a large number of seeds, the Voronoi diagram converges towards a hexagonal pattern [2]. The Voronoi diagram is named for Georgy F. Voronoy, who investigated the n-dimensional case in 1908 [12].

3 Simulation of a 3D Voronoi structure under load

Using Karamba3D [10], a structural engineering tool, we modelled three structures within a cube: a random Voronoi tessellation, a regular triangle mesh tessellation, and an optimized Voronoi tessellation. We use built-in components of Grasshopper to model the Voronoi structure which in turn is used as input for the Karamba3D model. Karamba3D transforms the Voronoi structure into beams which together with supports and loads are assembled into

[1] Photographs ©Georg Glaeser, with permission.

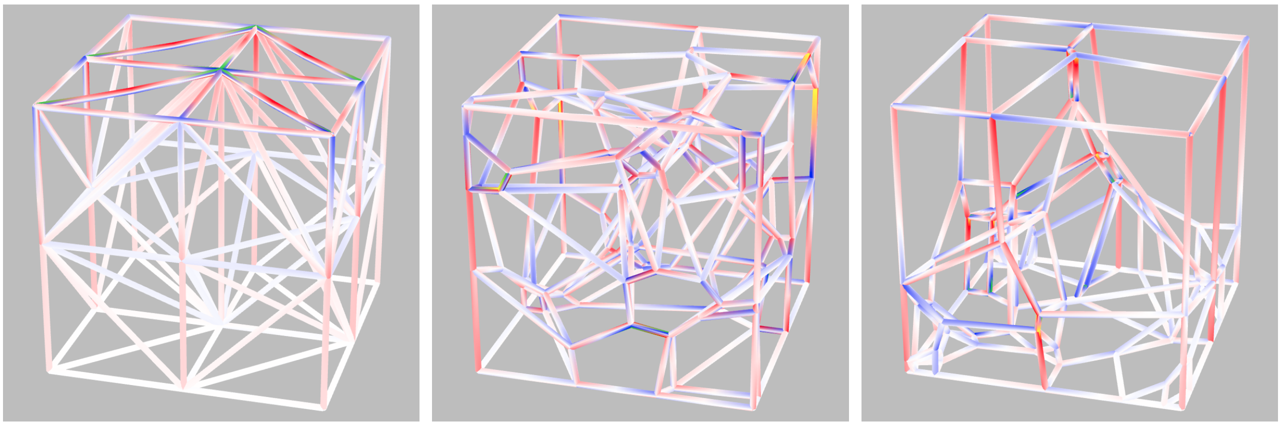

(a) Triangle mesh tessellation (b) Random Voronoi tessellation (c) Optimized Voronoi tessellation

Figure 2

a structural model. When building a structure, we usually aim for something which is light and stiff, saving on material cost while still preserving stability. For this reason, we compare the models in terms of mass and elastic energy, aiming for a minimum of both. Elastic energy can serve as a measure of stiffness, the resistance against deformation. It is given in kNm. All tessellations are confined to a cube of 5m length. Each steel-beam is modelled as a tube with a diameter of 114mm, and its walls have a thickness of 4mm. A uniformly distributed load is applied on top of the cube in negative z-direction, the points where the beams join on the xy-plane serve as supports.

For the initial Voronoi structure, we begin by randomly placing

$$s \in \{10, 20, 30, 40, 50, 75, 100\}$$

seeds within the cube to create the Voronoi cells. This is repeated 500 times, and elastic energy as well as mass are averaged for each N. Next, we create a triangle mesh by subdividing the cube into

$$n \in \{2^3, 3^3, 4^3, 5^3, 6^3, 7^3, 8^3\}$$

smaller cubes and splitting them into two tetrahedra. This way we can compare the irregular Voronoi tessellation to a triangle tessellation of similar mass. We chose this triangle mesh as being representative of a regular tessellation method.

Finally, we create random Voronoi cells with the same number of seeds as above, but this time we employ a genetic algorithm to find optimal positions for the seed points, minimizing both mass and elastic energy. To this end we use the multi-objective optimization package Octopus [11]. This introduces the Pareto principle for multiple goals.Octopus uses genome components as well as the objectives (mass and elastic energy) as input. We modelled the x,y, and z coordinates of the seed points as three genome components on the input side, which are further fed as input to the Karamba3D components creating the structural model. Mass and elastic energy, as calculated by the Karamba3D components, are then minimized by Octopus using a genetic algorithm. This means Octopus rearranges the x,y, and z coordinates of the input genomes, which in turn are used by Karamba3D to update the model. For optimization we need to pick a number of generations after which we stop the optimization process. Choosing a fixed number for all seeds gave an unfair advantage to the structures with a lower amount of seed points, as an optimal solution is found more quickly for a low amount of seeds. We instead set the number of generations to be twice the amount of seed points. This ensures that we can compare the results for a different amount of seeds. We then pick a solution on the Pareto front which satisfies both objectives equally well, by choosing the one closest to the bisector of the oriented coordinate axes. A better alternative would be to stop the optimization process when the optimal solution only shows a marginal change within a pre-defined timeframe. This, however, is not implemented as a standard feature in Octopus.

We now compare the models first by examining their structures visually in Fig. 2. The number of cells for the Voronoi structures is set to 20. The subdivisions for the triangle mesh were set to 2 in order to arrive at a similar mass. Fig. 2 shows the utilization plot of the three models with the lower and upper threshold set to 20% and 80% of the minimum and maximum utilization respectively. The utilization is plotted uniformly between its extremes in red and blue. Values outside the range are colored in green or yellow. For the triangle mesh model one can see that the bending and axial deformation energy is strongest on the top of the structure where the load is applied. The bottom

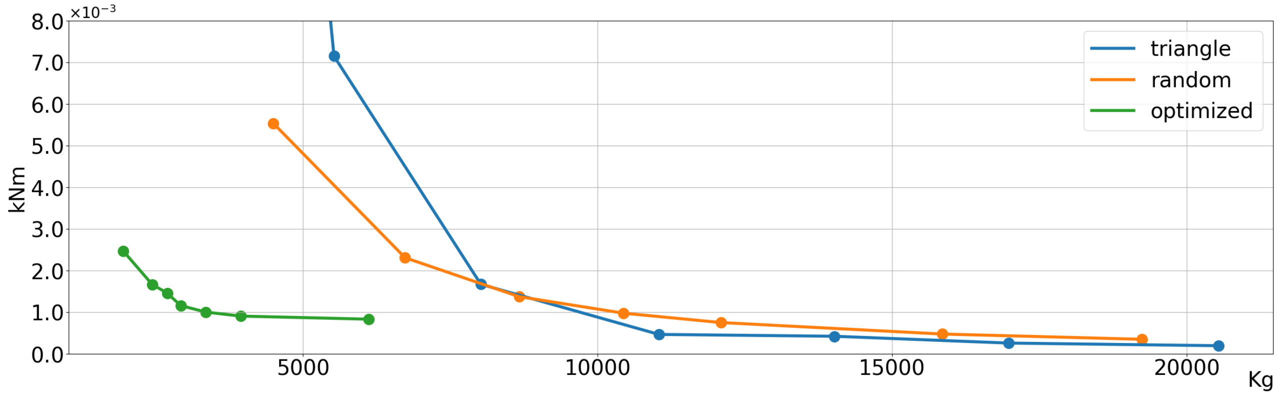

Figure 3: *Comparison of elastic energy as a function of mass for random Voronoi structure, triangle mesh structure and optimized Voronoi structure. Random Voronoi has a lower elastic energy for lower number of seeds than the triangle mesh tessellation. Optimized Voronoi structure outperforms both in terms of weight.*

part appears mostly rigid, which is in contrast with the random and optimized Voronoi structures. Here, higher deformation energy is present throughout the structures. However, the optimized structure shows this to a lesser extent than the random structure. This agrees with the plots in Fig. 3 described below. With regard to the triangle mesh, it should be noted that the larger angles found in the Voronoi structures make them easier to construct. A striking feature of the optimized Voronoi tessellation, is the apparent formation of a cupola-like structure in the lower parts of the cube, which distributes the load evenly. In Fig. 3 we compare the models by plotting their respective elastic energy as a function of their mass. Looking at triangle mesh and random Voronoi tessellation plots, we can see that for low subdivisions the triangle mesh shows a high elastic energy. Clearly the random Voronoi-modelled structure is superior for a lower mass. This changes at a mass around 9000kg. With more subdivisions the triangle structure is now more resistant to stress than the Voronoi structure of a similar mass. The optimized Voronoi structure is highly stable already at low mass. Comparing the mass of the three structures at an elastic energy of 0.001kNm, for example, we see that the optimized structure weighs only approximately 1800kg whereas the other two already have a mass of over 9000kg at this point. Consequently, from a material utilization point of view, the triangle mesh is superior, whereas when aiming for light and rigid structures, the optimized Voronoi structure is preferable. The "bump" in the graph of the optimized Voronoi that can be seen at the point for 30 seeds (third from left) can be explained by a local optimum, where the genetic algorithm might not have found the true optimum after the respective number of generations. Owing to the random nature of the algorithm, the results generally may vary, but the general trend of the graph will remain the same.

To compare their performance in terms of weight and rigidity, we plot the models' respective elastic energy as a function of mass in Fig. 3.

The plots generally show a trend towards low elastic energy the more mass ,*i.e.* beams are added. Comparing random and triangle mesh tessellation, we see that the random Voronoi outperforms the triangle mesh in terms of elastic energy up to a mass of about 9000kg. Heavier triangular structures, however, are more rigid than their Voronoi counterparts at approximately the same mass. The optimized Voronoi structures are much lighter than both random and triangle tessellation, while still retaining similar rigidity. For example, to reach an elastic energy of around 0.001kNm the optimized Voronoi structure weighs 1800kg, whereas random and triangular Voronoi structures have a mass of approximately 8600kg and 8000kg respectively at the same value for elastic energy.

To summarize: Random Voronoi structures give a good out-of-the-box solution when a low number of seeds is used and are comparable to regular triangle meshes. However, we can still optimize the position of the seeds to in turn create structures that clearly outperform triangle tessellations of similar weight.

4 Related Work

Finding that random Voronoi structures can still be improved by optimization processes, we have reviewed recent literature where structures can be manufactured or at least simulated by using Voronoi tessellation as an initial step before optimization. We identify two main areas where the structural properties of Voronoi diagrams are applicable: additive manufacturing and to a lesser extent architecture, where an important role is attributed to aesthetics, which is secondary to our interest.

4.1 Additive Manufacturing

More commonly known as 3D printing is the process of constructing a 3D-model from a digital model. There are a number of different ways to achieve this, a popular one being fused filament manufacturing. Here a thermoplastic material is melted to iteratively build a 3D-model through the use of a movable nozzle. Generally speaking, the surveyed papers all deal with the infill pattern of models, as printing a solid model needlessly wastes material. Since a completely hollow object would not be very resistant to stress, however, an infill pattern is sought that minimizes material use and maximizes resistance to stress. To this end a variety of optimization strategies are employed to find an optimal positioning of the Voronoi seed cells. As we will see, it is also possible to achieve different kinds of elastic behaviour.

Öncel and Yaman [8] use topological optimization under specific load and support conditions and finite element analysis to define a number of density regions where the average stress is larger, and thus, more seeds need to be placed. This creates an infill pattern using hollow Voronoi cells. The objective of the optimization process is a pattern that minimizes the maximum deflection and mass of the printed object. They test their approach on three different models by comparing the performance of random Voronoi tessellation to their approach. The approach can be used in a given geometry, and the optimized Voronoi infill pattern exhibited higher mechanical performance than random Voronoi structures for the same model.

In a similar approach by Lu et al. [4], an optimal strength-to-weight ratio for 3D-printed objects is found by using irregular Voronoi diagrams for a hollowed interior structure. In order to find an optimal placement of the Voronoi cells, an initial stress map is computed. Additionally, the hollowing of the cells is maximized so that interior and exterior stresses can be sustained while minimizing the amount of material used.

A more biomimetic approach is given in Deering et al. [3]: Here, porous scaffolds are proposed to mimic the natural structure of trabecular bone by using Voronoi tessellation with selective seeding. Stress shielding effects, where an implant's high stiffness results in a stiffness discrepancy between surrounding bone and the implant, are an important factor for osseointegration. Since the geometry and size of the pores in the material influence the effects of stress on the scaffold, this approach aims to mimic the anisotropic network of struts and plates of trabecular bone. This is done by selectively placing Voronoi seeds on periodic planes within the volume. The resulting structure has a similar performance as the one measured in human bone.

Contrary to the objectives of the papers before, in the work by Martinez et al. [5], the goal is a structure which exhibits elastic behaviour. Through the use of a polyhedral cone-like metric for the Voronoi diagram its geometry is changed. Varying the density, anisotropy, and angle of the design results in a graded elastic behaviour of the printed structure. This allows the printing of objects which can be both rigid and elastic in parts: for example, the creation of a cylinder which remains vertically rigid but allows for rotation in one direction. This is applicable to the design of prosthetics or wheels. Note that a rubber-like printing material is used in this case.

4.2 Architecture

To show whether the aforementioned properties of Voronoi-inspired techniques scale to larger structures, we survey approaches in the area of architecture. Since aesthetics play a larger role, the approaches are more limited.

Mele et al. [6, 7] investigate the mechanical properties of irregular structural patterns as applied to tube configurations for tall buildings at macro-scale. The aim being to investigate properties of irregular patterns, with respect to constructability. In a first step, hexagonal patterns - non-regular patterns based fully on Voronoi diagrams, mixed regular patterns, and irregular patterns - are examined. Patterns generated from a regular hexagonal pattern are characterized by density degree and irregularity degree which can be varied along the building's height. The resulting Voronoi tube structure carries tributary gravity loads and total wind load. The mechanical properties of the Voronoi-based structures were examined by representative volume elements-based approach. It was observed that irregular patterns are lighter, and the design procedure seemed useful for the initial design of such structures.

For use in the design of grid-shell structures, Pietroni et al. [9] propose a framework based on Voronoi diagrams which also exhibits good static performance, comparable to more conventional triangle or quad-based grid-shell structures. Using a finite element static analysis of the input surface, they create a stress tensor field according to which the tessellation's elements are sized and aligned. To account for aesthetics, they adapt the cell's geometry to form hexagons.

Common to the mentioned works is that Voronoi diagrams serve as an initial step in the design process but can be optimized towards fulfilling certain criteria. The Voronoi structure's properties of seed location, as well as the cells' size, orientation and geometry are due to change because of the optimization procedure. This approach scales from 3D printed objects to larger structures.

5 Conclusion

In this paper we have investigated the structural properties of Voronoi tessellations under stress, inspired by the occurrence of similar patterns in nature. In a simple simulation, we have shown that random Voronoi diagrams can be used for the creation of structures which are rigid under applied load while being significantly lighter than a regular triangle mesh tessellation up to a certain point. These Voronoi structures can still be optimized by selective placement of their seeds. We have surveyed papers where light and rigid structures are desired and identified two areas of application: additive manufacturing and to a lesser extent architecture. Voronoi structures give a good starting point, but their seed placement, cell-orientation, cell-size, cell-geometry can be further optimized to fulfil a stated objective.

References

[1] F. Aurenhammer, Voronoi diagrams - a survey of a fundamental geometric data structure, *ACM Computing Surveys (CSUR)* **23**(3) (1991), 345–405.

[2] A.M. Bronstein, M.M. Bronstein, R. Kimmel, *Numerical geometry of non-rigid shapes*, Springer Science & Business Media, 2008.

[3] J. Deering, K.I. Dowling, L.-A. DiCecco, G.D. McLean, B. Yu, K. Grandfield, Selective Voronoi tessellation as a method to design anisotropic and biomimetic implants, *Journal of the Mechanical Behavior of Biomedical Materials* **116** (2021), 104361.

[4] L. Lu, A. Sharf, H. Zhao, Y. Wei, Q. Fan, X. Chen, Y. Savoye, C. Tu, D. Cohen-Or, B. Chen, Build-to-last: Strength to weight 3D printed objects, *ACM Transactions on Graphics* **33**(4) (2014), 1–10.

[5] J. Martínez, S. Hornus, H. Song, S. Lefebvre, Polyhedral Voronoi Diagrams for Additive Manufacturing, *ACM Transaction on Graphics* **37**(4) (2018), 15.

[6] E. Mele, M. Fraldi, G. M. Montuori, G. Perrella, V.D. Vista, Hexagrid-Voronoi transition in structural patterns for tall buildings, *Frattura e Integrita Strutturale* **13**(47) (2019), 186–208.

[7] E. Mele, M. Fraldi, G. M. Montuori, G. Perrella, Non-conventional Structural Patterns for Tall Buildings: from Diagrid to Hexagrid and Beyond, *Frattura e Integrita Strutturale* (2016).

[8] A.C. Öncel, U. Yaman, Generation of optimized Voronoi based interior structures for improved mechanical properties, *Procedia Manufacturing* **38** (2019), 42–51.

[9] N. Pietroni, D. Tonelli, E. Puppo, M. Froli, R. Scopigno, P. Cignoni, Voronoi grid-shell structures, arXiv:1408.6591, (2014).

[10] C. Preisinger, Linking structure and parametric geometry, *Architectural Design* **83**(2) (2013), 110–113.

[11] R. Vierlinger, *Octopus*, `https://www.food4rhino.com/en/app/octopus`, Accessed: 2021-08-10.

[12] G. Voronoi, Nouvelles applications des paramètres continus à la théorie des formes quadratiques. Deuxième mémoire. Recherches sur les parallélloèdres primitifs, *Journal für die reine und angewandte Mathematik (Crelles Journal)* **1908**(134) (1908), 198–287.

Leonard Weydemann
e-mail: leonard.weydemann@uni-ak.ac.at

University of Applied Arts Vienna
Oskar-Kokoschka-Platz 2, A-1010 Vienna, Austria

Christian Clemenz
e-mail: christian.clemenz@uni-ak.ac.at

University of Applied Arts Vienna
Oskar-Kokoschka-Platz 2, A-1010 Vienna, Austria

Clemens Preisinger
orcid.org/0000-0002-0726-3335
e-mail: clemens.preisinger@uni-ak.ac.at

University of Applied Arts Vienna
Oskar-Kokoschka-Platz 2, A-1010 Vienna, Austria

https://doi.org/10.31896/k.25.9
Review
Accepted 28. 11. 2021.

Ana Katalenić
Aleksandra Čižmešija
Željka Milin Šipuš

Asymptotes of Plane Curves – Revisited

Asymptotes of Plane Curves – Revisited

ABSTRACT

In this paper we present a review of the basic ideas and results concerning asymptotic lines of plane curves. We discuss their different definitions, namely that of a limiting position of tangent lines, of the tangent line at infinity, and finally the one that requires that the distance between points of a curve and asymptotic line tends to 0 as the point moves along an infinite branch of the curve. We also recall the method of determining asymptotes of algebraic curves from the *leading coefficients* in their equation and provide examples.

Key words: plane curve, asymptote, limiting tangent line, tangent at infinity

MSC2010: 51-02

Asimptote ravninske krivulje - ponovni pogled

SAŽETAK

U ovom radu dajemo pregled osnovnih ideja i rezultata vezanih uz asimptote ravninskih krivulja. Raspravljamo o njihovim različitim definicijama, naime, o definiciji kao o graničnom položaju tangenata, o definiciji kao o tangenti u beskonačnosti, te konačno o definiciji koja zahtijeva da udaljenost između točke krivulje i asimptote teži 0 kako se točka kreće duž beskonačne grane krivulje. Također se prisjećamo metode određivanja asimptota algebarskih krivulja iz *vodećih koeficijenata* u njihovoj jednadžbi te navodimo primjere.

Ključne riječi: ravninska krivulja, asimptota, granična tangenta, tangenta u beskonačnosti

1 Introduction

Many plane curves have asymptotes. They are an inevitable part of the curve sketching. In this paper, the term asymptote will primarily refer to the asymptotic straight line, where, of course, there exist other asymptotic curves such as asymptotic parabolas or cubic curves, or asymptotic points.

In the first encounter with the notion an asymptote is very often described as *a straight line that approaches a curve but never touches it* which is a suitable description for the prototype school examples of curves, such as a hyperbola as the graph of a rational function $f(x) = 1/x$, the graph of an exponential and logarithmic function, or a hyperbola as a curve in analytic geometry. However, rigorous mathematical definition which developed through history includes the possibility that the curve intersects its asymptote or that it oscillates around the asymptote. In this historical development, we can mention Apollonius of Perga (262 BC-190 BC) who introduced the aforementioned description of an asymptote of a curve as "lines [a curve and its asymptote] which do not meet, in whatever direction they are produced" [21]. Much later, in his work on perspective, Desargues (1591-1661) took a different approach, namely that of projective geometry, and introduced asymptotes as *tangent lines at infinity*, whereas Newton (1643-1727) used asymptotes as the main tool in classification of cubics on the account of their points at infinity [1]. In historical calculus sources from the transition between 19^{th} and the 20^{th} century, an asymptote of a curve was given as the *limiting position of a tangent line to the curve when the point of tangency moves away from the origin*, or *a line, the distance of which from a point in a curve diminishes as the point moves away from the origin* [3, 4, 5, 6, 18, 22].

In school and early university mathematics asymptotes are considered for graphs of real (smooth) functions. There is no unique or *"the best"* choice of definition, which may be confirmed by the following quotations:

"My own preference is for the *limiting tangent definition*, partly because I feel that asymptotes have something to do with tangents, and partly because it is easier to use than the rival definitions" ([8], p. 281);
and
"The *limit of tangents* may not exist, even when asymptotes exist [in the sense of definition by distance]. This fact shows that the *limit of tangents* is not a suitable definition of an asymptote" ([6], p. 91).
In our previous work we were interested in students' recollection of the notion of asymptote [13, 12, 11]. Motivated by the richness of the notion, our aim here is to present a mathematical review of the basic ideas and results concerning asymptotes of plane curves that goes beyond school requirements.

2 Definitions of an asymptote

Definition 1 *[23] A line l is an asymptote to a curve if the distance from a point P to the line l tends to zero as P tends to infinity along some unbounded part of the curve.*

Definition 2 *[9] Asymptotes are the limits of tangent lines when the point of contact tends to infinity.*

Definition 3 *[19] An asymptote of a plane curve is a tangent to the projective curve determined by it at a point at infinity, which tangent is not the line at infinity.*

These definitions are not equivalent in general. In the following we first analyze what they imply.

Distance between points in Definition 1 is taken as the Euclidean distance. But if this distance tends to zero, then the vertical (for a horizontal or oblique asymptote) or the horizontal distance (for a vertical asymptote), also tends to zero [2, 6, 15]. The vertical or the horizontal distance is the absolute value of difference of the corresponding coordinates of a point on a curve and on an asymptotic line.
This consideration implies that, following Definition 1, a line $y = kx + l$ is an asymptote of a function $f : I \to \mathbb{R}$ of class C^1, where $I \subset \mathbb{R}$ is an open interval, if and only if $\lim\limits_{x\to\infty}(f(x) - kx - l) = 0$ [15]. Now it follows

$$k = \lim_{x\to\infty} \frac{f(x)}{x}, \; l = \lim_{x\to\infty}(f(x) - kx). \tag{1}$$

To use Definition 2, we start from a tangent line of a curve which is the graph of a function f at a point $(x_0, f(x_0))$, and given by

$$y = f'(x_0)x + f(x_0) - f'(x_0)x_0.$$

The graph of a function f has a limiting tangent line if and only if the direction of the tangent line and its intercept with y axis have limiting value, that is, the limits

$$\lim_{x_0\to\infty} f'(x_0), \quad \lim_{x_0\to\infty}(f(x_0) - f'(x_0)x_0)$$

exist [4, 8]. If $\lim\limits_{x_0\to\infty} f'(x_0) = \infty$ the function might still have vertical asymptote.
We reason similarly for parametrized curves or curves given by implicit equations; to find a tangent line of a curve $c(t) = (u(t), v(t))$ or a curve given by $F(x,y) = 0$ requires looking at the limiting value of the gradient v'/u' or $-\frac{\partial F}{\partial x}/\frac{\partial F}{\partial y}$, and if the limit exists, then looking at the limiting value of the intercept of the tangent line on the axis [4, 8].
Definition 3 is set up in projective plane which is also a natural way of thinking about asymptotes. We extend $\mathbb{R}^2$ and assume the following correspondence between $\mathbb{R}^2$ and $\mathbb{P}^2$, which maps a point at infinity of the curve in the direction of $x \to \infty$ to the origin of the real plane

$$(x,y) \mapsto [x,y,z] \mapsto [z,y,x] = \left[\frac{z}{x}, \frac{y}{x}, 1\right] \mapsto \left(\frac{z}{x}, \frac{y}{x}\right). \tag{2}$$

First arrow represents the mapping $P : \mathbb{R}^2 \to \mathbb{P}^2$, $P(x,y) = [x,y,z]$, where points in $\mathbb{P}^2$ are equivalence classes given with $[x,y,z] = \{(\alpha x, \alpha y, \alpha z), \alpha \in \mathbb{R}, \; \alpha \neq 0\}$. Second is projective transformation $T : \mathbb{P}^2 \to \mathbb{P}^2$, $T[x,y,z] = [z,x,y]$, such that $T^2 = id$. Last is the mapping $R : \mathbb{P}^2 \to \mathbb{R}^2$, $R[z,y,x] = (z,y)$. An asymptote, as the tangent at infinity, corresponds to the tangent line at the origin following the mapping in (2) [8, 10, 20].

Example 1. The curve c given by the equation $F(x,y) = y^3 - x^3 + 1 = 0$ has the line $y = x$ as an asymptote in the sense of all definitions.

Def.1. Let $P(x_P, y_P)$ be a point on the curve c, and $d = \frac{|x_P - y_P|}{\sqrt{2}}$ is the distance between the point P on the curve c and the line $y = x$. Since

$$d = \frac{\left(x_P - \sqrt[3]{x_P^3 - 1}\right)}{\sqrt{2}} \to 0, \text{ for } x_P \to \infty$$

the line $y = x$ is an asymptote.

Def.2. The equation of the tangent line to the curve c at point P is

$$\left(\frac{\partial F}{\partial x}\right)_P (x - x_P) + \left(\frac{\partial F}{\partial y}\right)_P (y - y_P) = 0.$$

The direction of the tangent line in a point (x_P, y_P) is given by $k_P = -\frac{\left(\frac{\partial F}{\partial x}\right)_P}{\left(\frac{\partial F}{\partial y}\right)_P} = \frac{3x_P^2}{3y_P^2}$, and the intercept of the tangent line with y axis by $l_P = y_P + \frac{\left(\frac{\partial F}{\partial x}\right)_P}{\left(\frac{\partial F}{\partial y}\right)_P} \cdot x_P = \frac{-3}{3\cdot\sqrt[3]{x_P^3-1}}$, both having the limiting values for $x_P \to \infty$ as $k_P \to 1$ and $l_P \to 0$ respectively. The line $y = x$ is a limiting tangent line.

Def.3. The homogeneous equation of the curve c in the projective plane $\mathbb{P}^2$ is given with $f(x,y,z) = y^3 - x^3 + z^3 = 0$. The equation of the tangent line to the projective curve at point with homogeneous coordinates $P[x_P, y_P, z_P]$ is

$$\left(\frac{\partial f}{\partial x}\right)_P x + \left(\frac{\partial f}{\partial y}\right)_P y + \left(\frac{\partial f}{\partial z}\right)_P z = 0,$$

that is, $(-3x_P^2)x + (3y_P^2)y + (3z_P^2)z = 0$. The point at infinity of the curve $f(x,y,z) = 0$ has homogeneous coordinates $[1,1,0]$ and the equation of the tangent line to the curve at the point at infinity is $-3x + 3y = 0$, that is, the line $y = x$ in the real plane. This line is a tangent at infinity.

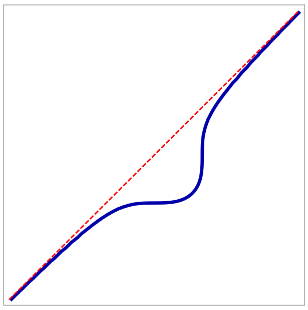

Figure 1: *Example 1*

Example 2. The graph of the function $f(x) = \frac{\sin x}{x}$ has the line $y = 0$ as an asymptote in the sense of Definitions 1 and 3, but not in the sense of Definition 2.

Def.1. Since $k = \lim\limits_{x\to\infty} \frac{f(x)}{x} = 0$ and $l = \lim\limits_{x\to\infty}(f(x) - kx) = \lim\limits_{x\to\infty} \frac{\sin x}{x} = 0$, the line $y = 0$ is the asymptote.

Def.2. The direction of the tangent line $f'(x_0) = \frac{\cos x_0}{x_0} - \frac{\sin x_0}{x_0^2} \to 0$ has a limiting value, but the intercept of the tangent line with the y axis, $f(x_0) - f'(x_0)x_0 = -\cos x_0$ has no limiting value as $x_0 \to \infty$. The function has no limiting tangent line.

Def.3. Following the correspondence (2) we obtain

$$(x, f(x)) \mapsto [x, f(x), 1] \mapsto [1, f(x), x] = \left[\frac{1}{x}, \frac{f(x)}{x}, 1\right]$$

$$\mapsto \left(t, t\cdot f\left(\frac{1}{t}\right)\right),\ t = \frac{1}{x}.$$

The tangent of the function $F(t) = t\cdot f\left(\frac{1}{t}\right)$, for $t = 0$ and $F(0) = \lim\limits_{x\to\infty}\frac{f(x)}{x} = 0$, is the limit of the secants through point $(0,0)$ and $(F(t), t)$, as $t \to 0$. Since $\lim\limits_{t\to 0}\frac{F(t)}{t} = \lim\limits_{t\to 0} f\left(\frac{1}{t}\right) = \lim\limits_{x\to\infty} f(x) = 0$, the limit of the secants is $y = 0$ which corresponds back to the line $y = 0$ as tangent at infinity.

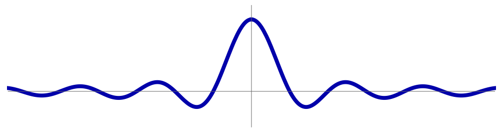

Figure 2: *Example 2*

To analyze relations between Definitions 1, 2 and 3, we introduce $c = (u(t), v(t))$ as a (parametrized) curve in $\mathbb{R}^2$, with continuous first derivatives and infinite branch in the direction $t \to t_0$, and without loss of generality $u(t) \to \infty$.

Theorem 1 *(1) If a line l is an asymptote of the curve c in the sense of Definition 2, then l is an asymptote of the curve c in the sense of Definition 1.*

(2) If a line l is an asymptote of the curve c in the sense of Definition 2, then l is an asymptote of the curve c in the sense of Definition 3.

(3) A line l is an asymptote of the curve c in the sense of Definition 3 if and only if l is an asymptote of the curve c in the sense of Definition 1.

$$\begin{array}{ccc} & \text{Definition 2.} & \\ \swarrow & & \searrow \\ \text{Definition 1.} & \Longleftrightarrow & \text{Definition 3.} \end{array}$$

Figure 3: *Relationship between the three definitions of an asymptote*

We provide the proof of the Theorem 1.

(1) **Proof.** Assume c has a limiting tangent line, that is,

$$y = \lim_{t\to t_0}\frac{v'(t)}{u'(t)}\cdot x + \lim_{t\to t_0}\left(v(t) - \frac{v'(t)}{u'(t)}\cdot u(t)\right) \quad (3)$$

where $k = \lim\limits_{t\to t_0}\frac{v'(t)}{u'(t)}$ and $l = \lim\limits_{t\to t_0}\left(v(t) - \frac{v'(t)}{u'(t)}\cdot u(t)\right)$.

The distance between the limiting tangent line and point on curve c is given by

$$d = \frac{|k\cdot u(t) - v(t) + l|}{\sqrt{k^2+1}}.$$

Since

$$\begin{aligned}\lim_{t\to t_0}(v(t)-k\cdot u(t)) &= \lim_{t\to t_0}\frac{\frac{v(t)}{u(t)}-k}{\frac{1}{u(t)}}\\ &= \lim_{t\to t_0}\frac{\frac{v'(t)\cdot u(t)-v(t)\cdot u'(t)}{(u(t))^2}}{-\frac{u'(t)}{(u(t))^2}}\\ &= \lim_{t\to t_0}\left(v(t)-\frac{v'(t)}{u'(t)}\cdot u(t)\right)=l,\end{aligned}$$

then $d\to 0$ as $t\to t_0$, and the limiting tangent given in (3) is an asymptote in the sense of Definition 1.□

(2) **Proof.** Assume c has a limiting tangent line $y = kx+l$ given in (3). By embedding $\mathbb{R}^2$ in $\mathbb{P}^2$ the homogenenous coordinates of a point on the curve c are

$$(u(t),v(t))\mapsto[u(t),v(t),1]=\left[1,\frac{v(t)}{u(t)},\frac{1}{u(t)}\right]$$

and the point at infinity of the curve c is

$$\left[1,\lim_{t\to t_0}\frac{v(t)}{u(t)},\lim_{t\to t_0}\frac{1}{u(t)}\right]=(1,k,0)$$

since by l'Hospital rule $k=\lim\limits_{t\to t_0}\dfrac{v'(t)}{u'(t)}=\lim\limits_{t\to t_0}\dfrac{v(t)}{u(t)}$.

Tangent at infinity corresponds to the limit of the secants (or the chords [6, 8]) joining the point at infinity of the curve with an arbitrary point on the projective curve, as it tends to the point at infinity. Following (2)

$$\begin{aligned}(u(t),v(t))&\mapsto[u(t),v(t),1]\mapsto\\ &\mapsto[1,v(t),u(t)]=\left[\frac{1}{u(t)},\frac{v(t)}{u(t)},1\right]\end{aligned}$$

and the chord joining points $(0,k)$ and $\left(\frac{1}{u(t)},\frac{v(t)}{u(t)}\right)$ on the corresponding curve is

$$\begin{aligned}y-k&=\frac{\frac{v(t)}{u(t)}-k}{\frac{1}{u(t)}-0}(z-0)\\ y&=(v(t)-k\cdot u(t))\cdot z+k\end{aligned}$$

which transforms back into $y=k\cdot x+(v(t)-k\cdot u(t))$. The tangent at infinity is thus given by

$$y=k\cdot x+\lim_{t\to t_0}(v(t)-k\cdot u(t)). \tag{4}$$

Since $\lim\limits_{t\to t_0}(v(t)-k\cdot u(t))=l$ the tangent at infinity given in (4) coincides with the limiting tangent given in (3). □

(3) **Proof.** Let $y = kx+l$ be a tangent at infinity of a curve c given in (4). Then $k=\lim\limits_{t\to t_0}\frac{v(t)}{u(t)}$, and $l=\lim\limits_{t\to t_0}(v(t)-k\cdot u(t))$. Distance between the tangent at infinity and a curve c is given by

$$d=\frac{|k\cdot u(t)-v(t)+l|}{\sqrt{k^2+1}}\to 0 \text{ as } t\to t_0.$$

Therefore, the tangent at infinity given in (4) is an asymptote in the sense of Definition 1.

To show the converse, let $y=kx+l$ be an asymptote of a curve c in the sense of Definition 1, that is,

$$d=\frac{|k\cdot u(t)-v(t)+l|}{\sqrt{k^2+1}}\to 0 \text{ as } t\to t_0.$$

Then

$$\lim_{t\to t_0}(v(t)-k\cdot u(t))=l \text{ and } \lim_{t\to t_0}\frac{v(t)}{u(t)}=k$$

which correspond to the coefficients of a tangent at infinity given in (4). □

However, as stated in [8] for algebraic curves the following theorem holds.

Theorem 2 *Definitions 1, 2, 3 are equivalent in the case of algebraic curves.*

3 Methods of finding asymptotes of algebraic curves

Definitions we discussed provide different ways how to determine asymptotes of plane curves. We summarize that the most common way how to determine slant asymptotes of a function graph is to look for them as $y = kx+l$ where coefficients k,l are given by (1). Furthermore, in the special case of a rational function $f(x)=\frac{P(x)}{Q(x)}$ its (linear or curvilinear) asymptote is the quotient of the polynomials in the numerator and denominator. For example, a function $f(x)=\frac{x^2+1}{x-1}$ can be rewritten as $f(x)=x+1+\frac{2}{x-1}$ which enables to recognize the equation of its slant asymptote as $y=x+1$. Its vertical asymptote appears as the zero of the denominator $x=1$ (see Figure 4 on the right). This procedure also gives asymptotes of algebraic curves when their equation can be expressed in the suitable form by expressing, for instance, y by x.

Generally, finding asymptotes of a real algebraic plane curve reduces to finding corresponding tangent lines at the points at infinity of the projective curve (see Example 1 and [10]) or at the origin for the corresponding curves obtained by projective transformations (see Examples 2, 4 and 5, and [17, 20]). In the purely algebraic context, finding asymptotes comes down to determining lines that reduce the degree of the equation of algebraic curve. Regardless of the chosen definition, an asymptote of the curve is *line that intersects the curve in at least two coincident points at an infinite distance* [2, 4, 5, 6, 7].

In the case of a hyperbola $b^2x^2-a^2y^2=a^2b^2$, if we analyze a number of common (real) points with a line $y=kx+l$ (which can be 0, 1 or 2), we arrive at the quadratic equation $(b^2-a^2k^2)x^2-2a^2klx-a^2l^2-a^2b^2=0$ with one solution in x if and only if $k^2a^2-b^2=l^2$. This is known as the tangency condition. However, when the leading coefficient vanishes, that is $b^2-a^2k^2=0$ (implying that $k=\pm\frac{b}{a}\neq 0$), and when the next coefficient vanishes as well, giving $l=0$, we arrive at the known equation of an asymptote of the hyperbola as $y=\pm\frac{b}{a}x$. This method of determining the asymptote can also be generalized. In [14] conditions for a quadratic curve

$$a_1x^2+a_2xy+a_3y^2+b_1x+b_2y+c=0 \tag{5}$$

to have asymptotes are explored, which can be further interpreted as conditions that ensure that a quadratic curve is a hyperbola. By substituting $y=kx+l$ in (5) we arrive at the quadratic equation in x, and by equating the coefficients of x^2 and x to 0, while the constant coefficient is not 0, we obtain the asymptotes of a curve. Summarizing [14], if

A1 $a_2^2-4a_1a_3>0$ and the equation (5) cannot be factorised into linear factors, it represents a hyperbola with asymptotes $y=kx+l$, where k and l are solutions of equations $a_1+a_2k+a_3k^2=0$ and $a_2l+2a_3kl+b_1+b_2k=0$.

A2 $a_3=0, a_2\neq 0$ and the equation (5) cannot be factorised into linear factors, it represents a hyperbola with a vertical asymptote $x=-\frac{a_1}{a_2}$ and a slant asymptote $y=-\frac{a_1}{a_2}x+\frac{a_1b_2-a_2b_1}{a_2^2}$.

Example 3.

(i) Let the curve be given by $-2x^2+xy+y^2-y-1=0$ (see Figure 4 above)

- From A1 it follows that the curve is a hyperbola and the coefficients of its asymptotes satisfy $-2+k+k^2=0$ and $l+2kl-k=0$. It follows $k_1=1$, $k_2=-2$ and $l_1=\frac{1}{3}$, $l_2=\frac{2}{3}$. Asymptotes are $y=x+\frac{1}{3}$ and $y=-2x+\frac{2}{3}$.
- The equation of the curve can be written as $(y-x)(y+2x)=y+1$. We have

$$y-x=\frac{y+1}{y+2x}\xrightarrow[x\to\infty,y\to x]{}\frac{x+1}{3x}=\frac{1}{3}+\frac{1}{x}.$$

The asymptote is $y-x=\frac{1}{3}$, and similarly the other asymptote is $y+2x=\frac{2}{3}$.

(ii) Let the curve be given by $-x^2+xy-y-1=0$ (see Figure 4 below)

- From A2 it follows that the curve is a hyperbola with the vertical asymptote $x=1$ and a slant asymptote $y=x+1$.
- The equation of the curve can be written as $x(y-x)=y+1$, and

$$y-x=\frac{y+1}{x}\xrightarrow[x\to\infty,y\to x]{}\frac{x+1}{x}=1+\frac{1}{x}.$$

The asymptote is $y=x+1$. From $-\frac{x^2}{y}+x-1-\frac{1}{y}=0$, it follows that when $y\to\infty$, then $x-1\to 0$. $x=1$ is vertical asymptote.

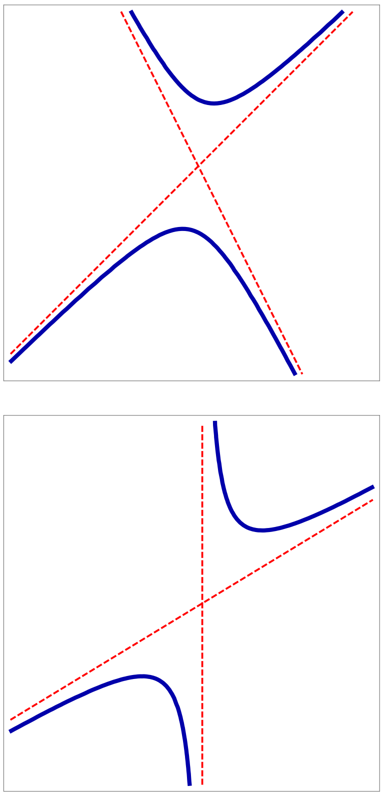

Figure 4: *Example 3*

We describe methods of finding asymptotes of general algebraic curves. Let c be an algebraic curve given by an equation.

$$F(x,y)=P_n(x,y)+P_{n-1}(x,y)+\cdots+P_1(x,y)+P_0=0 \tag{6}$$

where $P_m(x,y)$ is a term of degree m, $P_n=\sum\limits_{i=0}^{m}a_{m,i}x^{m-i}y^i$.

Assume $x \to \infty$. Substituting $y = kx + l$ results with an equation of degree n in x. For the line $y = kx + l$ to be an asymptote of the curve (6) the two coefficients of the top degree in the resulting equation must vanish, thus providing the coefficient k as the root of the leading term $P_n(x,y)$ in $(x,y) = (1,k)$. This method for finding asymptotes is reported in different sources, and in [6] it is summarized with the following theorem:

Theorem 3 *The line $y = kx + l$ is an asymptote of the algebraic curve* (6) *if and only if*

(1) k is a real root of equation $P_n(1,t) = 0$,

(2) for chosen k, the coefficient l is a root of equation $\psi(s,k) = 0$, where

$$\phi(s,k,x) = \psi(s,k) + \frac{1}{x}\psi_1(s,k) + \frac{1}{x^2}\psi_2(s,k) + \cdots = 0$$

and ϕ is obtained by reduction from $F(x, s+kx) = 0$, and

(3) for chosen k and l, equation $\phi(l+\varepsilon, k, x) = 0$ admits real root ε such that $\varepsilon \to 0$ for $x \to \infty$.

The equation of the curve (6) can be expressed as

$$x^n P_n\left(1, \frac{y}{x}\right) + x^{n-1} P_{n-1}\left(1, \frac{y}{x}\right) + x^{n-2} P_{n-2}\left(1, \frac{y}{x}\right) + \cdots$$
$$+ x P_1\left(1, \frac{y}{x}\right) + P_0 = 0.$$

By substituting $\frac{y}{x} = k + \frac{l}{x}$ and by Taylor's theorem we obtain [5, 6, 15]

$$x^n P_n(1,k) + x^{n-1}\left(P_{n-1}(1,k) + l \cdot P_n'(1,k)\right) +$$
$$x^{n-2}\left(P_{n-2}(1,k) + l \cdot P_{n-1}'(1,k) + \frac{l^2}{2} P_n''(1,k)\right) + \cdots = 0.$$

The simplest situation is when k is a simple root of $P_n(1,t) = 0$. Then $P_n'(1,k) \neq 0$ and for $x \to \infty$ the form $\psi(s,k)$ in condition (3) of Theorem 3 reduces to

$$P_{n-1}(1,k) + s \cdot P_n'(1,k).$$

But if k is r-tuple root of $P_n(1,t) = 0$, depending on the values of $P_i(1,k)$ and $P_i^{(j)}(1,k)$, and corresponding form $\psi(s,k)$, different situations can occur. For example, different branches can correspond to the same asymptote, the curve can have parallel asymptotes, or the curve can have no asymptotes. In the latter case, the curve could have a *parabolic branch* with a parabolic asymptote, or a general curvilinear asymptote, when the condition (3) of Theorem 3 fails.

The condition (3) of Theorem 3 is the necessary condition for the line $y = kx + l$ to be the asymptote of the curve (6), that is, that the curve must have an infinite branch in the direction of the line $y = kx + l$. Note that the method of *leading coefficients* following from conditions (3) and (3) in the Theorem 3 would still provide a line as an asymptote even if the curve has no infinite branch (see Example 4). Nunnemacher [16] noted that such spurious asymptotes correspond to the complex branch of the curve. He provided a simpler method for exploring asymptotes of algebraic curves, focused on the multiplicity of the factor $ax + by$ (rather than $y - kx$) in the term of the top degree in (6). This method simplifies the calculation, and parallel asymptotes and parabolic branches are easily discerned (see Examples 4 and 5) but the theorem does not resolve the issue of spurious asymptotes when no real branch can be associated with the obtained line.

Theorem 4 *Suppose that $ax + by$ is a factor of the top degree form P_n of multiplicity m with a and b real. Let $r \leq m$ denote the largest integer with the property that there exist polynomials $Q_j(x,y)$ for $n - r + 1 \leq j \leq n$ satisfying the conditions:*

$$P_n(x,y) = (ax+by)^r Q_n(x,y),$$
$$P_{n-1}(x,y) = (ax+by)^{r-1} Q_{n-1}(x,y), \ldots,$$
$$\text{and finally } P_{n-r+1}(x,y) = (ax+by) Q_{n-r+1}(x,y).$$

Then associated with the factor $ax + by$ is a set of at most r possible asymptotes $ax + by = t_0$, where t_0 is a real root of the equation

$$t^r Q_n(b,-a) + t^{r-1} Q_{n-1}(b,-a) + \cdots + t Q_{n-r+1}(b,-a)$$
$$+ P_{n-r}(b,-a) = 0.$$

All real asymptotes to the curve c arise in this way as $ax + by$ ranges over the real linear factors of $P_n(x,y)$. If $r > 1$ it may happen that some of these lines are spurious asymptotes.

We illustrate the methods and issues with asymptotes of algebraic curves in the following examples.

Example 4 Let c be the curve given by the equation

$$F(x,y) = x^4 - 2x^2y^2 + y^4 + x^3 - 2x^2y + xy^2 + 1 = 0.$$

Following Theorem 3, we find $k_1 = 1, k_2 = -1$ as the zeros of the leading term $P_4(1,t) = (t-1)^2(t+1)^2$ in the equation of the curve. We substitute for $y = kx + l$:

- If $y = x + l$, then $F(x, x+l) = l^2(2x+l)^2 + x \cdot l^2 + 1 = 0$.
  The condition (3) of Theorem 3 implies $4l^2 + \frac{1}{x}(4l^3 + l^2) + \frac{1}{x^2}(l^4 + 1) = 0$ and the coefficient l of the line derives from $\psi = 4l^2 = 0$, therefore $l = 0$.
  This is spurious asymptote since c has no a real branch for $x \to \infty$ in the direction of the line $y - x = 0$.

- If $y=-x+l$, then $F(x,-x+l)=(-2x+l)^2l^2+x\cdot(-2x+l)^2+1=0$.
  The condition (3) of Theorem 3 implies $4+\frac{1}{x}\cdot(4l^2-4l)+\frac{1}{x^2}(-4l^3+l^2)+\frac{1}{x^3}(l^4+1)=0$ and the coefficient l of the line derives from $\psi=4=0$, but asymptote is not obtained.
  c has a parabolic branch for $x\to\infty$ in the direction of the line $y+x=0$.

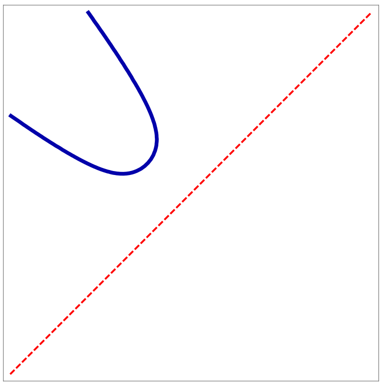

Figure 5: *Example 4*

We establish the same by Theorem 4. The terms in the equation of the curve are $P_4(x,y)=(y-x)^2(y+x)^2$, $P_3(x,y)=x(y-x)^2$, $P_2(x,y)=P_1(x,y)=0$. Depending on multiplicity, factors of the leading term are examined to obtain an equation for t as a coefficient in the equation of the line $ax+by=t$ as a potential asymptote.

- Factor $y-x$ can contribute with power $r=2$ in the point $(1,1)$.
  The terms factorise into $P_4=(y-x)^2\cdot Q_4$, $Q_4(x,y)=(y+x)^2$, $P_3=(y-x)\cdot Q_3$, $Q_3=(y-x)(y+x)$.
  The equation for t is $t^2\cdot 2^2+t\cdot 0\cdot 2+0=0\Rightarrow t^2=0$.
  This is a spurious asymptote since c has no a real branch for $x\to\infty$ in the direction of the line $y-x=0$.
- Factor $y+x$ can contribute with power $r=2$ in the point $(1,-1)$.
  The terms factorise into $P_4=(y+x)^2\cdot Q_4$, $Q_4(x,y)=(y-x)^2$, but P_3 has no factor $(y+x)$.
  The power of the factor $y+x$ needs to be reduced to $r=1$ in the same point.
  The terms factorise into $P_4=(y+x)\cdot Q_4$, $Q_4(x,y)=(y+x)(y-x)^2$, and the equation for t is $t\cdot 0+4=0$, and asymptote is not obtained.
  c has a parabolic branch for $x\to\infty$ in the direction of the line $y+x=0$.

Following idea from (2) and [20] curve c transforms so that its points at infinity correspond to the origin. In the projective plane, the homogeneous equation of the curve c is $(y-x)^2(y+x)^2-x(y-x)^2z+z^4=0$ and homogeneous coordinates of its points at infinity are $[1,1,0]$ and $[1,-1,0]$.

- For the point at infinity $[1,1,0]$, we use the following transformation of coordinates $X\equiv 1, Y\equiv y-x, Z\equiv z$ and the corresponding curve is
  $$Y^2(Y+2)^2-Y^2Z+Z^4=0 \quad\Rightarrow$$
  $$4Y^2=-4Y^3+Y^2Z-Y^4-Z^4.$$
  But the curve has an isolated point at $(Y,Z)=(0,0)$ and no tangent there.
  The curve c does not have a real branch for $x\to\infty$ in the direction of the line $y-x=0$. Its point at infinity $[1,1,0]$ is an isolated point.
- For the point at infinity $[1,-1,0]$, we use the following transformation of coordinates $X\equiv 1$, $Y\equiv y+x$, $Z\equiv z$ and the corresponding curve is
  $$(Y-2)^2Y^2-(Y-2)^2Z+Z^4=0 \quad\Rightarrow$$
  $$4Z=4Y^2+4YZ-4Y^3-Y^2Z+Y^4+Z^4.$$
  The tangent at $(Y,Z)=(0,0)$ is $Z=0$, which corresponds to the line at infinity. There is no asymptote, c has a parabolic branch for $x\to\infty$ in the direction of the line $y+x=0$.

Example 5 Let c be the curve given by the equation
$$F(x,y)=x^4-2x^2y^2+y^4+2xy-2x^2-1=0.$$

Following Theorem 3 we find $k_1=1, k_2=-1$ as the zeros of the leading term $P_4(1,t)=(t-1)^2(t+1)^2$ in the equation of the curve. We substitute for $y=kx+l$:

- $y=x+l\Rightarrow F(x,x+l)=l^2(2x+l)^2+2xl-1=0$.
  The condition (3) of Theorem 3 implies $4l^2+\frac{1}{x}(4l^3+2l)+\frac{1}{x^2}(l^4-1)=0$ and coefficient l of the line derives from $\psi=4l^2=0\Rightarrow l=0$.
  c has an asymptote $y-x=0$.
- $y=-x+l\Rightarrow F(x,-x+l)=(-2x+l)^2l^2+2x\cdot(-2x+l)-1=0$.
  The condition (3) of Theorem 3 implies $4l^2-4+\frac{1}{x}\cdot(-4l^3+2l)+\frac{1}{x^2}(l^4-1)=0$ and coefficient l of the line derives from $\psi=4l^2-4=0\Rightarrow l=\pm 1$.
  c has parallel asymptotes $y=-x-1$ and $y=-x+1$.

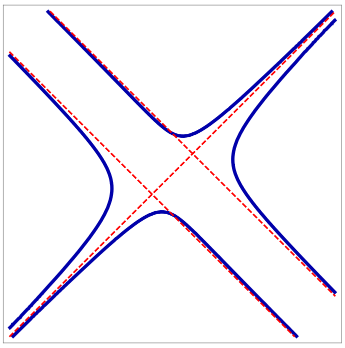

Figure 6: *Example 5*

We establish the same by Theorem 4. The terms in the equation of the curve are $P_4(x,y) = (y-x)^2(y+x)^2$, $P_3(x,y) = 0$, $P_2(x,y) = 2x(y-x)$, $P_1(x,y) = 0$. Depending on multiplicity, factors of leading term are examined to obtain equation for t as a coefficient in the equation of the line $ax+by=t$ as potential asymptote.

- Factor $y-x$ can contribute with power $r=2$ in the point $(1,1)$.
  The terms factorise into $P_4 = (y-x)^2 \cdot Q_4$, $Q_4(x,y) = (y+x)^2$, $P_3 = (y-x)\cdot 0$, and the equation for t is $t^2 \cdot 2^2 + t\cdot 0 + 0 = 0 \Rightarrow t^2 = 0$.
  c has an asymptote $y-x=0$.
- Factor $y+x$ can contribute with power $r=2$ in the point $(1,-1)$.
  The terms factorise into $P_4 = (y+x)^2 \cdot Q_4$, $Q_4(x,y) = (y-x)^2$, $P_3 = (y+x)\cdot 0$, and the equation for t is $t^2 \cdot (-2)^2 + t\cdot 0 + (-4) = 0 \Rightarrow 4t^2 - 4 = 0$.
  c has parallel asymptotes $y+x-1=0$ and $y+x+1=0$.

Following idea from (2) and [20] curve c transforms so that its points at infinity correspond to the origin. In the projective plane, the homogeneous equation of the curve c is $(y-x)^2(y+x)^2 + 2x(y-x)z^2 - z^4 = 0$ and homogeneous coordinates of its points at infinity are $[1,1,0]$ and $[1,-1,0]$.

- For the point at infinity$[1,1,0]$, we use the following transformation of coordinates $X \equiv 1, Y \equiv y-x, Z \equiv z$ and the corresponding curve is
  $$Y^2(Y+2)^2 + 2YZ^2 - Z^4 = 0 \quad \Rightarrow$$
  $$4Y^2 = -4Y^3 - 2YZ^2 - Y^4 + Z^4.$$
  The curve has tangent $Y=0$ at the cusp $(Y,Z) = (0,0)$, which corresponds to the asymptote $y-x=0$ of the two branches of the curve c.
- For the point at infinity $[1,-1,0]$, we use the following transformation of coordinates $X \equiv 1, Y \equiv y+x, Z \equiv z$ and the corresponding curve is
  $$(Y-2)^2Y^2 + 2(Y-2)Z^2 - Z^4 = 0 \quad \Rightarrow$$
  $$4Y^2 - 4Z^2 = 4Y^3 - 2YZ^2 - Y^4 + Z^4.$$
  The curve has tangents $Y-Z=0$ and $Y+Z=0$ at the node $(Y,Z) = (0,0)$, which corresponds to parallel asymptotes $y-x-1=0$ and $y-x+1=0$ of the curve c.

Finally, let us mention that a subtle and so far the most systematic analysis of asymptotes of algebraic curves in real plane, accompanied by an computational algorithm for finding asymptotes by polynomial root isolation was provided by Zeng in [23]. Similarly to the projective geometry approach, he introduced an indeterminate to extend the field $\mathbb{R}$ to a new structure that contains an infinitely large point and keeps the usual ordering and the Euclidean metrics. Based on Sturm sequences and Sturm's theorem, applied to root isolation of the leading polynomial coefficient of the two-variable polynomial defining an algebraic curve in real plane, he developed an algorithm for counting its infinite branches and determining the corresponding asymptotes, if they exist. We omit it here due to its complexity and lack of the space to elaborate its many technical details.

References

[1] W. W. R. Ball, *A Short Account of the History of Mathematics*, Dover Publications, 1960.

[2] A. F. Bermant, *Course of Mathematical Analysis: Part I*, The Macmillan Company, 1963.

[3] W. T. Brande, editor, *A Dictionary of Science, Literature, and Art: Comprising the History, Description, and Scientific Principles of Every Branch of Human Knowledge: with the Derivation and Definition of All the Terms in General Use*, Harper & Brothers, 1854.

[4] A. Dresden, *Introduction to the calculus*, Henry Holt and company, 1940.

[5] J. Edwards, *An elementary treatise on the differential calculus: With applications and numerous examples*, Macmillan and Co, 1892.

[6] R. H. FOWLER, *The elementary differential geometry of plane curves*, Cambridge, University Press, 1920.

[7] P. FROST, R. J. T. BELL, *An elementary treatise on curve tracing*, Macmillan, 1918.

[8] P. J. GIBLIN, What is an Asymptote?, *Math. Gaz.* **56**(398) (1972), 274–284.

[9] G. GLAESER, H. STACHEL, B. ODEHNAL, *The Universe of Conics: From the ancient Greeks to 21st century developments*, Springer Spektrum, 2016.

[10] W. E. JENNER, *Rudiments of algebraic geometry*, Oxford University Press, 1963.

[11] A. KATALENIĆ, A. ČIŽMEŠIJA, Ž. MILIN ŠIPUŠ, Asymptote in prospective mathematics teachers' graphing praxeologies, *Educação Matemática Pesquisa: Revista do Programa de Estudos Pós-Graduados em Educação Matemática*, **22**(4) (2020), 817–826.

[12] A. KATALENIĆ, A. ČIŽMEŠIJA, Ž. MILIN ŠIPUŠ, Prospective mathematics teachers' knowledge of asymptotes and asymptotic behaviour in calculus, *International Journal of Science and Mathematics Education*, in press.

[13] A. KATALENIĆ, Ž. MILIN ŠIPUŠ, A. ČIŽMEŠIJA, Asymptotes and Asymptotic Behaviour in Graphing Functions and Curves: An Analysis of the Croatian Upper Secondary Education Within the Anthropological Theory of the Didactic, *Int J of Sci and Math Educ* **18** (2020), 1185–1205.

[14] J. D. KEČKIĆ, A method for obtaining asymptotes of some curves, *The teaching of mathematics*, **III**(1) (2000), 53–59.

[15] G. KLAMBAUER, *Aspects of Calculus*, Springer-Verlag, 1986.

[16] J. NUNEMACHER, Asymptotes, Cubic Curves, and the Projective Plane, *Math. Mag.* **3** (1999), 183–192.

[17] T. P. NUNN, Asymptotes, *Math. Gaz.*, **13**(182) (1926), 97–103.

[18] C. B. READ, What is an Asymptote?, *Amer. Math. Monthly* **46**(8) (1939), 498–499.

[19] J. W. RUTTER, *Geometry of curves*, Chapman & Hall, 2000.

[20] E. H. SMART, The Nature of an Algebraic Curve at Infinity and the Conic of Closest Contact at Infinity, *Math. Gaz.* **13**(188) (1927), 357–361.

[21] D. E. SMITH, *History of mathematics*, Dover, 1925.

[22] I. TODHUNTER, *A Treatise on the Differential Calculus: With Numerous Examples*, Macmillan and Co, 1885.

[23] G. ZENG, Computing the asymptotes for a real plane algebraic curve, *Journal of Algebra* **316**(2) (2007), 680–705.

Ana Katalenić
orcid.org/0000-0001-9857-5758
e-mail: akatalenic@foozos.hr

Faculty of Education, University of Osijek
Cara Hadrijana 10, HR-31000 Osijek, Croatia

Aleksandra Čižmešija
orcid.org/0000-0002-5017-4143
e-mail: cizmesij@math.hr

Faculty of Science, University of Zagreb
Bijenička cesta 30, HR-10000 Zagreb, Croatia

Željka Milin Šipuš
orcid.org/0000-0002-0726-3335
e-mail: zeljka.milin-sipus@math.hr

Faculty of Science, University of Zagreb
Bijenička cesta 30, HR-10000 Zagreb, Croatia

https://doi.org/10.31896/k.25.10
Review
Accepted 2. 12. 2021.

CHRISTIAN CLEMENZ
LEONARD WEYDEMANN

Reflection Techniques in Real-Time Computer Graphics

Reflection Techniques in Real-Time Computer Graphics

ABSTRACT

Reflections have a long history in computer graphics, as they are important for conveying a sense of realism as well as depth and proportion. Their implementations come with a multitude of difficulties, and each solution typically has various trade-offs.

Approaches highly depend on the geometry of the reflective surface since curved reflectors are usually more difficult to portray accurately. Techniques can typically be categorized by whether they work with the actual geometry of the reflected objects or with an image of these objects. For curved surfaces, image-based techniques are usually preferred, whereas for planar surfaces the reflected geometry can be used more easily because of the lack of distortion. With current advances in graphics hardware technology, ray tracing is also becoming more viable for real-time applications. Many modern solutions often combine multiple approaches to form a hybrid technique.

In this paper, we give an overview of the techniques used in computer graphics applications to create real-time reflections. We highlight the trade-offs that have to be dealt with when choosing a particular technique, as well as their ability to produce interreflections. Finally, we describe how contemporary state-of-the-art rendering engines deal with reflections.

Key words: reflections, interreflections, real-time rendering

MSC2010: 51-04, 51p05, 78A05

Tehnike zrcaljenja u Real-Time računalnoj grafici

SAŽETAK

Zrcaljenja imaju dugu povijest primjene u računalnoj grafici zbog njihove važnosti u prenošenju realističnosti prikaza te prikaza dubine i omjera na slikama. Pri implementaciji zrcaljenja dolazimo do raznih teškoća i svako novo rješenje često imaju svoju cijenu.

Pristupi implementacije ovise o geometriji plohe na kojoj leži prikaz, što je ploha zakrivljenija, to je teže postići vjerni prikaz. Tehnike možemo kategorizirati u one koje rade sa stvarnom geometrijom zrcaljenih objekata te one koje rade samo sa slikama objekata. Kod zakrivljenih ploha koriste se tehnike bazirane na slikama, dok se kod ravninskih ploha koristi zrcaljena geometrija jer nema iskrivljenja. Zahvaljujući trenutnom razvoju tehnologije grafičkih hardvera, metoda praćenja zraka (ray tracing) postaje sve isplativija u real-time primjeni. Mnoga moderna rješenja kombiniraju razne pristupe i dolazi do hibridnih tehnika.

U ovom radu dajemo pregled tehnika korištenih u primjeni računalne grafike za postizanje real-time zrcalnih slika. Naglašavamo probleme koji nastaju pri korištenju određene tehnike te njihove mogućnosti u pogledu stvaranja međuzrcaljenja. Naposljetku, opisujemo kako moderni alati za renderiranje rješavaju probleme zrcaljenja.

Ključne riječi: zrcaljenje, međuzrcaljenje, real-time renderiranje

1 Introduction

Reflections have been a research topic in Computer Graphics for over forty years because of the big part they play in depicting realistic scenes. They have a great impact on how we perceive things. For example, mirrors can make small spaces look much larger by giving a sense of depth. They can also convey if a surface is rough or smooth and whether it is planar or curved. We were made aware of these important properties and the complex topic, when we created a scene that demonstrates the geometry of a C-60 fullerene using multiple mirrors as seen in Figure 1.

Recently, major advances have been made on the topic of real-time reflections. In addition, their field of application grew as well. Besides their typical use in video games, real-time reflections are now also used in architectural visualization and movie production. But older techniques are also still relevant to this day. Depending on the specific application, each technique has its own advantages and disadvantages.

In the following chapters, we give an overview of the current state-of-the-art techniques to provide the reader with an outline of the advantages and drawbacks one needs to consider (Section 2) and we discuss contemporary multipurpose rendering engines and how they deal with reflections (Section 3).

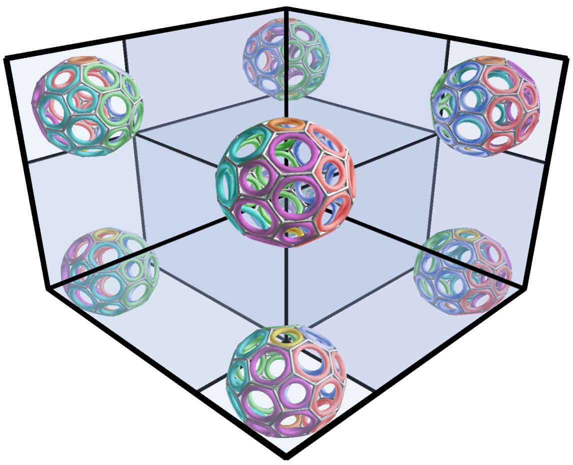

Figure 1: *Interreflections of a single C-60 fullerene created with our implementation of a geometry-based reflection technique. The fullerene is placed in front of three orthogonal mirrors, which are positioned on the XY, XZ and YZ plane respectively.*

2 Techniques

Over the years many different techniques have been developed to create real-time reflections. McReynolds and Blythe [12] categorize them into two groups: object-space and image-space techniques. The former work directly with the geometry while the latter uses textures to create reflections. So, henceforth, we will label these techniques *geometry-based* and *image-based* respectively. Historically, ray tracing was not used in real-time applications because of its long computation time per frame. In recent years, it has become more and more advanced to allow for interactive frame rates. Additionally, the development of new graphics hardware, that has dedicated ray tracing capabilities, has made it suitable for a wider range of real-time applications. Because of this, we include them as a category in our list of techniques. Besides those categories, there are many hybrid techniques that combine multiple approaches to alleviate their individual shortcomings. In this section, we discuss each category in detail, showing examples and considering their advantages and disadvantages.

2.1 Geometry-Based Techniques

McReynolds and Blythe [12] describe geometry-based techniques as approaches that directly transform the geometry of the reflected object. In other words, they create virtual objects that are transformed to represent reflections. This process highly depends on the surface of the reflector.

2.1.1 Planar Surfaces

For planar surfaces, a single affine transformation for each object is enough to describe its reflection, since the reflector's surface normal does not change. This means that it can easily be computed and applied as an additional transformation matrix for example.

Geometry-based techniques need an additional clipping stage, as the virtual object that is created can protrude the plane of reflection or extend beyond its boundary. According to McReynolds and Blythe [12] clipping can easily be done for planar reflectors either by defining custom clipping planes, which the graphics pipeline can use, or by using the stencil buffer to distinguish between pixels that belong to the reflective surface and those that do not. The stencil buffer approach can either be done by rendering the reflector first and then only render the reflected objects inside the stencil or by rendering the reflections first and clearing the image buffer around the stencil afterwards. The second approach can be faster, because the stencil is only used for one clearing operation and not for rendering every individual reflected object. The first approach is better suited for interreflections between multiple reflective surfaces, since the stencil can contain flags that distinguish between different reflectors and the depth of reflection. An example of our implementation using the stencil buffer is shown in Figure 2. We use the stencil to determine where to draw the virtual objects.

2.1.2 Curved Surfaces

In the case of curved reflectors, it gets more complicated. Reflections now also depend on the viewpoint, which can be seen in Figure 3. Therefore, they must now be computed for each vertex individually by finding the correct intersection point of the viewing ray and the reflector sur-

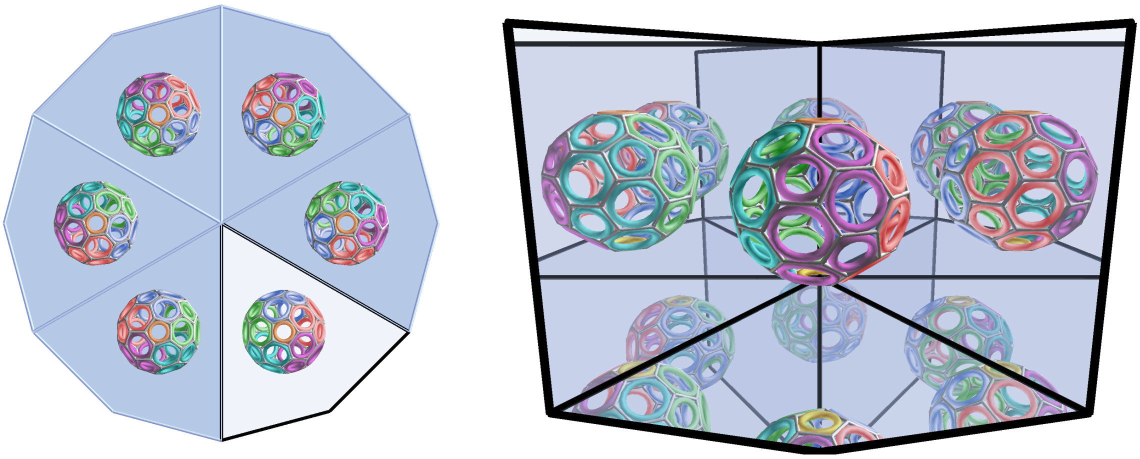

Figure 2: *Our simple reflection setup. We mirror the object for as long as it remains in front of any mirror plane. The left image shows a top-view of the reflections. The final result on the right is created by using a stencil buffer to only render pixels that are inside the mirrors bounds.*

face. McReynolds and Blythe [12] mention that a closed-form solution for finding the reflection point for arbitrary viewpoints, reflector positions, surface shapes, and vertex positions can be very difficult and is usually too complex to generalize.

Ofek and Rappoport [15] proposed a solution for reflections on curved reflectors that creates virtual objects by reflecting each polygon's vertices. They assume that the reflector itself is represented by a polygonal mesh. If this was not he case, they would tesselate the reflector. Each polygon on the reflector divides the space around the reflector into a hidden and a visible cell. Each reflected object is also tesselated depending on the desired resolution of the result. Afterwards, each polygon of the reflected object is reflected. This is done by finding the virtual reflected vertex for each vertex in the polygon. In order to reflect this vertex correctly, Ofek and Rappoport find the polygon on the reflector that is used as the mirror. To prevent the result from looking like a linear approximation, they use the barycentric coordinates of the mirrored vertices inside the cell above the reflector polygon to interpolate between the three tangent planes associated with the reflector polygon. This interpolation is then used as the final plane of reflection for that particular vertex. In order to quickly find out in which cells the vertices are located, Ofek and Rappoport [15] use an *explosion map* as their data structure. Explosion maps are very similar to environment maps, which we will discuss in Section 2.2.1. Instead of color information the map contains polygon IDs to quickly find surface polygons for any given UV coordinate. They claim that their method works best for convex surfaces but it also works for concave surfaces. Surfaces that have both convex and concave areas should be split into separate meshes.

McReynolds and Blythe [12] mention that clipping the virtual objects created by such a method against curved reflectors directly is possible but can be a time consuming operation if the reflector is complex. An alternative would be to use the depth buffer to only render objects with greater depth than the reflector, but this would also render them incorrectly if one virtual object occludes another one.
To summarize, creating reflections using curved reflectors paired with a geometric approach can be very complicated, depending on scene size and complexity. The results are relatively accurate but usually other approaches are preferred for curved reflectors, as we will see in the next section.

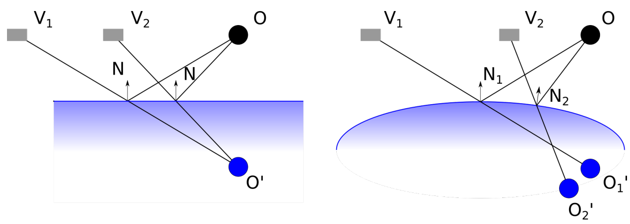

Figure 3: *A comparison of reflection rays on planar and curved surfaces. On the left the object O gets reflected to the same virtual position O' because the surface normal N does not change. On the right the same object's reflection point varies depending on the viewing position.*

2.2 Image-Based Techniques

As the name implies image-based techniques use images or textures to create reflections. McReynolds and Blythe [12] state that these textures are then used for the reflective surface which is the case for environmental mapping.

Additionally, we also include approaches into this category that use the final or intermediate rendered image itself.

2.2.1 Environment Mapping

An early technique that was developed to create reflections is *environment mapping*, which is also often called *reflection mapping*. The idea is to project the scene onto the surface of a primitive centered around the reflective object. This is done by rendering the scene, viewed from the center point of the reflective object, onto six images forming a cube. These images are mapped onto the primitive using a mapping function that depends on the type of primitive. During the rendering step, another function is needed to retrieve the information from the map.

One of the most popular environment mapping methods is cube mapping and was proposed by Greene [7]. The map is created as described above and uses the cube formed by the image planes directly without re-mapping. The cube can be aligned with the coordinate axes, so that the largest vector component of the reflected viewing direction determines the face that needs to be indexed directly. The texture coordinates are determined with the remaining two components. If the cube is not aligned, the cube faces have to be tested for intersection with the reflected viewing ray. An example of cube map indexing can be seen in Figure 4.

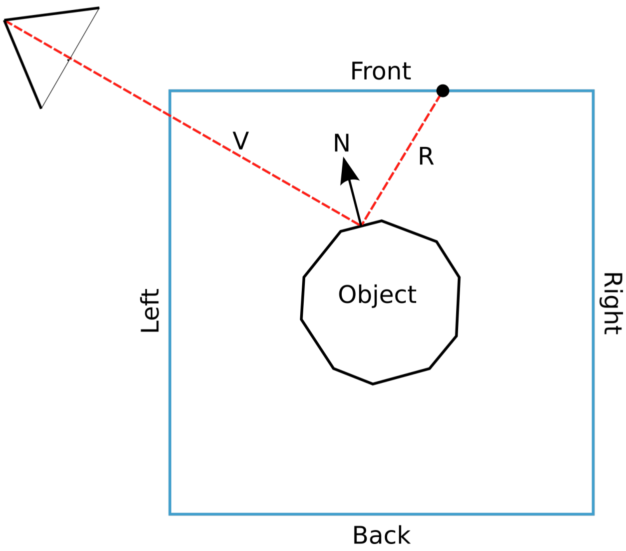

Figure 4: *A top-view of cube map indexing. The viewing direction V is reflected in the object's surface normal N. The reflected direction R determines the cube face and the texture coordinates to use for the final color value.*

Another technique that was proposed very early on by Blinn and Newell [4] is sphere mapping, which uses a sphere as the primitive onto which to map the environment. The key difference is that the image planes get mapped onto a sphere whose surface is then re-mapped to a circular shape inside a 2D texture. This has the advantage that all information is contained in only a single image. However, sphere maps also have drawbacks. Some texture space is wasted since the texture itself is rectangular. But more importantly, they introduce sampling problems. While texture coordinates are interpolated linearly, sphere maps are non-linear. This leads to interpolation artefacts, especially close to the edge of the circular image.

Regardless of which primitive is used, environment mapping is especially useful for curved reflectors, because reflections can be calculated without complex geometrical transformations for each object's vertex in the scene. In some cases, it is also convenient that the maps can be preprocessed if the surroundings or the reflectors are static. On the other hand, if either the surroundings or the position of the reflector, i.e. the reflection center, change, the map needs to be recalculated. The resolution of the texture map is also important since it influences how accurately the reflection can be depicted. In addition, their accuracy depends on the distance between the reflected object and the reflector and will be better for more distant objects. According to McReynolds and Blythe [12] interreflections are possible by iteratively creating the environment maps for each reflector and then applying them for the next iteration.

More information and specific calculations for the mappings mentioned above can be found in the work of Mizutatni and Reindel [13] and in McReynolds and Blythe [12].

Building on these environment mapping methods, Yu et al. [20] developed a technique to improve on regular environment maps by using 4D *light fields* instead of 2D textures. Light fields are a collection of images on a 2D image plane. From those images, every possible viewing ray can be synthesized inside a given region, according to Yu et al. By surrounding the reflector with six such light fields, they can support dynamic reflections for moving reflectors inside the cube, including motion parallax.

Another extension to environment mapping can be found in Popescu et al. [16]. In addition to environment maps, they use two types of impostors to approximate the geometry of objects in the scene. The first type is the billboard. It approximates an object by mapping its image to a textured quadrilateral which can easily be intersected with reflected viewing rays. Optionally, they can also store surface normals per texel, to facilitate interreflections. The second type of imposter they use, is the depth map which is a billboard with an added depth channel. The depth maps improve reflections in cases where the object is close to the reflector or when the object and the reflector intersect. They also allow for motion parallax. Popescu et al. suggest that their method can be regarded as a middle ground between environment maps and ray tracing. The impostors use more geometric information than the environment, but do not have as much geometric complexity as ray tracing.

2.2.2 Screen Space Techniques

A modern approach that has been developed in the last decade is called *Screen-Space Reflections* (SSR). The method was introduced as Real-Time Local Reflections by Sousa et al. [17]. This approach creates the reflections in a post-processing step. First, the scene is rendered into a buffer structure called *G-Buffer*. The G-Buffer is a collection of render targets that contains diffuse color information but also the geometrical information for each pixel of the rendered scene. It stores depth, surface normal and position values. After rendering to the G-Buffer, a ray is shot from the viewing position towards each surface point stored in the G-Buffer and then it is traced along its reflected ray using the stored surface normal. This ray is sampled at specific intervals. The sample points are mapped into the 2D screen space, where the sample point's depth is checked against the G-Buffers depth value. If the depth value in the G-Buffer is lower, this marks an intersection. An illustration of this process can be seen in Figure 5.

Sousa et al. [17] mention that, while it is a relatively fast technique, it can have problems due to the very limited information in screen space. McGuire et al. [11] give detailed information on the implementation of Screen-Space Reflections and improve the path sampling for more efficiency. A major drawback of this method is that it can only produce reflections of objects that are contained inside the current view. Tracing rays outside the image is not possible. This can lead to artefacts on the image boundary.

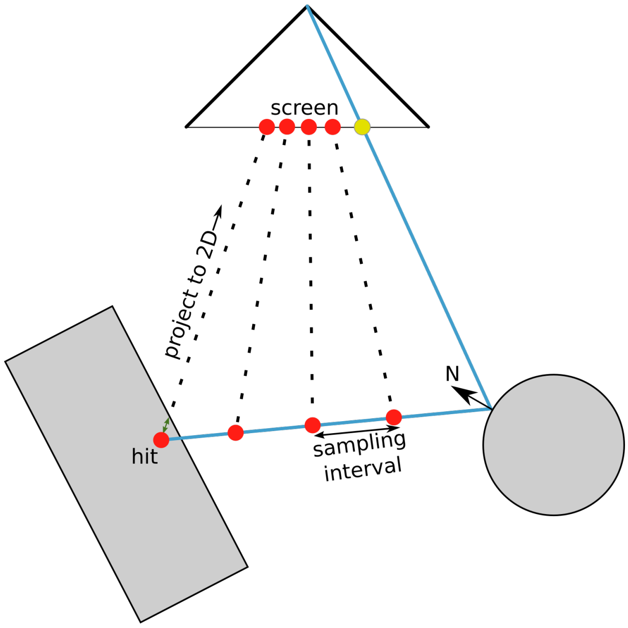

Figure 5: *A top-down overview of Screen-Space Reflection. A ray is shot through the current pixel in yellow. It is reflected using the surface normal N, that is contained in the current pixel of the G-Buffer. The reflected ray gets sampled and projected into Screen-Space. As soon as the sample depth is bigger than the depth in the G-Buffer, an intersection has been found. The color value of the intersection in the G-Buffer is then used for the final color in the current pixel.*

2.3 Real-Time Ray Tracing Techniques

An early implementation of ray tracing goes back to the work of Whitted [19]. He proposed a method for realistic rendering by following the viewing ray through the scene and recursively applying the intersection information to the current pixel. The number of how often the ray is reflected needs to be limited to keep the computation time low, but the higher the number the better the result. While this method works very well to create realistic images, it is computationally expensive. It heavily relies on visible surface algorithms to only test for intersections on an object if the ray crosses its bounding volume, instead of testing all objects in the scene. This technique alone is not sufficient for high-resolution images at interactive frame rates in complex scenes. There have been many improvements to this ray tracing algorithm, but only in recent years it was getting to a point where the results became real-time viable through advanced techniques and dedicated ray tracing hardware.

Bounding Volume Hierarchies (BVH) and *KD-trees* are essential for improving ray tracing speed, as they reduce the number of objects that need to be checked for intersection. An overview of these ray tracing data structures and architectures can be found in Deng et al. [5]. Recent advances have made it possible to construct a BVH in real-time as shown in Lauterbach et al. [9]. This allows for highly complex and dynamic scenes where the spatial data structure needs to change every frame. Denoising algorithms also greatly reduce the number of reflected rays needed per pixel to generate images without visible artefacts. State-of-the-art techniques for denoising ray traced images can be found in the papers by Bako et al. [1] and Marrs et al. [10]. Bako et al. use neural networks to denoise the images. Marrs et al. introduce an improved temporal antialiasing technique that uses adaptive ray tracing.
The most recent GPU architectures come with ray tracing cores that are capable of computing the above-mentioned algorithms in parallel directly on the GPU, allowing for notably faster image generation. Details on the most recent algorithms and architecture can be found in the Turing architecture white paper by NVIDIA [14].

To summarize, the biggest advantage of real-time ray tracing are the accurate reflections they produce. Interreflections are not only possible but inherently come with the algorithm. Despite the recent improvements real-time ray tracing is still dependent on dedicated hardware.

2.4 Hybrid Techniques

Each of the before mentioned techniques has its own shortcomings. Some of them can be avoided or alleviated by using more than one technique.

An early hybrid technique can be found in the work of Kilgard [8]. It combines planar reflections with stencil buffer clipping. This improves the clipping stage in certain cases. Interreflections, for example, can be done quite easily with the stencil buffer as it allows for marking individual pixels with the interreflection recursion depth.

Bastos and Stürzlinger [3] developed a hybrid approach that improves upon traditional environment mapping. They call it a hybrid between a geometry-based and an image-based solution. They warp the texture contained in the environment map into the space of the reflected viewpoint. In addition to the color information stored in the environment map, they also store the depth value of the texels. Their method preserves the depth of the reflected scene and corrects the perspective distortion that appears in classic environment mapping techniques. A detailed description for viewpoint warping can be found in their paper [3].

A more recent hybrid approach was proposed by Ganestam and Dogget [6]. They wanted to seamlessly trace paths in the scene, without using a full ray tracing approach. So, they developed a heuristic scene tracing approach. They divide the scene into different volumes. In a volume that is close to the camera, objects are placed inside a BVH (see Section 2.3), which is updated every frame. Outside this first volume, objects are rendered into a cube map structure of G-buffers. These buffers can be used for tracing the path in image space, reducing the complexity of the scene outside the innermost volume. Rays can be seamlessly traced between these two volumes. The combination of those two techniques is very efficient in avoiding the long computation times of ray tracing and the problems that come with the image-based buffer technique.

Walewski et al. [18] developed a method for hybrid rendering that determines which parts of the scene are to be rendered with secondary effects, like shadows and reflections, by calculating an importance value for them. They estimate the time it takes to render an object using ray tracing and weigh it against the importance value. Then they sort the scene into a graph, putting the more relevant objects at the top. When calculating the secondary effects, they start with the objects with the highest importance value and then follow the graph towards the most important objects that can still fit into the remaining available calculation time for the current frame. The importance value depends on multiple variables. Most of them are calculated every frame, like the size in the viewport, for example. Some are also determined by the user beforehand, for example, how important it is to select objects that were previously chosen for secondary effects. For a detailed description of how the importance value is calculated see the paper of Waliewski et al. [18].

The *PICA PICA* hybrid rendering pipeline is a hybrid rendering approach by Barré-Brisebois et al. [2] that combines traditional rasterization shaders with compute shaders and ray tracing shaders for the entire rendering pipeline. Their method does not specifically focus on reflections, but they are included as an integral part of their feature set. They state that reflections are one of the main features that benefit from ray tracing. Although they incorporated Screen-Space Reflections into their approach, they mostly use ray tracing for the final result to keep it simple. They also make use of denoising algorithms we previously mentioned in Section 2.3, that work on the final image to remove artefacts in areas where the number of traced rays was not high enough.

3 State-of-the-Art Rendering Engines

Currently, there are many real-time rendering engines publicly available. Most of them use state-of-the-art computer graphics techniques to portray realistic scenes and effects. Among those techniques, reflections are only a small subset of their capabilities, albeit a very important one. We will discuss two examples of freely available engines and compare their approaches and capabilities to give an insight into how they can produce real-time reflections. We chose these two because of their popularity and their extensive documentation.

3.1 Unreal Engine 4

The Unreal Engine 4 offers multiple different ways to produce real-time reflections. The first one uses planar reflections. This is Unreal Engine's geometric approach to render the scene a second time using a user-defined plane as a mirror. The engine handles clipping and reflective objects around the plane are taken care of automatically. This feature must be turned on deliberately in the engine's settings before it is available to the user, as it is potentially expensive to compute. Furthermore, they advise to only use a few of these planes if any at all, since it directly corresponds to the scene's complexity. To compensate for this the engine has multiple parameters to limit the number of reflected objects, for example, a maximum distance. More information can be found in the Unreal Engine Documentation on planar reflections [24].

The second method the Unreal Engine offers is Screen Space Reflections. This method is turned on by default. It generates little computational overhead as compared to other methods. There are only very few parameters to tweak the result, but the most notable one certainly is the quality setting that can be set between 0 and 100, with 50 as the default. The documentation [26] does not mention exactly how this parameter affects the algorithm.

The third option for reflections uses environment mapping. This method comes in multiple different forms. The Unreal Engine defines these as *Reflection Capture Actors* and *Scene Capture Actors* [23] that can be placed inside the scene. The former ones only map reflections inside a user-defined volume. This volume is either a cuboid or spherical. Their reflections are computed before run time and do not affect per frame computation time very much, since they are just environment maps which we already discussed in Section 2.2.1. The latter ones are fully dynamic cube maps. Their maps capture the entire scene and are recalculated on every frame, according to the documentation. This comes with a large computational cost. There is also the option for a 2-dimensional screen capture that works similarly but only maps to one texture instead of six cube map faces.

The final method for real-time reflections in Unreal Engine 4 is one that uses real-time ray tracing [25]. Its ray tracer is actually a hybrid between conventional ray tracing and raster effects, according to the documentation. A key ingredient for real-time viability is the denoising algorithm used by the engine. This allows for fewer samples during ray tracing.

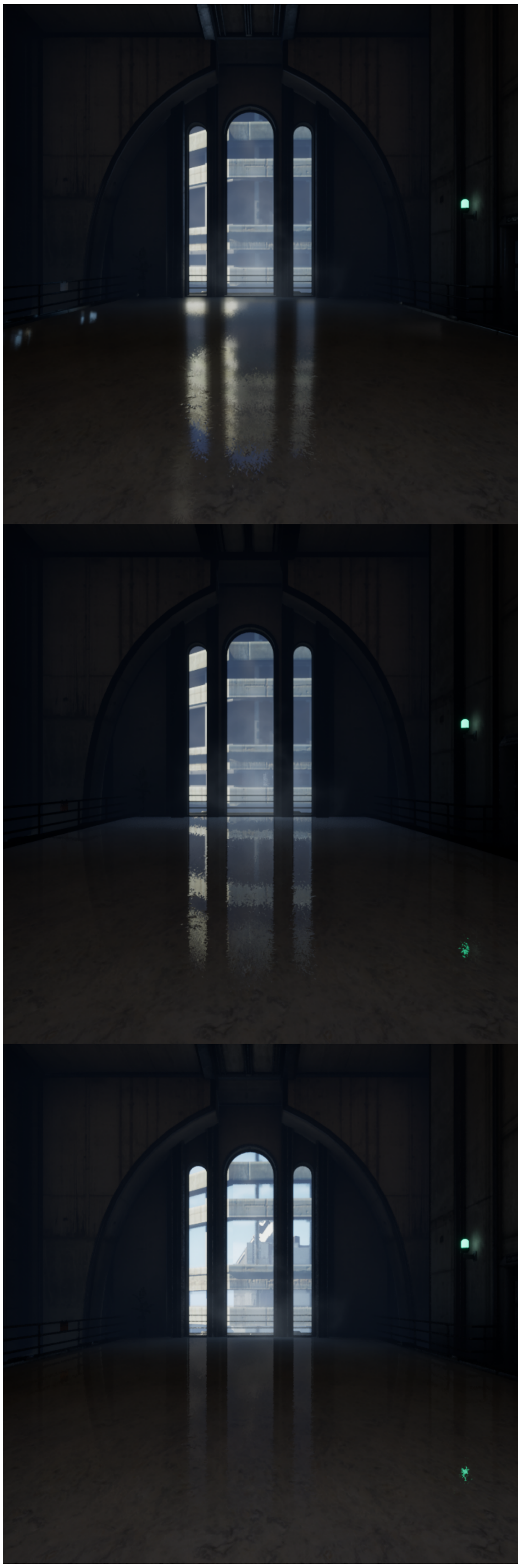

Figure 6: *A comparison of environment mapping (top), screen-space reflections (middle) and ray tracing (bottom) using Unreal Engine 4. The images are taken from the* BlueprintOffice *scene by Epic Games with the default rendering settings. The top image uses only* Reflection Capture Actors. *Notice how the reflection of the blue light source is not captured here. The reflections on the floor are blurry due to the limited environment map resolution. The windows of the building in the background are not encompassed by an environment map and therefore do not show reflections. In the middle image, only screen-space reflections are used. Thereby, the windows of the opposite building cannot show reflections because the outside walls of the room are not contained in the rendered image. The reflections on the floor are sharper because they use information from the rendered image directly. The bottom image uses ray tracing with a single bounce after the first intersection. The biggest difference in this image, compared to the other two, is that the windows of the building in the background show reflections of the exterior. The reflections on the floor are also sharper but much more subtle.*

Figure 6 shows a comparison of images that were created using different reflection techniques which are available in Unreal Engine 4.

3.2 Unity

Unity also supports multiple reflection techniques but their rendering engine is split into three separate rendering pipelines supporting different effects. When choosing a specific reflection technique, this has to be taken into account. See the Unity rendering pipeline documentation [22, 21] for a comparison between the rendering pipelines.

Similar to the Unreal Engine, Unity offers environment mapping in the form of cube maps. Here they are called *Reflection Probes*. They are placed inside the scene and can be used by any reflective object that comes close to the Reflection Probe. If there are multiple probes close to reflectors, the final reflection gets interpolated between their environment maps. According to the Unity documentation, this technique is available in every currently supported rendering pipeline, albeit with some minor differences.

Screen Space Reflections are available as a post-processing effect, but only in the High Definition Rendering Pipeline.

Real-time ray tracing is currently in preview and only available inside the High Definition Rendering Pipeline. Their approach is to completely replace other rasterized effects with ray tracing. This means that the ray traced reflections replace the screen space reflections. Additionally, ray tracing is not supported in combination with Reflection Probes.

4 Conclusion

Reflections in real-time scenes can be achieved in multiple ways. Geometry-based techniques can produce realistic results and are easy to calculate for planar reflectors, but curved surfaces are too complex to find a generalized solution. Image-based techniques can break the complexity of curved reflectors, since they work in image space rather than object space. Although not accurate, environment maps give a good approximate solution that can be calculated before run-time. Screen-Space Reflections work well for accurate reflections in real-time but are limited to the information of the camera view. Real-time ray tracing is getting more viable with dedicated hardware and improved algorithms to reduce tracing complexity. Hybrid approaches can compensate for the drawbacks of individual methods and can also produce fast and accurate results even though they can be more complex. Current state-of-the-art engines offer the user a variety of techniques to choose from to fit their individual needs.

References

[1] S. Bako, T. Vogels, B. Mcwilliams, M. Meyer, J. Novák, A. Harvill, P. Sen, T. Derose, F. Rousselle, Kernel-predicting Convolutional Networks for Denoising Monte Carlo Renderings, *ACM Transactions on Graphics (TOG)* **36**(4) (2017), 1–14.

[2] C. Barré-Brisebois, H. Halén, G. Wihlidal, A. Lauritzen, J. Bekkers, T. Stachowiak, J. Andersson, Hybrid Rendering for Real-Time Ray Tracing, *Ray Tracing Gems: High-Quality and Real-Time Rendering with DXR and Other APIs*, Apress, 2019, 437–473.

[3] R. Bastos, W. Stürzlinger, Forward Mapped Planar Mirror Reflections, *University of North Carolina at Chapel Hill, Computer Science Technical Report TR98-206* (1998).

[4] J.F. Blinn, M.E. Newell, Texture and Reflection in Computer Generated Images, *Communications of the ACM* **19**(10) (1976), 542–547.

[5] Y. Deng, Y. Ni, Z. Li, S. Mu, W. Zhang, Toward Real-Time Ray Tracing: A Survey on Hardware Acceleration and Microarchitecture Techniques, *ACM Computing Surveys (CSUR)* **50**(4) (2017), 1–41.

[6] P. Ganestam, M. Doggett, Real-time Multiply Recursive Reflections and Refractions Using Hybrid Rendering, *The Visual Computer* **31** (2015), 1395–1403.

[7] N. Greene, Environment Mapping and Other Applications of World Projections, *IEEE computer graphics and Applications* **6**(11) (1986), 21–29.

[8] M. Kilgard, Creating Reflections and Shadows Using Stencil Buffers, *At Game Developers Conference* **7** (1999).

[9] C. Lauterbach, M. Garland, S. Sengupta, D. Luebke, D. Manocha, Fast BVH Construction on GPUs, *Computer Graphics Forum* **28**(2) (2009), 375–384.

[10] A. Marrs, J. Spjut, H. Gruen, R. Sathe, M. McGuire, Improving Temporal Antialiasing with Adaptive Ray Tracing, *Ray Tracing Gems: High-Quality and Real-Time Rendering with DXR and Other APIs* (2019), 353.

[11] M. McGuire, M. Mara, Efficient GPU Screen-Space Ray Tracing, *Journal of Computer Graphics Techniques (JCGT)* **3** (2014), 73–85.

[12] T. McReynolds, D. Blythe, *Advanced Graphics Programming Using OpenGL*, Elsevier, 2005.

[13] Y. Mizutani, K. Reindel, *Environment Mapping Algorithms*, `https://www.reindelsoftware.com/Documents/Mapping/Mapping.html`, Accessed: 2021-8-4.

[14] NVIDIA, *NVIDIA Turing GPU Architecture*, White Paper, 2018.

[15] E. Ofek, A. Rappoport, Interactive Reflections on Curved Objects, *Proceedings of the 25th annual conference on Computer graphics and interactive techniques* (1998), 333–342.

[16] V. Popescu, C. Mei, J. Dauble, E. Sacks, Reflected-scene Impostors for Realistic Reflections at Interactive Rates, *Computer Graphics Forum* **25**(3) (2006), 313–322.

[17] T. Sousa, N. Kasyan, N. Schulz, Secrets of CryENGINE 3 Graphics Technology, *SIGGRAPH, Advances in Real-Time Rendering in 3D Graphics and Games* (2011).

[18] P. Walewski, T. Gałaj, D. Szajerman, Heuristic Based Real-Time Hybrid Rendering with the Use of Rasterization and Ray Tracing Method, *Open Physics* **17**(1) (2019), 527–544.

[19] T. Whitted, An Improved Illumination Model for Shaded Display, *Proceedings of the 6th annual conference on Computer graphics and interactive techniques* **17**(1) (1979), 14.

[20] J. Yu, J. Yang, L. McMillan, Real-Time Reflection Mapping with Parallax, *Proceedings of the 2005 symposium on Interactive 3D graphics and games* (2005), 133–138.

[21] *Unity High Definition Rendering Pipeline Documentation*, `https://docs.unity3d.com/Packages/com.unity.render-pipelines.high-definition@12.0/manual/Feature-Comparison.html`, Accessed: 2021-9-14.

[22] *Unity Universal Rendering Pipeline Documentation*, `https://docs.unity3d.com/Packages/com.unity.render-pipelines.universal@12.0/manual/universalrp-builtin-feature-comparison.html`, Accessed: 2021-9-14.

[23] *Reflections in the Unreal Engine Manual*, `https://docs.unrealengine.com/4.26/en-US/Resources/Showcases/Reflections/`, Accessed: 2021-5-27.

[24] *Planar Reflections in the Unreal Engine Manual*, `https://docs.unrealengine.com/4.26/en-US/BuildingWorlds/LightingAndShadows/PlanarReflections/`, Accessed: 2021-7-28.

[25] *Ray Tracing in the Unreal Engine Manual*, `https://docs.unrealengine.com/4.26/en-US/RenderingAndGraphics/RayTracing/`, Accessed: 2021-9-22.

[26] *Screen-Space Reflections in the Unreal Engine Manual*, `https://docs.unrealengine.com/4.27/en-US/RenderingAndGraphics/PostProcessEffects/ScreenSpaceReflection/`, Accessed: 2021-9-22.

Christian Clemenz
e-mail: christian.clemenz@uni-ak.ac.at

University of Applied Arts Vienna
Oskar-Kokoschka-Platz 2, A-1010 Vienna, Austria

Leonard Weydemann
e-mail: leonard.weydemann@uni-ak.ac.at

University of Applied Arts Vienna
Oskar-Kokoschka-Platz 2, A-1010 Vienna, Austria

INSTRUCTIONS FOR AUTHORS

SCOPE. "KoG" publishes scientific and professional papers from the fields of geometry, applied geometry and computer graphics.

SUBMISSION. Scientific papers submitted to this journal should be written in English, professional papers should be written in Croatian or English. The papers have not been published or submitted for publication elsewhere.
The manuscript should be sent in PDF format via e-mail to the editor:

Ema Jurkin
ema.jurkin@rgn.hr

The first page should contain the article title, author and coauthor names, affiliation, a short abstract in English, a list of keywords and the Mathematical subject classification.

UPON ACCEPTANCE. After the manuscript has been accepted for publication authors are requested to send its LaTex file via e-mail to the address:

ema.jurkin@rgn.hr

Figures should be titled by the figure number that match to the figure number in the text of the paper.

The corresponding author and coauthors will receive hard copies of the issue free of charge.

How to get KoG?

The easiest way to get your copy of KoG is by contacting the editor's office:

Marija Šimić Horvath
marija.simic@arhitekt.hr
Faculty of Architecture
Kačićeva 26, 10 000 Zagreb, Croatia
Tel: (+385 1) 4639 176

The price of the issue is €15 + mailing expenses €5 for European countries and €10 for other parts of the world.

The amount is payable to:

ACCOUNT NAME:	Hrvatsko društvo za geometriju i grafiku Kačićeva 26, 10000 Zagreb, Croatia
IBAN:	HR8623600001101517436

ISSN 1331-1611